THE INTERPRETATION OF MAGNETOTELLURIC MEASUREMENTS FROM THE GLENNIE DOMAIN TO THE FLIN FLON BELT, EASTERN SASKATCHEWAN: PART OF THE LITHOPROBE, TRANS-HUDSON OROGEN TRANSECT

by

Kevin Maxwell Stevens

Department of Geological Sciences

A thesis submitted in partial fulfillment
of the requirements for the degree of
Master of Science, in Geophysics

Faculty of Graduate Studies,
The University of Manitoba,
Winnipeg, Manitoba
November, 1998

THE UNIVERSITY OF MANITOBA

FACULTY OF GRADUATE STUDIES

*****

COPYRIGHT PERMISSION PAGE

THE INTERPRETATION OF MAGNETOTELLURIC MEASUREMENTS FROM THE GLENNIE DOMAIN TO THE FLIN FLON BELT, EASTERN SASKATCHEWAN: PART OF THE LITHOPROBE, TRANS-HUDSON OROGEN TRANSECT

BY

KEVIN MAXWELL STEVENS

A Thesis/Practicum submitted to the Faculty of Graduate Studies of The University of Manitoba in partial fulfillment of the requirements of the degree of

MASTER OF SCIENCE

ABSTRACT

During 1992 broadband magnetotelluric (MT) and audiofrequency magnetotelluric (AMT) surveys were completed on a continuous profile across the Trans-Hudson Orogen. These surveys followed the LITHOPROBE deep seismic reflection survey along the transect. A 200 kilometre section of this transect, immediately west of the Saskatchewan-Manitoba border, traverses the Glennie Domain (GD) and Hanson Lake Block (HLB) and extends into the western Flin Flon Belt (FFB). The GD is composed of arc volcanic and plutonic rocks and the HLB is composed of mixed arc derived gneisses. Both of these tectonic units are believed to be underlain by Archean crust. The GD-HLB boundary is defined by the north-south striking Tabbernor Fault Zone (TFZ) and the eastern edge of the HLB is marked by the Sturgeon Weir Thrust (SWT). Seismic reflection images provide indirect evidence that the TFZ and SWT are steeply dipping structures. The FFB consists of mostly low metamorphic grade, mafic to felsic, metavolcanic rocks with subordinate metasediments.

Data from twenty-eight AMT and MT sites along the LITHOPROBE transect have been analyzed in order to resolve the electrical conductivity structure of the crust and subcrustal lithosphere in the GD-HLB region. Detailed analysis of the MT data using dimensionality and directionality methods including induction vectors and Groom-Bailey tensor decomposition, identified frequency ranges in which groups of MT sites have a quasi-two dimensional MT response and a geologically plausible strike. Upon completion of this analysis the data set was divided into several

components with distinct geoelectric responses: 1) AMT data for sites over Phanerozoic cover, 2) low frequency (<0.1 Hz) MT data for all sites and 3) the MT responses of five sites straddling the TFZ-HLB area.

Analysis of the data from 14 AMT/MT sites located on the Phanerozoic cover overlying the Glennie Domain showed that a one dimensional (1-D) interpretation provides a reasonable representation of the resistivity structure of the Phanerozoic sedimentary cover and upper crustal structure. Apparent resistivity and phase pseudo-sections show similar responses for both MT polarization modes. One dimensional and two dimensional (2-D) inversion of data from the sites on Phanerozoic cover was done using both the Bostick transform and the Occam inversion methods. These results suggest a fairly uniform low resistivity (50-200 Ω.m) layer extending to about 250 metres depth. This layer thins to the east along the profile towards the margin of the Phanerozoic rocks. Below sites between M23 and M22 the upper crust includes a conductive region (<100 Ω.m) extending to depth (10 km) within a background of more resistive material (>1000 Ω.m).

Examination of the other two MT data sets showed that these data could be treated using a 2-D approach. This analysis indicated a large scale, layered conductivity structure, dipping east, a model which is in good agreement with the geological interpretation provided by the seismic data. These data also provided direct evidence that the TFZ and SWT are both low resistivity features (<1000 Ω.m). Additional 2-D analysis was performed to assess the MT results. The calculation of the MT response of starting models derived from seismic information allowed for an additional

comparison of the seismic and MT results. Overall there is good correlation between the seismic and MT models, however, the MT responses better resolved the structures of the TFZ, HLB and SWT. In addition, the MT data resolved spatial variations within the Proterozoic and Archean units that were not evident in the seismic information.

ACKNOWLEDGMENTS

Many individuals and organizations deserve recognition for their role in the development of this project. Phoenix Geophysics performed the data collection and achieved a high level of data quality throughout the survey. The THOT MT data collection was 'bird dogged' by Colin Farquharsson (University of British Columbia), Trevor Boyce (University of Manitoba) and Ian Ferguson (University of Manitoba). Alan Jones (Geological Survey of Canada) performed general coordination of the THOT MT data collection and Jim Craven (Geological Survey of Canada) supplied valuable software support.

I would like to thank LITHOPROBE for funding the various aspects of the data collection, my travel to THOT workshops and the rental of a SUN LX workstation for data reduction/interpretation.

Dr. Ian Ferguson was my thesis adviser and has provided great guidance and support during the development of this thesis. His ideas, advice and knowledge are greatly appreciated.

Finally, I would like to thank my wife, Carman, for her continuous support and patience over the extended period it took to complete this work.

TABLE OF CONTENTS

LIST OF FIGURES

LIST OF TABLES

CHAPTER 1

INTRODUCTION

1.1 Overview of the Thesis

In the past decade, the Canadian LITHOPROBE program has explored the crustal structure of orogenic belts ranging in age from Archean to recent (Clowes, 1993) via integration of reflection and refraction seismology, deep electromagnetic (EM) soundings such as magnetotellurics (MT), and other geophysical-geological studies. In this thesis I will analyze and discuss the results of MT investigations along a 200 km east-west transect spanning part of the Paleoproterozoic Trans-Hudson Orogen (THO) in northern Saskatchewan and Manitoba. The MT data sets were collected across the Glennie Domain to Flin Flon Belt (GD-FFB). Details of the reduction of the MT data through statistical as well as empirical means will be presented. The capability of the processed data to show horizontal and vertical components of the Earth's lithospheric structure below the MT sites will be examined through two-dimensional (2-D) pseudosection imaging of the crustal conductivity. Inversion results obtained from the MT data will be compared with recent seismic and geological studies of the same region. Structural and petrophysical constraints derived from seismic, geological and other geophysical means will then be integrated into the modelling and interpretation of the MT data. The geoelectric structure and ultimately the contributions of the MT investigations to the overall objectives of the

transect will then be assessed by identifying new crustal information obtained by using the MT method.

1.2 LITHOPROBE and the Trans-Hudson Orogen Transect (THOT)

LITHOPROBE is Canada's national, collaborative, multidisciplinary Earth Science research project established to develop a comprehensive understanding of the evolution of the North American continent (Clowes, 1993). The nature of this continental evolution is understood by determining the present three-dimensional (3-D) structure and the geotectonic processes that formed that structure. A series of ten transects (study areas), aimed at a number of specific geological target areas, form the basis of LITHOPROBE's principal scientific and operational components. The transects span the country from Vancouver Island to Newfoundland; from the US border to the Yukon and Northwest Territories; and in geological time, from four billion years ago to the present (Clowes, 1993). Figure 1.1 shows a simplified tectonic element map of North America with the locations and names of each transect.

Located in northern Saskatchewan and Manitoba, the Trans-Hudson Orogen Transect (THOT) is the only fully preserved Early Proterozoic orogenic belt in North America (Clowes, 1993). The THO is the principal component of a series of belts formed by Proterozoic crustal accretion and collision with pre-existing Archean continents. The exposed Archean continents of the THO are the Superior

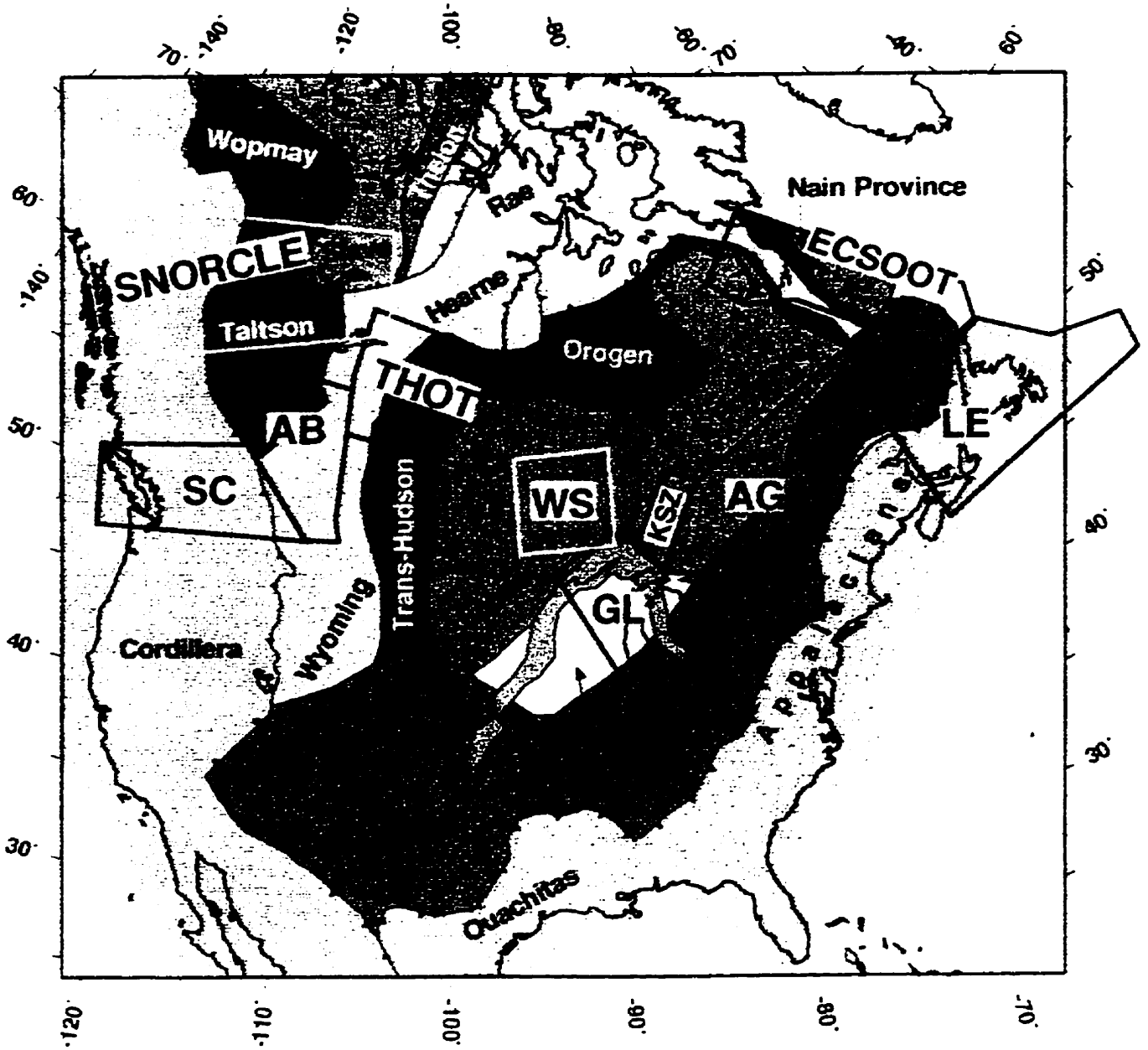

Figure 1.1 *Location of LITHOPROBE transects (study areas) on a simplified tectonic element map of North America. The transects are: SC - Southern Cordillera; AB - Alberta Basement; SNORCLE - Slave-Northern Cordillera Lithospheric Evolution; THOT - Trans-Hudson Orogen; WS - Western Superior; KSZ - Kapuskasing Structural Zone; GL - Great Lakes International Multidisciplinary Program on Crustal Evolution (GLIMPCE); AG - Abitibi-Grenville; LE - Lithoprobe East; and ECSOOT - Eastern Canadian Shield Onshore-Offshore. Archean provinces are Slave, Wyoming, Hearne, Rae, Superior and Nain. Proterozoic elements include Wopmay, Taltson, Thelon, Trans-Hudson Orogen, Keweenawan Rift System, Penokean Fold Belt and the Grenville Province. Phanerozoic orogens are the Cordillera, Ouachitas and Appalachians.* (after Clowes, 1993)

Province to the southeast, the Hearne and Rae provinces to the northwest and the Wyoming province to the southwest (Figure 1.1). In northern Saskatchewan and Manitoba, the 500 km wide orogen includes four major lithotectonic zones: a southeast foreland zone, an internal zone of juvenile Proterozoic crust, an Andean type magmatic arc batholith and a northwest hinterland zone, each of which is divided into contrasting smaller domains. The THO is one of the Earth's great examples of a preserved collisional belt representing the 'glue' that stuck together older pieces (Archean microcontinents) of North America while simultaneously generating significant volumes of new material (Clowes, 1993).

1.3 THOT Objectives and the Role of Magnetotelluric (MT) Measurements

The THOT was designed to investigate the present lithological, structural, petrophysical and geometrical characteristics of one of the best preserved and exposed Early Proterozoic orogenic belts in the world (Clowes, 1993). The overall objective of the THOT work is to better understand the geotectonic processes involved in its evolution. This is done by revealing and examining the structures in the crust as well as other lithospheric characteristics of its primary components. Specific major objectives are:

* determination of the subsurface position and attitude of the margins of the bounding Archean cratons and their possible extension beneath the younger rocks of the internal zone;

* to establish whether geological indications of gross northwesterly subduction polarity are supported by the deep crustal structure of the collisional zone;
* delineation of the three dimensional geometry of major faults and shear zones within and at the margins of the various domains and to define the nature of structural boundaries at the northwestern edge of the orogen;
* to test the hypothesis of major nappe/thrust sheets in the Reindeer Zone;
* to establish the spatial structural affiliation of the North American Central Plains conductivity anomaly to lithotectonic elements of the orogen (Jones et al., 1993); and,
* to compare and contrast integral features of the Trans-Hudson Orogen with more recent collision zones such as the western Himalayas where comparable oceanic rocks are sandwiched between convergent continents (Clowes, 1993).

The scale and scope of the investigations in the LITHOPROBE transects requires that remotely sensed geophysical measurements must be used to supply information on the subsurface structure to great depths. For the most part two main deep penetrating geophysical means were employed to obtain this information. These were reflection and refraction seismics and deep and ultra deep EM soundings. In particular, stable and accurate data over periods sufficiently long to penetrate to the lower crust and uppermost mantle were required to provide electrical conductivity information to complement seismic studies. These data were collected along corridors, usually on or parallel to roads, across various segments of each transect (Clowes, 1993).

In the case of EM studies the subsurface structure is revealed in terms of the physical property of electrical conductivity. Electrical conductivity is extremely sensitive to composition, texture and fluid content within the rocks and thus provides another facet to integrated programs of the crustal studies. In the continental crust, saline water in interconnected pores and fractures is possibly the most widespread cause of high electrical conductivity. Alternate explanations involve the presence of metalliferous components, graphite or partial melt (Jones, 1992).

LITHOPROBE EM studies generally comprise two types of field surveys. Regional coverage along the transects is provided by broadband tensor MT soundings, recorded with station spacings of a few tens of kilometres. Naturally occurring time-varying EM fields generated by electric currents in the magnetosphere and ionosphere are used as the source in the EM soundings. The fields are recorded over a wide range of frequencies enabling derivation of conductivity structure from near the surface to upper mantle depths. Since it is known that the Earth's aesthenosphere is a more ductile layer underlying the more rigid lithosphere and is thought to consist of partially molten material, the boundary between the two represents a significant contrast in electrical conductivity. With the lithosphere typically being 100 or more kilometres thick, extremely long period recording of MT signals is required to achieve the necessary depth penetration. Extremely long period MT recordings have been made using Long-period Magnetotelluric System (LiMS) instruments developed by the Geological Survey of Canada and can provide conductivity information to depths in excess of 500 km. These measurements have

provided a natural complement to the deep refraction/reflection seismic investigations (Clowes, 1993).

CHAPTER 2

GEOLOGY OF THE STUDY AREA

2.1 General Geology of the Trans-Hudson Orogen

The THO is one of the best-preserved and best-exposed Early Proterozoic orogenic belts in the world (Hoffman, 1981). The THO is the chief component of a more extensive orogenic system that in North America includes not only the Wopmay, Penokean, and Ketidilian orogens but also several younger Early Proterozoic belts (Hoffman, 1980, Van Schmus, 1980 and Allaart, 1976; as discussed in Clowes, 1993), lying south of the Superior and Wyoming cratons (Figure 1.1), which are obscured by ca. 1.0 Ga Grenvillian orogenic overprinting and/or by Phanerozoic cover. A major episode of North American continental accretion is coincident with the evolution of this orogenic system and with the more general Early Proterozoic assembly of the Laurentian supercontinent. This assembly is known as the "Pan-American" orogenic system and available data suggests that it evolved via essentially uniformitarian plate tectonic processes: phases of initial continental rifting and passive margin development, ensuing subduction, arc generation and closure, juvenile terrain accretion and terminal continental suturing at collisional plate boundaries. These have all been identified within the THO with varying degrees of confidence (Clowes, 1993). Ophiolite remnants are now well documented and pre-orogenic seafloor spreading and subsequent closure may have been comparable in

magnitude to that occurring in the evolution of Phanerozoic orogens (Lewry and Collerson, 1990).

As commonly defined, the THO extends in the subsurface from South Dakota, where it is apparently transected by juvenile terranes of the slightly younger (ca. 1.8-1.7 Ga.) Central Plains Orogen northward to the edge of the Canadian Shield and through the exposed shield and across Hudson Bay at least as far as the Cape Smith Belt, in northern Ungava (Lewry and Collerson, 1990). The THO is considered to incorporate variably reactivated margins of at least three and possibly more, formerly independent Archean continental paleoplatforms (together with their inboard epicontinental cover and fringing rifted to passive margin miogeoclinal wedges), and a variety of intervening accreted Early Proterozoic juvenile terranes. The lithotectonic subdivision and nomenclature in the western parts of the orogen (Dakota and northwest segments) are relatively well established (Lewry and Collerson, 1990).

The THO study area incorporates accreted Proterozoic arc rocks, continental margin metasedimentary rocks and variably reworked parts of the Archean Superior and Hearne provinces. Lithotectonic subdivisions of the northwest segment have been made by Lewry et al.(1990) and included the Superior paleoplatform margin, Reindeer Zone and the Rae-Hearne paleoplatform. More recent literature (Lewry et al., 1994) describes the THO as including four composite lithotectonic zones (shown in Figure 2.1) namely: the Thompson belt, forming part of the superior Boundary zone; the internal Reindeer Zone, mostly comprising juvenile Proterozoic rocks; the Wathaman-Chipewyn Batholith, an Andean-type continental margin plutonic

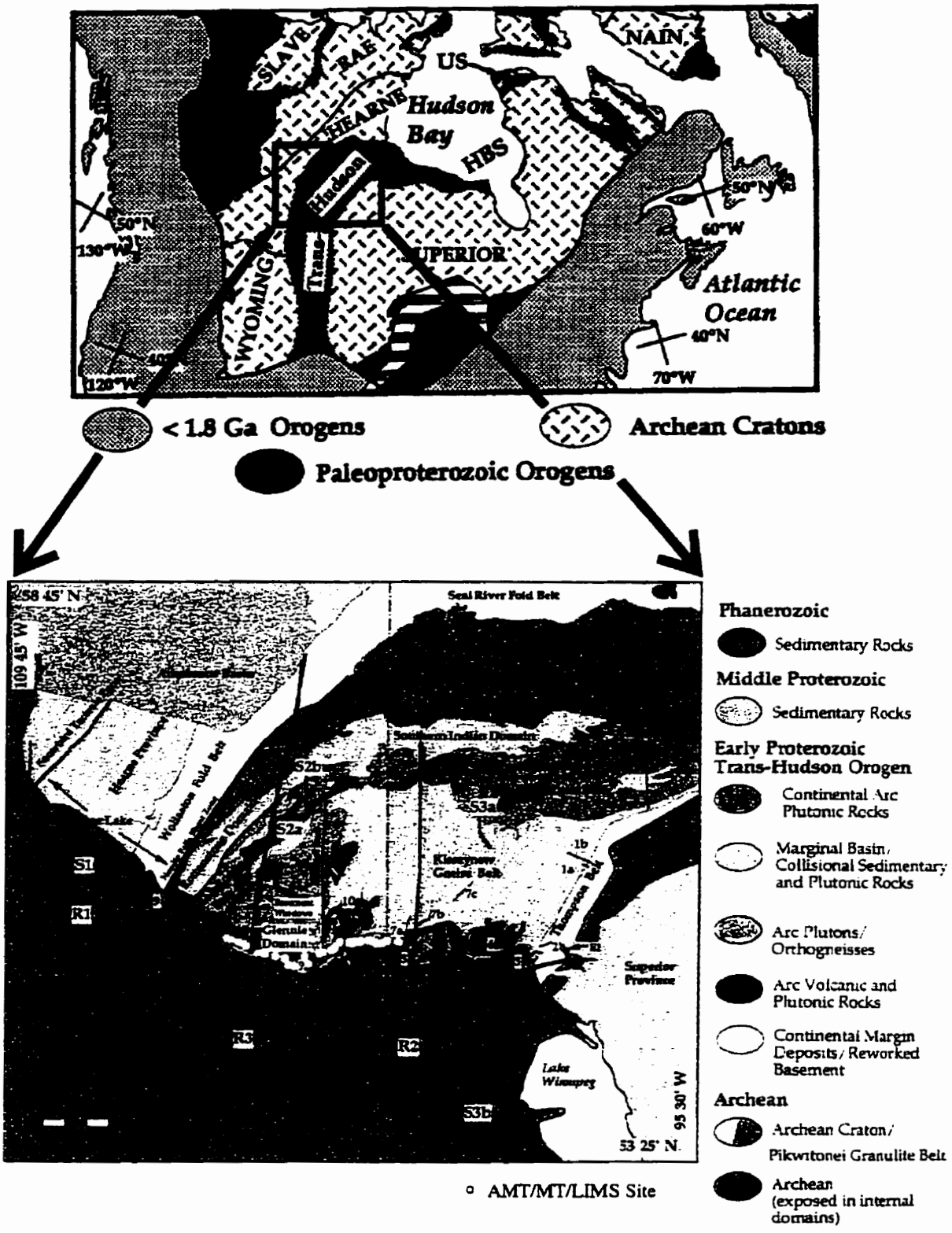

Fig. 2.1. Geological map of the exposed Trans-Hudson Orogen and the boundary regions with locations of 1991 seismic reflection lines (red, numbered). E1 to E4 are locations of expanding reflection spreads for velocity information. Lines S1, S2a, S2b, S3a, S3b and lines R1, R2 and R3 were part of the seismic reflection/refraction program. Yellow circles indicate the location of AMT/MT stations of the GD/HLB study area collected in 1992 (after Clowes, 1993).

complex; and the Cree Lake Zone, which constitutes a broad, reworked northwestern continental hinterland. LITHOPROBE MT data presented and discussed in this thesis have been collected from sites within the northwest segment of the western orogenic segments of the THO. Further detailed geological description of the study area will be restricted to the Reindeer Zone, specifically the Glennie Domain to the west Flin-Flon Belt, since all of the MT sites discussed within this thesis lie entirely within this area.

2.2 Geology of the Reindeer Zone

The Reindeer Zone is a collage of arc volcanic and plutonic rocks, coeval and derived volcanogenic sediments, arkosic molasse and late post-kinematic intrusions. Geochemical and isotopic data indicate that most igneous rocks formed in an oceanic arc or backarc setting (Stern et al., 1992). This zone has "suspect" provenance relative to adjoining continental margins, in that no pre-orogenic lithostratigraphic connections can be established across either the Wathaman-Chipewyan Batholith in the west, or shear zones at the western margin of the Thompson Belt (Figure 2.1). Thus, the Reindeer Zone is interpreted as an assembly of accreted juvenile arc terranes. Structural synthesis and Nd and Pb isotopic data from late post-kinematic granitoids suggest that much of the zone was emplaced as a stack of early nappes and thrust imbricates, now folded (Lewry et al., 1994). Terminal collision between the Reindeer Zone juvenile rocks and Superior craton, bracketed between 1830 and 1790 Ma, involved south to southwest translation of Reindeer Zone allochthons over

Archean footwall basement of unknown affinity in the internal zone (Lewry et al., 1994).

Within the Reindeer Zone, the gross scale geology of the Flin Flon and western La Ronge domains comprise abundant, mostly low metamorphic grade, mafic to felsic metavolcanic rocks and granitoid plutons, with subordinate metasediments (Lewry et al, 1994). The Kisseynew and eastern La Ronge domains comprise high grade metasedimentary migmatites. In the Rottenstone tonalite-migmatite belt, Glennie, Hanson Lake and southwest La Ronge domains, supracrustal rocks are subordinate to minor, and variably deformed granitoid rocks dominate. Major structural features located within the Reindeer Zone include the Needle Falls Shear Zone (NFSZ), the Stanley Shear Zone (SSZ), the regional north-south trending Tabbernor Fault Zone (TFZ), and Sturgeon Weir Thrust (SWT).

The Glennie Domain (GD) forms the core of a late, northeast plunging, regional anticlinorium (Lewry et al., 1990). However, the structural geometry of the south Glennie and adjoining Hanson Lake domains is controlled by three older north trending folds (Figure 2.2): the Nunn Lake antiform in the southwest Glennie domain, the highly asymmetric Deschambault synform in the eastern Glennie domain, and the Jan Lake antiform which dominates the Hanson Lake Block (HLB). For much of its extent the subvertical common limb of the Deschambault and Jan Lake folds is paralleled by strands of the late TFZ (Lewry et al 1994). Archean basement (Figures 2.1 and 2.2), exposed only at deepest exhumed crustal levels, occupies tectonic windows produced by late cross-folding of the Nunn Lake (Iskwatikan and Hunter

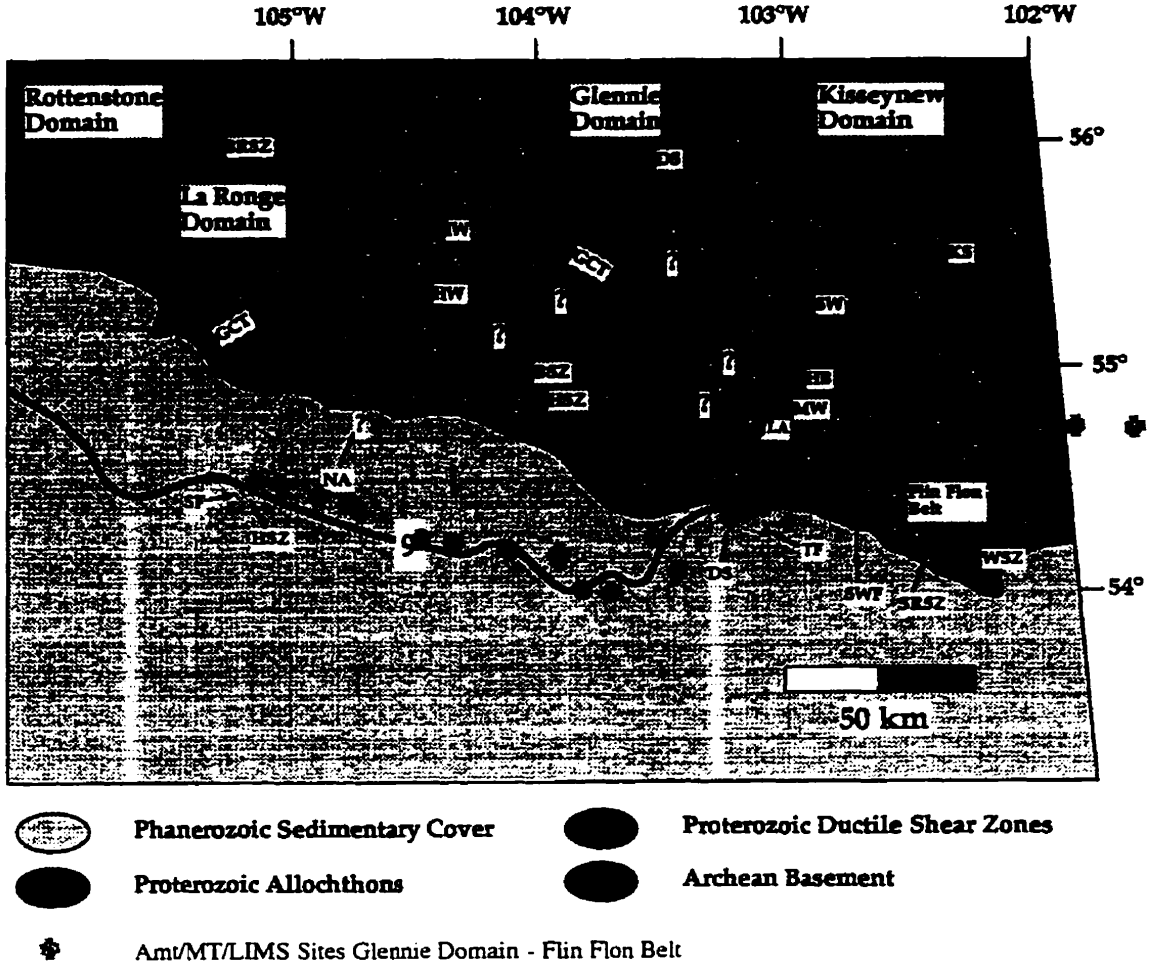

Figure 2.2

Major structural features of the southern Glennie domain, Hanson Lake block and adjacent areas, showing the locations of exposed Archean basement at deepest structural levels, in tectonic "windows" produced by northerly (closed symbols) and later northeasterly (open symbols) refolding of earlier thrust sheets and shear zones. *IW* = Iskwatikan window; *HW* = Hunter Bay window; *SW* = Sahli window; *MW* = MacMillan Point window; *NA* = Nunn Lake antiform; *DS* = Deschambault Lake synform; *JLA* = Jan Lake antiform. NE-trending late folds are unnamed. *HSZ* = Hartley shear zone; *BSZ* = Brownell Lake shear zone; *GCT* = Guncoat "thrust"; *SRSZ* = Snake Rapids shear zone; *WSZ* = Wolf Lake shear zone; *KS* = sole zone of Kisseynew gneisses; other early thrusts unnamed; *SWF* = Sturgeon Weir fault; *TF* = Tabbernor fault zone; *SF* = Stanley fault; *BRSZ* = Birch Rapids "straight belt"; *HB* = Hanson Lake block.

Bay windows) and Jan Lake (Sahli and MacMillan Point windows) anitiforms (Lewry et al., 1994). This basement is everywhere separated from Proterozoic allochthons by early mylonitic gneisses. This geometry and the wide occurrence of reworked Archean crust and its plutonic derivatives in sub-Phanerozoic drill core farther south suggest that Archean rocks may underlie much or all of the Reindeer Zone (Lewry et al., 1994).

Additional geological and structural information will be discussed in later sections relative to the implications of the magnetotelluric investigations and the interpretation of the seismic and other geophysical data for the area.

CHAPTER 3

GEOPHYSICAL INVESTIGATIONS OF THE THOT

3.1 Recent Contributions of Gravity and Magnetic Analysis to the Reindeer Zone

Regional aeromagnetic and gravity surveys cover the Manitoba-Saskatchewan area containing the LITHOPROBE THOT. In addition to providing invaluable auxiliary information to assist in the geological interpretation of the reflection seismic sections, these data allow the seismic results to be extrapolated away from the transect lines and provide a means of investigating structures removed from the seismic lines. The gravity and magnetic data also play a critical role in mapping the buried Precambrian basement geology south of the Precambrian Shield margin under Phanerozoic sedimentary rocks (Thomas, 1994).

Regional gravity surveys in the area of the THO have a station spacing of 10 to 15 km. Additional detailed gravity surveys have been completed along all LITHOPROBE seismic reflection lines reducing the station spacing along these corridors to 1 or 2 km (Thomas, 1994). Gravity trends are predominantly NNE-SSW to N-S over the western half of transect, between the Wollaston Domain and the Tabbernor Fault (Figure 2.1), following the overall trend of the orogen. Strongly developed NE-SW trends near the Churchill-Superior boundary also conform to the trend of the orogen. However an E-W grain is superposed on the gravity pattern in

the eastern part of the region, both north and south of the Flin Flon - Snow Lake Belt (Thomas, 1994).

Figure 3.1a shows the gravity profile along the east-west transect across the Reindeer zone of the THOT. These detailed gravity data along the LITHOPROBE lines and specifically along line 9 across the Glennie Domain, Hanson Lake Block and eastern Flin Flon - Snow Lake Belt (the GD-FFB, region of MT study reported in this thesis), show a number of associations with the regional geology. The tonalite-migmatite complex of the Rottenstone Domain and La Ronge Belt just east of the Needle Falls Shear Zone and the Wathaman Batholith, correlate with a distinct, linear gravity high suggestive of a crustal block of fairly homogeneous composition extending to significant depth (Thomas, 1994). Between the complex and the Tabbernor Fault Zone, the principal structural domains are not associated with distinctive gravity signatures, suggesting that they are relatively thin, consistent with Lewry et al.'s (1990) premise that the upper crust in this area comprises a series of subhorizontal structural sheets. Discrete NE-SW linear anomalies crossing the western part of the Glennie Domain may therefore be related to relatively thick crustal units residing in underlying Archean crust. Within the Glennie Domain, the Archean windows of the Istiwatikan and Hunter Bay Domes (IW, HW, Figure 2.2) fall within a prominent gravity low. The lack of correlation between gravity anomalies and geological domains persists east of the Tabbernor Fault Zone over the Hanson Lake Block. The Archean Sahli granite of the Hanson Lake Block, differs from the Archean windows of the Glennie Domain, in not being associated with a sizable gravity low. The prevailing gravity

Figure 3.1a

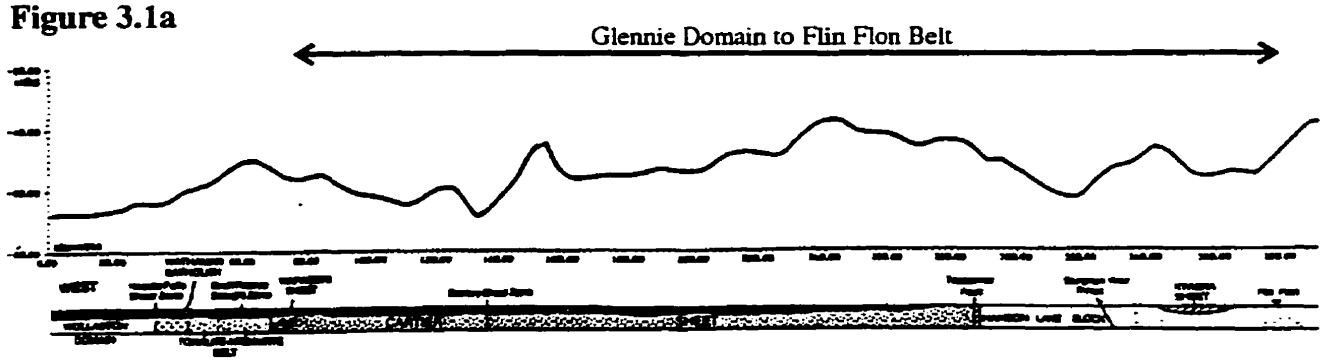

Composite E-W gravity profile along LITHOPROBE lines (from east to west) 3, 5, 6, 9, 11 and 12; in the east, this line is extended SE along line 2. A corresponding schematic geological section is also portrayed. Note the overlap between the longer E-W section and the shorter NW-SE section near the Churchill-Superior boundary. The profiles and sections were derived by projecting the gravity data and geology, respectively, on to a number of straight-line segments which approximate the somewhat irregular paths of the various lines. In the figure, the profile and section are broken into upper, western segments and lower, eastern segments; these segments are contiguous.(after Thomas, 1994)

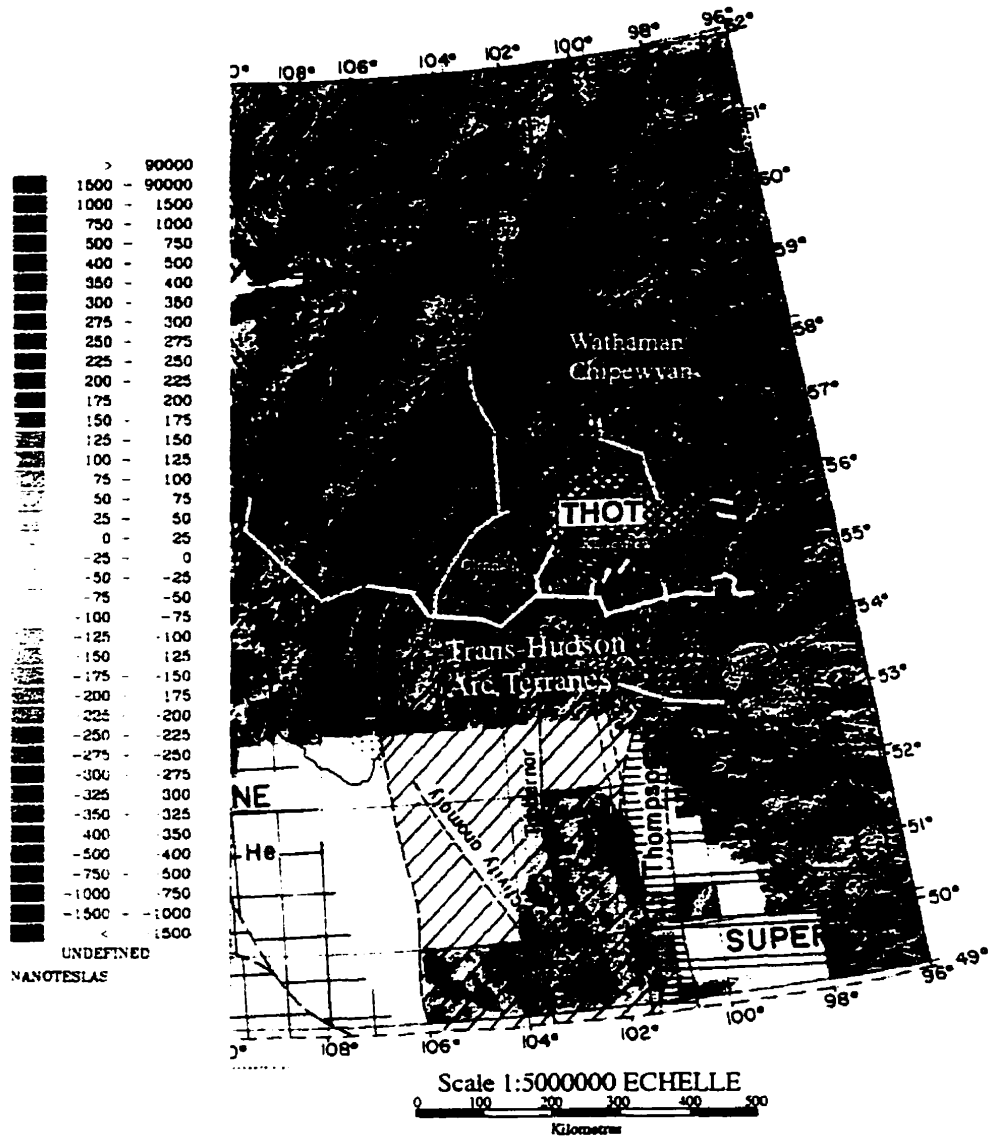

Figure 3.1b. Aeromagnetic anomaly map of part of Saskatchewan-Manitoba encompassing the THOT region. Artificial illumination from the southeast highlights the northeast-trending fabric of the region (after Clowes, 1993).

field in the area has the form of a moderate gradient. The Flin Flon Belt is characterized by highs and lows reflecting the predominantly granite-greenstone composition of this domain (Thomas, 1994).

The Stanley Shear Zone lies within a prominent, linear gravity low, across which there is a noticeable change in the level of the gravity field. Positive linear anomalies to either side of the low can be traced back to the Precambrian Shield where they fall over areas containing mafic volcanics; another positive anomaly in the eastern part of the Glennie Domain, likewise may indicate buried mafic volcanic rocks. The Sturgeon Weir Thrust coincides with a gravity minimum, east of which the gravity field increases sharply over the Flin Flon and Snow Lake Belts. This signature indicates the possibility of a steeply dipping easterly orientation of the thrust (Thomas, 1994).

Aeromagnetic data for all of the study area have been obtained at ~ 300 m altitude along flight lines spaced ~ 800 m apart (see Figure 3.1b). Total field magnetic anomaly and vertical magnetic gradient maps prepared from these data and used in concert prove to be a powerful tool for mapping and modelling geological units (Thomas, 1994). A strong contrast in magnetic intensity occurs at the boundary between the Mudjatic (magnetic low) and Wollaston (magnetic high) domains. The Wathaman Batholith is characterized by a strong magnetic high, the western margin of which is approximately coincident with the Needle Falls Shear Zone (NFSZ). A narrow zone of relatively low magnetic intensity within the Wollaston Domain adjacent to the NFSZ, by analogy with the low, featureless field over the Birch

Rapids Straight Zone, may indicate a zone affected by pervasive shearing and/or mylonitization. A good correlation between magnetic patterns and sections of the eastern bounding thrust of the Wapassini Sheet (La Ronge Belt) is observed. In the Glennie Domain, the Stanley Shear Zone coincides in part with a pronounced magnetic low, which allows it to be traced from the shield to the LITHOPROBE line. Magnetic highs on either side of the low coincide with gravity highs which, on the shield, extend over areas containing mafic volcanic rocks and are the probable source of coincident magnetic and gravity anomalies. East-west breaks in the magnetic pattern are imaged near the southern margin of the Glennie Domain and its proposed subsurface extension near the LITHOPROBE line 9. The Tabbernor Fault Zone and Sturgeon Weir Thrust both have prominent expressions in the magnetic data, which could enable their attitude to be modeled. The Archean Istwatikan, Hunter Bay and Sahli Granite windows individually exhibit variable correlation with magnetic features. In the Flin-Flon to Snow Lake Belt, granitic intrusions typically are characterized by slightly negative or neutral levels of magnetic field, as are many of the area's greenstones (mainly mafic volcanics) (Thomas, 1994).

3.2 Seismic Reflection Signature Along Line 9 of the THOT

Lewry et al. (1994) summarize and interpret the results of recent seismic profiles which traverse the Trans-Hudson Orogen. The seismic profiles form a complete section across this continent-continent collision zone (Figure 2.1; lines 2,3,9). Reflection data were also acquired along cross-lines (Figure 2.1; lines 4,5,7,10) at

high angles to the main E-W transect in order to provide 3-D control. All THO seismic lines cross, or are close to, exposed, parts of the Canadian Shield, thus affording an exceptional opportunity to correlate surface geology with deep crustal architecture in a Paleoproterozoic orogen. Seismic reflection data collected along line 9 (Figure 2.1) crosses the region of the GD-FFB MT survey sites discussed in this thesis. It should be noted that road access limitations required that much of the E-W THO transect be run south of the shield edge, across thin flat-lying Phanerozoic cover (see Figure 2.1). Correlation between shield and sub-Phanerozoic geology and features seen in the seismic profile, was achieved mainly via total intensity and vertical gradient aeromagnetic data, locally augmented by drill core data.

The line 9 seismic profile (Figure 3.2a) images highly reflective crust from near-surface to the Moho across much of the THOT. Figure 3.2b presents an overall interpretation of this profile. Several significant first order features are clearly imaged (Lucas et al, 1993):

(1) A well-defined, laterally continuous reflection Moho (M, Figure 3.2a) is evident along the whole line 9 profile. The reflection Moho has significant relief (38 km to > 48 km depth), although for much of line 9 it has fairly constant depth (38 - 41 km). The main Moho relief is provided by a narrow (~50 km) crustal 'root' below the western Glennie Domain, across which the reflection Moho deepens by 6-9 km, to about 48 km.

(2) Line 9 is dominated by a crustal-scale reflection culmination whose crest underlies the western Glennie Domain, directly above the crustal root noted above. To the west

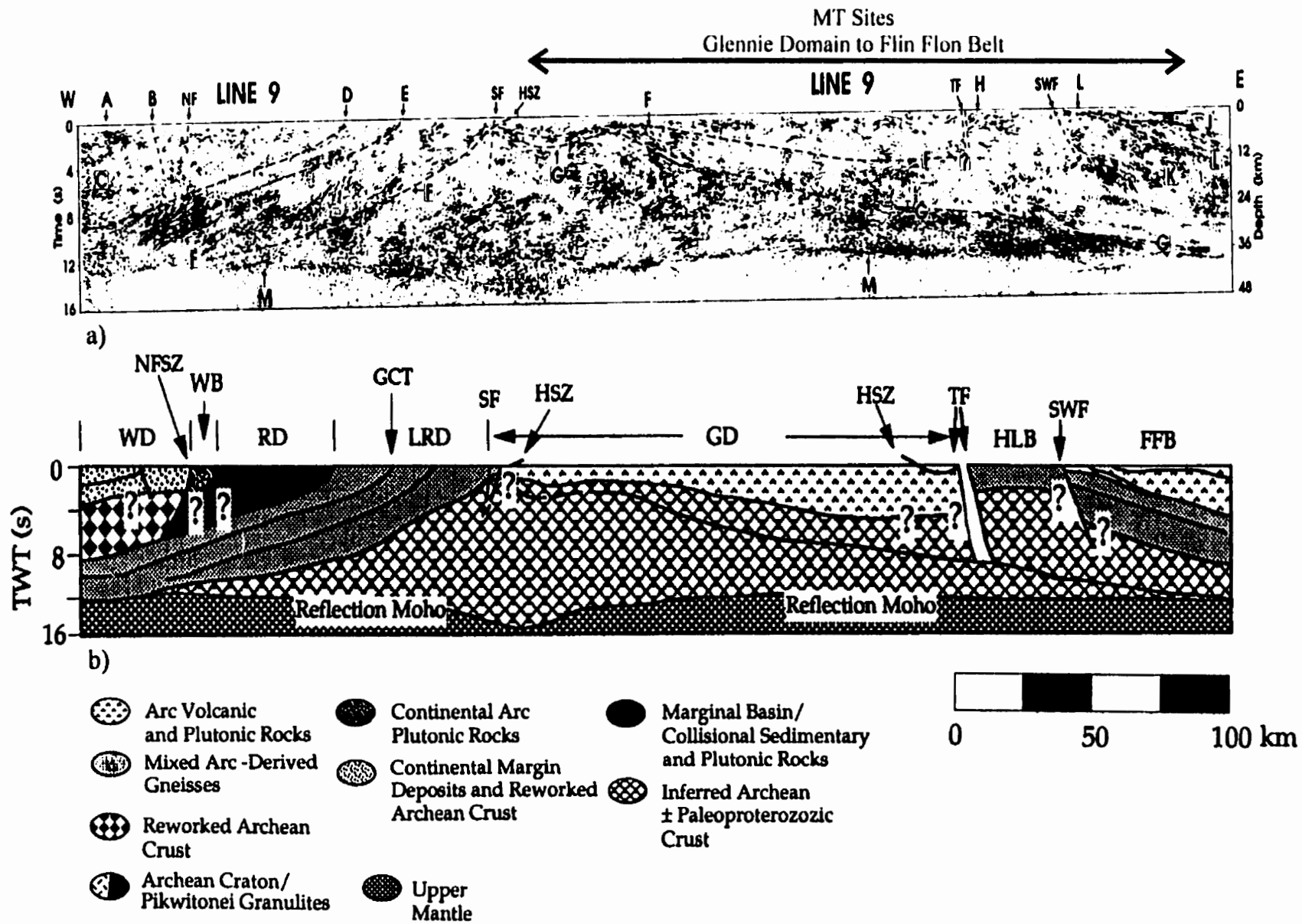

Figure 3.2. a) Line drawing of migrated seismic reflection section recorded along line 9. NF = Needle Falls shear zone; SF = Stanley Fault; HSZ = projection of Hartley shear zone; TF = Tabbernor fault zone; SWF = Sturgeon weir fault. b) Interpretative geological cross-section for the western portion of the trans-orogenic transect (line 9) (after Lewry et al., 1994).

of this culmination (also just west of the study area), prominent upper and mid crustal reflections are uniformly west dipping, whereas the eastern two-thirds of the orogen is dominated by well-defined east dipping reflections through most of the crust.

(3) Strong reflections dip beneath both bounding Archean cratons. Such reflection zones extend from near-surface, where most can be correlated with juvenile rocks of the Reindeer zone.

(4) Throughout the western two thirds of the orogen, the lowest 2-3 s (two-way travel time) of recorded energy from the crust images mainly subhorizontal events interpreted to represent the lower crust to upper mantle lithosphere. Locally, the top of this 'flat zone' appears to truncate overlying inclined reflections.

(5) Many geologically mapped subvertical shear zones and faults, such as the Tabbernor Fault Zone are indirectly interpreted from steep 'transparent' zones on the migrated sections and are marked by truncation of reflections and by diffractions on the unmigrated sections (Lewry et al., 1994).

3.2.1 A Geological Interpretation of the GD-FFB Seismic Reflection Profile

A crustal-scale reflection culmination underlies the sub-Phanerozoic extension of the western Glennie Domain and apparently coincides with the extrapolated crest of the Nunn Lake antiform (Figure 2.2) and persists to mid-crustal depths (Lewry et al., 1994). The western flank of the culmination incorporates strongly reflective crustal domains that correlate with imbricated juvenile arc rocks. On the eastern flank, E to NE dipping arc granitoid and supracrustal rocks of the Glennie Domain extend across

the transect line. In the seismic section the core of the culmination shows discontinuous reflections of varying attitude. Such variations may for the most part be an artifact of changing angle between the seismic line and geological strike.

Lewry et al., (1994) postulate that the Glennie culmination is cored, at least in part, by Archean basement (Figure 3.2b) based on tectonic windows of Archean rocks, a gravity low and isotopic data. The location of the contact between inferred Archean basement and overlying Proterozoic rocks on the seismic profile (F, Figure 3.2a) is geologically ill-constrained and far from obvious on the basis of reflectivity. Farther east, the Archean-Proterozoic contact cannot be reliably extrapolated across the Tabbernor Fault Zone, as the fault coincides with the subvertical common limb between the Deschambault and Jan Lake folds.

The most clearly imaged crustal feature on the east flank of the Glennie culmination is a narrow, moderately east dipping zone of prominent reflections (G, Figure 3.2a) which is traceable from near surface at the crest of the culmination to >12 km depth near the Tabbernor Fault Zone. This feature is interpreted to be a crustal scale detachment fault, either compressional or extensional (Lewry, et al., 1994).

In the Hanson Lake Block, much of seismic line 9 is subparallel to geologic strike: affording, little correlation between surface geology and seismically-imaged features. Subhorizontal reflections in the upper, west portion of this section (H, Figure 3.2a) probably correspond to exposed strike-parallel, southeast dipping mylonitic orthogneisses. Diffuse upper-crustal reflectivity in the eastern Hanson

Lake Block, adjacent to the Surgeon Weir Thrust, corresponds to foliated arc volcanic and plutonic rocks heavily intruded by post tectonic granite and pegmatite. Both the Tabbernor Fault Zone and the Sturgeon Weir Thrust are indirectly imaged. The steeply east dipping Sturgeon Weir Thrust appears to extend to > 15 km and the subvertical Tabbernor fault to > 30 km (Lewry, et al., 1994). Further to this work Hajnal et al. (1996), examine in closer detail the seismic reflection images of high angle faults and linked detachments in the THO. Hajnal et al., (1996) characterize the Tabbernor faults, the Strugeon Weir Thrust and the Needle Falls Shear Zone as three excellent examples of high angle faults. In the GD-FFB area the Tabbernor Fault Zone, which is a 10 km wide zone of ductile to brittle strands separating steeply dipping panels (Lewry et al., 1990), is imaged as a seismically transparent zone indicated by truncated reflectors on either side of the fault zone. The TFZ abruptly terminates at the top of a regional, moderately dipping crustal-scale detachment at ~28 km depth (G, Figure 3.2a). Below the surface trace of the Sturgeon Weir Thrust a thick package of east dipping reflections is abruptly terminated along a plane dipping at 70^0 east and is thought to mark the depth extent and location of the SWT (Hajnal et al., 1996).

East of the Sturgeon Weir Thrust, east-dipping reflection domains project from near surface to middle and lower crust. Most of these domains correlate at surface with thrust imbricated juvenile rocks of the Flin Flon Domain (J, Figure 3.2a). These are underlain by a more uniformly reflective, moderately east dipping domains (K, Figure 3.2a), the uppermost part of which projects up-dip to arc plutonic

orthogneisses and subordinate supracrustal rocks in the vicinity of the Sturgeon Weir Thrust. This highly reflective package is separated from the overlying reflective package corresponding to the Flin Flon Domain by a well defined zone of reflections which is interpreted as a major structural detachment (L, Figure 3.2a). This may correspond at surface to the Snake Rapids Shear Zone. Thus it seems likely that imbricated upper to mid crustal juvenile arc rocks (domains J and K) extend to at least 25 km depth at the east end of line 9. The nature of the crust below domain K is unknown but it may include Archean material (Lewry, et al., 1994).

3.3 Previous MT Soundings in the GD-FFB Area

Magnetotelluric measurements were made with the SPAM (Short Period Automatic MT) field system in the frequency range 0.01-130 Hz at ten sites along highways 106 and 165 in northern Saskatchewan in the summer of 1992 (Jones and Correia, 1992). This profile corresponds to the GD-HLB portion of the line 9 THOT corridor. Four sites were located on the shield area (HLB) and six sites were located on Phanerozoic cover (overlying the GD).

The general observations made from the MT data were that the measured apparent resistivities over the shield sites were considerably higher than those measured over the Phanerzoic sites to the west. The initial one dimensional (1-D) inversions of the MT data suggest that in the shield near surface moderate resistivity (600 Ω.m) rocks overlie more resistive (>5000 Ω.m) rocks at depth. On the Phanerozoic cover, the near surface resistivity values are considerably less (70 Ω.m), but there is a

substantial increase in resistivity with depth (>2000 Ω.m) and evidence of a decrease in resistivity below 10 km depth. Sites even further west exhibit even lower near surface resistivities (10-20 Ω.m), with an increase in resistivity with depth (Phanerozoic to resistive basement transition) and again with some evidence of a decrease in resistivity below 10 km. The interpretation of these results indicated a thickening of the Phanerozoic cover to the west (Jones and Correia, 1992).

Jones et al. (1993) reported the results of MT surveys that were completed in the Phanerozoic Williston basin in southern Saskatchewan and Manitoba west of the GD-FFB area with the purpose of delineating the North American Central Plains (NACP) conductivity anomaly in the underlying THO. East and south of the present study area, Ferguson et al. (in prep), describe an analysis of MT data from 34 sites spanning the Flin Flon Belt and adjacent geological domains.

CHAPTER 4

MT MEASUREMENTS ON THE GD-FFB

4.1 Overview of the MT Method and the Theory of MT Response Analysis

The terms 'magnetotelluric' and 'telluric' are generally used to refer to certain large-scale (generally low-frequency) magnetic fields and the terrestrial current systems induced by these fields respectively (Telford et al., 1976). Several deep sounding geophysical techniques utilize these fields. MT surveys simply involve the stationary recording of naturally occurring magnetic and electric fields at the Earth's surface over a length of time. Orthogonal components of the horizontal electric (E) and magnetic (H) field strengths, as a function of frequency, are combined to yield a measure of the electrical impedance (Z) at the Earth's surface which is used in turn to estimate the conductivity structure, with depth, below the measurement station. The main advantage of the MT method is the unique capability for exploration from very shallow depths (<10m) to very great depths (>hundreds of kilometres) without artificial power sources and with little or no environmental impact.

The main natural source of MT fields at frequencies above about 1 Hz are worldwide thunderstorms, from which lightning radiates fields which propagate to great distances. Sources of low-frequency MT fields (10^{-3}-10^{-1} Hz) are EM fields radiating from the hydromagnetic waves in the magnetosphere (Vozoff, 1991). When

MT measurements are made at audio-frequencies using energy from sferics (natural atmospheric fluctuations of the EM field, generally at frequencies from 1 to 10^5 Hz, Sheriff, 1984) then the method is referred to as the audio-magnetotelluric method (AMT). In both MT and AMT measurements, the E and H components of the EM field generated by the source's activity have complicated but measurable amplitude, phase and directional relationships at the Earth's surface that depend on the distribution of electrical conductivity in the subsurface. The MT method involves the simultaneous measurement of orthogonal components of the horizontal electric and magnetic fields as a function of frequency.

The application of the MT method can be simplified by making the assumption that the primary field is a uniform plane wave and that the Earth consists of uniform horizontal layers (Sheriff, 1984). Most of the energy from the source is reflected at the surface, but a small amount propagates vertically downward into the earth. Although the layered-earth model may not be applicable in many surveys, it does provide a convenient starting point for modelling the MT response. Two and three dimensional computer modelling of measured data is a much more complex process. Processing of the MT recordings is normally done in the frequency domain because the theory is simpler than in the time domain, although in recent years and with the advent of ever faster computers, time domain analysis and modelling shows promise (Spagnolini, 1994).

Introduced in the early-1970's, Controlled Source Audio-Magnetotellurics (CSAMT) is a frequency-domain EM sounding technique which uses a fixed

grounded dipole or horizontal loop as an artificial signal source. The use of an artificial signal source at a finite distance is the chief difference between the CSAMT and MT and AMT methods (Zonge and Hughes, 1991). The artificial source in CSAMT provides a stable, dependable signal, resulting in higher-precision and more economical measurements than are usually obtainable with natural source measurements in the same bandwidth. The source size (length of the electric dipole) generally dictates the depth of investigation with CSAMT and the maximum achieved in many cases is often only a few kilometres.

CSAMT and AMT have been used to map groundwater, base metal deposits and geothermal resources at depths from 50-100 m to several kilometres. The major commercial application of MT however, has been petroleum exploration in areas where reflection seismology is very expensive or ineffective, such as in extreme terrain and beneath volcanics (Vozoff, 1991).

4.1.1 Source Fields for MT/AMT and CSAMT Soundings

As outlined above, the MT method is dependent on natural EM fields which, with respect to data collection and analysis, is both the method's major attraction and it's greatest weakness (Vozoff, 1991). Other EM techniques using controlled sources require a great deal of equipment and logistical support in order to establish a source field for low frequency, deep penetration work. In addition the geometry of these sources dramatically complicates multi-dimensional interpretation compared with traditional MT. On the other hand there can be considerable cost involved in MT data

collection in the presence of artificial EM noise. However, with present MT equipment, loss of survey time while waiting for signal to exceed system noise in the frequency ranges, 0.001-.1 Hz (MT) and $10\text{-}10^3$ Hz (AMT) is unusual.

Natural EM signals come from an enormous variety of processes and from sources ranging from the core of the earth to distant galaxies (Vozoff, 1991). Only two source regions are important within the usual frequency range of interest for exploration ($0.001\text{-}10^4$ Hz), these are the atmosphere and the magnetosphere. The major features of the magnetospheric current systems are shown in figure 4.1. This region includes the ionosphere and the atmosphere. Changes in pressure with altitude make the charged particles of ionized oxygen and nitrogen gases more dense in the lower atmosphere. This results in a region of relatively high conductivity called the ionosphere and it is an anisotropic electrical conductor (see figure 4.2). EM hydromagnetic waves or plasma waves can occur in conductive fluids containing magnetic fields. These waves travel at relatively low velocities and can set up resonances along magnetic field lines in the magnetopshere producing signals with frequencies in our range of interest.

The EM fields generated in the magnetosphere must travel through the ionosphere and then the insulating atmosphere to reach the Earth's surface. The vertical E and H fields do not penetrate the atmosphere and thus the horizontal components are strongly modified (Vozoff, 1991).

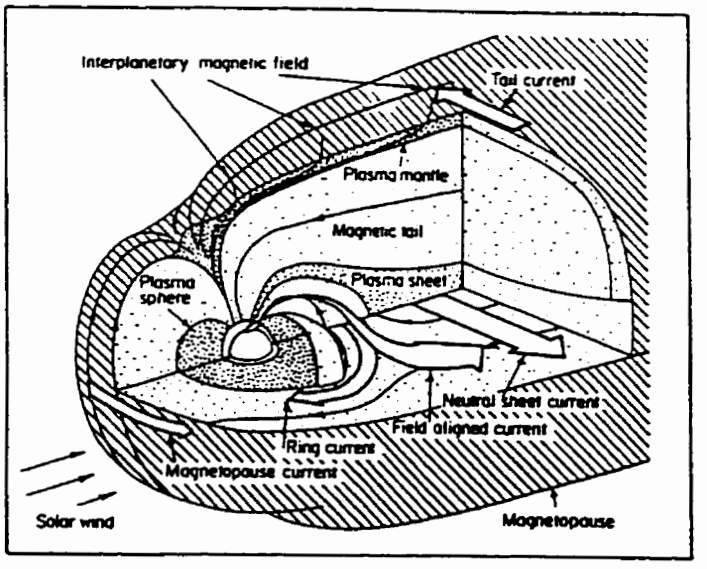

Figure 4.1 Major features of the magnetospheric current systems. The earth and atmosphere are the small spherical features in the center (after Vozoff, 1991).

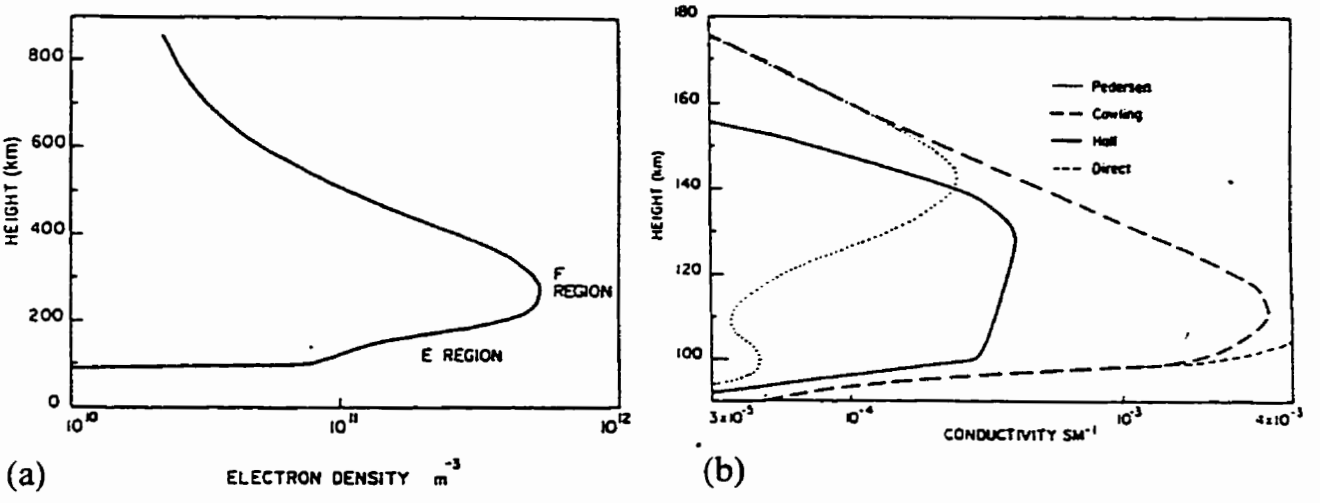

Figure 4.2 (a) Ionosphere electron density at winter noon, midaltitude. (b) Electrical conductivities in the anisotropic ionosphere, mid-day. (after Vozoff, 1991).

EM sources at frequencies near 1 Hz are varied making good data collection in this range sometimes costly and laborious. The source regions for this range as well as other types of observed atmospherics are shown in figure 4.3.

At frequencies above 1 Hz the radiation and propagation of EM signals from lightning discharges produces signal over most of the globe. Lightning generally consists of a sequence of discharges called strokes. The sequences called flashes consist of a cloud to ground leader which ionizes an atmospheric path that facilitates the ground return stroke which is the principle radiator of EM energy. A typical ground return is 20000 amperes lasting 40 microseconds. Estimates of the occurrence frequency of lightning flashes around the world vary between 100 and 1000 per second (Vozoff, 1991). Fields detected by AMT systems are highly dependent on cloud conditions etc. and the spherics are largest in the tropics.

In the CSAMT method orthogonal electric and magnetic field components are measured ideally in the plane wave portion of the field far from the source. Apparent resistivities and phase angles can be obtained from measurements usually made in the frequency range of 10^{-1} Hz to 10^{4} Hz (Zonge and Hughes, 1991). The development of the controlled source for MT work came about primarily due to the need for a solution to the signal strength variability problem encountered when using natural source fields in the MT and AMT methods.

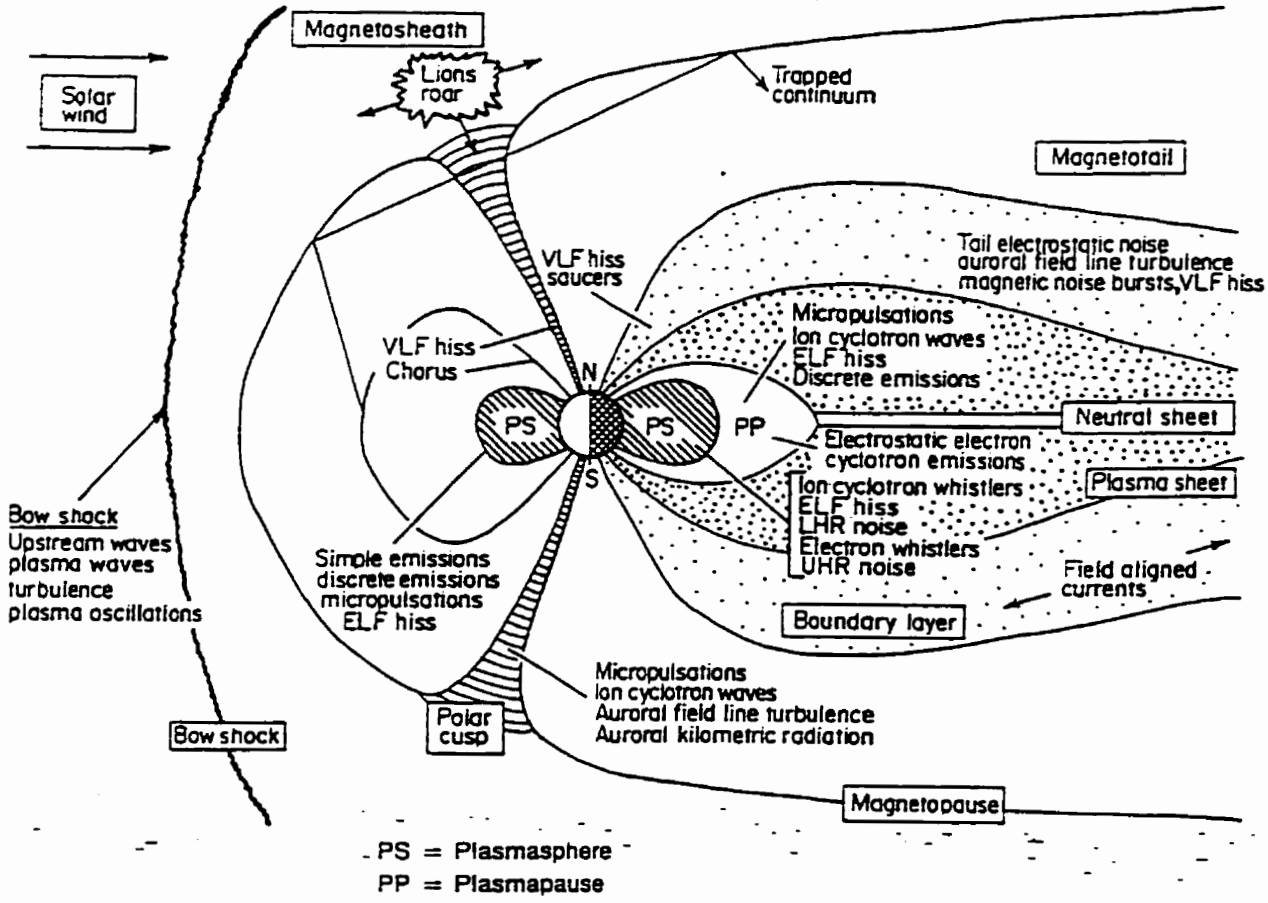

Figure 4.3a Source regions in the magnetosphere for various types of observed atmospherics (after Vozoff, 1991).

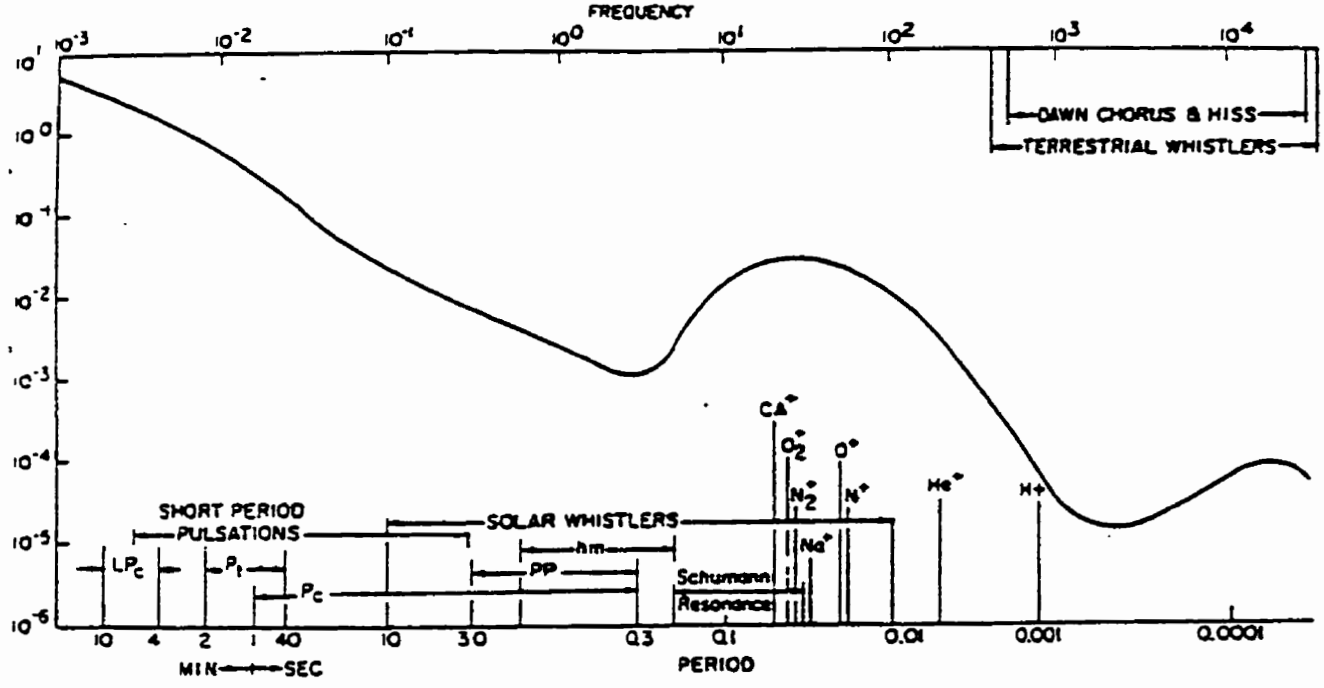

Figure 4.3b Geomagnetic frequency spectrum (after Jiracek, 1984).

4.1.2 Field Measurement, Equipment Setup and Remote Reference

The equipment used in MT work can be quite complicated because there is a need to measure at least two orthogonal components of the electric and magnetic fields at each station. Figure 4.4a shows a schematic of the MT field equipment set up. Five orthogonal components of the electric (E_x, E_y) and magnetic (H_x, H_y and H_z) fields are typically recorded. The electrical components are measured with a set of electrodes. A coil consisting of many turns on a large diameter frame (~1m) may be used to measure the components of the magnetic field (H) at each station. Alternatively a fluxgate magnetometer can be employed if the main interest is in very long periods (i.e. large penetration depths). Proper choice and calibration of sensors for both the E and H fields is critical to the collection of acceptable field data.

The electric field is measured by recording the potential *V* versus time between a pair of grounded electrodes, distance *l* apart, and determining the electric field using $E=-V/l$. The S.I. units for E are *V*/m. One of the major problems associated with the E measurements is electrode-generated noise. An electrode in contact with the earth is an electrochemical cell and subsequently a voltage exists at the interface which depends on the chemical natures and interactions of the materials involved. It is therefore important to choose the right type of electrode in an MT survey. Common electrodes are non-polarizing Cu, Pb, Cd and Ag based cells. A second important source of noise in electric field measurements is noise induced in the wire by wind motion. Finally, at high frequencies the wire joining the electrodes must be straight or an additional voltage will be induced in the wire by time variations in H_z. To

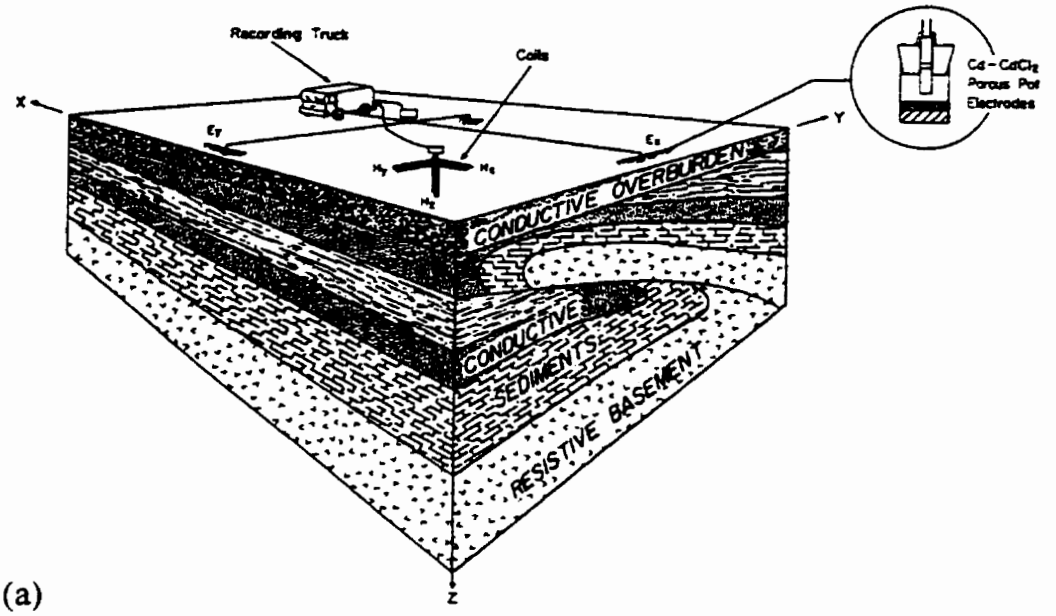

(a)

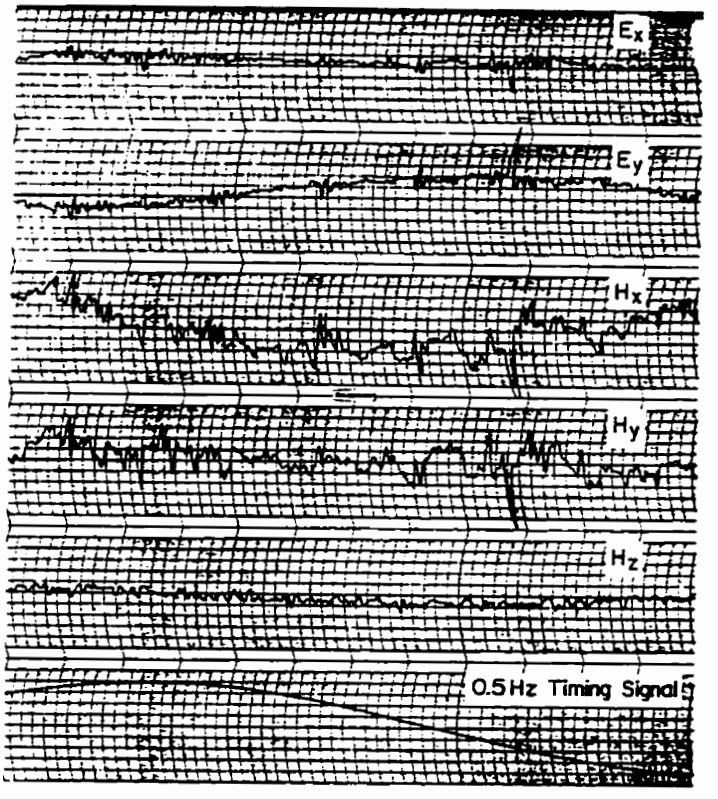

(b)

Figure 4.4 (a) Typical field setup for 2 electric field (Ex and Ey) and 3 magnetic field (Hx, Hy, Hz) component collection. (b) Typical noise-like telluric signals. Sine wave at bottom shows time scale (after Vozoff, 1991).

combat noise problems preamplifiers are often used which have very high common mode noise rejection and rapid response. These features minimize the effects of very rapid, large changes in the earth currents due to power systems and lightning (Vozoff, 1991). In exploration practice it is possible to increase the electric signal just by increasing *l*, the electrode spacing, although the logistical effort increases proportionally.

The instrumentation for measuring the magnetic field must be very sensitive because the magnetic field variations are on the order of fractions of nanoTeslas (nT). This requirement makes the receiver setup very sensitive to slight motions of the coil that would create minute noise voltages. Successful MT recordings require the magnetic field strength to be greater than the equivalent magnetic noise in the sensors. For this reason a great deal of care must be taken in the field setup and may include the development of better techniques or better sensors. Three varieties of magnetometers are in general use for measurement of the H field components, induction coils, fluxgates and SQUIDS. The induction coil is a loop of wire which produces a voltage proportional to its area multiplied by the time derivative of the magnetic field normal to the loop. The additional use of many turns of the coil in the loop results in output proportional to the number of turns. To decrease the size of loops, effective loop area is increased by winding turns around a core of high magnetic permeability. Alloys of molybdenum and nickel are used for lower frequencies while nonconductive ceramics such as MN-60 (Ceramic Magnetics Inc.) are used for higher frequencies. The frequency dependence of induction coil response

below resonance is ideally suited to the measurement of natural fields at frequencies below $10\text{-}10^2$ Hz, where it very nearly compensates for the 1/frequency fall-off of the average spectrum (Vozoff, 1991). For the LITHOPROBE work the induction coil magnetometer is used in preference to SQUIDS. The fluxgate magnetometer is capable of detecting changes in the magnetic field of the order of 0.2 nT. This magnetometer measures the magnetic field component along the axis of its core and must be oriented with the field if the total intensity is to be measured (Sheriff, 1984).

The other magnetometer commonly used in MT is the SQUID, based on the Josephson junction effect in superconductors. This instrument combines a high dynamic range with the lowest noise theoretically possible. The operating principle of the SQUID will not be described here however two varieties of SQUID magnetometers, dc and RF, have been built. Only the RF SQUID is available for geophysical magnetometers. The active sensor in the SQUID is supercooled with liquid helium therefore prolonged surveys in remote areas would be difficult. A persistent problem with SQUID magnetometers has been the effect of spherics. Their frequency content shifts the phase faster than the response time of the electronic circuitry so a low-pass filter has been introduced to overcome this.

Finally, it is important to look at the noise levels of various sensors, with respect to signal levels and to one another. At present induction coils generally have lower noise than SQUIDS above 100 Hz, but it remains to be determined which is superior in the critical 10^{-1} to 10 Hz band (Vozoff, 1991).

4.1.3 Methods of Impedance Estimation

As discussed above, in the field, five components of the E and H field signals are recorded as time series (see Figure 4.4b). Today's signals are digitally collected, amplified, filtered, and multiplexed. Digital storage gives rise to easy application of filters to remove the mean, to detrend, or to low-pass filter or window the data. Time to frequency domain conversion is facilitated with the use of the fast Fourier transform.

In natural source MT measurements, the relationships among the orthogonal electric and magnetic field components (E_x, E_y, H_x, H_y) at a single site are systematically contained in the impedance and the tipper (see below). One seeks to determine the elements of the frequency (f) domain impedance tensor ($Z(\omega)$), relating the horizontal electric and the horizontal magnetic field components, i.e.

$$\mathbf{E}(\omega) = \mathbf{Z}(\omega)\mathbf{H}(\omega) \qquad (1)$$

where

$$E(\omega) = \begin{bmatrix} E_x(\omega) \\ E_y(\omega) \end{bmatrix}, H(\omega) = \begin{bmatrix} H_x(\omega) \\ H_y(\omega) \end{bmatrix}, Z(\omega) = \begin{bmatrix} Z_{xx}(\omega) & Z_{xy}(\omega) \\ Z_{yx}(\omega) & Z_{yy}(\omega) \end{bmatrix} \qquad (2)$$

and, x and y are arbitrary orthogonal directions, (usually x is north and y is east), and $\omega = 2\pi f$, by using in spectral analysis methods. This step additionally requires an estimate of the confidence limits on the terms in the impedance.

In a multi-dimensional earth or an anisotropic 1-D earth Madden and Nelson (1964) postulated that horizontal E and H are no longer orthogonal but

$$E_x(\omega) = Z_{xx}(\omega)H_x(\omega) + Z_{xy}(\omega)H_y(\omega),$$
$$E_y(\omega) = Z_{yx}(\omega)H_x(\omega) + Z_{yy}(\omega)H_y(\omega) \quad (3)$$

where the terms are in the frequency domain unless otherwise stated. In equation (3), $H_x(\omega)$, $H_y(\omega)$, $E_x(\omega)$ and $E_y(\omega)$ are the Fourier transforms of the time varying horizontal magnetic and electric fields ($H_x(t)$, $H_y(t)$, $E_x(t)$, $E_y(t)$) (Gamble et al., 1979a). Since there are only two tensor impedance equations with four unknown impedance values, it is clear that there is an underdetermined system which requires at least two more independent estimates of $H_x(\omega)$, $H_y(\omega)$, $E_x(\omega)$ and $E_y(\omega)$ to be solved. 'Independent' implies that each set of values corresponds to a different polarization of the magnetic source. Such data are obtained from different time segments from within the recorded time series. Note that each of the equations in (3) involve complex quantities and by separating real and imaginary parts each equation can be divided into two independent equations containing only real terms.

Several methods of impedance estimation have evolved over the years. The earliest methods of impedance estimation used very simple methods in which approximately sinusoidal segments of recorded data were used to estimate values of $H_x(\omega)$, $H_y(\omega)$, $E_x(\omega)$ and $E_y(\omega)$ and these values used to solve equations in (3). These simplistic estimates provided no means of noise reduction or error estimation. More reliable impedance estimates can be obtained by using multiple data sets of $H_x(\omega)$, $H_y(\omega)$, $E_x(\omega)$ and $E_y(\omega)$ which results in an overdetermined system of equations.

Modern approaches to impedance estimation include:

a) Least Squares Impedance Estimation

In MT analysis, the estimation of the impedance tensor involves solving for Z in equations 1 and 2, now written:

$$Z_{ij}(\omega) = \left(\frac{E_i(\omega)}{H_j(\omega)} \right) \tag{4}$$

where,

i = x or y, j = x or y,

In the two equations i = x,y are independent, allowing the solutions for Z_{xx} and Z_{xy} to be obtained separately from Z_{yx} and Z_{yy}. An exact solution for each equation may be obtained from two exact independent estimates of (H_x,H_y) and (E_x,E_y). Observed data contain noise (eg. random noise arising from spectral analysis) and in general a large number of data values are used in the determination of the impedance. We can use the least squares (LS) method to determine Z from a large number of (H_x,H_y) and (E_x,E_y) values.

Adopting the notation of Gamble et al., (1979a) in which:

$$[AB] = \begin{bmatrix} S_{A_1 B_1} & S_{A_1 B_m} \\ S_{A_m B_1} & S_{A_m B_m} \end{bmatrix} \tag{5}$$

where S_{AlBm} is the crosspower between the l-component of field A and the m-component of field B (and A and B would correspond to electric E, and magnetic, H fields). Using this notation the (spectral) least squares estimate for the impedance is:

$$Z^{LS} = \frac{[EH^*]}{[HH^*]} \tag{6}$$

and examining the solution for the Z_{XX} term in this new notation, we get:

$$Z_{xx}^{LS} = \frac{S_{E_x H_x} S_{H_y H_y} - S_{E_x H_y} S_{H_y H_x}}{S_{H_x H_x} S_{H_y H_y} - S_{H_x H_y} S_{H_x H_y}} \quad . \tag{7}$$

The denominator in (7) is repeated in all four impedance terms. We can again see the requirement for a range of polarizations of the source. If the source does not contain a time varying polarization the denominator will be zero. The full set of solutions is obtained by replacing E_x by E_y from which we obtain equations for Z_{YX} and Z_{YY}. These are:

$$Z^{LS}_{XX} = (S_{ExHx}\, S_{HyHy} - S_{ExHy}\, S_{HyHx})/D \tag{8}$$

$$Z^{LS}_{XY} = (S_{ExHy}\, S_{HxHx} - S_{ExHx}\, S_{HxHy})/D \tag{9}$$

$$Z^{LS}_{YX} = (S_{EyHx}\, S_{HyHy} - S_{EyHy}\, S_{HyHx})/D \tag{10}$$

$$Z^{LS}_{YY} = (S_{EyHy}\, S_{HxHx} - S_{EyHx}\, S_{HxHy})/D \tag{11}$$

where,

$$D = S_{HxHx}\, S_{HyHy} - S_{HxHy}\, S_{HxHy} \tag{12}$$

The LS solution for the impedance will provide an unbiased estimate of the true impedance only if there is no noise present on the magnetic components and if there is no noise correlated with the signal. Errors on the electric field components will not introduce any bias into the impedance estimates (Ferguson, 1988).

The LS estimate has considerable advantages. The LS estimate is biased by random noise on the magnetic field. However, in most recordings the magnetic field

is less noisy than the electric field consequently the LS estimate is quite good. It should be noted that any type of estimation using sampled data is subject to some degree of error therefore estimates of the MT parameters such as the impedance must be evaluated in terms of the confidence limits associated with them.

b) Remote Reference Impedance Estimation

A preferred method of estimating the impedance is to use a remote reference recording R(t) which is a recording (usually magnetic but possibly electric) from a site near the main MT site. For optimal results the signal at the remote reference should be fully coherent with the signal at the main site and the noise should be completely uncorrelated.

The desire to minimize the effect of noise on MT data sets has resulted in much experimenting with data collection methods. The remote reference method (Gamble et al.; 1979a, 1979b) uses electric or magnetic data from a site remote from the main MT site in order to correct for noise. The method is capable of correcting for all noise except that which is coherent between the remote and the main site. It is capable of correcting for noise which is correlated between the magnetic and electric time series at the MT site. The distance of the remote site from the MT site is limited by the requirement that the geomagnetic source-field is coherent between the two sites (Gamble et al., 1979a).

The general equation for the remote reference impedance estimate, Z^R will be

$$Z^R = \frac{[ER^*]}{[HR^*]}. \qquad (13)$$

Gamble et al. (1979a) is cited as the source for the following derivation of the remote reference equations. Remote referenced data will be denoted (R_x, R_y) where R may be either the electric or magnetic field (frequency-dependent) Fourier transform at the remote site. Starting with equation 3 we can multiply by the complex conjugates R^*_x and R^*_y to obtain

$$E_xR^*_x = Z_{xx}H_xR^*_x + Z_{xy}H_yR^*_x + e_xR^*_x \quad (14)$$

$$E_xR^*_y = Z_{xx}H_xR^*_y + Z_{xy}H_yR^*_y + e_xR^*_y \quad (15)$$

where E_x is the error caused by noise in E_x, H_x and H_y. With uncorrelated errors due to the noise and/or signals at the remote reference site, summing over many values of E,H and R will cause the last term in equations 14 and 15 to go to zero. The noise could be associated with either the electric or magnetic components. The corresponding spectral estimate is given by:

$$S_{ExRx} = Z_{xx}S_{HxRx} + Z_{yx}S_{HyRx} \quad (16)$$

$$S_{ExRy} = Z_{xx}S_{HxRy} + Z_{yx}S_{HyRy} \quad (17)$$

and we may now solve for Z_{xx} and Z_{xy}. A similar approach may be used to obtain Z_{yx} and Z_{yy} leading to the following remote reference equations:

$$Z^R_{XX} = (S_{ExRx}S_{HyRy} - S_{ExRy}S_{HyRx})/D^R \quad (18)$$

$$Z^R_{XY} = (S_{ExRy}S_{HxRx} - S_{ExRx}S_{HxRy})/D^R \quad (19)$$

$$Z^R_{YX} = (S_{EyRx}S_{HyRy} - S_{EyRx}S_{HyRx})/D^R \quad (20)$$

$$Z^R_{YY} = (S_{EyRy}S_{HxRx} - S_{EyRx}S_{HxRy})/D^R \quad (21)$$

$$\text{where } D^R = S_{HxRx}SH_{yRy} - S_{HxRy}S_{HyRx} \quad (22)$$

Since these impedance equations contain only crosspowers between remote and electric time series or remote and magnetic time series, the results will be unbiased by any noise at the main MT site that is uncorrelated with noise and/or signal at the remote site. They will in fact be unbiased even when there is correlated noise between the electric and magnetic components at the main MT site (Ferguson, 1988). The remote reference impedance solution can be shown to be equivalent to the application of two LS solutions. The first is for the transfer function between the magnetic field and the remote field and the second determines the transfer function between the electric field and the signal component of the magnetic field. The final remote-reference transfer function is therefore unbiased by uncorrelated noise on either the magnetic or electric field recordings.

The remote reference site chosen should be sufficiently distant such that there is no correlated noise between the two sites but close enough for coherent geomagnetic source fields between sites. All that is required is that the remote reference is able to be related to the magnetic field at the MT site through a linear transfer function

$$\mathbf{B}(\omega) = \mathbf{N}(\omega)\mathbf{R}(\omega). \qquad (23)$$

It is therefore acceptable for the impedance to be different between the two sites and the remote reference may be either an electric or magnetic recording.

The remote reference operates on the magnetic field and not the electric field therefore one could alternatively formulate a remote reference method based upon the admittance estimate for the impedance in which the remote reference operates on the

electric field. In the absence of correlated noise components the impedance estimates would ultimately be the same (Ferguson, 1988).

c) Robust MT Estimation

The remote reference method described above corrects for bias caused by the presence of noise in an MT time series. Any non-Gaussian noise influencing the time series is not recognized or corrected. Chave et al. (1987) describe a method for estimation of transfer functions (such as impedance) which takes into account the unknown and unlikely non-Gaussian error distribution. This procedure is known as the robust estimation method and it corrects for the presence of 'outliers' in the error distribution which cause departures from a Gaussian distribution and can significantly bias least squares impedance estimates. Two types of data 'outliers' are common: point defects and local nonstationarity. Point defects are isolated outliers that exist independent of the structure of the process under study. Typical examples include dropped bits of data and transient instrument failures. Local nonstationarity means a departure from a stationary base state that is of finite duration. The influence of these types of outliers on regression problems can be complicated (Chave et al., 1987). Robust estimation will not correct bias caused by the correlated noise between the MT electric and magnetic time series but will correct for phenomena such as long period diurnal signals and/or short high magnitude noise pulses on the MT data recordings.

Up to this point the statistical analysis methods used for estimating the power have not been considered. However, because MT recordings do not consist of simple

stationary time series there are several aspects of the power estimation which must be noted.

Long period MT data will contain diurnal signals with a period of 24 hr and harmonics which may be significant to periods as short as 4 hr, as well as tidal signals. The spectral analysis of such signals may produce spectral peaks with magnitudes much larger than the background stochastic power. It is desirable that no leakage occur from these peaks to adjacent frequencies therefore the utmost care must be taken to avoid this. Without appropriate windowing of the time series the frequency domain response will contain the spectral peaks convolved with the Fourier transform of the boxcar function defining the length of the time series. Ideally the MT analysis should be performed on time series from which the periodic signals have already been subtracted.

Robust spectral estimation has become the standard for MT analysis over the last five to ten years and is necessary because of the time variations in the impedance response (bias errors) and the time variations in the level of random noise in the data (random errors). Robust estimation basically involves the analysis of the segmented time series and downweighting of the response from those segments which do conform to the expected statistical distributions.

The impedance response will depend on the wavelength structure of the source as well as the frequency, ie. $Z=Z(\omega,k_x,k_y)$, where k_x and k_y are the spatial-frequency domain wavenumbers. At mid-latitudes, it is assumed that the field is approximately uniform ($k_x \sim= 0$) and this assumption forms the basis for much of the MT modelling

that proceeds after spectral analysis. During intense magnetic storms, the fields are not uniform and an impedance estimate made from data collected during the storms would differ from the uniform field case. Robust estimation will downweight the response from such storms because the impedance derived from the time series segments during the storm will differ from that derived from the rest of the time series. Some time series recordings may contain short batches of large noise (e.g. recordings from near an isolated road). Robust processing will reduce the contribution of these segments to the response.

Robust processing can take many forms. In the simplest form, visual inspection of the time series is used to remove bad segments. In the next most advanced form a statistical parameter, such as the coherence between the electric and magnetic fields, is used to define the weighting of a particular segment to the final response. In robust statistical estimation, typically now used in MT analysis, an iterative least-squares approach is adopted in which data are downweighted until the expected statistical distribution of the response is obtained.

Chave et al. (1987) describes in detail the principles of robust statistics and their adaptation to univariate and multivariate spectral analysis within a geophysical context. In short, the robust method for computing impedance estimates follows statistical definitions of robustness in the estimation of location and scale and maximum likelihood or M-estimators for computing robust averages and solving robust regression problems. Diagnostic plotting is used to help elucidate the extent of the outlier contamination or nonstationarity. These tools are then combined with the

section-averaging method of spectral analysis and applied to the estimation of power spectra, transfer functions and coherences.

4.1.4 Methods in MT Response Analysis, 1-D, 2-D and 3-D

The object of data processing, described above, is to extract from the stochastic signals a set of smooth, repeatable functions representing the earth's MT response, which can be used to interpret conductivity structure (Vozoff, 1991). New developments in this interpretation are occurring most rapidly in the areas of 3-D modelling and impedance tensor analysis. As a first step in the tensor analysis, there are two functions, as outlined above, impedances and tippers, and their attributes: magnitude, phase, special directions, skew and ellipticity that form the basis for MT response analysis. Sections of apparent resistivity and phase as a function of depth can be calculated from the impedance responses modeled from the field data.

First-order analysis of the MT response extracted from the measured signal is often done assuming a 1-D layered earth approach where the conductivity structure is assumed to vary in only one direction (z, vertical). While this assumption is usually not the case for most applications, it does allow for the introduction of some simple concepts that aid in the evaluation of the MT response. One such concept is that of the MT skin depth (δ). This is the depth where $E_x(z)$ reduces to 1/e or ~37% of its surface value and is expressed as:

$$\delta = \sqrt{\frac{2}{\sigma\omega\mu}} \tag{24}$$

where, σ is the conductivity in S/m, $\mu = \mu_0 = 4\pi \times 10^{-7}$ H/m. This quantity offers an estimate of the MT depth sensitivity at a given frequency.

It can easily be shown that for an n-layered, one dimensional earth, the surface impedance (Z_s) can be found in a recursive manner in which the MT impedance at the surface of a layer is defined in terms of the MT impedance at the surface of the layer below it (e.g. Jiracek, 1984). The impedance value then gives rise to a simple estimate of the apparent resistivity (ρ_a) value as a function of frequency. The impedance estimate (Z(f)) is readily transformed into the apparent resistivity by the relation:

$$\rho_a(f) = \frac{1}{\mu\omega}|Z(f)_s|^2 \tag{25}$$

The apparent resistivity as a function of frequency can then be modeled to produce an estimate of the conductivity structure as a function of depth below the measurement station. Another useful value is the phase angle (ϕ) which is the phase lead of the E over the H fields as a function of frequency and is given by:

$$\phi_{ij}(f) = \tan^{-1}\left(\frac{E_i(f)}{H_j(f)}\right) \tag{26}$$

In a, uniform medium the electric field leads the magnetic field by 45° and as a general rule for interpretation, if the phase angle increases with decreasing frequency then the earth is getting more conductive with increasing depth. Conversely, if the phase angle decreases with decreasing frequency then the earth is getting more resistive at depth.

A more common approach to the analysis of the MT response is to assume a 2-D earth, in which the regional conductivity varies in z and either x or y, with one component constant, and where data are collected approximately across strike. When the earth is 2-D with $\rho = \rho(x,z)$, y is the geoelectric strike direction so that the conductivity structure is striking along the y-axis. The total EM fields then split into two independent modes:

1) E-polarization or Transverse Electric (TE): The electric field component is transverse to the plane of symmetry or parallel to geoelectric strike. This polarization mode will involve the E_y, H_x, and H_z components.

2) B-polarization or Transverse Magnetic (TM): The magnetic field is transverse to the plane of symmetry or perpendicular to the geoelectric strike. This polarization mode will involve the H_y, E_x, and E_z components.

For 2-D structures the TE mode is often considered a pseudo-1-D response, providing information on the conductivity structure beneath the site (Jiracek, 1984). In the TM mode the need for current continuity across strike requires the E_x field component to change rapidly across strike, providing high lateral structural resolution. E_x will be discontinuous across surface boundaries. The TM mode therefore is very useful for distinguishing lateral changes in conductivity structure (electrical continuity), whereas the TE mode is most useful in distinguishing conductivity structure as a function of depth and thus estimating the magnitude of enhanced conductivity (Jiracek, 1984).

In the 2-D case only two impedances are needed to completely describe the impedance tensor:

$$Z = \begin{bmatrix} 0 & Z_{xy} \\ Z_{yx} & 0 \end{bmatrix} \tag{27}$$

where, (for the y-direction corresponding to the strike direction)

$$Z_{yx} = -Z_{TE} = \frac{E_x}{H_y} \text{ and } Z_{xy} = Z_{TM} = \frac{E_y}{H_x} \tag{28}$$

with the corresponding apparent resistivities and phases:

$$\rho_{yx} = \rho_{TE} = \frac{1}{\mu\omega}|Z_{TE}|^2 \text{ and } \phi_{yx} = \phi_{TE} = phase(Z_{yx}) \tag{29}$$

$$\rho_{xy} = \rho_{TM} = \frac{1}{\mu\omega}|Z_{TM}|^2 \text{ and } \phi_{xy} = \phi_{TM} = phase(Z_{xy}). \tag{30}$$

Another important measure known as the 'tipper' (magnetic transfer function) was devised by Vozoff, (1972), from general tensor relations for the MT fields over a 2-D earth. This is a complex quanitity whose amplitude is the ratio between the vertical magnetic field and the horizontal magnetic field perpendicular to strike (H_z/H_x). In the tipper function (T), H_z is assumed to be linearly related to H_x and H_y by

$$H_z = T_x H_x + T_y H_y \tag{31}$$

The tipper magnitude is defined by

$$|T| = \left(|T_x|^2 + |T_y|^2\right)^{\frac{1}{2}} \tag{32}$$

and the phase Φ_T by

$$\phi_T = \frac{\left(T_{xR}^2 + T_{xI}^2\right)\tan^{-1}\left(\frac{T_{xI}}{T_{xR}}\right) + \left(T_{yR}^2 + T_{yI}^2\right)\tan^{-1}\left(\frac{T_{yI}}{T_{yR}}\right)}{|T|^2} \tag{33}$$

where R and I subscripts refer to the real and imaginary parts of T_x and T_y, respectively.

Even if the Earth is ideally 2-D, the geoelectric strike is often unknown during data aquisition. Consequently the measuring axes generally do not coincide with axes parallel and perpendicular to geoelectric strike. In a 2-D earth, the impedance tensor can however be rotated into a coordinate system where the diagonal components of the impedance tensor go to zero and thus the x or y axis is parallel or perpendicular to geoelectric strike (Sims and Bostick, 1969). These two directions are called principal directions. The tipper is used to define which of the two principal directions is the geoelectric strike direction in a 2-D earth and the tipper can be rotated just as the impedance tensor.

Induction vectors are a means of graphically displaying information contained in the magnetic transform function (tipper). The information contained in the transform function can be displayed as two vectors, the real and imaginary induction vectors. In general, the real induction vectors (reversed) point towards zones of enhanced conductivity and can be used to map lateral changes in conductivity. The magnitude or length of the induction vector is an indicator of proximity and magnitude of horizontal variations in electrical structure. The length of the vectors is proportional to the conductivity contrast but also decreases with distance from the conductor.

The orientation of the principal axis is useful in mapping changes in the conductivity structure of the survey region. The apparent strikes are subject to a 90^0 rotational ambiguity, and the determination of whether the conductivity structure is parallel or perpendicular to the recovered strike direction must be inferred from other evidence (e.g. the tipper). Both the geoelectric strike and induction vector are frequency dependent features.

In a fully 3-D MT tensor analysis concepts such as skew and ellipticity (see Eggers, 1982) are used as 3-D indicators relating the ratios of the major and minor axes of the rotation ellipse to the dimensionality of the MT response.

4.1.4.1 Raw Data Quality and Signal to Noise Ratios

The first procedure in the analysis of an MT data set is an evaluation of the raw data quality through an examination of the data scatter, coherences, signal to noise ratios (SNR) and error estimates. This can be accomplished manually by a site by site inspection of the signal spectra; apparent resistivity and phase; and the four tensor component magnetic and electric SNR plots. Abrupt transitions, spikes and 'bumps', in the apparent resistivity and phase curves as a function of frequency associated with large error bars and/or low SNR suggest that the data for that frequency or frequency range are unreliable and therefore unsuitable for inclusion in the data analysis. The identification of these 'bad frequencies' is an important first step in the MT data reduction. It often is the case that common frequencies or frequency bands will be identified as suspect for a set of MT sites. There are often a few bad points at

frequencies between 10^3 and 10^4 Hz and the highest frequencies (~10^4 Hz) may not be unsuitable for analysis. Also there may be a few bad points at the lowest frequencies (<10^{-3} Hz).

4.1.4.2 Dimensionality/Directionality

It is often found in the interpretation of MT data collected in complex resistive environments such as the Canadian Precambrian Shield that there is no coordinate axis system in which the diagonal elements of the impedance tensor completely disappear. In this situation, 1-D and 2-D conductivity models are unable to explain the measured impedance tensor and, a strict approach to the interpretation, should be based on a 3-D conductivity distribution. While the 3-D conductivity structure is required to explain all aspects of the recorded data, 3-D interpretation is often impractical as the spatial density of the recorded data set is insufficient to allow for an independent 3-D interpretation. In this case the response must be approximated by a 2-D structure and the final models interpreted considering this approximation.

One of the first steps in the interpretation of MT data is to determine the dimensionality and directionality (geoelectric strike) of the data. This step is important as the accuracy of the interpretation relies upon an understanding of the directionality and dimensionality inherent in the data. Additionally, dimensionality analysis provides the interpreter with a direction and justification for further interpretation (1-D, 2-D or 3-D).

Two aspects of the measured MT data can be analyzed to determine the dimensionality and directionality of the conductivity structure. The impedance tensor can be examined with tensor decomposition algorithms (Groom-Bailey decomposition, see 4.1.4.3) and the magnetic transfer functions can be examined through the calculation of induction vectors.

The information obtained from the dimensionality and directionality analysis for multiple sites exceeds the information available from a single site and allows the interpreter to identify groups of adjacent sites that show common 1-D or 2-D characteristics over a broad frequency range(s). This information is based on the assumption that a group of sites will sense a common regional structure. Once these site groups and bandwidths have been identified, then 1-D or 2-D interpretation and modelling of the conductivity structure can be undertaken.

4.1.4.3 Tensor Decomposition and the Groom-Bailey Method

Local distortion of the electric field by near-surface inhomogeneities can have significant effects on the MT impedance tensors and must therefore be recognized and corrected (Groom and Bahr, 1992). The distortions of the regional data are caused by charge accumulations on the electrical boundaries of surficial inhomogenieties. A number of techniques have been proposed to deal with this problem using various mathematical and physical tensor decomposition approaches (see Eggers, 1982; LaTorraca et al, 1986; Zhang et al, 1987; Groom and Bailey, 1989; Chakridi et al, 1992). The Groom-Bailey (GB) decomposition (Groom and Bailey,1989; Groom et

al., 1993) is based on a physical model of distortion, and includes statistical tests for model validity. It has therefore been applied to the GD-FFB MT data set.

The Groom-Bailey tensor decomposition method is based on the assumption that the measured impedance tensor is the result of the superposition of large scale (structures of interest or target structure) and small scale (local inhomogeneity) conductivity structures. The GB method tests quantitatively the hypothesis that the regional geoelectric structure can be characterized by a 1-D or 2-D model, with conductive or resistive near-surface 3-D anomalies causing galvanic distortion of the Earth's electric fields (Groom and Bailey, 1989). The goal is to determine the inherent dimensionality of the large-scale structure and, if it is 2-D, to obtain a regional strike direction and the 2-D regional impedances (Groom and Bailey, 1989).

If the local inhomogeneity is small compared to the skin depth and wavelength of the EM wave in the larger scale structure, (a condition which is reasonable at low frequencies if there is sufficient scale difference between the local and regional anomalies), the spatial gradients of the electric field are small over the inhomogeneity. Under this condition it can be assumed that the inhomogeneity is excited by a uniform electric field. The small size of the inhomogeneity allows us to assume in addition, that the inhomogeneity is inductively small, and therefore induced secondary electric fields can be neglected. Under these assumptions the local inhomogeneity results in an electrostatic (galvanic) distortion of the regional structure's electric field, and an anomalous magnetic field associated with the anomalous electric field.

The validity of the galvanic distortion model can be judged only by the success or failure of the model to explain observed data, since the observer usually has no information on the scale of the local inhomogeneity, and often little information on the target geoelectrical structure. The validity of the model is dependent on both the frequency of observation and location, with the assumptions generally holding at low frequencies and in locations removed from sharp boundaries in the larger scale structure (where the electric field gradients are small). Numerous authors have discussed the conditions of validity of galvanic distortion (Berdichevsky and Dmitriev, 1976; Larsen, 1977; Bahr, 1988; Groom and Bailey, 1991; Groom and Bahr, 1992), to which the reader is referred for further details.

The electric field measured in the presence of a distorter is related to the regional or undistorted electric field through a 3x3 electric distortion matrix C_3 (Chave and Smith, 1994). The elements of this distortion matrix will be real if the distorting inhomogeneity is inductively small. Under the assumptions usually made in the MT method (i.e. observer at surface of flat Earth), the normal electric current (E_z) vanishes at the surface of the Earth and the distortion matrix reduces to a 2x2 distortion tensor C. The electric field measured at the surface of the Earth is therefore given by,

$$\bar{E}_m = C\bar{E}_u = \begin{bmatrix} C_1 & C_2 \\ C_3 & C_4 \end{bmatrix} \bar{E}_u \tag{34}$$

where subscript m refers to the measured field and subscript u refers to the undistorted field. The anomalous magnetic field produced as a result of a galvanic

distortion is related to the undistorted electric field through a 3x3 magnetic distortion matrix D_3 (Chave and Smith, 1994). At the surface of the Earth this distortion matrix reduces to a 2x2 tensor D which describes the distortion of the horizontal magnetic field, and a 2-element row vector Q which describes distortion of the vertical magnetic field (Chave and Smith, 1994). The elements of D and Q will be real under the same conditions as the electric distortion tensor. The anomalous horizontal magnetic field (H_{hanom}) produced by the distorter is given by,

$$\vec{H}_{hanom} = D\vec{E}_u = \begin{bmatrix} -\gamma & \alpha \\ -\beta & \varepsilon \end{bmatrix} \vec{E}_u , \tag{35}$$

and the anomalous vertical magnetic field (H_{zanom}) by,

$$\vec{H}_{zanom} = Q\vec{E}_u = \begin{bmatrix} Q_{zx} & Q_{zy} \end{bmatrix} \vec{E}_u . \tag{36}$$

The horizontal and vertical magnetic fields (H_{hm} and H_{zm}) measured in the presence of a galvanic distortion therefore become the sum of the undistorted magnetic (H_{hu}) and anomalous magnetic fields,

$$\vec{H}_{hm} = \vec{H} + \vec{H}_{hanom} = \vec{H}_{hu} + D\vec{E}_u \tag{37}$$

and

$$\vec{H}_{zm} = \vec{H}_{zu} + Q\vec{E}_u . \tag{38}$$

The impedance tensor measured in the coordinate system of the larger structure is given by,

$$Z_m = \frac{\vec{E}_m}{\vec{H}_{hm}} = \frac{C\vec{E}_u}{\vec{H}_{hu} + D\vec{E}_u} = \frac{CZ_u}{I + DZ_u}, \tag{39}$$

where Z_u is the response of the larger one or two dimensional conductivity structure and I is the identity matrix.

The magnetic transfer functions T (T_{zx},T_{zy}) relating the observed vertical and horizontal magnetic fields are given by,

$$\bar{T}_m = \frac{H_{zm}}{\bar{H}_{hm}} = \frac{H_{zu} + Q\bar{E}_u}{\bar{H}_{hu} + D\bar{E}_u} = \frac{\bar{T}_u}{(I + DZ_u)} + \frac{QZ_u}{(I + DZ_u)}, \tag{40}$$

Using equation 39 the measured transfer function can be expressed as

$$\bar{T}_m = \frac{\bar{T}_u}{(I + DZ)} + \frac{QZ_m}{C}. \tag{41}$$

Examination of the equation for the distorted impedance tensor (39) indicates that although the distortion matrices C and D are both constant for any given distorter, only the electric field distortion matrix C will have a frequency-independent effect on the measured impedances. This distortion results in measured impedances which are distortion dependent combinations of the undistorted impedances.

The magnetic distortion matrix D results in distorted impedances which are both frequency-dependent and distortion-dependent mixtures of the undistorted impedances. The frequency-dependence of magnetic distortion stems from the undistorted impedance tensor's (Z_u) dependence on frequency.

Figure 4.5a shows the effect of magnetic distortion (for a D of 0.08) on the magnitude of the scalar impedance calculated for a 5000 Ω·m halfspace. The magnetic distortion can be neglected at periods exceeding approximately 10^{-1}s. As period increases the magnitude of Z_u decreases making the term DZ_u in the

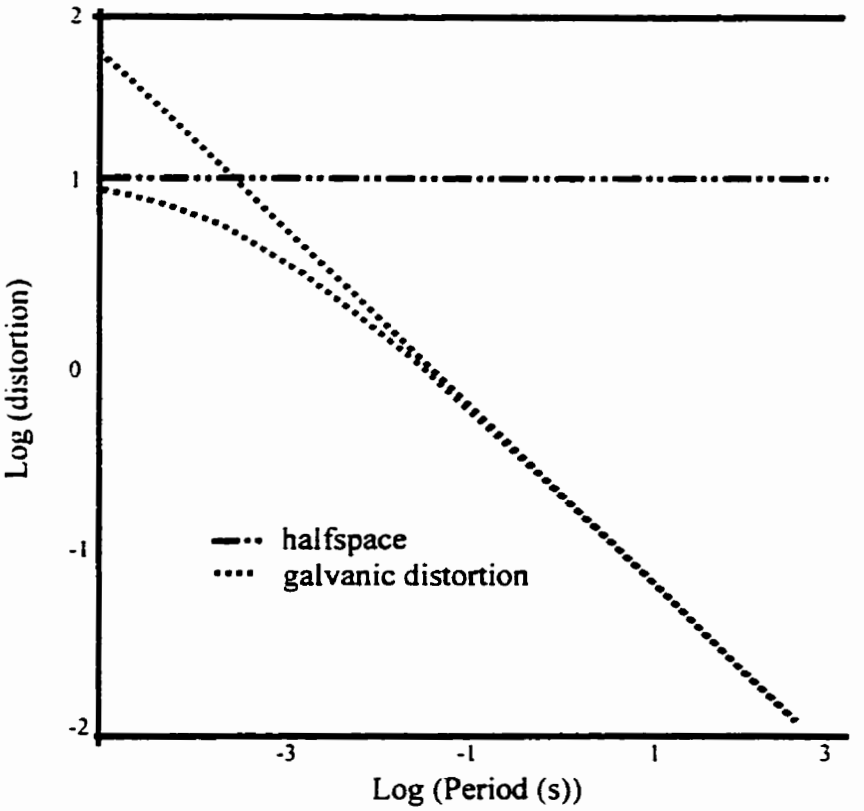

Figure 4.5a. Galvanic magnetic distortion of the 5000 ohm-m halfspace impedance magnitude as a function of period. Distortion of the measured impedance becomes negligible at longer periods.

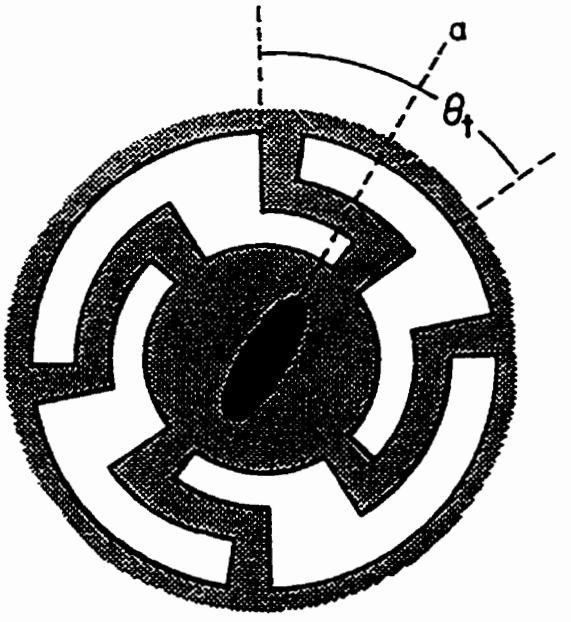

Figure 4.5b A contrived example of distortion. A moderately conductive overburden (dotted) is shown on an insulating substratum (white). An elliptical and highly conductive surface region (black) exists in the central region of the overburden (after Groom and Bailey, 1989)

denominator of equation 39 insignificant ($I \gg DZ_u$). As the magnitude of the regional impedance tensor generally decreases with increasing period it is reasonable to assume that the first order effects of galvanic distortion are explained solely by the distortion matrix C, especially at lower frequencies.

Equation 41 shows that in the presence of a galvanic distorter with negligible magnetic distortion ($DZ \ll I$), the measured magnetic transfer function is the sum of the regional transfer function (first term) and a local transfer function (second term) produced by the distorter (Zhang et al., 1993). As the magnitude of the undistorted impedance tensor decreases, the measured transfer function will approach that of the regional structure (T_u). The importance of distortion of the transfer functions is dependent on the magnitude of the undistorted transfer function, with the local transfer functions possibly making up a significant portion of the measured transfer function when the regional transfer function is small. This is especially the case at high frequencies where the magnitude of the undistorted impedance tensor is large.

The distortion of the magnetic fields is dependent on the regional conductivity structure, having its greatest importance in structures where the magnitude of the regional impedance tensor decays slowly as a function of frequency. Magnetic distortions will be most important, therefore, in regions having a conductive-over-resistive structure and of lesser importance when the conductivity structure, is resistive-over-conductive as is often the case on the exposed Precambrian Shield.

When considering only the first-order effects of galvanic distortion the measured magnetic field is assumed to be that of the larger structure,

$$\vec{H}_m = \vec{H}_u . \tag{42}$$

Therefore, the distortion is represented by four real parameters and the measured impedance tensor in the coordinate system of the larger structure is given by

$$Z_m = CZ_u . \tag{43}$$

If the larger conductivity structure is 2-D, with the strike in the x-direction, the measured impedance tensor is given by:

$$Z_m(\omega) = C\begin{bmatrix} 0 & Z_{TE}(\omega) \\ -Z_{TM}(\omega) & 0 \end{bmatrix}. \tag{44}$$

For measurements in a different coordinate system (rotated clockwise from the strike of the structure) the observed impedance Z' will become:

$$Z_m' = RZ_mR^{-1} \tag{45}$$

where $R = \begin{bmatrix} \cos\theta & \sin\theta \\ -\sin\theta & \cos\theta \end{bmatrix}$, the rotation operator. (46)

In this form the decomposition is represented by nine parameters per frequency (the strike θ, four parameters contained in C and four parameters contained in the two complex impedances). In order to recover the undistorted impedances, two of the parameters of C are absorbed into the impedances as 'static shifts' (see section 4.1.4.4) allowing one to fit the remaining seven parameters (strike, shear, twist and the two complex impedances) to the eight real components of the measured impedance tensor. The static shift is a frequency independent multiplication factor that can be observed in MT data such that the apparent resistivity curves are translated

up or down on a log apparent resistivity plot, while the phase data are unaffected (Vozoff, 1991).

As described above the Groom-Bailey method provides a model for the galvanic distortion of a regional 1-D or 2-D impedance (Groom and Bailey,1989). In their 2-D/3-D model, the distorted impedance, in the actual measurement coordinate system, has the form:

$$Z_{=}^{'} = RgTSAZ_{u}R^{T} \tag{47}$$

where the capitalized terms correspond to matrices and Z_u is the undistorted tensor in the regional strike coordinate system. In the Groom-Bailey tensor decompositions it is not possible to determine two of the distortion parameters g and A independently from the undistorted impedance tensor. The term g is a scale factor and the matrix A is an anisotropy or splitting operator which in normalized form is:

$$A = \frac{1}{\sqrt{1+s^2}}\begin{bmatrix} 1+s & 0 \\ 0 & 1-s \end{bmatrix} \tag{48}$$

The matrix A thus creates a static shift in the response. It can be removed (or at least reduced) by using the accepted methods (e.g. matching the two impedance curves at high frequencies or matching the impedance to controlled source constraints). The terms g and A are incorporated into Z_u to give the distortion model:

$$Z_{=}^{'} = RTSZ' R^{T} \tag{49}$$

where

$$Z' = \begin{bmatrix} 0 & a \\ b & 0 \end{bmatrix} = gAZ_{u} \tag{50}$$

The remaining terms in the distortion model R, T, and S correspond to the rotation between the conductivity and measurement axes, the *twist* of the electric field, and the *shear* of the electric field respectively. The twist is defined by:

$$T = \frac{1}{\sqrt{1+t^2}}\begin{bmatrix} 1 & -t \\ t & 1 \end{bmatrix} \tag{51}$$

where t is the twist and may be characterized by the angle

$$\theta_t = \tan^{-1} t \tag{52}$$

The shear is defined by:

$$S = \frac{1}{\sqrt{1+e^2}}\begin{bmatrix} 1 & e \\ e & 1 \end{bmatrix} \tag{53}$$

where e is the shear and may be characterized by the angle

$$\theta_e = \tan^{-1} e \tag{54}$$

From above we see that there are four independent distortion parameters required to represent the most general distortion tensor (g, s, t, and e). A physical interpretation of the twist, shear and split can be demonstrated through the example in figure 4.5b, from Groom and Bailey (1991). A moderately conductive region of overburden (dotted) is shown on an insulating substratum (white). Inside the circular central region of overburden, an elliptical and highly conducting surface region (e.g. a swamp) exists (black). Measurements are made at the center of the swamp. The regional telluric currents are first twisted through an angle θ_t; the difference between regional and local strike. The elongation of the swamp then leads to anisotropy with principle axis parallel and perpendicular to the direction a. The shear is the rotation to

the principle axis of the swamp. The splitting operator imposes the anisotropy caused by the elongation and conductivity contrast of the swamp.

The channelling matrix C combines the distortion terms

$$C=gTSA \tag{55}$$

The parameters g, T, S and A are defined above and if e = s = 0 then by substitution of equation 14, the channeling matrix reduces to:

$$C = \frac{g}{\sqrt{1+t^2}} \cdot \begin{bmatrix} 1 & -t \\ t & 1 \end{bmatrix} \tag{56}$$

and this operator corresponds to the skew as mentioned above.

An important aspect of applying the 1-D, 2-D and fully 3-D physical models (equations 44, 43, 47) to real data is the computation of some measure of misfit to appraise quantitatively the appropriateness of the model (Groom et al, 1993). After obtaining the model parameters through the application of one of the physical hypotheses, the model hypotheses can be tested with a χ^2-like misfit variable. This is a residual error for the fit of the model to the data, normalized by estimates for the variance (σ^2_{ij}) of each element of the tensor data:

$$\gamma^2 = \frac{1}{4}\sum_{i=1}^{2}\sum_{j=2}^{2}\frac{\left|Z_{ij}^{m} - Z_{ij}\right|^2}{\sigma_{ij}^2} \tag{57}$$

where Z_{ij} and Z^{m}_{ij} are the modelled and measured tensor elements respectively and the variances are usually estimated from the sample population of the tensor elements. The misfit γ^2 would be expected to lie within the range of 0-4 if the errors in the mean impedance estimates are randomly distributed and the model tensor elements have

been fitted to within two standard deviations of the data (Groom et al., 1993). If the data cannot be fit to within these levels, it implies either that not all physical effects have been included (i.e., 3-D induction), or that the variances are poorly estimated. A graphical display of the fit of the impedance tensor to a particular parameterization has proven most useful since the γ^2 statistic can vary significantly between adjacent frequencies due to either the randomness of the noise or poor variance estimation (Groom et al., 1993).

The best way to illustrate the Groom-Bailey methodology, and the associated graphical analysis techniques, is by demonstration using a synthetic 3-D impedance data set which is generated by superimposing 2-D numerical and 3-D analytic responses. Such a model is shown in figure 4.6a and comprises a 3-D homogeneous hemisphere embedded in a 2-D regional structure (Groom and Bailey, 1991). Inductive responses due to the embedded body are negligible however the conductivity contrast between the host and the hemisphere produces a charge distribution which has significant effects upon both electric and magnetic fields. The resulting impedance data can be rotated into any coordinate frame and be contaminated with Gaussian noise such that the variance of this noise is identical for all four tensor components.

Considering only a fully 3-D parameterization of the model, a 3-D site is located 16 m outside the hemisphere at an angle of 22.5^0 clockwise of the regional strike (figure 4.6a). The data measurement axis is 30^0 counterclockwise. Figure 4.6b presents the parameters and the fit for the fully 3-D model (equation 47) without any

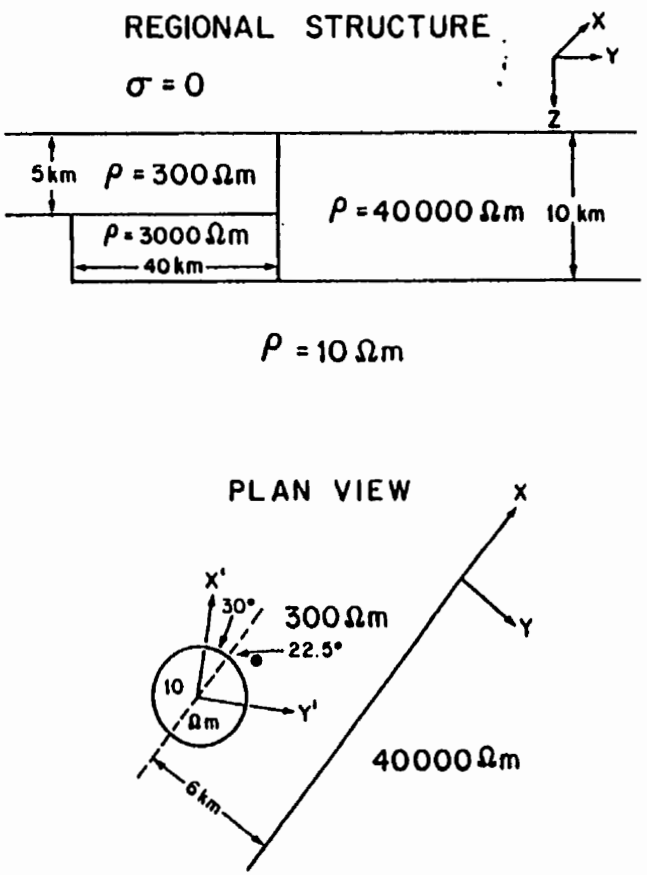

Figure 4.6a A synthetic regional 2D conductivity structure. The measurement site is shown (black dot). The hemisphere is 50m radius, 6 km from a vertical contact. Measurement axes are rotated 30 degrees anticlockwise from the 2D coordinate system (after Groom and Bailey, 1989).

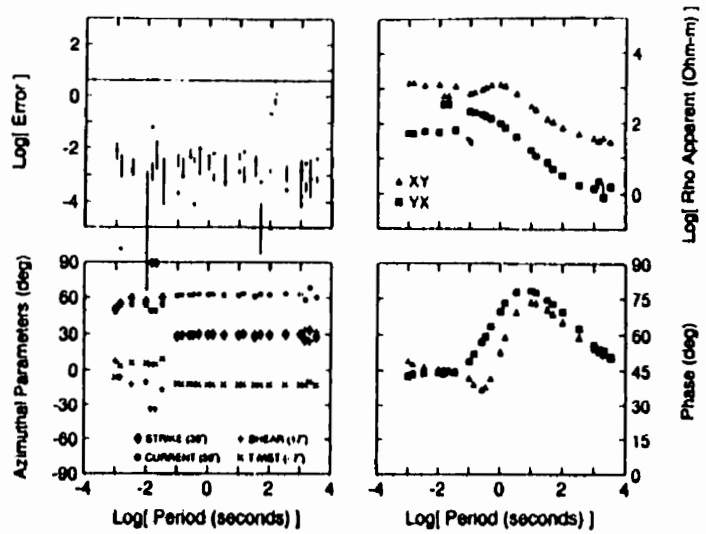

Figure 4.6b Standard parameter display of the i) residual error fit, ii) azimuthal parameters; strike, twist, shear, channeling, iii) regional impedance estimate and iv) regional phases for an unconstrained 3D model parameterization of 3D data (after Groom-Bailey, 1989).

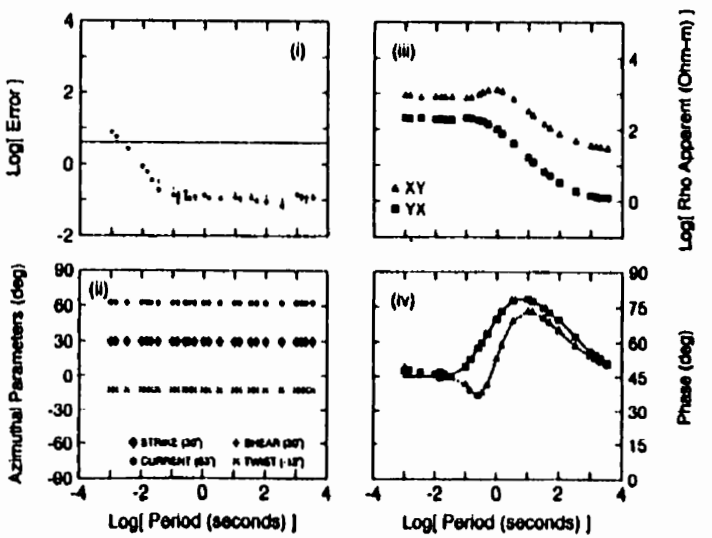

Figure 4.6c Standard parameters display of fully constrained 3D parameterization of 3D data. Solid and dashed lines show true 2D phase responses parallel and perpendicular to regional strike (after Groom and Bailey, 1989).

constraints. For each site four separate graphs of GB parameters are shown. These plots are:

1) The χ^2-like measure, γ^2, error statistic that tests the 3D model hypothesis.

2) Four azimuthal parameters (geoelectric strike, current, twist and shear) plotted together on the same graph allow for the identification of frequency ranges with common distortion features and geoelectric strike features,

3) & 4) Apparent resistivity and phase curves are shown for data in the off-diagonal components of the MT impedance tensor (Z_{xy} and Z_{yx}) incorporating those parameters calculated from the GB statistics. These curves are plotted with error bars attached to each data point.

Figure 4.6b shows that for frequencies less than 10 Hz, a strike direction is obtained which is reasonably close to the correct strike of 30^0. However at the highest frequencies, the combination of a strike which is physically poorly defined and the phase effects caused by anomalous magnetic field of the current channeling, have disrupted the strike determination. The twist and shear parameters are almost frequency independent below 10 Hz. However, at higher frequencies (shorter periods) these parameters vary with frequency as they are functions of the determined strike direction. Since the synthetic data are expected to produce a relatively smooth model, the twist, shear and regional strike should be frequency independent. The regional phases are well recovered, as are the shapes of the regional apparent

resistivities, but the local anisotropy has split the regional responses even at the highest frequencies. The unconstrained data also show very low γ^2 residual misfits over all frequencies. This example illustrates the trade-off between the smoothest or simplest model, and the lowest average residual. Although the residual plot indicates an extremely good fit to the data, the model is rather rough as the 3-D parameters and the 2-D strike are free to vary at each frequency.

In considering the resolution and stability of the decomposition parameters in the presence of noise, figure 4.6b would indicate that a constrained strike of about 30^0 over the entire frequency range and frequency independent distortion parameters should fit the data adequately. Figure 4.6c shows such a decomposition model where strike, current, twist and shear azimuths are constrained to constant levels averaged over the entire frequency range. For frequencies lower than 10 Hz, a smooth model with acceptable residuals can be obtained. However, at high frquencies the residual increases to a maximum value near 5. The poor fit is attributable to the anomalous galvanic magnetic field (Groom and Bailey, 1991).

This example has illustrated a process, based on statistical and graphical representations of the data that may be used to identify frequency ranges at a single site or across many sites, where the distortion and strike parameters can be constrained such that the model residual error is minimized. The corrected 2-D regional impedance data can then be recovered for use in an improved interpretation of the subsurface conductivity structure. It is also worth noting that the best model is

not neccesarily the one with the lowest average residual (averaged over period) because there is a trade-off between minimizing the residual and maximizing the smoothness. The increase in the residual associated with any smoothing must be appraised to assess if the response of the constrained model is representative of the observed data (Groom et al., 1993).

Methodologies for recovering regional impedances in the presence of 3-D galvanic distortion are based on the most complete physical model of the impedance tensor currently available (Groom et al., 1993). The model (equation 34) on which these methodologies are based includes simpler physical models as special cases, and as such the 3-D galvanic distortion model is the most widely applicable physical model of the impedance tensor. The impedances recovered with these methodologies can be interpreted using available 1-D and 2-D forward and inverse procedures. In situations where the measured impedance tensor is not adequately fit by the 3-D distortion model, the decomposition still provides constraints on the conductivity structure (Groom et al., 1993) and allows the data to be modeled using an optimum 2-D approximation.

4.1.4.4 Static Shift

After fitting of a distortion model that removes the phase mixing caused by galvanic scattering it is necessary to correct the impedances for the combined effect of the site gain, g, and the local static shift, s (Groom and Bailey, 1989). This combined effect corresponds to the static shift observed in MT data. The static effects, as

previously mentioned, are observed as the vertical displacement between the apparent resistivity curves at adjacent sites or between TE and TM curves at the same site without affecting the curve shapes or phase data (Vozoff, 1991). Sources of static shifts can be either 2-D or 3-D and their affect on either the TE or TM mode is dependent on the nature of the source. In 2-D structures the TE mode is essentially considered a pseudo-1-D-response (Jiracek, 1984), the electric field component is parallel to strike and therefore the TE mode is sensitive to, and provides the most information on, conductivity structure in the vertical dimension, beneath the site. Site-to-site TE static shift should then be small and if the causitive body is narrow enough, no shift should be observed. The TM mode requires that the electric field component perpendicular to strike be continuous across strike therefore this component will change rapidly across the strike of an anomalous body since this mode is more sensitive to charge build up on lateral changes in conductivity. This has the benefit of providing high lateral structural resolution and also the apparent resistivity will be shifted by a constant factor when the thickness of the body is much less than the skin depth in either the host or the body (Vozoff, 1991). The procedures for static shift corrections are described in section 4.4.1.

4.1.4.5 MT Response Presentation

As a first pass inspection, corrected MT responses are often viewed as ρ_{TE} and ρ_{TM} sounding curves with their ϕ_{TE} and ϕ_{TM} counterparts. Such plots provide a quick assessment of the general subsurface conductivity structure as a function of increasing period (increasing depth), and the differences in the polarization mode responses

provides insight into the 1-D/2-D nature of the response, as well as an estimate of the site-to-site frequency-independent static shift.

In 2-D analysis, pseudosection presentations of corrected MT profile data are commonly used. In these plots the horizontal axis is the x-distance with site positions projected onto this axis. The vertical axis is usually in log period increasing downwards. Values of constant log apparent resistivity or phase are contoured. This type of plot not only provides the interpreter with an estimate of the lateral geoelectric variations in the subsurface but also provides a means of identifying poor data not recognized during data processing. Pseudosections of other parameters (e.g. regional strike angle) are also widely used during the MT response analysis phase for comparisons of site-to-site distortion etc.

In 3-D surveys, when a grid of sites has been measured or when dispersed sites cannot be projected onto a 2-D line, frequency-slices can be used to view apparent resistivity and phase variations on a contoured surface. Such data, with adequate spatial sampling, can be viewed as a volume or iso-surface rendered 3-D displays (analgous to time slices from 3-D seismic surveys). These presentation methods provide excellent means of quick litho-structural evaluations of 3-D MT data.

4.2 The GD-FFB MT Survey Sites and Pre-Processing of the MT Data

In 1992, MT surveys were performed by the contractor Phoenix Geophysics as part of the EM measurement component of LITHOPROBE's Trans-Hudson Orogen Transect data collection phase. A total of 108 AMT/MT and LiMS survey sites were spaced along an 800 km long east-west profile extending from western Saskatchewan

to central Manitoba. At 56 sites. MT recordings spanned a seven decade period range from 10^{-2}s to $2x10^{3}$s and AMT measurements with a period range from 10^{-4} to 0.1s were made at all 108 sites. LiMS data were collected at 15 sites with a period range of 10^{-1} to 10^{-4} Hz. Seven component recordings were made at all MT and AMT sites, comprising three components of the magnetic field, two components of the electrical field and two remote components. The recorded data were of consistently high quality throughout the survey (Jones et al., 1993). Data presented and discussed in this thesis comprise 28 AMT,MT and LiMS sites collected between the Glennie Domain in the west and the Flin Flon Belt in the east. Site positions are shown in figure 4.7 and Appendix A1 lists site locations. From west to east, sites A24 through M18 were located on Phanerozoic cover above the GD, sites M16 and D009 straddle the Phanerozoic to Precambrian boundary at the western edge of TFZ, sites M15 and A15 are in the HLB and near the eastern margin of the TFZ, sites M13, A13 and M12 straddle the HLB to FFB boundary at the SWT, and sites A12 through M46 are located in the western FFB. Note that the format of the site names on the figures and appendices conform to the full LITHOPROBE designation (e.g. THO-92-M25S = M25). Also the prefix 'A' in a site name refers to a site where AMT data was collected while the prefix 'M' in a site name refers to a site where both AMT and MT data were recorded.

The 28 data sets have been field edited and computer processed using modern robust remote reference techniques as described above (e.g. Jones et al., 1993; Ferguson et al., in review). The contractor provided the time series data (where

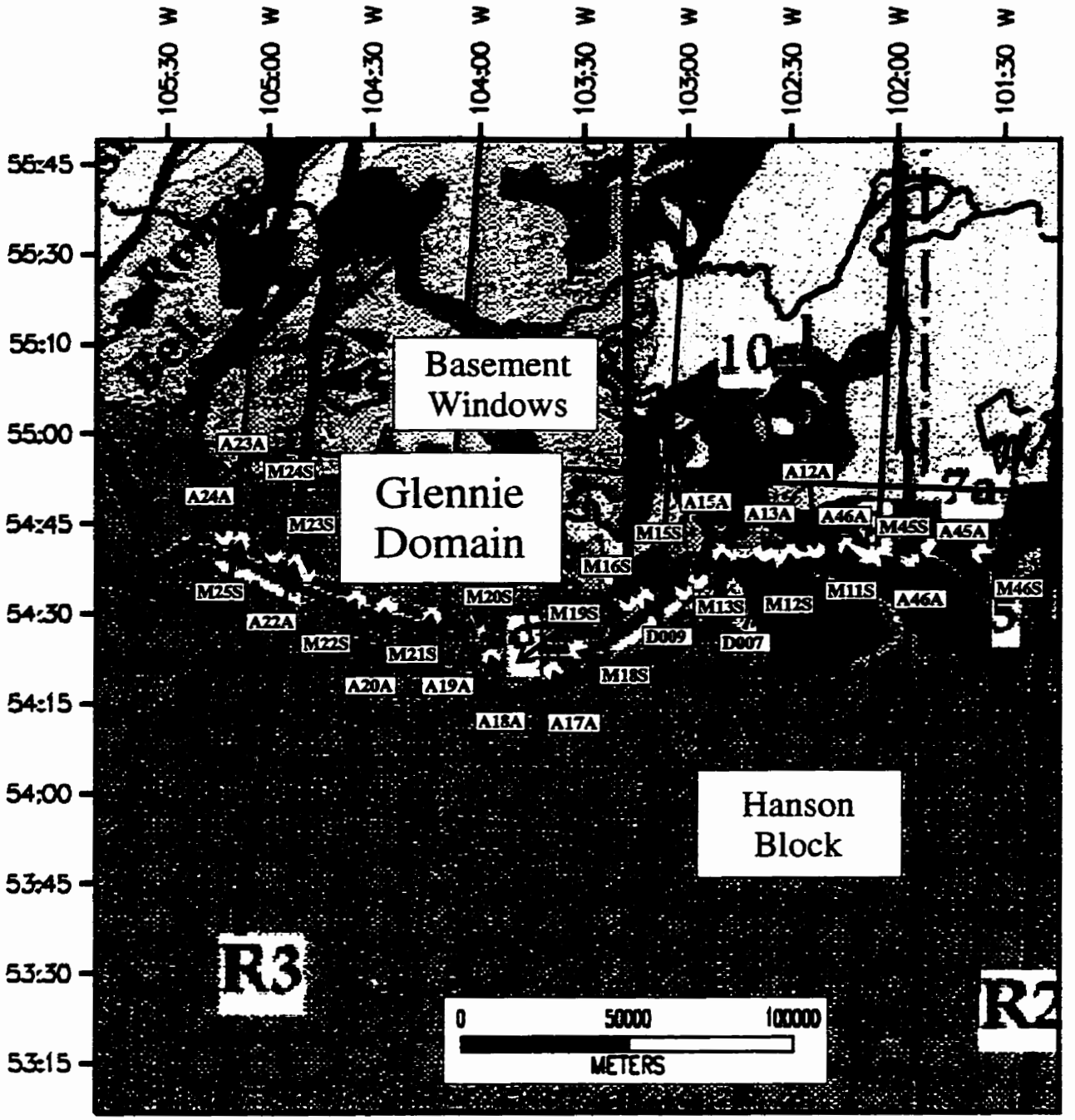

○ AMT/MT/LIMS Site

Fig. 4.7 Geological map of the GD-FFB study region and locations of AMT/MT stations THO-92-M11S thru THO-92-M46S and LiMS stations DTH007 and DTH009 on line 9 of the of the THOT (after Clowes, 1993).

available) as well as crosspower and autopower spectra estimates calculated using the cascade decimation technique. This technique computes power spectra estimates for single and multi-channel time series data (Wight and Bostick, 1980). The technique was originally developed for processing broadband, low frequency geophysical data in real time using a small digital processor. Sine and cosine transforms are applied to sequences of data produced by successively applying a low pass digital filter and decimation by two operator to the original data. The resulting spectra are the average of estimates which are independent in time and represent constant percentage bandwidths. Thus, the technique is particularly well suited to applications where it is desirable to reject intervals of unacceptable data. These data were remote-referenced processed using cascade decimation spectral estimates to provide full tensor impedance data spanning 50 frequencies for the MT sites and 25 frequencies for the AMT sites outlined above. The long period data sets from LiMS sites comprise impedance data at 18 frequencies.

4.3 The MT Response Analysis of the GD-FFB MT Data

The THO data set has been collected mainly along a single line and is therefore too sparse spatially to permit full 3D interpretation. Interpretation of the GD-FFB data set is therefore based on 2-D interpretation techniques. The results should resolve the first-order conductivity structure of the region. An inspection of data quality and signal-to-noise ratios are first used to discard frequencies, or bands of frequencies, containing poor impedance estimates. Tensor decomposition analysis follows, and is used to determine the dimensionality and the best coordinate frame for

2-D interpretation. The decomposed impedance data are then grouped into site and/or frequency sets demonstrating common dimensionality. This step is followed by error analysis, static shift correction and generation of final corrected impedance data sets. Additional data or information from other sources (borehole information or other geophysical information) is used to constrain interpretation where appropriate.

4.3.1 Raw Data Quality and Signal to Noise Ratios

Figure 4.8 shows data quality displays for four sites spanning the study area, M25, (located on Phanerozoic cover), M18 and M15 (located near the Phanerozoic/Precambrian boundary), and, M45 located on the exposed shield (west Flin-Flon belt). Review of these plots reveals that data quality is consistent with that described in section 4.1.4.1. Unreliable data, based on relative error bars and low SNR are primarily restricted to the 10^3 - 10^4 Hz and the 10^{-3} - 10^{-4} Hz frequency range. This result is demonstrated especially clearly by the ρ_{xx} and ρ_{yy} plots. In general the magnetic components are noisier than the telluric components in the frequency ranges containing poor data. From an examination of all the sites in the study area, reliable data lie in the range 10^3 Hz to 10^{-3} Hz.

In the 10^3 Hz to 10^{-3} Hz range there still exist frequencies exhibiting noise at either single or multi-sites. One source of noise can be seen as a peak in amplitude spectrum at 700-800 Hz in H_z, one or both of H_x and H_y and one or both of E_x and E_y. The noise is also recognizable as larger tippers which reach a magnitude of >1 in a relatively narrow frequency band. It is present at sites M45, M11, M13, M16, M18

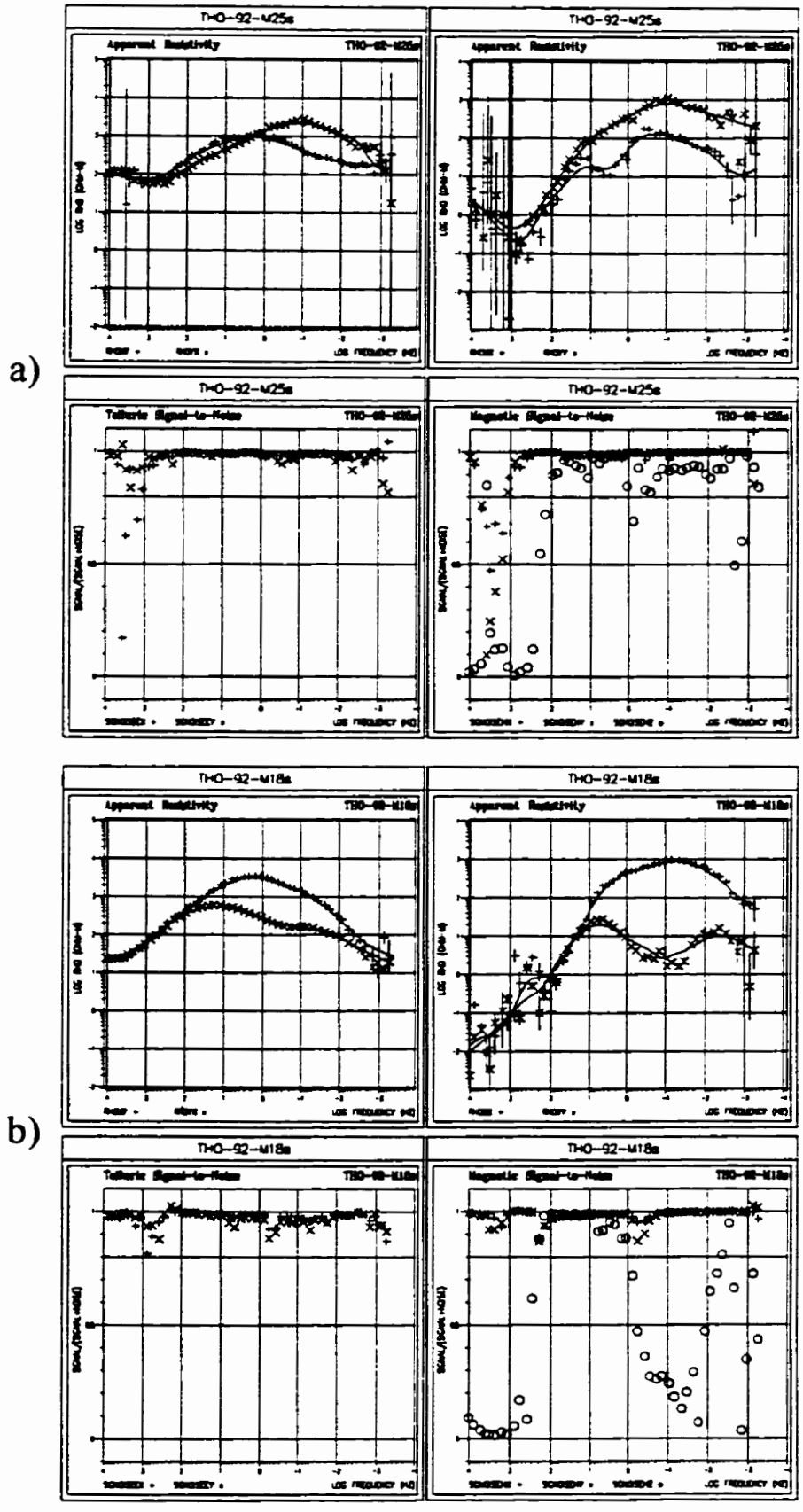

Figure 4.8 a,b Plots of rho_{xyyx} , rho_{xxyy} , and the signal to noise ratios for the magnetic and electric components of impedance tensor data from THOT, GD-FFB sites - M25 (a) and M18 (b).

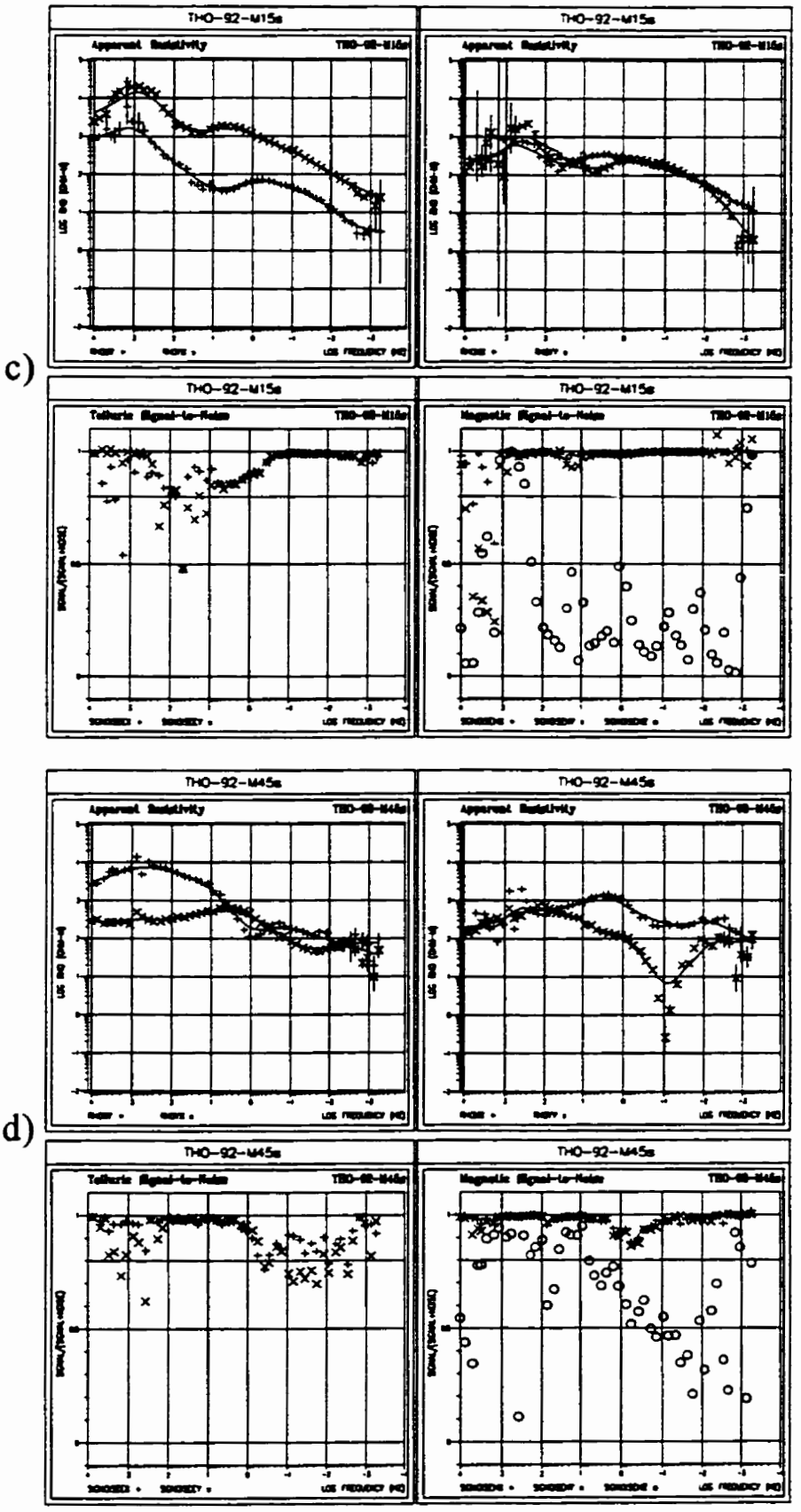

Figure 4.8 c,d Plots of rho_{xyyx} , rho_{xxyy} , and the signal to noise ratios for the magnetic and electric components of impedance tensor data from THOT, GD-FFB sites - M15 (c) and M45 (d).

and A46, A11, A15 and A16. This noise may affect the MT response within the frequency range of 10^5 to 10^2 Hz so this frequency range will be discarded for those sites. Further investigation of this noise reveals that all frequencies >192 Hz will need to be omitted for a number of sites and frequencies >10 Hz will need to be omitted for sites M16 and A15. Ferguson et al. (in review) discuss possible sources of the noise.

The response at M45 and M11 (not shown) exhibits characteristics that are unrealistic of an MT response. In particular the M45 response (figure 4.8d) shows rapid phase changes (not shown) around 1 Hz suggesting the infuence of noise. The M45 response is sufficiently perturbed that it is removed from further analysis. The M11 response, as used in further analysis, is restricted to the frequency range of 10 to 10^{-1} Hz. These results cast some suspicion on the response at site A46. Appendix A2 details the discarded frequency ranges and bad frequencies for the GD-FFB data.

4.3.2 Application of Dimensionality and Directionality Analysis

A detailed analysis of the directional characteristics and distortion parameters was applied to the GD-FFB data set through the use of the induction vector response and Groom-Bailey tensor decomposition. The goal was to identify groups of sites which shared a common 1-D or 2-D character over discrete frequency bands. The implementation of this analysis is outlined in the following steps:

Step 1 - Unconstrained decomposition on a site-by-site basis to determine the frequency bands for which the GB decomposition model is applicable.

Step 2 - Calculation and plotting of geoelectric strike directions as determined for discrete frequency bands (of one decade width) covering the entire data bandwidth.

Step 3 - Calculation and plotting of induction vectors as determined for discrete frequency bands (one-decade wide) covering the entire data bandwidth.

Step 4 - Using the information obtained in steps 1 to 3 identification of spatial subsets of sites sharing a common regional response over a broad frequency range.

Step 5 - Completion of constrained tensor decompositions over the frequency ranges in which the data have a common regional response. This step is performed to determine the strike direction to use in 2-D inversion and to determine distortion parameters.

Step 6 - Decomposition of the raw impedances using the strike and distortion parameters found in step 5 in order to obtain regional TE and TM impedance responses for 2-D inversion.

4.3.2.1 Identification of GD-FFB MT Data Subsets With 1-D/2-D Character: Steps 1-4

Step 1

Unconstrained MT decomposition was performed for each site of the GD-FFB data set. In the GB decomposition procedure, the seven unconstrained model parameters; namely the regional 2-D strike, two parameters partially describing the effects of the local electric field distortion (twist and shear), and the two 2-D complex

regional impedances (Z_{TE}, Z_{TM}), were determined from the eight data parameters defined by the four complex impedance terms.

Figure 4.9 shows the results of an unconstrained GB decomposition for two MT sites along the GD-FFB segment. Site M24 is located on Phanerozoic cover and site M11 is located on Precambrian rocks (see figure 4.7). For each site four separate graphs of GB parameters are shown as described in section 4.1.4.3.

For both sites M24 and M11, the error of misfit lies above the statistically acceptable level of four for periods between 0.1 to 100 s. In general, the misfit at periods less than 0.1 s and greater than 100 s is within the acceptable limits. For site M24 the apparent resistivity and phase response are similar for the TE and TM components, however for site M11 there are more substantial differences between the TE and TM components. The site M11 data may have been affected by artificial noise at that site.

The results for sites M11 and M24 are typical for sites on Precambrian and Phanerozoic rocks in the GD-FFB segment. Unconstrained decomposition results for all sites are shown in Appendix B. It is evident from these results that it is not possible at periods between 0.1 and 100 s to fit the model of galvanic distortion acting on a 2-D regional response. However, at periods below 0.1s and above 100 s the model fits to within the data errors. This generalization suggests that either the error estimates are unrealistic at periods between 0.1 to 100 s or the regional MT response in this period range contains influences from structures with a different strike near the

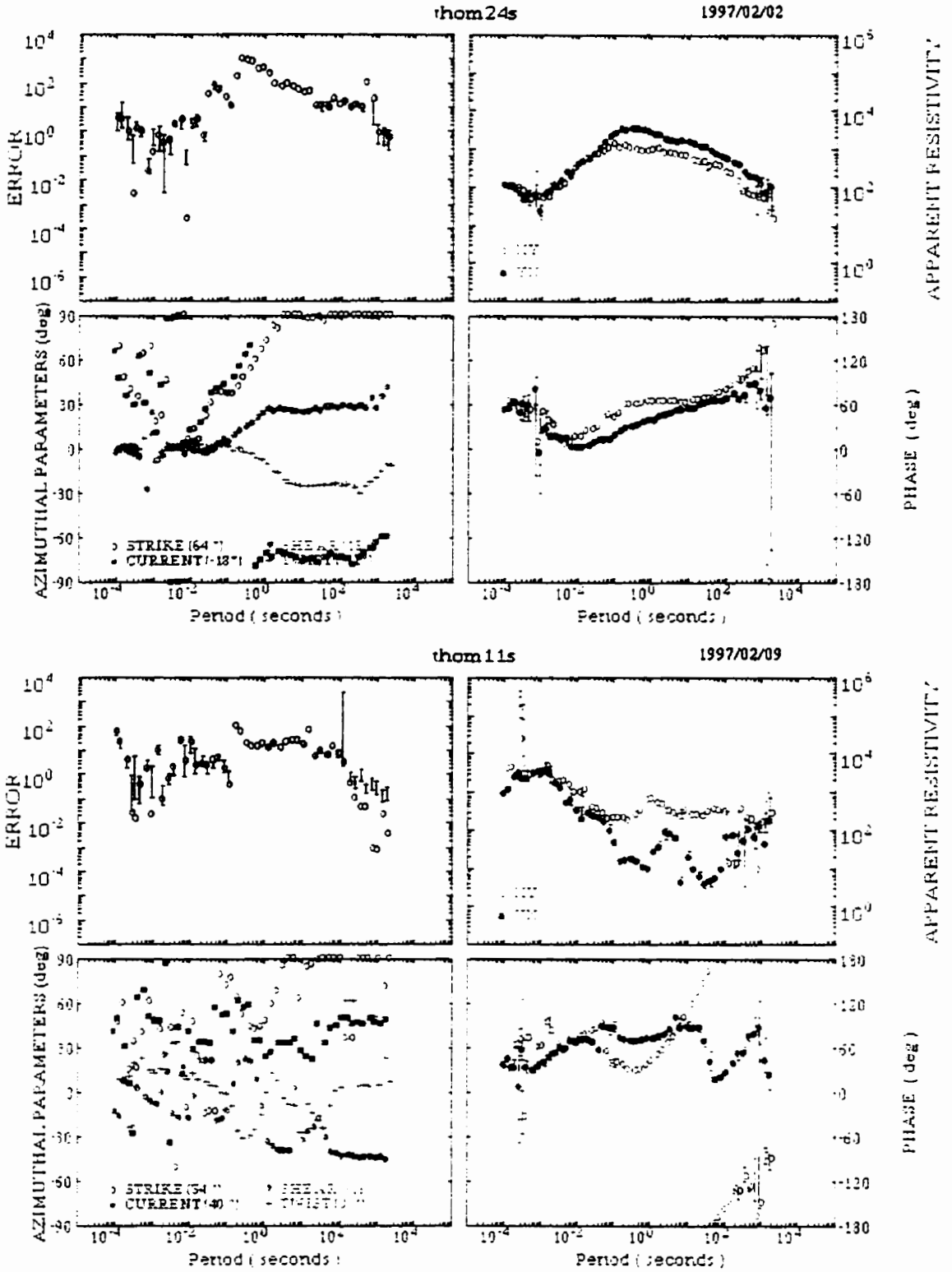

Figure 4.9 3-D unconstrained Groom-Bailey parameterization permiting both the distortion parameters and the 2D regional strike to vary with frequency for sites THO-M24S and THO-M11S located on the Proterozoic and the Archean terrains respectively.

surface than at depth. It is worth noting that when the distortion parameters are not constrained to be uniform within a frequency band, a strike that simply varies with frequency could still be accomodated by a GB model. However, in that circumstance an analysis of the true 3-D response with influences from both shallow and deep structures must be implemented.

Another way to analyze these data is to perform a decomposition in which the strike angle is incremented between 0^0 and 90^0 and to examine how the error and telluric distortion parameters vary with strike angle. These plots are nicknamed 'wall paper plots' and have been generated for all the GD-FFB sites (Appendix B). These plots can be inspected to see if there is a stable azimuth for which the distortion parameters are frequency independent and for which the error is minimized. If this is the case one can be more confident that the distortion model is appropriate over the observed frequency range (Groom et al., 1993).

Figure 4.10 shows examples of these wall paper plots for sites M24 and M11 as reproduced from Appendix B. An inspection of these plots confirms that the relative error or misfit is high for the period range of 0.1 to 100 s (10 to 10^{-2} Hz) at all strike angles. Stable, low values of the two plotted distortion parameters (twist and shear) can be achieved at most strike angles at frequencies above 10 Hz for site M24 (on the Phanerozoic cover). This is not the case for site M11 (on the Precambrian rocks). At frequencies less than 0.1 Hz it is obvious that the values of the distortion parameters are stable and/or minimized over more discrete strike azimuths.

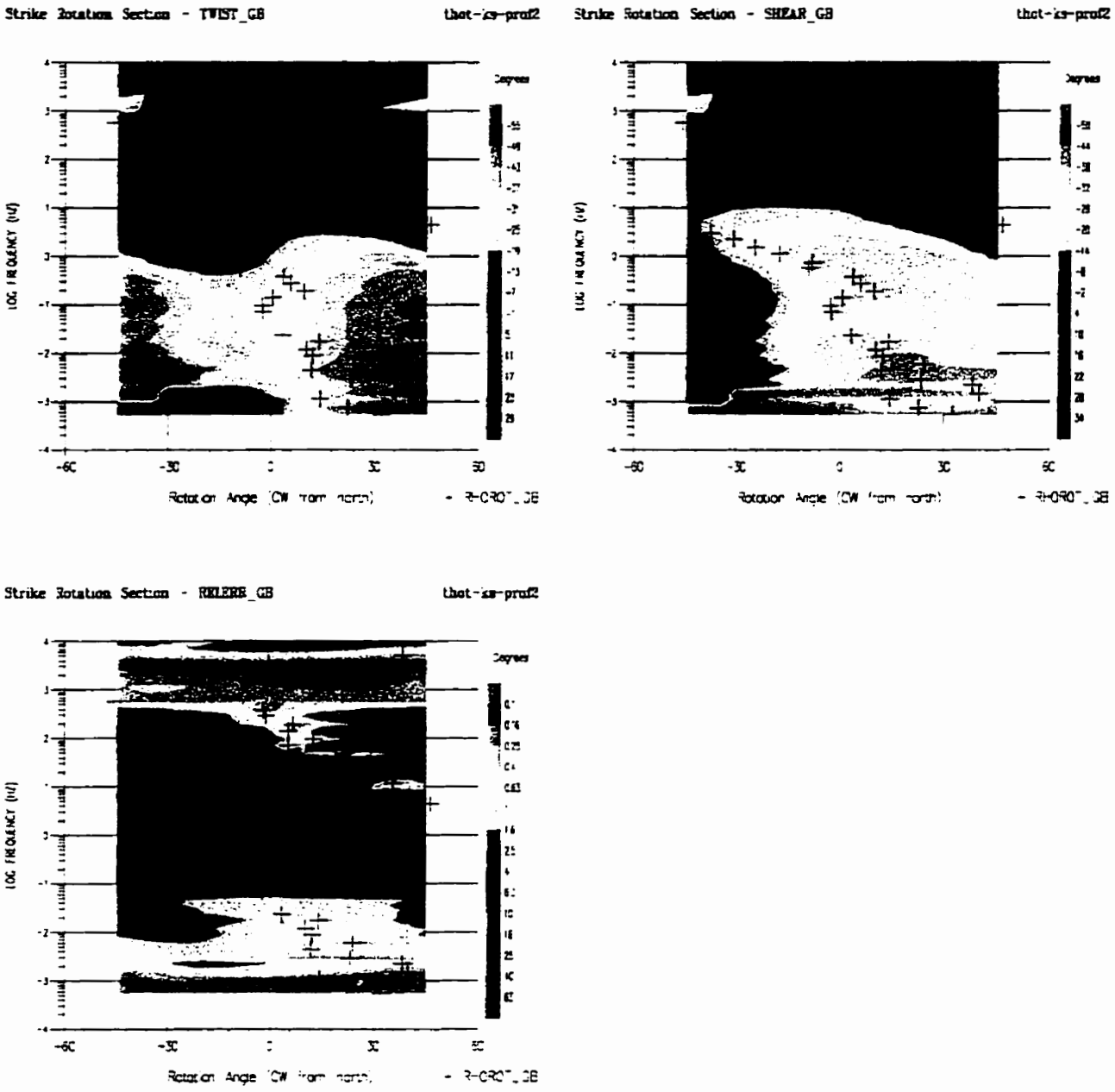

Figure 4.10a "Wall paper" plots of Groom-Bailey parameterization varying the strike angle between 0 to 90 degrees, using 3 degree increments, for site THO-92-M24S.

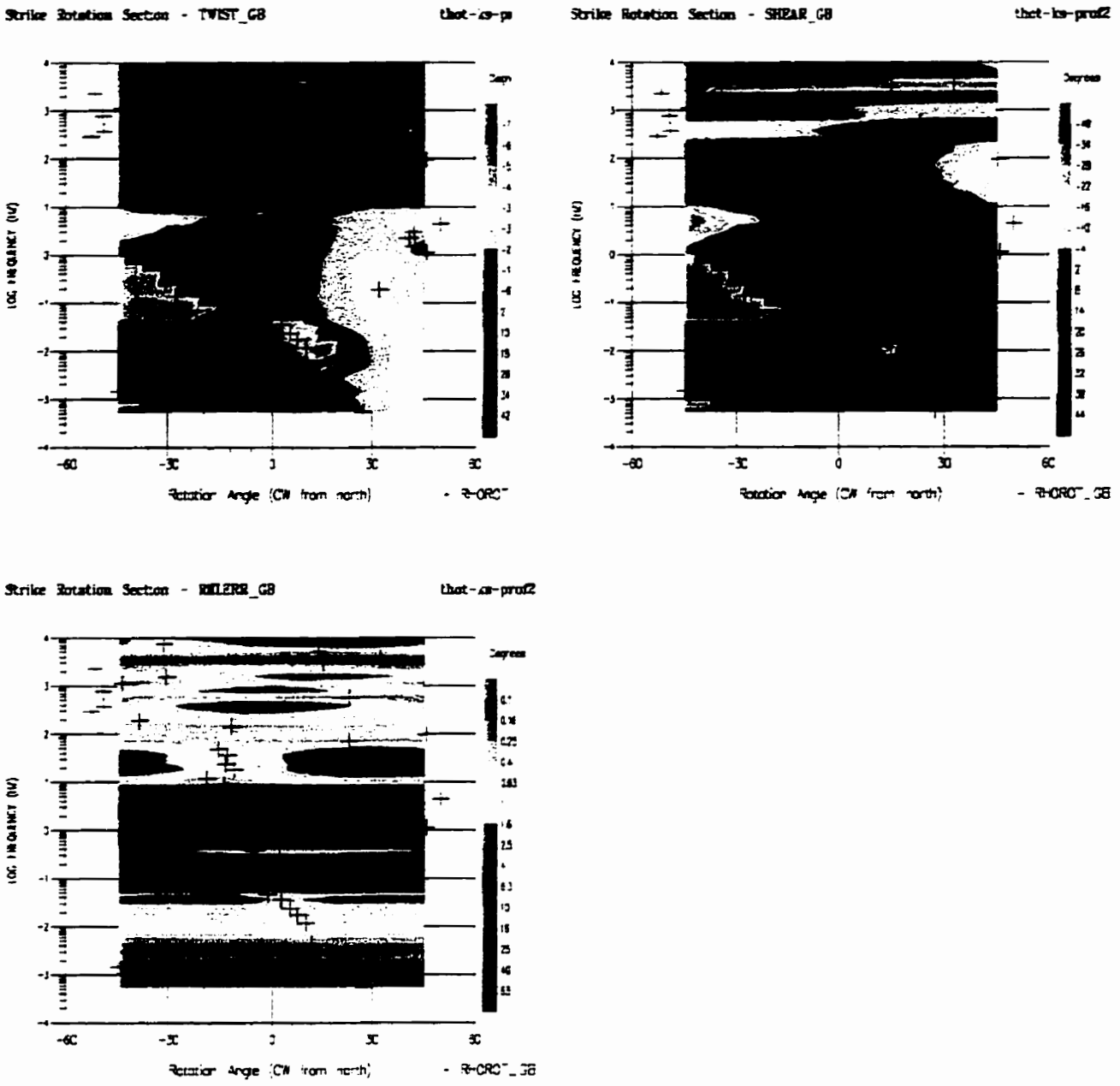

Figure 4.10b "Wall paper" plot of Groom-Bailey parameterization varying the strike angle between 0 to 90 degrees, using 3 degree increments, for site THO-92-M11S.

It is useful at this point to characterize the galvanic distortion observed in the GD-FFB study area by dividing the response into a series of domains with geological significance. At sites in the west of the transect, the decomposition results are characterized by data in which the strike is random at periods less than 10^{-2} s (and at several sites to 10^{-1} s). At these sites the GB distortion (twist and shear) is usually very low. The response can be interpreted as showing low levels of galvanic distortion occurring at sites on the Phanerozoic cover. In general the GB distortion at sites in the east of the transect and at longer periods at sites in the west of the transect is high. The observed shear angles indicate the galvanic distortion is moderate to high at nearly all sites in the segment (i.e. sites on the GD, HLB, FFB are characterized by high levels of distortion). This in turn indicates these Precambrian units contain a relatively complex resistivity structure in the upper crust with numerous resistivity contrasts.

Considering the statistics of the GB decompositions, it is evident that the GB model provides only a first-order approximation for the response from the GD-FFB MT sites. There are only a few sites showing frequency-independent distortion parameters over most of the frequency range. However, in order to proceed with the analysis it is necessary to approximate the observed response by a GB model. For this approach to be most valid, the data set will need to be divided into different subsegments of sites and frequency ranges as discussed in the next section.

Jones & Grant (1997) performed multi-site response analysis on all of the THOT MT data. They found a moderately well-constrained response for sites M24-M19.

However for a group of sites from M18 - M46 the GB model is extremely poorly fit. At most of these sites the shear becomes extremely high when the best-fitting strike is imposed. As can be seen in the "wall paper" plots (Appendix B), the unconstrained single-site GB fits suggest the shear angle for the best-fitting strike at these sites is typically >35°. This characteristic allows a subdivision of the galvanic distortion response for areas east and west of M18 and M19. In terms of geology this sub-division corresponds to the Glennie Domain having a different galvanic-distortion response to the HLB and FFB domains. This also corresponds to the Phanerozoic to Precambrian transition.

Based on a detailed inspection of the unconstrained GB analysis for each site (Appendix B) the frequency bands over which the GB distortion model is most reasonable were determined. The results are listed in Table 4.1.

Table 4.1. Frequency ranges where the GB distortion model is reasonable for the GD-FFB MT data

Site	Frequency Range (Hz)
M25	10^{4}-10^{2}, 10^{0}-10^{-3}
A23	10^{4}-10^{2}
M24	10^{4}-10^{2}, 10^{0}-10^{-3}
A22	10^{4}-10^{2}
M23	10^{4}-10^{2}, 10^{0}-10^{-3}
M22	10^{4}-10^{2}, 10^{0}-10^{-3}
A20	10^{4}-10^{2}
M21	10^{4}-10^{2}, 10^{0}-10^{-3}
A19	10^{4}-10^{2}
A19	10^{4}-10^{2}
M20	10^{4}-10^{2}, 10^{0}-10^{-3}
A18	10^{4}-10^{2}
M19	10^{4}-10^{2}, 10^{0}-10^{-3}
A17	10^{4}-10^{2}
M18	10^{4}-10^{2}, 10^{0}-10^{-3}
M16	10^{0}-10^{-3}
M15	10^{0}-10^{-3}
A15	GB model is poor
M13	10^{0}-10^{-3}
A13	GB model is poor
M12	10^{0}-10^{-3}
A12	GB model is poor
M11	10^{0}-10^{-3}
A46	GB model is poor
A45	GB model is poor
M46	10^{0}-10^{-3}

Step 2

Figure 4.11 shows plots of the regional strikes determined from the unconstrained Groom-Bailey procedure for representative frequencies spanning from 10^{4} to 10^{-3} Hz. There is a 90^{0} ambiguity in the azimuth strikes.

Apparent in Fig 4.11 are the following:

1) At many sites the regional strike direction is dependent on the frequency, however there is a general clockwise rotation with decreasing frequency.

2) At frequencies in the 10 Hz to 1 Hz range, corresponding to penetration depths of >5-10 km into the crust, the geoelectric strike is generally NNW to N.

3) At frequencies less than 1 Hz, where the fields are sampling the middle and lower crust, the strike rotates clockwise to NNE, and at even longer periods (> 100 s) where the fields are sampling the uppermost mantle, this azimuth changes to a strike of NE.

An additional method for determining the geoelectric strike direction is the 'maximum phase split direction plot' as a function of frequency. For quite a few data sets this parameter provides a more robust estimate of geoelectric strike than GB analysis. It is based on fitting fewer parameters than a full GB decomposition. For a 2-D structure the phase will be different between the E- and B-polarization modes.

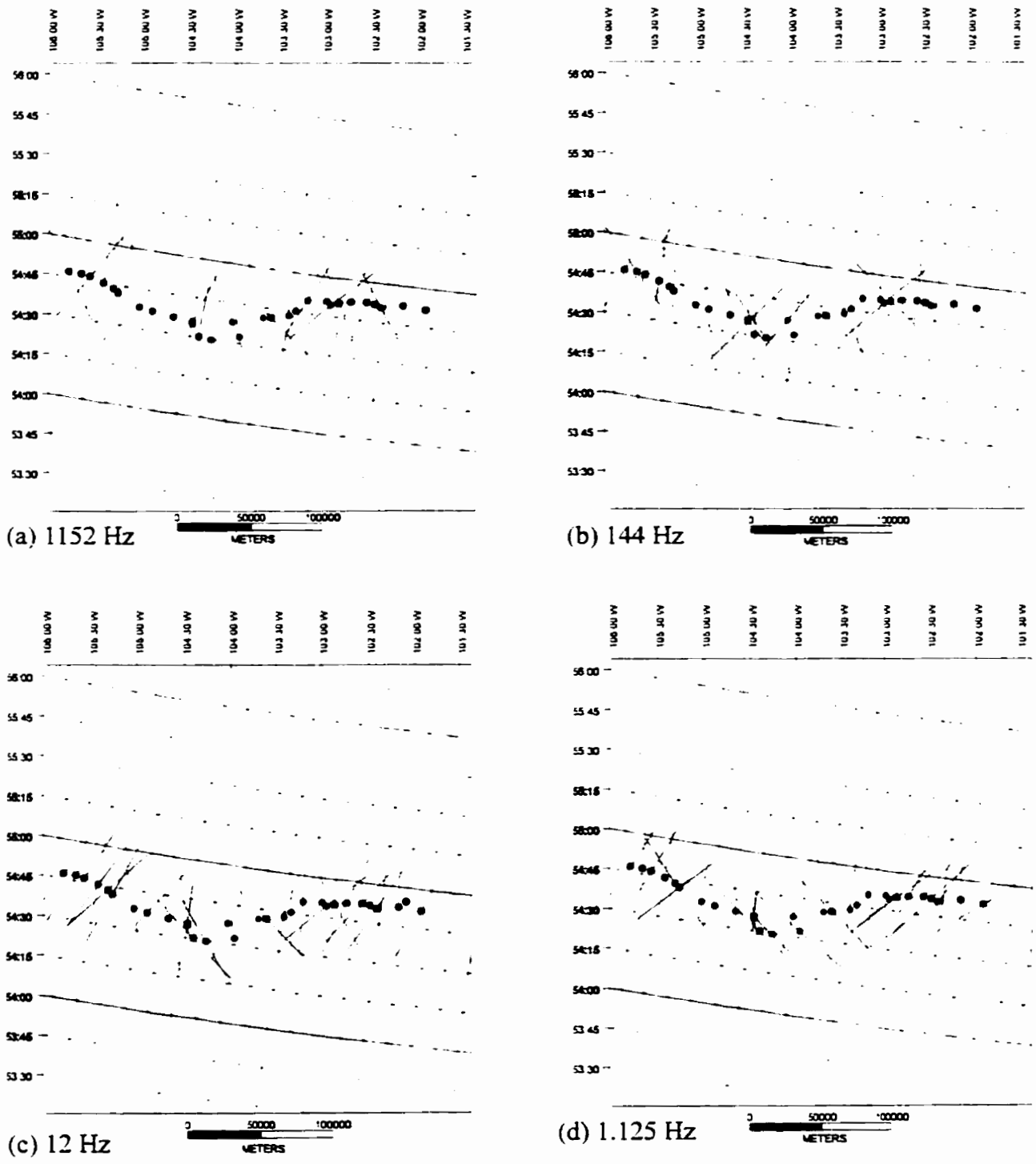

Figure 4.11 Plot of the regional strikes determined from the unconstrained Groom-Bailey procedure for four frequencies: (a) 1152 Hz , (b) 144 Hz, (c) 12 Hz, (d) 1.125 Hz..

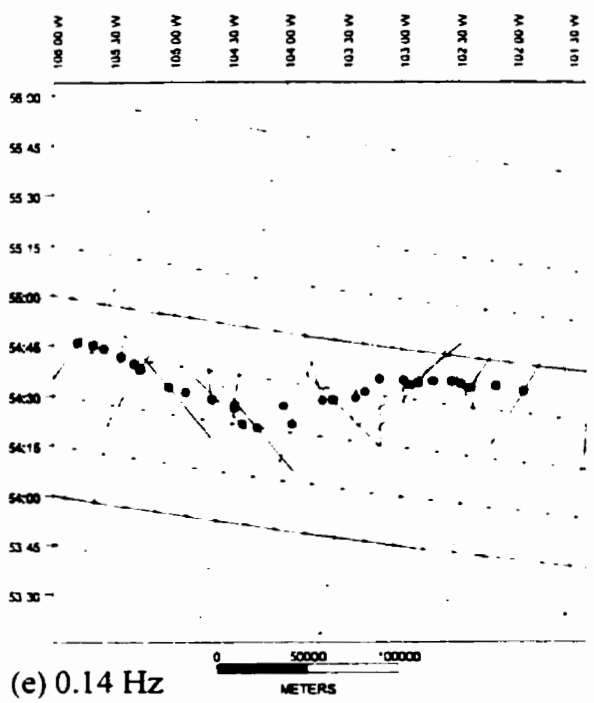

(e) 0.14 Hz

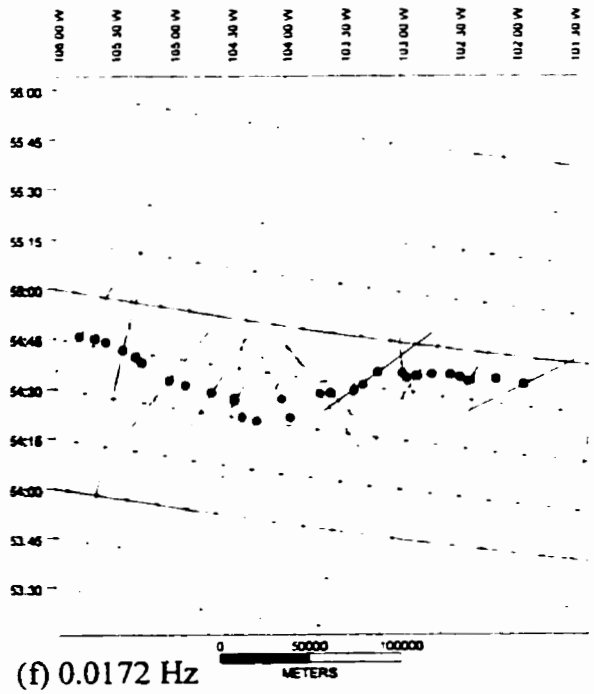

(f) 0.0172 Hz

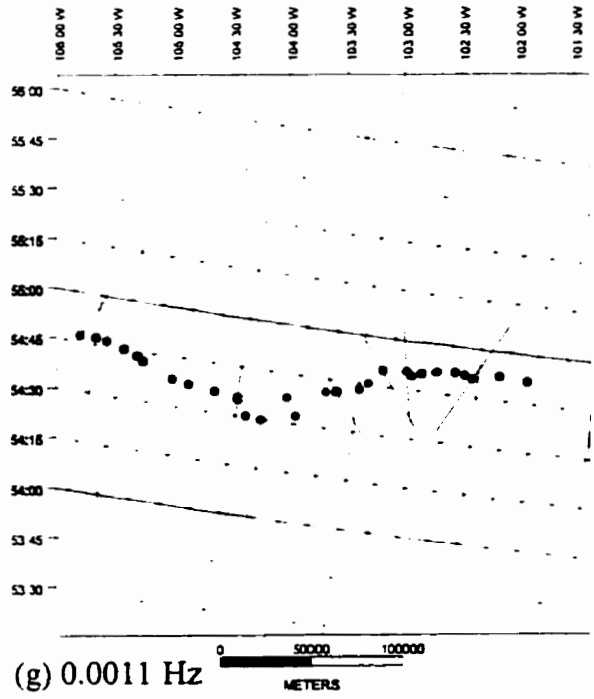

(g) 0.0011 Hz

Figure 4.11(cont'd) Plot of the regional strikes determined from the unconstrained Groom-Bailey procedure at three frequencies: (e) 0.14 Hz, (f) 0.0172 Hz, (g) 0.0011 Hz.

This fact allows the phase response to be used to determine geoelectric strike. For data measured in an arbitrary coordinate system over a 2-D structure the phase of the off-diagonal impedance terms will represent a weighted average of the E- and B-polarization phase. If such data are progressively rotated through a range of coordinate-system orientations, then the angle at which the difference between phase terms is greatest will correspond to the orientation of the conductivity structure (to within a 90° ambiguity, which may often be resolved by considering the magnitude of the two phase values). The analysis of the maximum phase split plots for the transect indicates the following:

1) A moderately consistent response across the GD with orientations swinging from NE-NNE in the west to N-NNW in the east for a broad frequency range. The change in orientation occurs at around 104° 30' W near site M22.

(2) A transitional region across the TF, HLB, an SWT with somewhat varied orientations, but with several sites having a north orientation (most clearly seen at frequencies $>10^2$ Hz).

(3) Sites in the east of the transect having a WNW to W orientation at short periods (10^2 Hz) swinging around to NW at long periods.

In general, the phase split orientation observations suggest that in the west and centre of the transect the geoelectric strike of the upper crust is approximately north-south. This orientation corresponds with the local geological strike of the Glennie Domain and Hanson Lake Block area to the western portion of the Flin Flon belt (figure 4.7) but not the more regional NNE trend of the Reindeer Zone or the Trans

Hudson Orogen itself (figure 2.1). To the east, the strike in the FFB is indicated by the phase split data to be approximately east-west and the response is probably associated with the margin of the FFB and Kisseynew Gneiss Belt. The clockwise rotation of the strike direction for most of the transect at lower frequency ($<10^{-2}$ Hz), yields an azimuth that coincides with the overall trend of the Trans Hudson Orogen. This result suggests that the Glennie Domain and Hanson lake Blocks are features that may be limited in depth extent or are subject to structural distortion in the middle to lower crust.

The overall change in geoelectric strike from the upper to lower crust indicates the 3-D complexity of the crustal structure in this region. It also supports Jones and Groom's (1993) assertion that geoelectric strike at a particular frequency cannot be assumed to correspond to local geological or even regional surface strike. The strike direction must be determined from the geoelectric data itself. In this case a strike based on the regional geology would be in error by $20\text{-}30^0$ for analysis of structures in the upper crust.

Step 3

Figure 4.12 is a plot of real (reversed) induction vectors of representative frequencies for discrete frequencies sampled from 10^{-4} to 10^{4} Hz. A review of the error ellipses associated with these real responses shows that at frequencies of <0.003 Hz the ellipses are larger than the arrows themselves, indicating that the response is not well resolved. Consequently, there is little value in an interpretation of the responses for frequencies <0.0011 Hz. An inspection of the imaginary responses (not

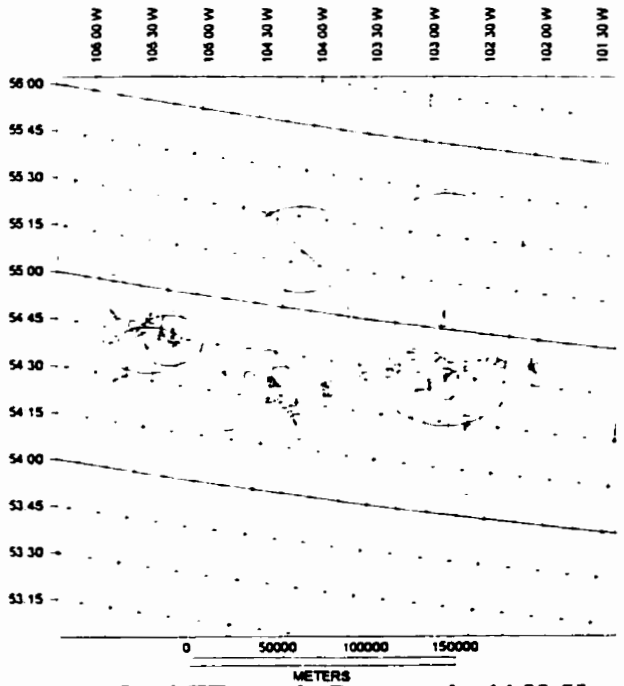

(a) Real TF Angle Reversed - 1152 Hz

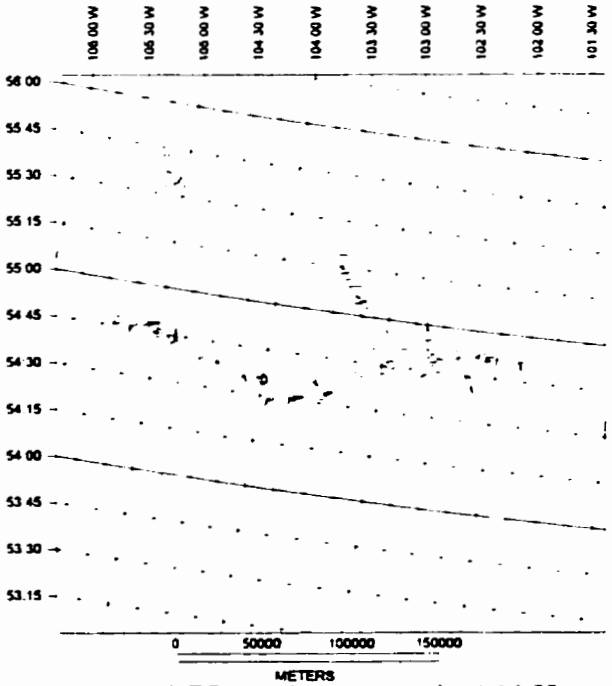

(b) Real TF Angle Reversed - 144 Hz

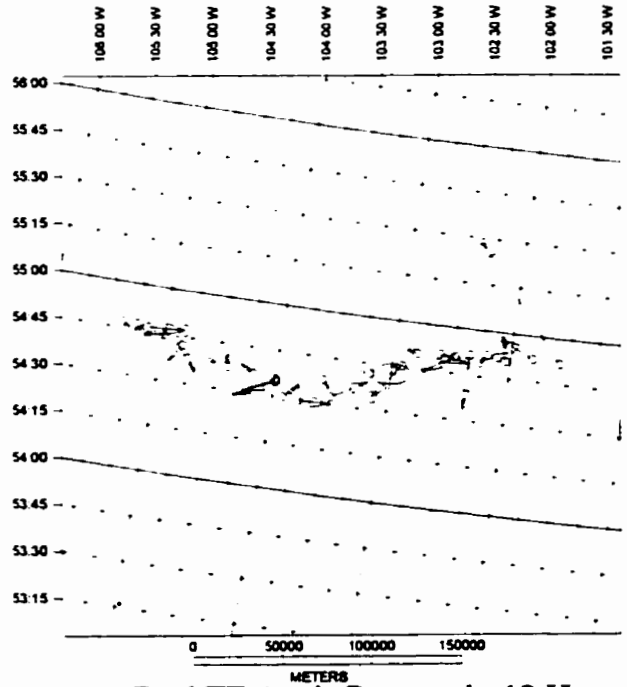

(c) Real TF Angle Reversed - 12 Hz

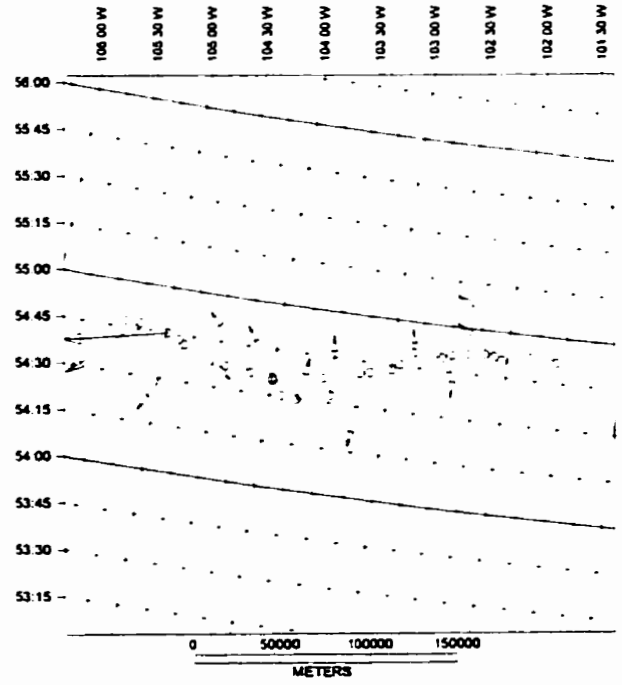

(d) Real TF Angle Reversed - 1.125 Hz

Figure 4.12 A plot of the real (reversed) induction vectors for four frequencies (a) 1152 Hz, (b) 144 Hz, (c) 12 Hz and (d) 1.125 Hz. Vectors are plotted at 100 km/unit magntiude. Real response error ellipses indicate the response > 1000 Hz is not resolved.

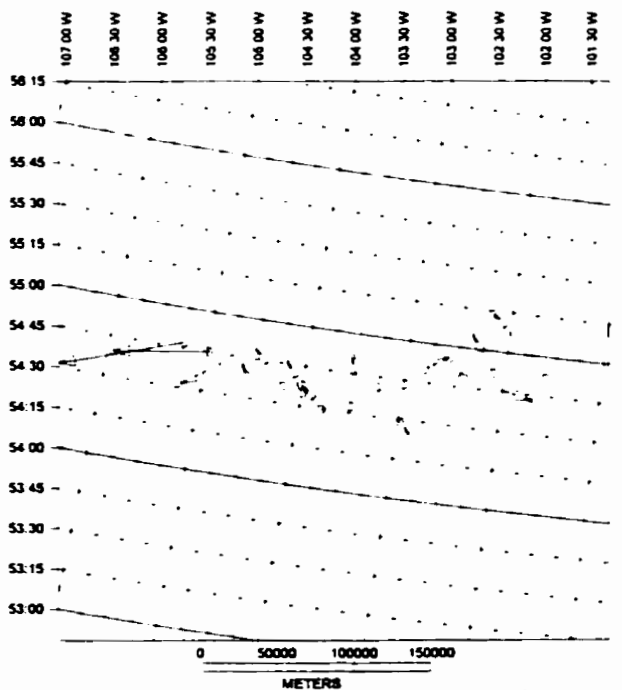

(e) Real TF Angle Reversed - 0.14 Hz

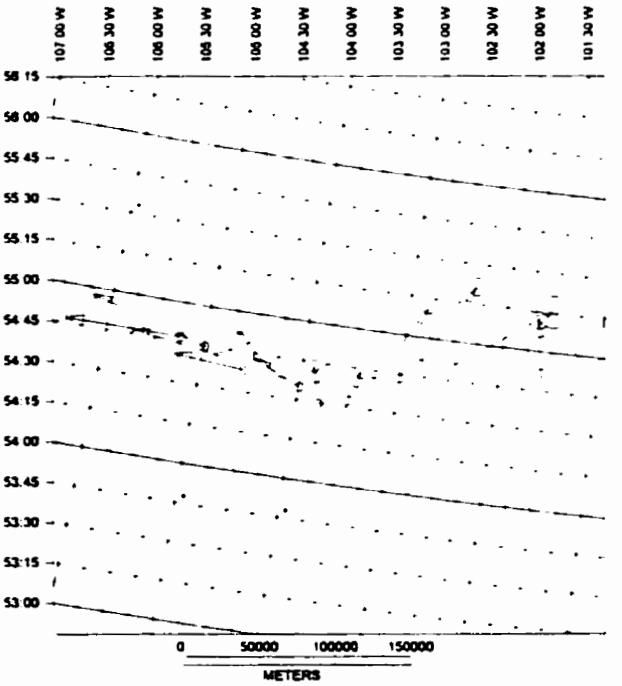

(f) Real TF Angle Reversed - 0.0172 Hz

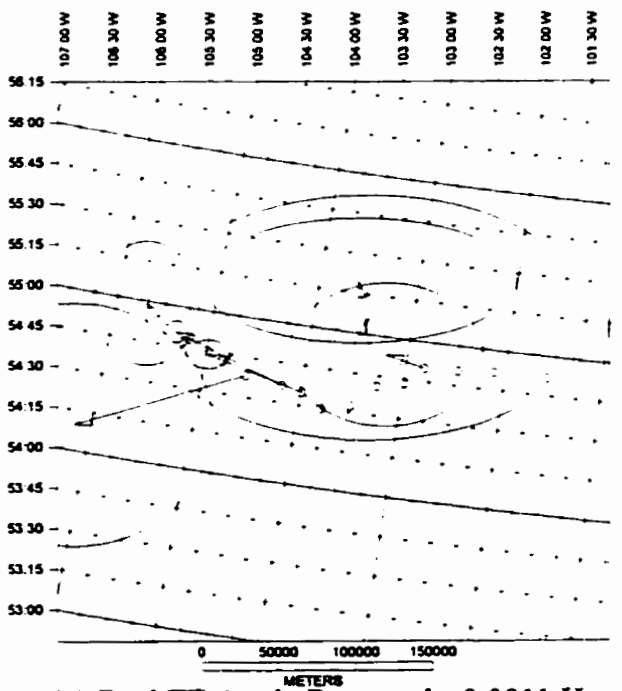

(g) Real TF Angle Reversed - 0.0011 Hz

Figure 4.12(cont'd) A plot of the real (reversed) induction vectors for three frequencies (e) 0.14 Hz, (f) 0.0172 Hz, and (g) 0.0011 Hz. Vectors are plotted at 100 km/unit magnitude. Real response error ellipses indicate the response < 0.005 Hz is not resolved.

shown) confirms the complexity of the responses in the study area. For a truly 2-D structure, the imaginary and real responses will both be orthogonal to the strike. However, for many of the GD-FFB sites the imaginary and real vectors are oriented at 90^0 to each other indicating the presence of structure with a 3-D component.

With the above results in mind the following observations and interpretations can be made from the induction vector plots (figure 4.12):

1) There are very short vectors for frequencies greater than 10 Hz at stations on the Phanerozoic cover (west half of site line, sites M18-M25). These data indicate low conductivity contrast (i.e. the sedimentary units of the Phanerozoic).

2) Near oppositely-directed arrows across the Tabbernor Fault zone (sites M16, DTH009, M15 and M13) suggest a narrow relative conducting region extending from surface (high frequencies, e.g. figure 4.12c). The effect is prominent through the lower frequencies to 10^{-2} Hz where the signature is overwhelmed by a conductor to the west.

3) A general transition from S and SE directed arrows to N and NW directed arrows occurs at sites M23 to M22 and M21 to M20 respectively at about 10 Hz.

4) Large vectors with a dominantly WNW to west orientation are prominent on most sites west of the Sturgeon Weir Thrust (west of site M13), at frequencies less than 0.1 Hz. This may indicate a response to the NACP at long periods.

Step 4

Using information obtained in steps 1 to 3 it is now possible to identify several spatial subsets of sites sharing frequency ranges with common directional and dimensional characteristics. These subsets are listed below with supporting evidence:

1) Phanerozoic Sites: Frequencies 10^2 to 10^4 Hz

The data for frequencies above 10^2 Hz for all sites located on the Phanerozoic cover or the west part of the GD-FFB MT segment exhibit a consistent response. As listed in Table 4.1 the GB distortion model is reasonable for sites M18 to M25 and A17 to A24 (15 sites) at frequencies from 10^2 to 10^4 Hz. Within this frequency band the distortion model fits the data for these sites to within the statistical errors. The unconstrained GB analysis plots for these sites (see Appendix B) indicates that the strike directions are relatively inconsistent, and galvanic distortion is small with twist and shear angles near zero ($|\theta_e|, |\theta_t| < 5^0$). The induction vectors also indicate low conductivity contrast.

Apparent resistivity plots also provide discrimination of sites with a consistent repsonse (e.g., overlaying these curves will indicate the site to site variance in the conductivity structure). The apparent resistivity curves derived from the determinant of the impedance tensor for 15 MT sites (M11 to M46) located in the study area is shown in figure 4.13a. There is a clear separation at high frequencies (>100 Hz) between sites located on the Phanerozoic cover (ρ_a = 10 to 100 Ω·m) and those

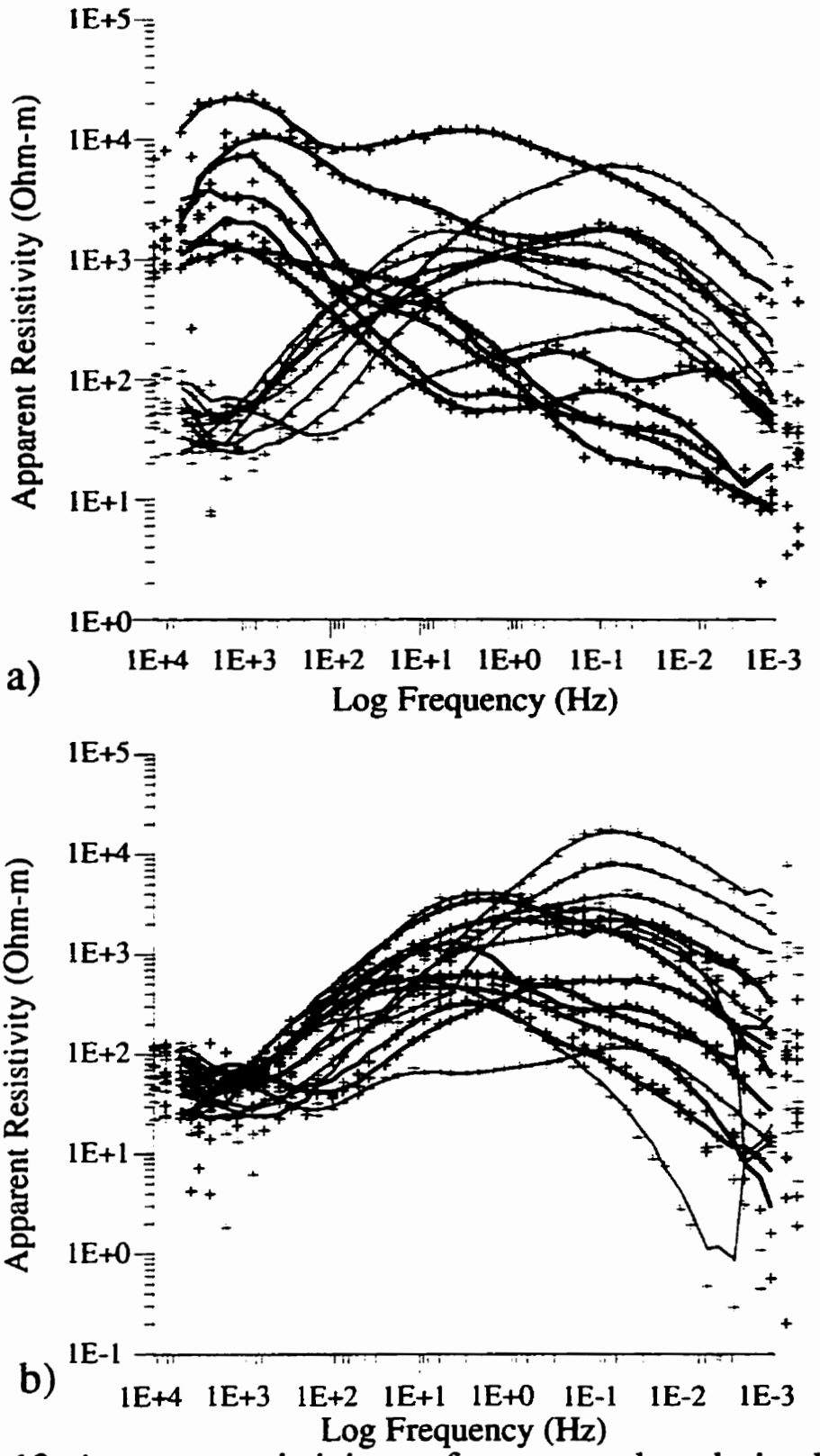

Figure 4.13 Apparent resistivity vs frequency plots derived from the impedance tensor for: a) 15 MT sites (determinant) spanning the Phanerzoic (red) to Precambrian (black) rocks, note the clear separation between high frequency responses, b) 8 MT sites on Phanerozoic cover, (red - xy; black - yx), note high frequency response due to Phanerozoic sediments.

located on the Precambrian rocks (ρ_a = 1000 to 10000 Ω·m). The greater scatter of the data for the shield results is due in part to the greater distortion of the response by local near-surface features. Figure 4.8 also illustrates the general differences in the apparent resistivity curves from sites located on Phanerozoic cover and those on the Precambrian rocks. At frequencies above 1-10 Hz the two off-diagonal apparent resistivity components of sites located on Phanerozoic cover tend to coverge and are almost identical at frequencies above 10^2 Hz. For sites located on Precambrian rocks the off-diagonal tensor components do not converge above 10^2 Hz and generally show a static shift of 0.5 to 1 decades.

These observations indicate several things:

1) the Phanerozoic sediments are conductive as indicated by the decrease in relative apparent resistivity to values of 20-100 Ω.m, at frequencies above 10^2 Hz,

2) the 1-D nature of the Phanerozoic sediments is indicated by the convergence of off-diagonal impedance tensor elements at high frequencies,

3) strong static shift at high and mid-range frequencies over the Precambrian sites indicates strong local galvanic distortion.

The apparent resistivity for eight MT sites (M18 to M25) located on the Phanerozoic cover (overlying the Glennie Domain) is shown in figure 4.13b for two EM polarizations. The responses at high frequency (>10 Hz) represent contributions from the upper crust, specifically the Phanerozoic sedimentary rocks, the sedimentary rock to basement transition zone, and the top 10 km of the crust. There is strong agreement between the apparent resistivities at high frequencies for all of the sites on

the Phanerozoic cover. Generally these responses fall within a one decade range at frequencies higher than 10 Hz, indicating low site-to-site static shift. There is also a close agreement between the ρ_{xy} and ρ_{yx} polarizations for all of these sites at frequencies higher than 10 Hz.

The above evidence shows that the response above 10^2 Hz is strongly dependent on the Phanerozoic cover, with only a minor influence from the underlying structure. The combination of evidence from the GB parameters, maximum phase split orientations, induction vector response and the determinant apparent resistivity curves clearly suggests that this data subset can be modeled using 1-D methods (for the sedimentary cover) or 2-D methods if the structure within the Precambrian crust is also to be resolved.

2) All Sites: Frequencies < 0.1 Hz

As shown in Table 4.1 the GB distortion model holds for most of the MT sites across the transect at frequencies from 10^{-1} to ~10^{-3} Hz. Within this frequency band the distortion model fits most data to within the statistical limit (see Appendix B). The lower-frequency GB strikes suggest an overall NNE orientation.

Support for a 2-D interpretation approach to this group of data stems from the analysis performed by Grant and Jones (1997) in which the entire THOT MT data set was processed to identify regional strike parameters. Jones and Grant (1997) found that a good case could be made to interpret the entire data set using a regional strike direction of 34^0E for the frequency band from 10^0 to 10^{-2} Hz. Specifically, for sites

M24 to M19 a strike direction of 34.2° was found, for sites M18 to M46 a strike direction of 17.4° was found, and for sites M24 to M46 an average strike direction of 31.2° was found. For the slightly lower frequency range of 10^{-1}-10^{-3} Hz these angles are respectively 32.2°, 33.5°, and 33.7°. The results suggest a strike direction of around 32° so modelling should be performed with sites projected onto a line oriented at 122°.

The results from the eastern end of this model should be interpreted with care:
(a) higher frequency results (not modelled) suggest a more east-west strike (WNW phase-split orientations at 10^{2} Hz), Jones and Grant (1997) multisite angle for M18-M46 of 71°).
(b) very low frequency results provide some evidence for a NW strike (NW phase-split orientations at 1- 10^{-2} Hz; NE induction vectors at 1- 10^{-2} Hz; Jones and Grant (1997) comment that only M18 and M46 provided strong constraint on the 33.5° result for sites M18-M46).

In the analysis of the GD-FFB MT data performed in this thesis, the strike directions (figure 4.11) suggest a general trend of 20^{0} - 40^{0} E for the 10^{-1} to ~10^{-3} Hz frequency band. The induction vectors (figure 4.12) indicate more spread in the azimuth over this frequency range suggesting the influence of a more complex structure.

The determinant apparent resistivity plots for the Phanerozoic sites (figure 4.13a) show a response that with decreasing frequency becomes more resistive and then more conductive. This response suggests high resistivity in the upper to mid crust

and lower resistivity in the lower crust and/or upper mantle. The sites located on Precambrian rocks show an apparent resistivity response that decreases steadily with lower frequency. The response suggests the presence of conductive material in the mid-lower crust with an increase in conductivity in the upper mantle. Note the two most resistive profiles from the Precambrian sites (figure 4.13a). These profiles are significantly shifted relative to the other Precambrian sites. These two sites are located at positions near the boundary between the GD and the HLB, at the TFZ. Another interesting feature is the difference in apparent resistivity below 0.1 Hz for sites east and west of the TFZ. Finally note that in the low frequency window (10^{-1} to 10^{-3} Hz) the responses generally fall within two decades suggesting the occurrence of site-to-site static shift that will need to be removed before detailed interpretation and modelling.

3) Tabbernor Fault Zone to Sturgeon Weir Thrust: A Special Case

The area around the Tabbernor Fault Zone and Sturgeon Weir Thrust represents an interesting geological and geophysical area with unique characteristics (see Chapter 2). Five MT sites straddle this transitional zone, they are: M18, M16, M15, M13 and M12. The data from these sites, for which the GB model is valid at frequencies spanning 10^{3} to 10^{-3} Hz, will be considered as a group and interpreted using a 2-D approach. This procedure is justified mainly by the surface geological structure with some support from the induction vector and maximum phase split orientation responses. Although there is limited geoelectric strike evidence to support

a 2-D analysis across the entire frequency range, decomposition regional strike, transfer function and phase angle data suggest that an approximate response angle of between 0 and 40^0E could be used to represent the regional strike. It is important to consider these data to reveal information on the nature and depth extent of the TFZ and the HLB.

4.3.2.2 Processing of GD-FFB MT Data Subsets With 1-D/2-D Character: Steps 5-6

1) Phanerozoic Sites: Frequencies 10^2 to 10^4 Hz

According to Groom et al. (1993), a data set can be determined to be 1-D by testing the rotational invariance of the impedance. After fitting the data to a 1-D GB parameterization, the misfit to the model (γ^2) is then determined, and if 95 per cent of the misfits lie below four, then this 1-D model fits the data and no further decomposition analysis is appropriate or required (except, of course, for modelling).

The present study did not include this 1-D test, however, 2-D GB decomposition provides evidence that the conductivity structure at the Phanerozoic sites is 1-D. As outlined above, Appendix B contains plots of unconstrained 2-D GB decomposition results for all the GD-FFB MT data. Inspection of these plots for sites M18 to M25 and A17 to A24 reveals that the γ^2 variable has a value generally less than four for frequencies $>10^2$ Hz. The strike azimuths for these sites is inconsistent at frequencies above 10^2 Hz, there is little difference between the phases of the two modes, and the apparent resistivity curves are either coincident or parallel. In addition the galvanic

distortions are small (i.e. $|\theta_e|, |\theta_t| < 5^0$) and the GB model fits with the impedance data are very good. Given this assessment further analysis (i.e. steps 5-6) is not necessary and each site of this group can be fitted using a 1-D model.

2) All Sites: Frequencies <0.1 Hz

Inspection of the GB decomposition plots for sites M25 to M45 reveals that the γ^2 variable has a value generally less than 4 at frequencies less than 0.1 Hz. Also the strike azimuths at these frequencies is fairly consistent between sites. The distortion parameters for these data are relatively high but are generally independent of frequency for each site. Inspection of the "wall paper" plots for this data subset (Appendix B) indicates that at rotation angles of 20^0 - 40^0 consistent twist and shear angles can be identified and coincide with minimum error. This evidence indicates that a 1-D approach is invalid but a 2-D tensor decomposition approach should be sufficient to model the data.

The method outlined by Groom et al. (1993) for finding the most consistent telluric and regional azimuthal parameters for the frequency range of interest was applied to each of the data sets in this subset. As outlined above this procedure involves performing constrained tensor decompositions over the frequency range within which each data subset is considered 2-D.

In this decomposition the twist and shear are constrained to be frequency independent for frequencies < 0.1 Hz., although site dependent. The strike is chosen to be the same for all sites. The strike and distortion parameters determined for the 14

MT sites in this data subset are given in Table 4.2. These parameters describe the best 2-D impedance representation of the measured data for each site.

According to Groom et al (1993), it is necessary upon determining the decomposition parameters, to ensure that the strike angle is appropriate for the data, and not one obtained by inappropriate choices of twist and shear. Therefore, as a check, it is wise to constrain the strike angle to the value determined and permit the twist and shear to vary with frequency. If appropriate, the values of twist and shear from the constrained inversion should approximately match those from the unconstrained inversion. The results in Table 4.2 represent final values obtained after several iterations between constrained and unconstrained inversions. Appendix C contains plots of the standard parameter display for the fully constrained decompositions for each site in this data subset.

Table 4.2 GB decomposition parameters determined for 14 sites at <0.1 Hz

Site	Strike (degree)	Shear (degree)	Twist (degree)
M25	34	-5	-30
M24	34	-30	-40
M23	34	-10	-30
M22	34	-18	-9
M21	34	24	0
M20	34	33	-18
M19	34	18	6
M18	34	-15	24
M16	34	36	18
M15	34	34	30
M13	34	39	-9
M12	34	36	-39
M11	34	39	-36
M46	34	15	-18

The best estimate of 2-D TE and TM impedances are recovered by removing the distortion described by the decomposition parameters. For the low frequency data from the 14 sites in this data subset, the decomposition model describes the data reasonably well. It appears that the mid-lower crust and upper mantle can be reasonably represented by a 2-D geoelectric structure. As mentioned earlier, in the

event that the conductivity structure is moderately 3-D the resultant data set is the optimal 2-D representation (Groom et al., 1993).

3) Tabbernor Fault Zone to Sturgeon Weir Thrust: A Special Case

Inspection of the GB decomposition plots for the five MT sites, M18 to M12, in the TFZ to SWT area, reveals that the γ^2 variable has a value generally less than 4 at the highest frequencies (>10 Hz) and over part of the low frequency range (0.1 to 10^{-2} Hz). The strike azimuths for these sites is fairly consistent across the frequency range from 10^3 to 10^{-2} Hz. Figure 4.14 shows the strike azimuth for each of the five sites for discrete frequencies between 10^3 and 10^{-2} Hz. The average strike azimuth for each site over this frequency range is between 355^0 to 360^0. The distortion parameters are highly variable across the frequency range and from site to site (Appendix B). This evidence indicates that a 1-D approach is invalid but a 2-D approach may be sufficient to model the data for all sites between 10^3 to 10^{-2} Hz.

Groom-Bailey decomposition was again performed for these data introducing constraints to solve for the most consistent strike. The decomposition parameters determined for the five MT sites in this data subset are given in Table 4.3. The results were obtained using the same methods as for the previous subset and plots of the results are again shown in Appendix C.

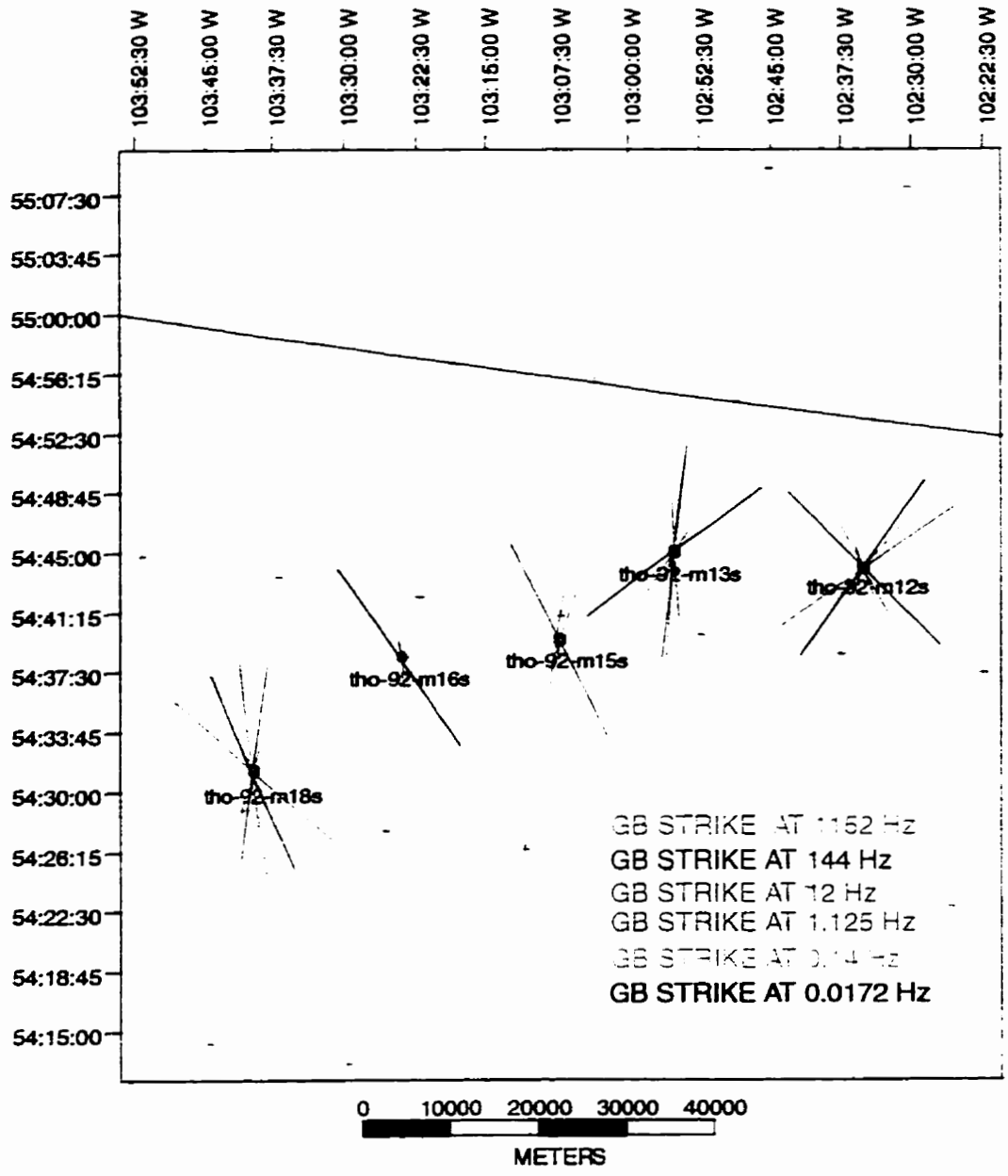

Figure 4.14 Strike azimuth results for discrete frequencies between 1000 to 0.01 Hz for five sites spanning the TFZ. The average strike direction is 355 to 360 degrees.

Table 4.3. GB decomposition parameters determined for TFZ - SWT MT sites

Site	Strike (degree)	Shear (degree)	Twist (degree)
M18	10	-15	20
M16	-15	-9	9
M15	10	15	25
M13	0	30	12
M12	-10	30	-15

For the frequency range of interest for the five sites in this data subset, the GB decomposition model describes the data reasonably well and the strike estimate of 0^0 is fairly consistent over the entire profile. From these observations it appears that the upper to mid crust can be reasonably approximated by a 2-D geoelectric structure with a strike of 0^0.

4.4 Static Shift Corrections and Resistivity, Phase Pseudo-sections

4.4.1 Static Shift Corrections

As discussed previously, sites located on the exposed Precambrian shield show significant static shift (figure 4.13) that will need to be corrected prior to modelling and interpretation. As can be seen in Appendix B, the similarity in the phase plots (at low frequencies) is in sharp contrast to the spread in the apparent resistivity curves which generally have the same shape but are displaced vertically from one another. In addition, the TE and TM mode phases at most sites have similar values at low

frequencies which indicates that the deep resistivity is close to 1-D (i.e. the deeper part of the section is close to horizontally layered). Sites located on the Phanerozoic cover exhibit only minor site to site static shift (figure 4.13) and very little local anisotropy at high frequency and therefore no static shift corrections were deemed necessary.

Static shift (see section 4.1.4.4) was reduced on the GB corrected data in the low-frequency data subset by correcting partially for the local static shift (anisotropy,s) but mostly for the site gain (inter-site static shift,g). The procedure followed is a combination of that used by Jones and Dumas, (1993) and Marquis et al., (1995). At each site the local static shift was corrected by shifting the two apparent resistivity curves to a determination of the high-frequency asymptote (i.e. the curves are forced to coalesce at high frequency). The simplest approach to the site gain correction is to assume that the earth below a given depth is 1-D, which requires the site-to-site apparent resistivity curves in the TE polarization to have the same low frequency asymptote (Berdichevsky et al., 1989). A more thorough approach is to further consider the regional levels of the TE apparent resistivity curves at periods which sample deeper than the region of interest, as followed by Jones and Dumas, (1993) and in this case is the upper mantle (50-100 km depth). For this data subset, at periods greater than 100 s, the skin depth of the EM fields for all sites is greater than 100 km, well into the mantle. A review of the TE apparent resistivity curves for all sites at periods greater than 100 s reveals a trend to a value of 50-100 Ω.m at the lowest frequencies. For this study the TE apparent resistivity data curves were shifted

such that the value at the lowest frequency sampled, (0.000549 Hz) was 50 Ω.m. The same correcting factor was then applied to the TM mode apparent resistivity data.

Although all of the data has been static corrected as described above, the limitations of the GEOTOOLS (V. 7.23) implementation of the 2-D inversion codes prohibits the inclusion of the static information into the inversion of the GB corrected data. Consequently, the static shifts will not be included in the inversion modelling. An alternative approach will be to increase the errors on the apparent resistivity information while forcing the inversion to fit the phase and tipper information more closely.

4.4.2 2-D Apparent Resistivity and Phase Pseudosections

After correction of galvanic distortion and static shift, the data can be viewed in a pseudosection format, by projecting the MT sites onto the appropriate 2-D line orientation (i.e. an azimuth parallel to the TM direction). Apparent resistivity and phase pseudosections of the TE and TM polarization modes can provide an overview of the true resistivity structure of the earth.

1) Phanerozoic Sites: Frequencies 10^2 to 10^4 Hz

Figure 4.15 shows apparent resistivity and phase pseudosections along a best fit profile connecting the sites (112°) for TE and TM polarization modes for sites located on Phanerozoic cover and for frequencies above 1 Hz (TE = xy, TM = yx). The pattern of high phase values at short periods (>10^3 Hz) across the profile indicate

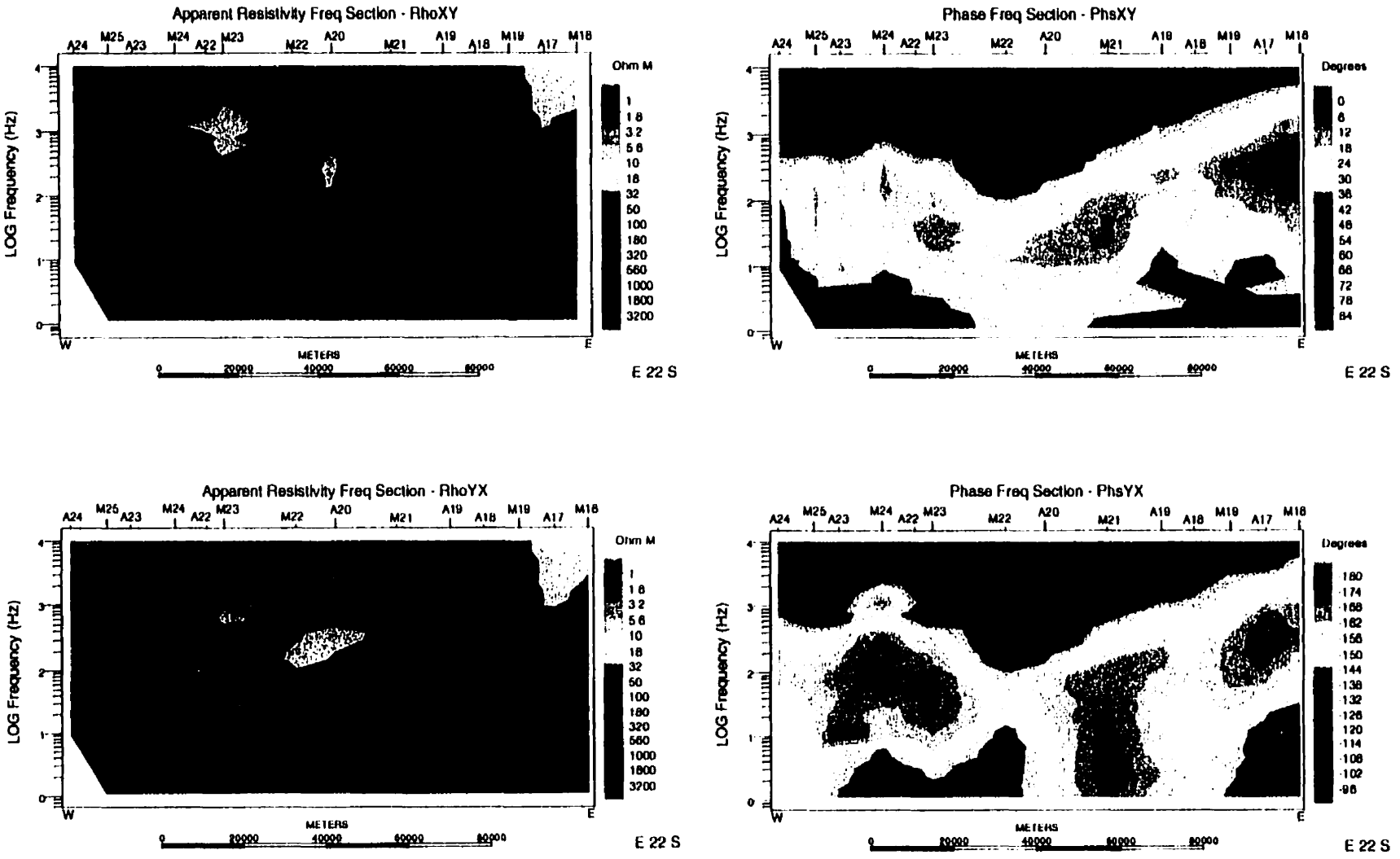

Figure 4.15 Apparent resistivity and phase pseudosections for both polarization modes (TE - xy and TM - yx) generated from those sites located on Phanerozoic cover and for frequencies above 1 Hz. "Bad" data points have been removed and a 0.04 horizontal and vertical smoothing factor has beed applied.

conductive near-surface material that thins to the east. The apparent resistivity pseudosections indicate near-surface material of <100 Ω.m including an area below sites M24 to A19 of material with resistivity < 50 Ω.m. Note the similarity in the apparent resistivity and phase sections for both polarization modes providing support for treatment of this data subset in a 1-D interpretation.

2) All Sites: Frequencies < 0.1 Hz

Figure 4.16 shows apparent resistivity and phase pseudosections for the TE (xy) and TM (yx) polarization modes for sites crossing the transect at frequencies less than 10 Hz. These data have both Groom-Bailey and static corrections applied. Note that the apparent resistivity sections show the static shift correction applied as described in section 4.4.1

TE and TM phase pseudosections show similar features. Low phase values are observed at higher frequencies (> 1 Hz) especially at sites on the western end of the transect. The low phase values extend to lower frequencies in both TE and TM data for sites M21 and M22. At lower frequencies (i.e. < 0.1 Hz) both phase pseudosections show increasing phase responses especially at the eastern end of the transect. Overall, relatively smoothly varying TE and TM apparent resistivity pseudosections have been obtained. These sections indicate that material at the eastern end of the transect (below sites M11, M12 and M46) is one to two orders of magnitude less resistive than material west of the TFZ. Two resistive lobes extending to frequencies as low as 10^{-1} to 10^{-2} Hz are in both the TE and TM data, below sites

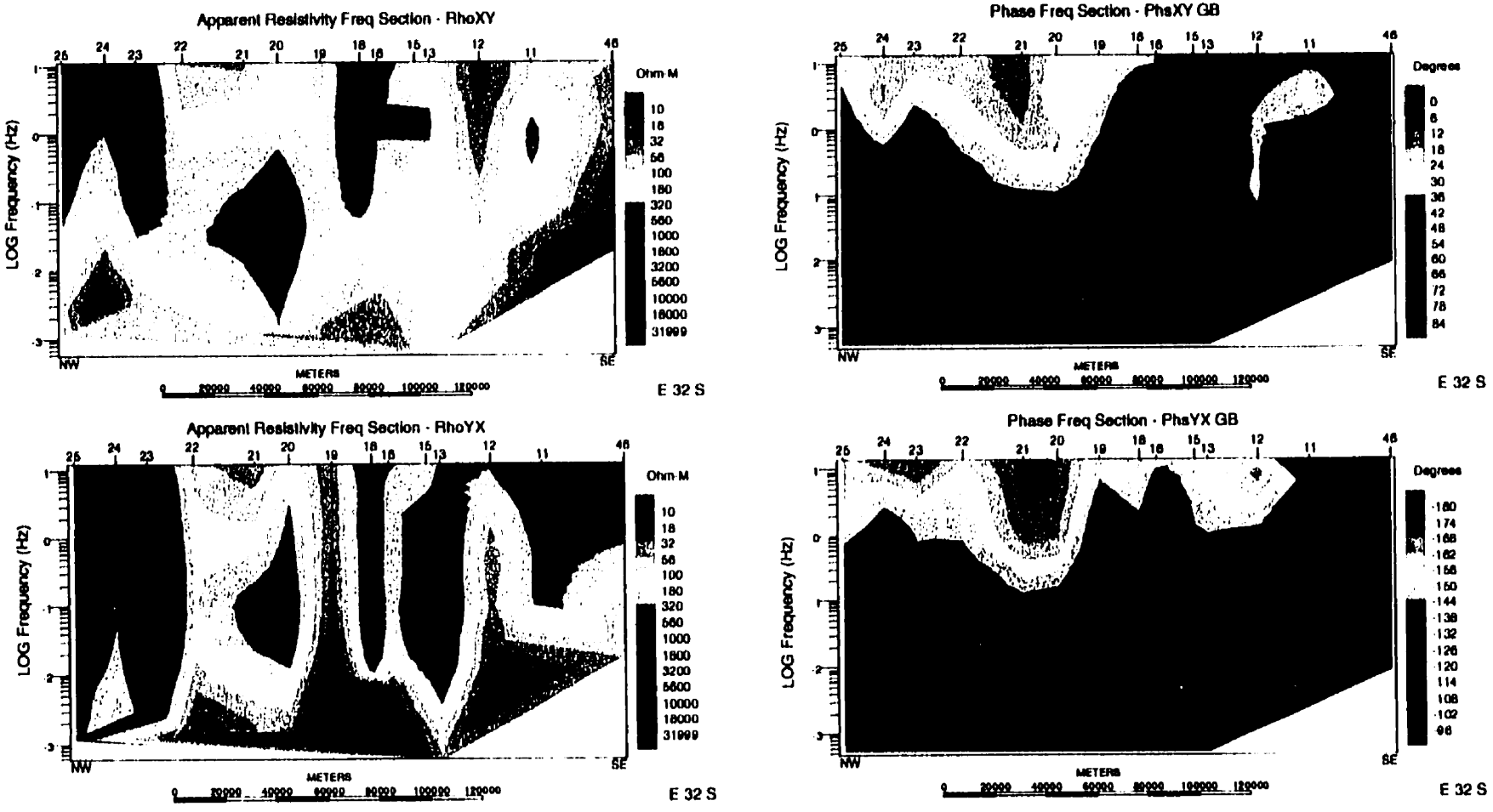

Figure 4.16 Static shifted and distortion corrected apparent resistivity and phase pseudosections for both polarization modes (TE - xy and TM - yx) generated from all MT sites located in the study area at frequencies below 10 Hz. "Bad" data have been removed and a 0.04 horizontal and vertical smoothing factor has beed applied.

M25 to M23 and M18 to M13. A general low resistivity zone exists in the 1 to 10^{-2} Hz range in the eastern part of the transect.

In a geological context, the apparent resistivity and phase pseudosections indicate that at the mid-to lower crustal depths the lithostructure is one to two orders of magnitude more resistive below sites west of the SWT than in the crust to the east. The low resistivity material indicated east of the SWT is likely representative of the rocks of the FFB. The phase data exhibits less smoothly varying responses at the eastern sites, as compared to the western sites. At the lower frequencies ($< 10^{-2}$ Hz) high phases are observed at most sites, likely representing the influence of more conductive rocks in the upper mantle.

The Tabbernor Fault Zone and Hanson Lake Block (sites M16 to M12) to Flin Flon Belt transition (sites M12 to M46) are detected in both the TE and TM data.

3) Tabbernor Fault Zone to Sturgeon Weir Thrust: A Special Case

Figure 4.17 shows apparent resistivity and phase pseudosections for both polarization modes for the five sites straddling the TFZ and SWT. Although the pseudosections indicate smoothly varying data, the effect is partly due to the small number of sites and the smooth interpolation applied to the pseudosections. The TFZ is located just east of site M16 and the SWT is located just west of site M12.

TE and TM phase pseudosections show similar features. Relatively high phase values occur in the frequency range from 10^{3} to 10^{-1} Hz at sites M16 to M13 for the TE data and very high values at site M15. This effect is less pronounced in the TM pseudosection. Both TE and TM sections show low phase values centered on 10^{2}-10^{3}

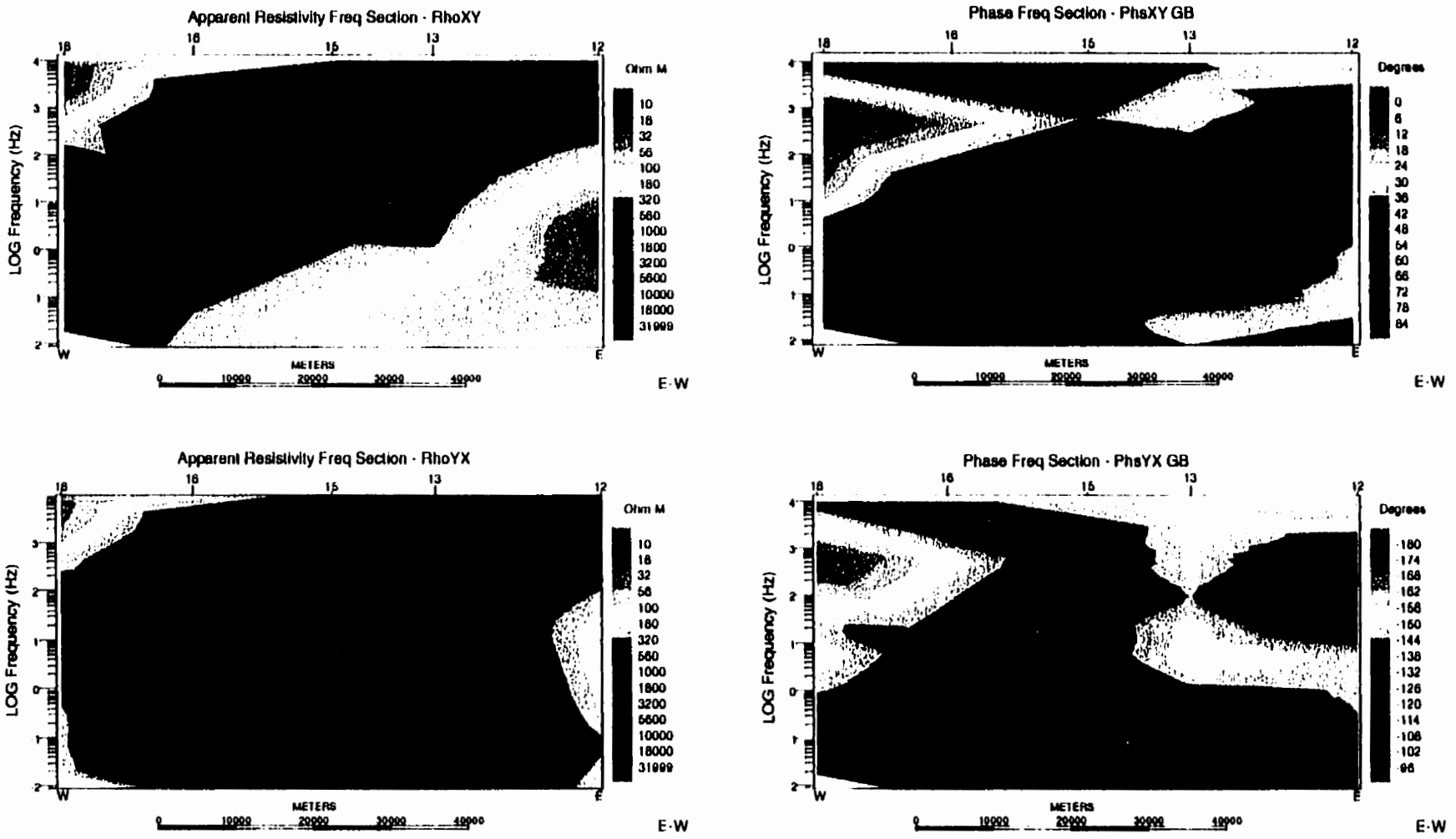

Figure 4.17 Static shifted and distortion corrected apparent resistivity and phase pseudosections for both polarization modes (TE - xy and TM - yx) generated from five MT sites spanning the the TFZ for frequencies between 10000 to 0.01 Hz. "Bad" data points have been removed and a 0.04 horizontal and vertical smoothing factor has beed applied.

Hz at the western end of the profile and centered on 10^4 and 10^1 Hz at the eastern end. At frequencies below 10^{-2} Hz the phase generally increases at all sites. The TE and TM apparent resistivity pseudosections indicate a relatively low resistivity response to the east of site M13 (<500 Ω.m) at frequencies less than 10^2 Hz. To the west of site M15, a lower resistivity response (<200 Ω.m) occurs at frequencies above 10^2 Hz. A resistive response (>1000 Ω.m) is indicated at frequencies below 10 Hz in the west part of pseudosection.

In a geological context, the apparent resistivity and phase pseudosections indicate that the effects of the TFZ and SWT, are apparent in both polarization modes. Phases generally increase at frequencies above 1 Hz from west to east of the TFZ-HLB-SWT which (sites M16, M15, M13 and M12, barring near surface effects, is a reliable indication of a transition from resistive to more conductive rocks.

CHAPTER 5

MODELLING AND INVERSION OF THE GD-FFB MT DATA

5.1 Introduction to MT Modelling and Inversion

Forward modelling of any EM data is the process of calculating the theoretical response of geoelectric models. It may include "curve matching" observed EM data with the EM response of geoelectric models constrained by surface or drill hole geologic data. In mathematical terms, forward modelling can be defined as

$$d_{pred} = F[m] \tag{58}$$

where d_{pred} indicates a vector containing data,

m a vector containing model parameters, and

F is the functional relating the model to the forward response.

The forward modelling approach, while open ended, is a means of establishing a group of geoelectric models that is most consistent with the EM and other information available.

Inversion modelling involves fitting observed data (to within some level defined by error estimates) with geoelectric models. Inversion can be notionally (*cf.* mathematically correctly) written as:

$$m = F^{-1}[d_{obs}, \sigma] \tag{59}$$

where F^{-1} is the process of choosing a model which fits the observed data to within some misfit,

d_{obs} is the observed data and,

σ is some misfit defined by the error estimates.

As with forward modelling, the process of data inversion is somewhat 'open ended' since a range of models may be fitted to the observed data. This fact has steered researchers to develop regularized inversion codes that result in models that both fit the data and are optimal in some other sense (e.g. they contain as little structure as possible).

The purpose of the forward modelling and inversion process, as applied to the GD-FFB MT data sets, will be to estimate the geoelectric structure from the near-surface to lower crustal depths beneath the observation sites. The inversion will initially involve an unconstrained approach where no apriori geological knowledge is introduced. Subsequent to this, constrained forward modelling, using the information from deep seismic reflection surveys, will be discussed.

5.2 Forward Modelling Methods

Forward modelling can be approached in a 1-D, 2-D and 3-D fashion depending on the complexity of the geological/geoelectric situation. 1-D forward modelling is the simplest and most well understood method since it is based on a recursive calculation of the MT impedance at the surface of a layered conductivity structure. Since the early to mid 1970's greater attention has been paid to the 2-D and 3-D modelling of EM phenomena based on the integral equation (IE), finite element (FE), finite difference (FD) and thin sheet approaches. Wannamaker et al. (1984), describe

an IE algorithm for MT problems that can handle a 3-D body in an arbitrarily layered 1-D earth. A 2-D FE code has also been developed by Wannamaker et al. (1986) and hybrid methods involving both IE and FE codes are also in use (Best et al., 1985). An approach using thin sheet modelling has become a viable means for treating surface inhomogenieties. As machines that were once supercomputers become available as desktop computers and more advanced computational algorithms become widely available, 2-D and 3-D modelling is becoming more common. However it should be remembered that approximate solutions to EM problems are often as useful as the more complex, full solution (West and Edwards, 1985).

The 2-D forward models presented in this thesis were constructed, and their response computed, using the PW2D forward modelling code written by Dr. Philip Wannamaker and implemented in the GEOTOOLS software package, version 7.23 (for Windows, PC). This algorithm represents the Earth as a "stack of bricks", each with an assigned resistivity. Computation of the 2-D model response is based upon a finite element mesh that consists of a rectangular area of columns and rows of arbitrary widths. Each rectangular element is further subdivided into four triangles. The forward modelling was performed on a dual 100 MHz, Pentium machine with the average run time for a realistic geological model being approximately 0.5 hours.

5.3 Inversion Modelling Methods

Inverse modelling can also be approached in a 1-D, 2-D and most recently 3-D fashion depending on the complexity of observed data. In 1-D inversion there is only one complex response to fit, consisting of both a magnitude and a phase term. The

phase term is more robust to static shift and tensor distortion effects. Most common 1-D inversion codes set up a layered model and iteratively adjust the thickness and conductivity of these layers until the best fit is achieved. EM data are Frechet differentiable, as addressed by many authors in the early 1980's, using various uniqueness theorems for ideal data (MacBain and Bednar, 1986). However most MT data sets are usually somewhat less than ideal. Real MT data are always discrete and have errors associated with them. Parker (1983) showed that when no 1-D model fits a data set exactly, then the conductivity model with the smallest least squares or χ^2 misfit will always consist of a set of infinite spikes or delta functions in conductivity. This is known as the D^+ case, and its application, although requiring the MT data sets to contain noise, has become increasingly widespread as a method for determining the most reasonable level of fit to a given MT data set.

In 2-D modelling there are typically two or three complex responses to fit corresponding to the TE and TM impedances and the tipper. The TE mode is more sensitive to the conductance of conductive regions of the model than TM, but provides lower resolution of the position of structures. The TM response is more sensitive to lateral boundaries than the TE mode. The tipper is usually sensitive to the local structure but can also be strongly affected by conductivity boundaries at the edges or outside of the region modelled. Inversion of TE data resolves well only the depth and the conductivity-thickness product of the conducting regions, whereas inversion of only TM data resolves well their horizontal extent and the presence of

thin resistive layers (Agarwal et al., 1993). Using both modes in the inversion allows for a much better evaluation of the resistivity structure over a large area.

While 2-D and 3-D inversion of MT data is ultimately more important for investigating the Earth, the theory and algorithms are less advanced than those of its 1-D counterpart. Most 2-D inversion schemes implemented in the past decade fall into two categories:

1) Expansion of the model using a limited parameterization (i.e. a small number of blocks) and adjusting the values of the parameters to fit the data to within some prescribed tolerance. Jiracek et al. (1986), developed a code along these lines where the forward calculation of the Frechet derivatives uses self-adjusting finite elements.

2) A second type of parameterization strategy picks one of the infinite number of 2-D solutions by finding the one that is closest to some prescribed structure.

Some groups have developed algorithms for minimum structure inversion in which the resulting models contain only those structures that are actually required by a given data set. Constable et al., (1987) introduced **Occam's inversion**: a practical algorithm for generating smooth 1-D models from EM sounding data. The method generates the smoothest model possible by fitting the data to within an expected tolerance (e.g., the D^+ misfit). This method was later extended into the inversion of MT data for smooth 2-D models (deGroot-Hedlin and Constable, 1990). A rapid 2-D MT inversion for minimum structure, called the **Rapid Relaxation Inversion (RRI)** has been developed by Smith and Booker (1990). The method represents the structure as a series of 1-D models with a correction for lateral field gradients, but use the full

2-D forward model to calculate the response. In general, the Occam code generates the smoothest model possible by fitting the data to within an expected tolerance (i.e. D^+ misfit) and the RRI code seeks the smoothest model in terms of least variation of conductivity both laterally and vertically which fits the data. In theory the RRI method could be applied to the 3-D inverse problem where even greater time and storage savings may be realized provided an accurate 3-D forward problem is incorporated. Madden and Mackie (1989) have developed a full 3-D MT inversion method which may incorporate a priori constraints or, in principle, minimum structure to regularize the solution.

One disadvantage of any inversion approach is the importance of ideality in the data. Data with non-Gaussian errors or with 3-D effects when a 2-D algorithm is being applied, may all introduce spurious features to the final model.

The 1-D and 2-D inverse models presented in this thesis were generated from the GEOTOOLS implementation of the Bostick 1-D, Occam 1-D, Occam 2-D and RRI 2-D codes. The Bostick 1-D transform method (Bostick, 1977) uses the Bostick transform of the selected data and simply assumes one layer for each frequency and finds a best fitting solution. The Occam 1-D inverse method fits the data more accurately in an iterative approach providing a minimum structure model. Static shifts in apparent resistivity data may be mapped by Occam inversion into the resistivity models so care must be taken in the interpretation of these results. Computation of the Occam 2-D inverse model response is based on a rectangular regularization grid superimposed onto a finite element mesh. The GEOTOOLS

implementation of the Occam inversion supports constraints which can be used to incorporate other information in the model search. The RRI algorithm provides an inversion model using much less computational effort than is required for other 2-D inverse techniques. A disadvantage of RRI is that it does not fir the vertical field transfer functions (tipper). A further disadvantage of RRI 2-D inversion is that it can only introduce structures in the model beneath specified observation points.

The inverse modelling presented in this thesis was performed on a dual 100 MHz. Pentium machine with the average run time of a few seconds for the 1-D inversions, 1-2 hours for the RRI 2-D inversion and up to several days for the Occam 2-D inversions. Specific inversion parameters will be discussed in subsequent sections. More general inversion parameters are defined in the references cited above.

5.4 Inverse Modelling of the Responses From the Phanerozoic Sites

5.4.1 Purpose

The purpose of the modelling of the shallow resistivity structure at sites located on the Phanerozoic cover is to investigate the structure and thickness of sedimentary units and the Phanerozoic to basement transition, as well as a preliminary evaluation of the upper crustal features below the Phanerozoic cover. While this work is subsidiary to the primary LITHOPROBE objective of defining Precambrian geological structure, it stands alone as a useful and interesting sub-project.

5.4.2 1-D Inverse Modelling

One dimensional models of the data from the Phanerozoic subset of the GD-FFB sites were obtained using Bostick transformation and Occam inversion. The Bostick transform was based on the use of both apparent resistivity and phase responses. Both apparent resistivity and phase data were used for the Occam 1-D inversion with equal weighting assigned each data type. A D+ inversion was used to set the inversion termination criteria and the maximum iterations was 10 for the Occam inversion. The model fitted consisted of 40 layers with 10 layers per decade and a top layer with thickness of 10 m. The starting model was a half-space. The data used in the inversions were essentially unprocessed, except for the exclusion of 'bad' data points, and the entire frequency range (10^{4} - 10^{-4} Hz) available was used. However, only the data for frequencies above 10 Hz was inspected in comparing the observed and modeled data.

One dimensional inversion of MT data can be done on a site-by-site basis and the resulting resistivity models can be 'stitched' together, to provide an approximate 2-D section of the subsurface resistivity structure. The results in figure 5.1 show resistivity sections for both the TE and TM polarization obtained using 1-D Bostick transformations and 1-D Occam inversions. In general the results show a 1-D layered structure above 1 km corresponding to the conductive Phanerozoic sedimentary rocks overlying the Proterozoic rocks. An Approximately 1-D structure extends down to 10 km. Note the conductive region extending to depth between sites M23 and M22.

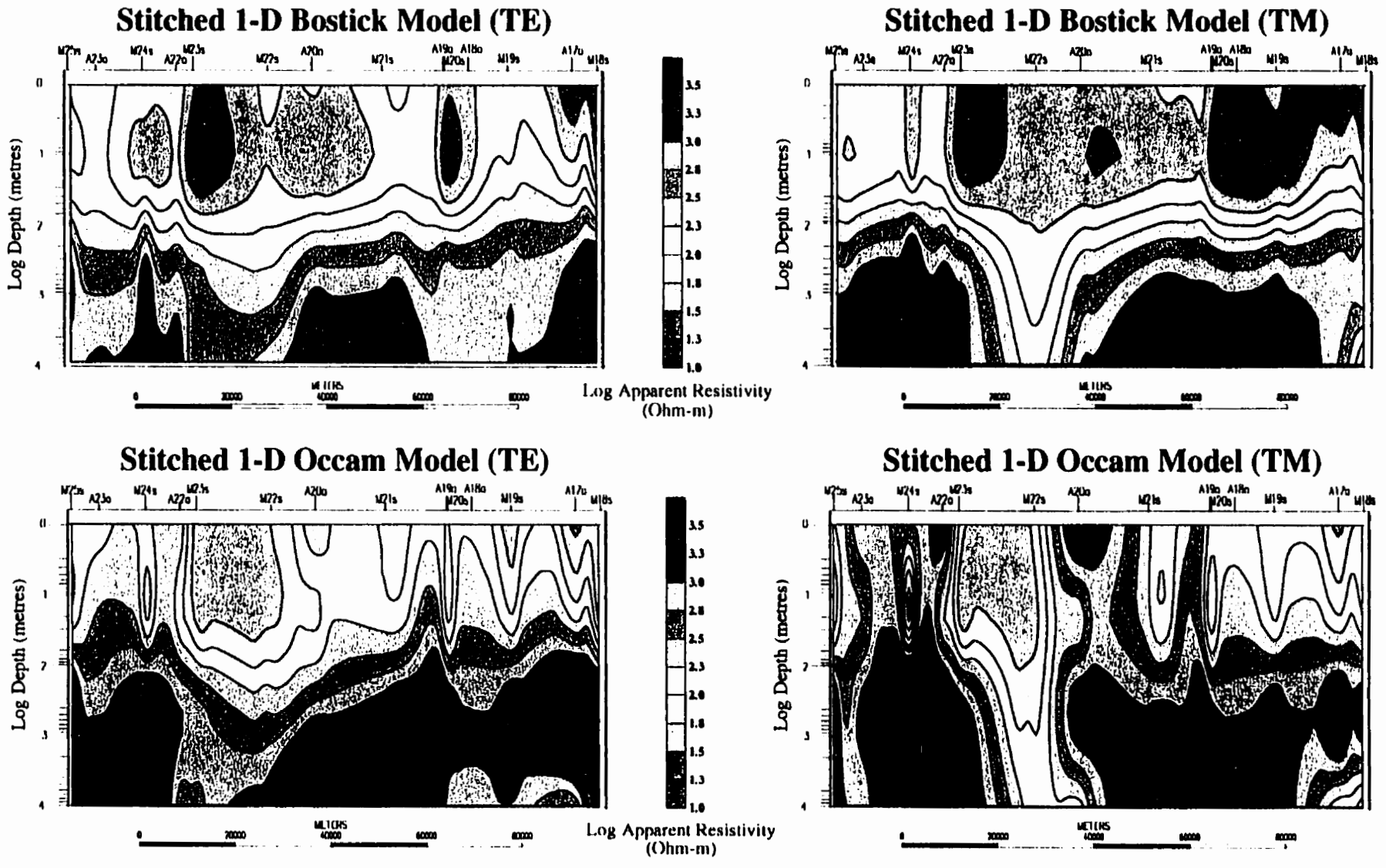

Figure 5.1 1D stitched resistivity sections for both TE and TM modes of polarization using 1D Bostick and 1D Occam inversions for sites located on Phanerozoic cover. Note that log depth and log resistivity are displayed to emphasize the near surface features.

This zone corresponds with a high reflectivity zone (F) observed in the seismic data (see Figure 3.2a).

5.4.3 2-D Inverse Modelling

Two-dimensional inversion of the data from the Phanerozoic sites was performed to more accurately resolve 2-D features in the upper crust. Simultaneous inversion of the TE and TM data was performed using the RRI method. Both apparent resistivity and phase data were used in the inversion. Error estimates on the data were set to +/- 0.0217 log units for the apparent resistivity and +/- 3^0 for the phase. To ensure adequate frequency coverage, 22 frequencies above 1Hz, corresponding exactly to those in the observed data, were used in the inversion. The values of the detailed inversion parameters (i.e. the number of standard and Huber iterations, eta parameter etc) were set at GEOTOOLS default values. The starting model was a 1000 Ω.m half-space. The inversion terminated after 29 iterations

The resulting model from the RRI inversion is shown in figure 5.2. Figures 5.3 and 5.4 show the individual apparent resistivity and phase curves for the 14 sites used superimposed with the resulting model data. As can be seen in these plots, good to excellent fits to the observed data are achieved at all sites by the RRI modelling. However, there is significant misfit of the TM mode data at frequencies less than 50 Hz. Fits to the data are best above 100 Hz indicating that the characteristics of the Phanerozoic material and the Phanerozoic/Proterozoic transition are best resolved and that information on the upper crustal Proterozoic rocks is less well defined by this

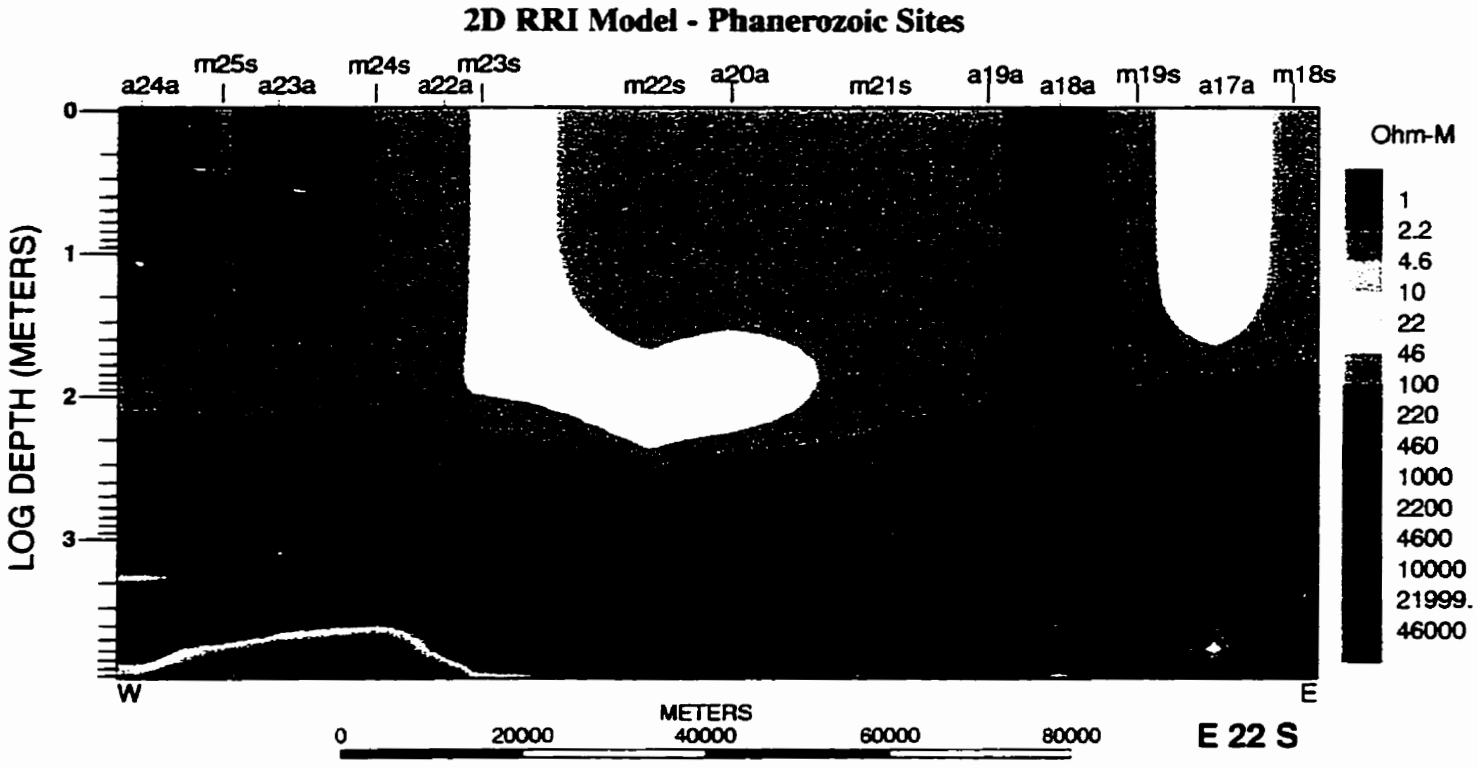

Figure 5.2 2D RRI inversion results for MT data from the Phanerozoic sites, concentrating on data above 10 Hz. Note that log depth has been used to emphasize those features above 1 km.

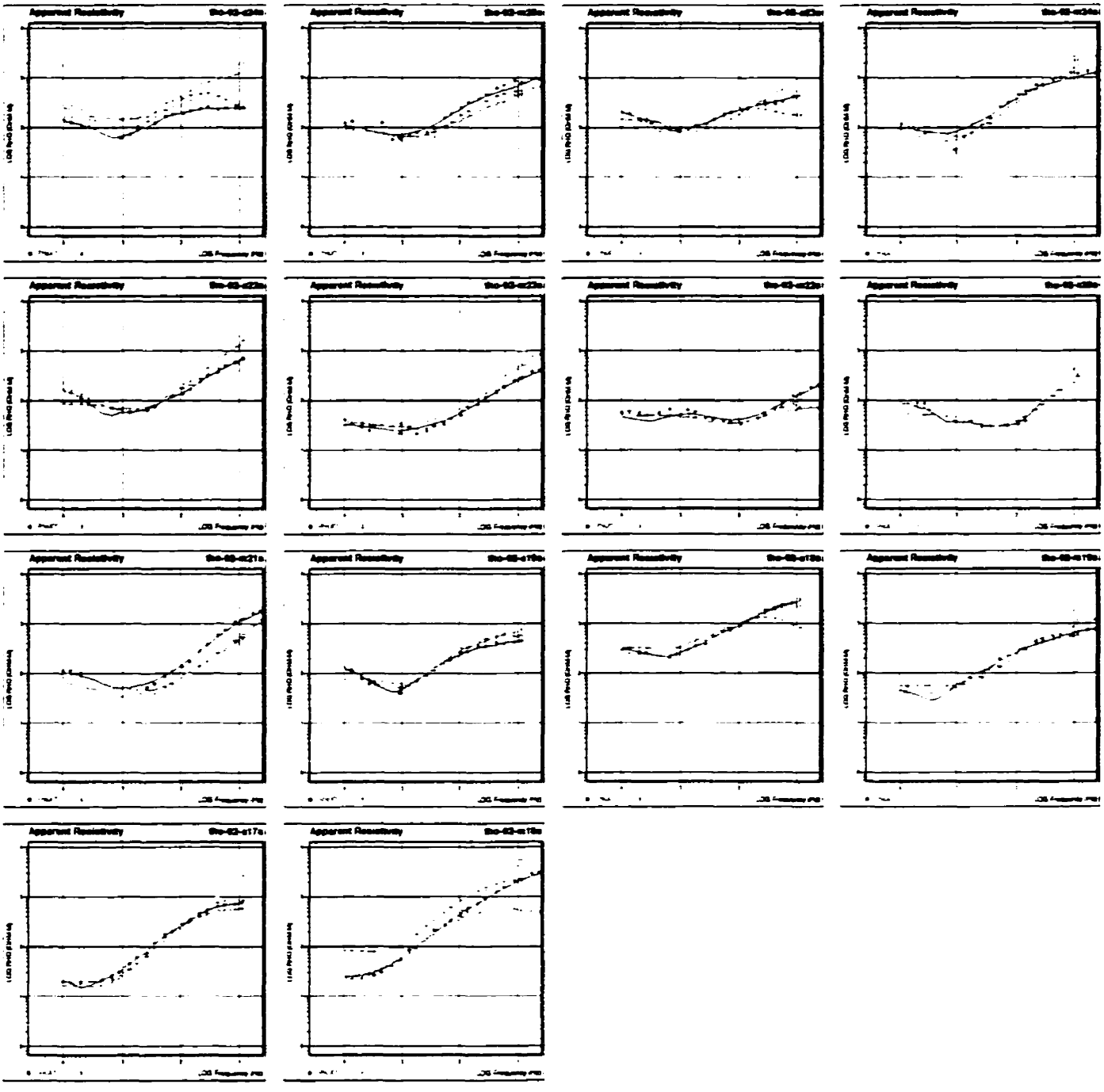

Figure 5.3 Individual apparent resistivity curves for the 14 Phanerozoic sites used in the 2D RRI inversion (solid symbols with best fit line) superimposed with modeled reponses (crosses) for a frequency range from 1 to 10000 Hz.

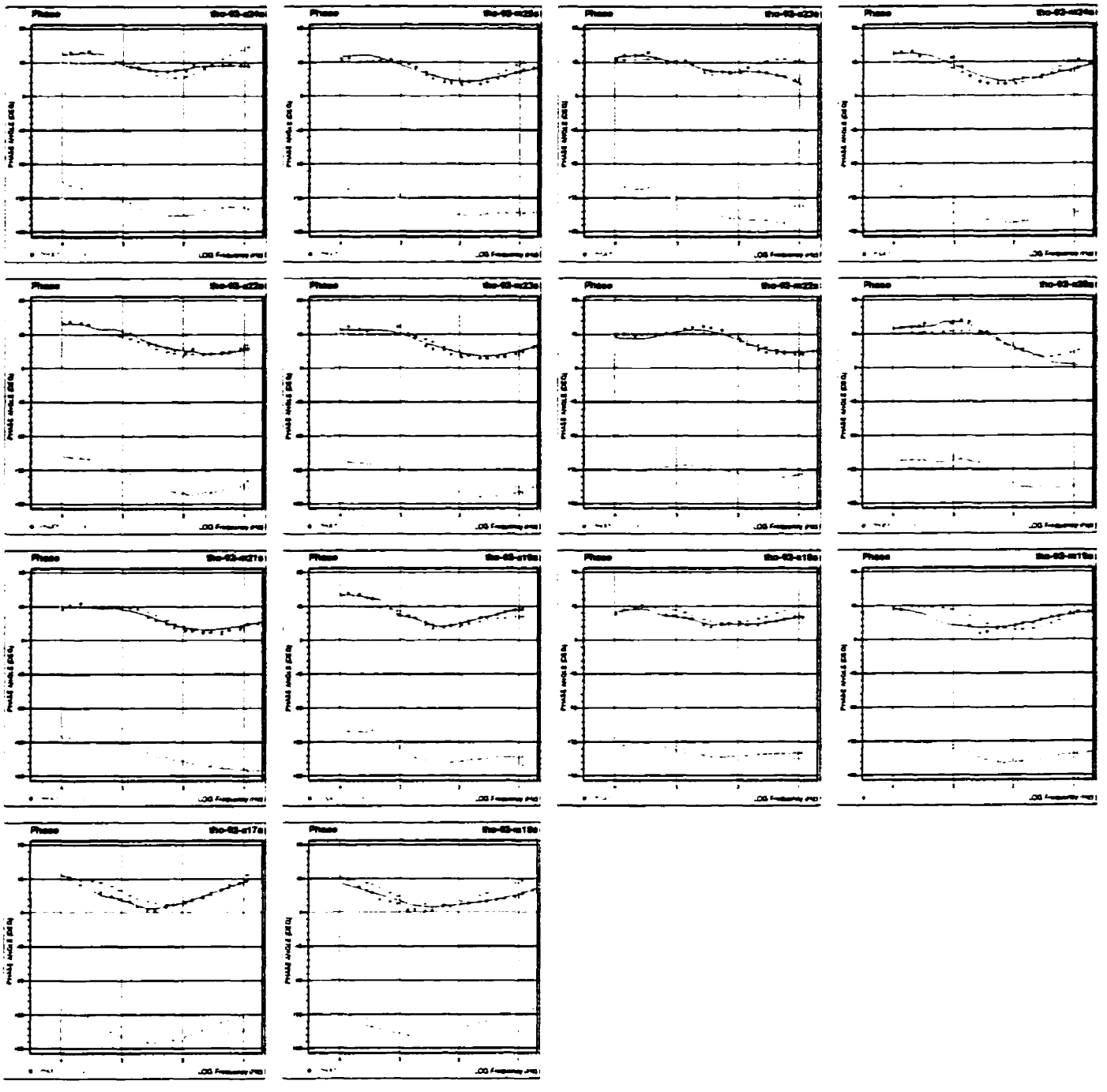

Figure 5.4 Individual phase curves for the 14 Phanerozoic sites used in the 2D RRI inversion (solid symbols with best fit line) superimposed with modeled reponses (crosses) for a frequency range from 1 to 10000 Hz.

inversion. The model obtained from the 2-D inversion process shares some common features with the model obtained from the 1-D analysis, specifically the overall thickness of the sedimentary units and their apparent resistivity. A thickening of the Phanerozoic sedimentary rocks around site M22 is also indicated in both the 1-D and 2-D inversion results.

Several features in the 2-D inversion model may be artifacts of the inversion. As an example, the vertical resistive feature beneath site A18 may be due to a static shift not incorporated into the RRI inversion. The 2-D RRI model contains some extremely high and low resistivities, particularly near its base. For example, beneath M24 the resistivity varies from >50,000 Ω.m at 2 km depth to <1 Ω.m at 6 km depth, which is an unlikely structure in this geological environment. RRI may produce extreme resistivities if a component of the data is overfitted. The same effect occurs when over-fitting 1-D data and delta-function like models occur. Therefore, in the interpretation of the 2-D model the emphasis is placed on features in the Phanerozoic and upper few kilometres of the underlying Proterozoic rocks.

5.4.4 Consideration of the Final Models

The results of the 1-D and 2-D inversions indicate that the average thickness of the Phanerozoic sedimentary cover is 100 to 200 m, and that the thickness decreases slightly to the east towards the margin with the Precambrian rocks. The resistivity of the Phanerozoic cover is 50-200 Ω.m and both the 1-D and 2-D TE and TM results show the lowest resistivity in the Phanerozoic section at sites M23 and M17. These

data also show that the TE and TM models differ somewhat near sites A19 to M19 and the 2-D model contains near-surface structure in this area. These results suggest the presence of shallow structures in the Phanerozoic rocks at this location. All inversion results show that in the vicinity of site M22, the Phanerozoic material thickens to at least 300 m. The Phanerozoic to Proterozoic transition is abrupt with the resistivity of the underlying material exceeding 1000 Ω.m across the entire section. (e.g. Figure 5.2).

5.5 Inverse Modelling of the Responses for All sites < 0.1 Hz

5.5.1 Purpose

The purpose of this section is to describe the modelling of the crustal structure of the Precambrian rocks along the GD-FFB profile. This work is directly associated with the primary LITHOPROBE objective of defining Precambrian geological crustal structure in this part of the THOT. The work is aimed at resolving the 2-D form of geological structures with differing resistivities and correlating them with other geophysical data (i.e. seismic and potential field results).

5.5.2 1-D Inverse Modelling

Preliminary 1-D modelling was performed to provide an examination of the gross geoelectric structure. The 1-D modelling gives an approximate mapping of the resistivity versus depth that helps in the initial interpretation and in the parameterization of subsequent 2-D models.

As an initial investigation of the deeper structures, the static shifted, decomposed TE and TM polarization mode data for all of the MT sites on the GD-FFB profile were inverted for minimum 1-D structure using the Occam code of Constable et al. (1987) as implemented in GEOTOOLS. Different models are fit to the TE and TM modes respectively. Note that 1-D modelling of the data at frequencies above 0.1 Hz has been included to partly account for variations in the upper crust. Figure 5.5 shows 1-D Occam inversions for three sites, one from the west end of the profile (M25), one from the mid section of the profile over the TFZ (M13) and one from the east end of the profile (M46). Overall the 1-D inversions fit the data quite well except the low frequency responses at site M13. The general characteristics of the 1-D models are as follows:

1) At site M25, in the western part of the transect, the TM results indicate increasing resistivity (to >10000 Ω.m) in the 1 to 4 km depth range followed by a transition toward less resistive material at depths of 5-10 km. The TE data models include a stronger contrast between the resistivities above and below 10 km. In the TE model the upper crust material has a lower apparent resistivity than in the TM model.

2) At site M13 in the central portion of the transect, the TE results indicate high resistivity material (>50000 Ω.m) in the 1 to 4 km depth range followed by a zone of lower resistivity (10000 - 50000 Ω.m) material to 20 km then very resistive material (>50000 Ω.m) to 50 km. The TM results primarily indicate resistive material (>10000 Ω.m) below 2 km. In the TE model the crustal material has a higher apparent resistivity than in the TM model.

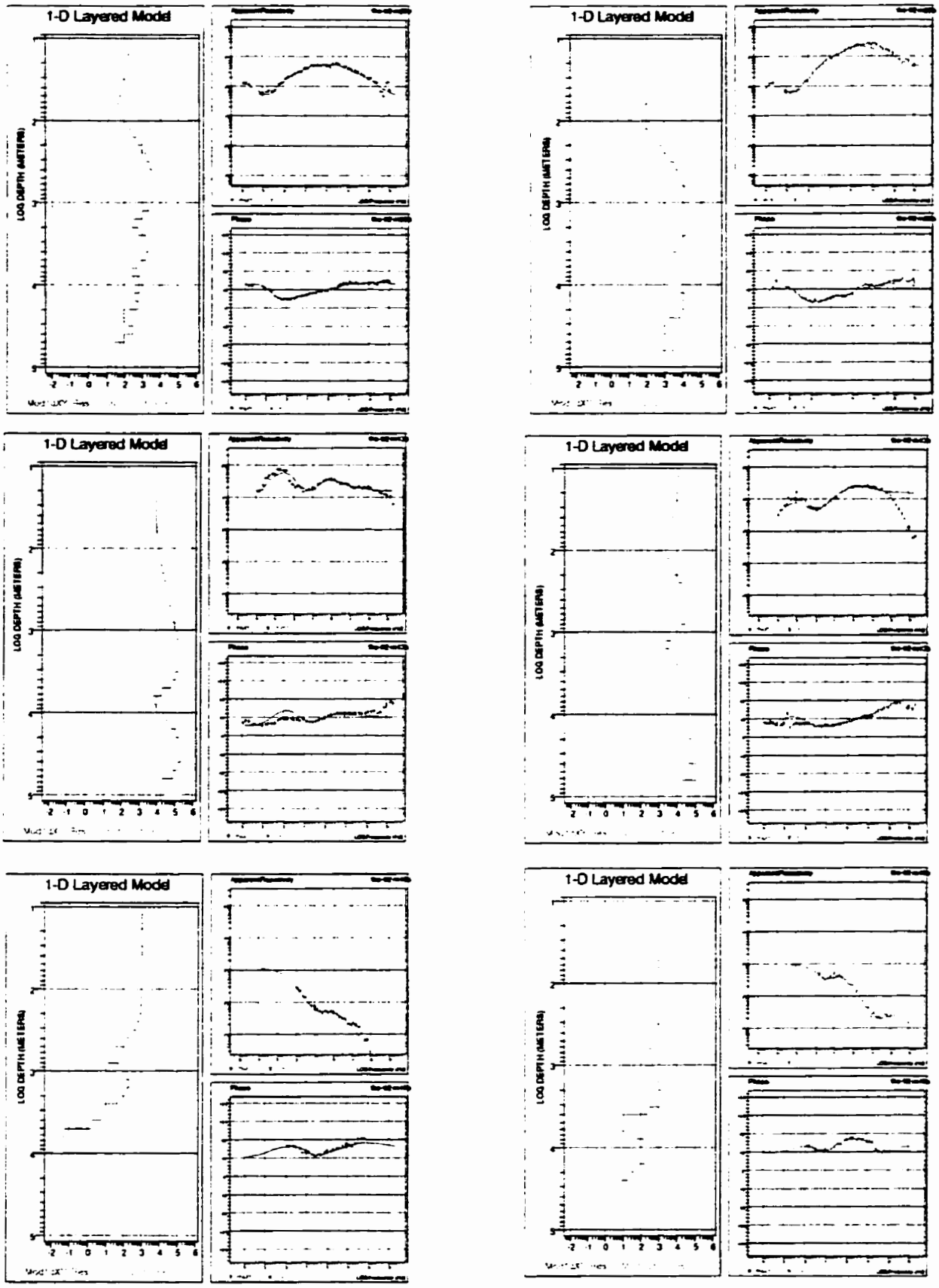

Figure 5.5 1D Occam inversion results for three sites spanning the GD-FFB segment: M25, M13 and M46. 1D layered models outline the general geoelectric structure across the transect.

3) The models for site M46 in the eastern portion of the transect indicate that generally low resistivity material (< 2000 Ω.m) is pervasive through the upper-middle crust. A very low resistivity layer (< 100 Ω.m) is indicated from 4 to 6 km for both TE and TM data followed by an increase in resistivity (100 Ω.m) from 7 to 20 km in the TM model and then very low resistivity material to greater depths.

Figure 5.6 shows the 1-D Occam inversion models, stitched together as a pseudo-2-D model, for all of the MT sites in the data subset. Apparent in these sections is the low to moderate resistivity material (400-4000 Ω.m) in the upper to mid crust (5-15 km) in the west portion of the transect (sites M25 to M15) and a very low resistivity zone (< 200 Ω.m) at similar crustal depths between sites M12 through M46 on the east half of the profile. The TE model in the area of sites M15 and M13 (crossing the TFZ and HLB), includes resistive material (> 5000 Ω.m) extending from shallow to 15 km depth. The TM model in the same area indicates resistive material (> 5000 Ω.m) from surface to >30 km. At mid to lower crustal depths (i.e. 20-40 km) high resistivity material (> 5000 Ω.m) is indicated below sites M21 to M20. Common areas of low resistivity material lie at mid to lower crustal depths between sites M12 to M46 and to a lesser degree between sites M19 to M16 in both TE and TM models. The TE and TM model results differ the most at mid to lower crustal depths at sites M25 to M23 where low resistivity material (< 10 Ω.m) is indicated by the TE model and moderate resistivity material (> 1000 Ω.m) is indicated from the TM model. The general indication of these data is that the mid to lower crust of the west part of the

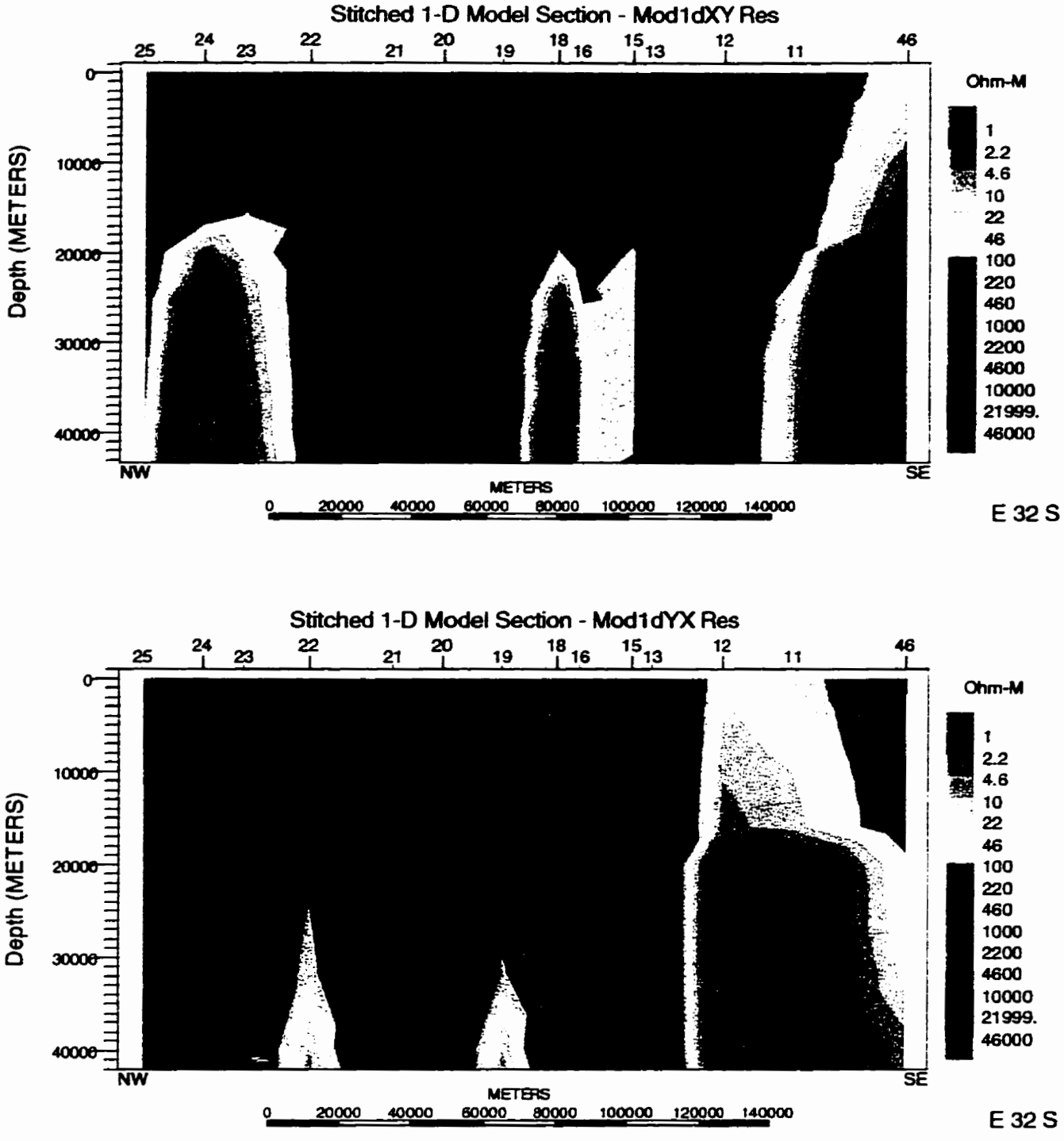

Figure 5.6 Stitched 1-D Occam inversion results for 14 MT sites across the GD-FFB transect segment. Note the similarity between the two polarization modes.

profile is relatively more resistive than the east part of the profile, the transition occurring in the TFZ and SWT area.

5.5.3 2-D Inverse Modelling

The MT data subset was modeled with the Occam 2-D Occam inversion code in order to resolve the features of the crust more accurately.

The data for the entire profile were the GB corrected data as described above. Static shift information was not included in the inversion process, as explained in section 4.4.1. The frequency range was extended to 10^2 Hz in order to provide overlap with the modelling of the MT subset of Phanerozoic sites and to extend the interpretation into the upper crust. However, since the GB tensor analysis was based on data at frequencies <0.1 Hz, the interpretation will focus on the mid and lower crustal features. As outlined in the response analysis section, the decomposition results suggest a TE direction of around 32° N, so modelling will be performed with sites projected onto a line oriented at 122° N. Simultaneous inversion of both TE and TM data was undertaken with the Occam 2-D code. Apparent resistivity, phase and tipper (vertical transfer function) data of both polarization modes were used in the inversion. Error estimates on the data were set to +/- 0.34 log units for the apparent resistivity (to accommodate to some degree for static shift effects), +/- 2.866^0 for the phase data and +/- 0.05 for the tipper data. Note that a ρ_a error of e_r means that the value of $\log(\rho_a)$ becomes $\log(\rho_a) \pm e_r$ *ie.* $\rho_a/10^{er}$ to $\rho_a \times 10^{er}$. Thus an error of +/- 0.34 on a value of 1000 Ω.m means the error range for the apparent resistivity is 1000/2.18

to 1000x2.18 or 460-2200 Ω.m. Review of the tipper data indicated that for most sites the data was reliable to down to 100s. At longer periods the error limits were increased to reflect the lower reliability of these data. To ensure adequate frequency coverage, 12 frequencies between 100 to 0.001 Hz, corresponding exactly to those in the observed data, were used to fit the data in the inversion. The starting model was a 1000 Ω.m half-space. The FE mesh consisted of 143 (lateral) and 54 (vertical) elements. The inversion terminated after 4 iterations with a final root mean square (RMS) fit of 4.22.

The resulting Occam model together with a comparison of observed and modeled response apparent resistivity, phase and tipper transfer function curve fits are shown in figure 5.7, 5.8, 5.9 and 5.10. In general the TE data is fit much better than the TM data. The apparent resistivity model curves have a similar shape to the observed curves at most sites whereas the phase model curves more accurately conform to the shape and magnitude of the observed data. It should be noted that while the general form of the resistivity and phase curves are similar for the observed and modeled data, the fits to the observed data are at best only moderately good over the whole data set. The tipper data fits (figure 5.10) are fairly good at sites west of the TFZ (i.e. west of site M15) and not so good at sites between M15 and M46. In general the TM tipper data is fit better than the TE data. Some of the misfit to the tipper data may be related to a distortion effect on the magnetic response as described by Zhang et al., 1993.

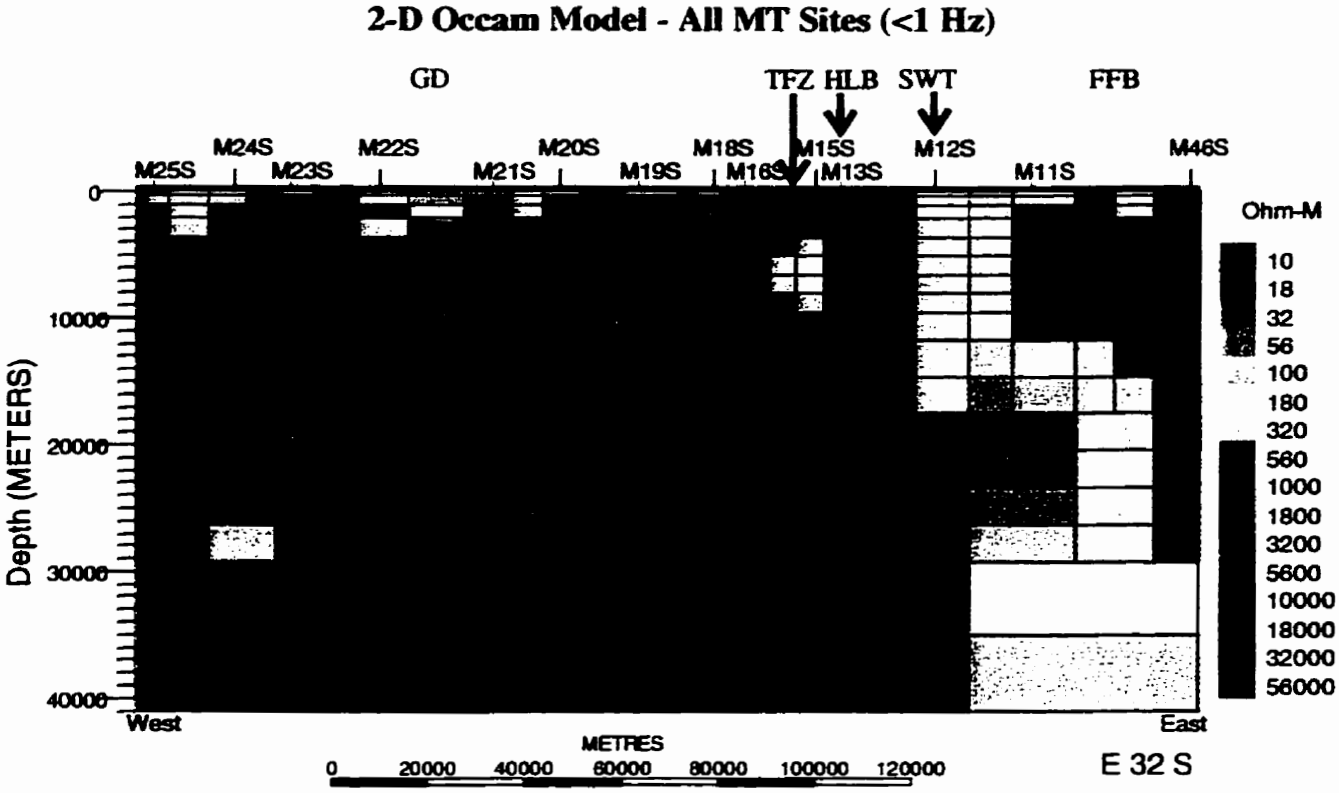

Figure 5.7 2D Occam inversion results after 4 iterations for 14 MT sites across the GD-FFB segment of the THOT transect. A linear depth resistivity section is shown..

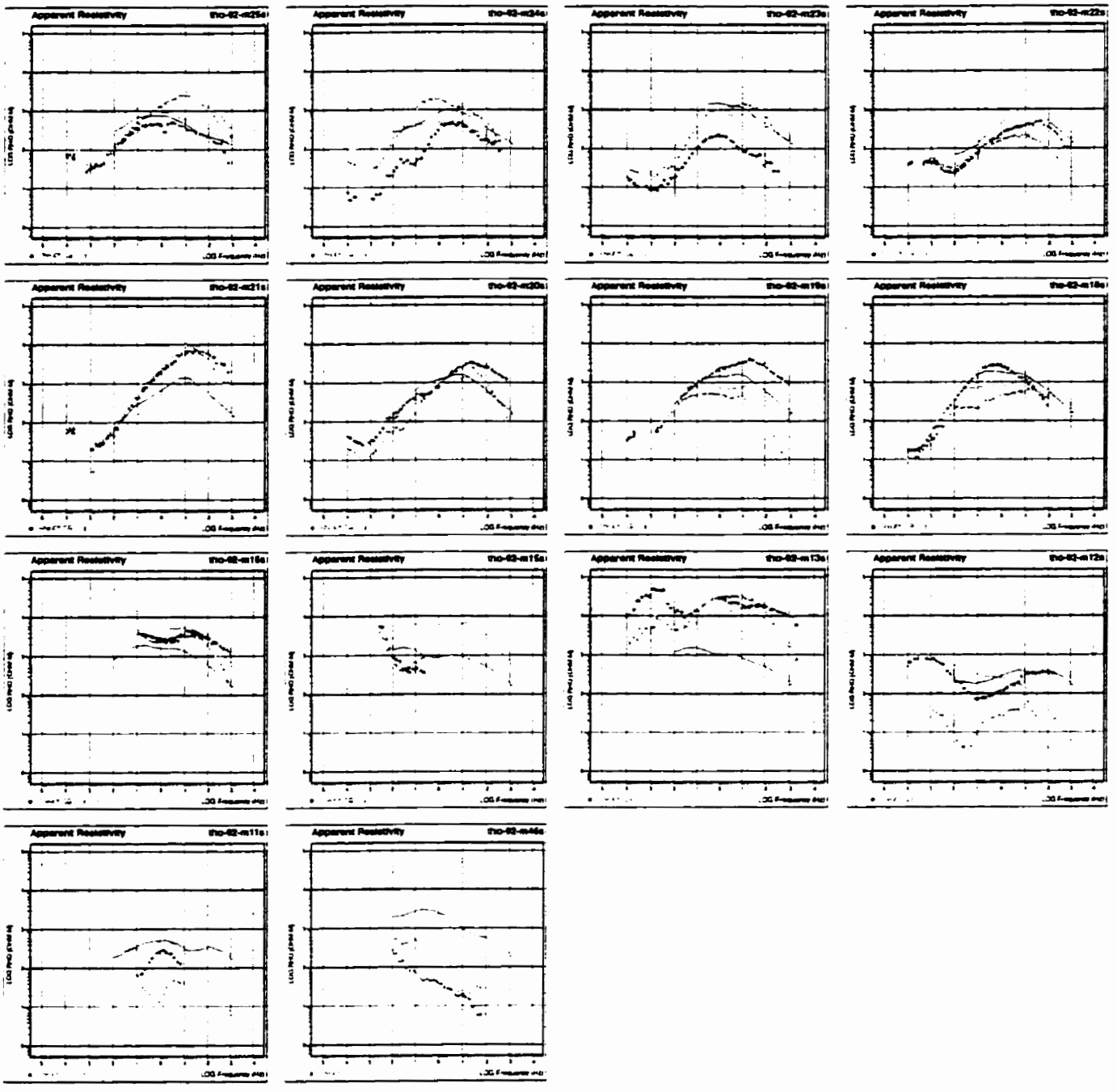

Figure 5.8 Individual TE and TM apparent resistivity curves for the 14 MT sites across the GD-FFB segment of the THOT used in the 2D Occam inversion (solid symbols) superimposed with modeled responses (solid lines) for a frequency range from 100 to 0.0005 Hz.

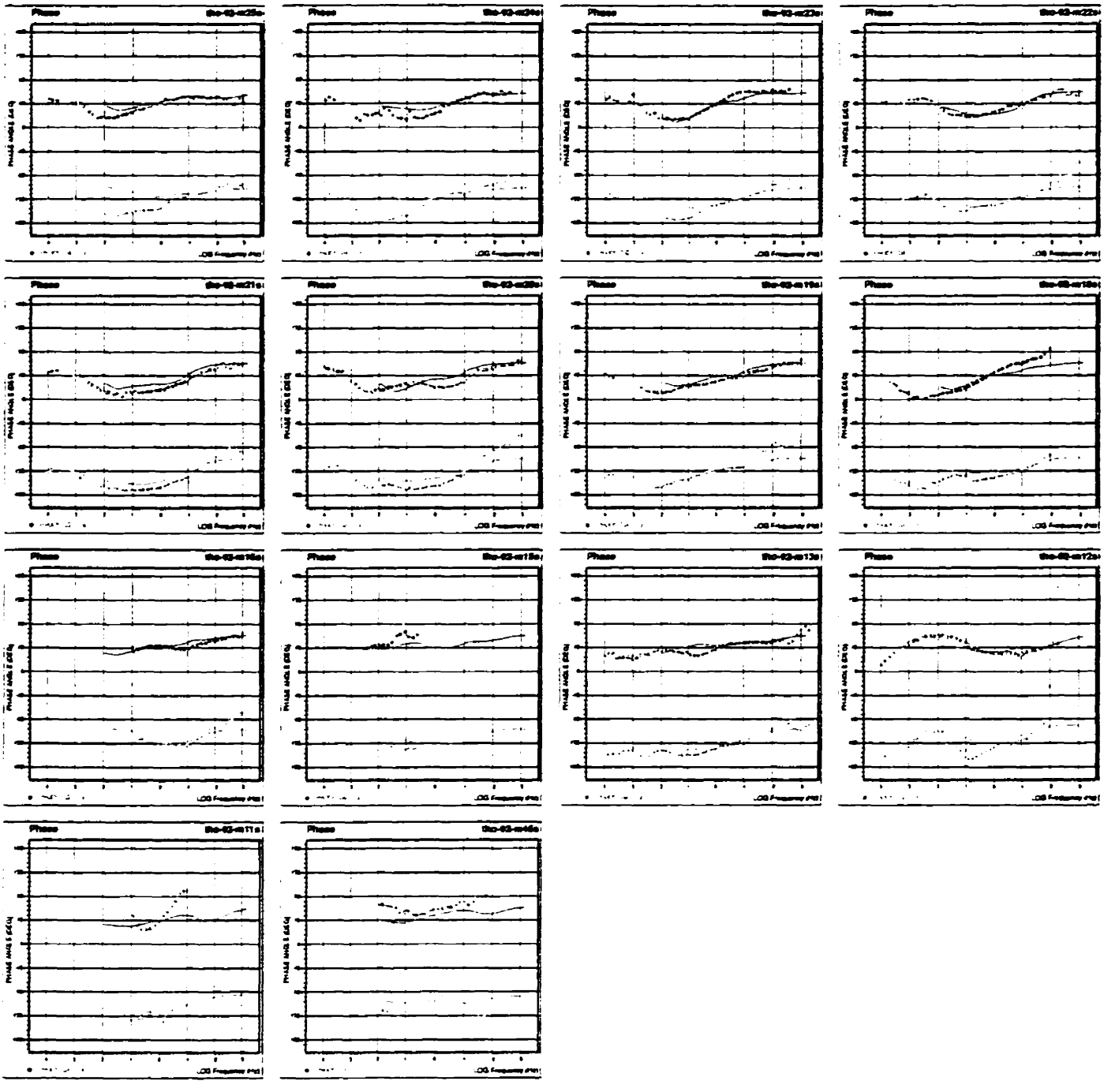

Figure 5.9 Individual TE and TM phase curves for the 14 MT sites used in the 2D Occam inversion (solid symbols) across the GD-FFB segment of the THOT superimposed with modeled responses (solid lines) for a frequency range from 100 to 0.0005 Hz.

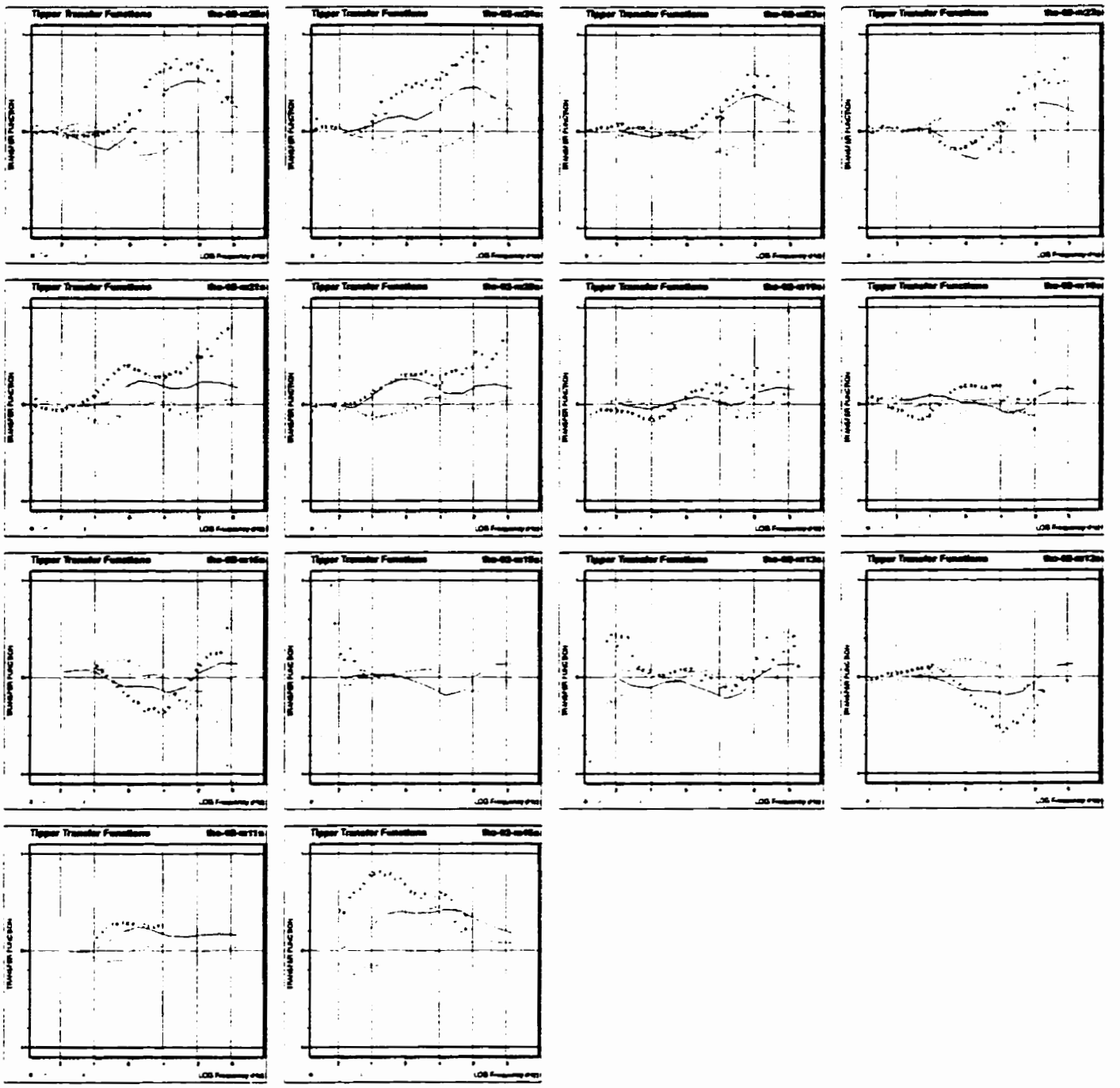

Figure 5.10 Individual TE and TM tipper curves for the 14 MT sites used in the 2D Occam inversion (solid symbols) across the GD-FFB segment of the THOT superimposed with modeled responses (solid lines) for a frequency range from 100 to 0.0005 Hz.

Overall, the data and model overlap fairly well in the frequency range from 1 to 10^{-2} Hz for both TE and TM modes and the best fitted data occurs for sites M21 to M18. The response from sites M25 to M22 data is the next best fit and the sites on the eastern half of the profile (M16 to M46) have the worst model fits to the data. Site M15 and M11 data was significantly edited due to noise problems and the overall noise level was more significant at the east sites. This may partially explain the poorer model-to-data fits for these sites.

The inversion model presented here represents a preliminary result and is meant to be used to describe the gross scale conductivity structure of the region. Future refinement of the model could include: i) reduction of phase errors for sites M25, M24, M22, M21, M19 and M18 at frequencies from 1 to 10^2 Hz, for improved resolution on the upper crustal conductivity; ii) separation of apparent resistivity curves at site M19 for frequencies <0.01 Hz suggests the influence of some structure not yet accounted for in the model, therefore a reduction in apparent resistivity errors may aid in fitting these data; iii) in general the data fits for the sites east of the TFZ (sites M15 to M46) is poor and more emphasis on the fitting of the tipper data may be warranted.

It should be noted that two additional 2-D inversions were performed on this data set. An inversion excluding the tipper data fit the responses to a similar degree as that described above. However, the model was more smoothly varying laterally and lacked the details in spatial information in the upper-mid to lower crust as seen in the model including the tipper data. An additional inversion including the tipper data but

with different error levels was also performed on this data set. The phase errors were set to +/- 2.0^0 while the apparent resistivity and tipper errors remained at +/- 0.34 and +/-0.05. The regularization grid was also further discretized laterally in the 20-40 km range in this model. The resulting model was very similar to that in figure 5.7 with a slight overall upward shift in apparent resistivity. The phase curves were fit slightly better with the observed responses, however, the tipper data were poorly fit with this subsequent model. It is for this reason, and the fact that the models were quite similar, that the model as presented in figure 5.7 is used.

5.5.4 Consideration of the Final Models

Since it is important to concentrate on the results associated with frequencies <1 Hz the model will be described emphasizing those features below 5 km. The influence of the TFZ, HLB and SWT (sites M18 to M13) is clearly seen in these results. In particular the site on the TFZ (M15) is flanked by resistive blocks. These blocks extend to ~17 km under sites M18 and M16 and 20-25 km under site M13. The data collected at site M15 indicates low resistivity material in the 5 to 12 km range and that collected near the SWT (sites M12 and M11) indicate low resistivity material from surface to great depth with an easterly dip. Low resistivity (<1000 Ω.m) features can be seen at 20 km and 10 km depth at the west and east ends of the profile respectively. The upper and mid crust on the west end of the profile exhibit moderate resistivities (1000-5000 Ω.m). The low resistivity block extending from the surface

to lower crustal depth on the eastern end of the profile (site M12 to M46) correlates with the western edge of the FFB.

The overall results of the 1-D and preliminary 2-D inversions indicate that a fairly complex geoelectric structure exists within the crust while suggesting a regional easterly dip to the rock units. A zone of resistive material (1000-10000 Ω.m) extends from the upper-middle crust (5-20 km depth) beneath sites M25 to M19 to lower crustal depths in the central part of the profile. A zone of high resistivity material (5000 to >10000 Ω.m) exists beneath sites M18 and M16, as well as beneath site M13 from shallow to mid crustal depths. An abrupt transition to low resistivity material (20-400 Ω.m) occurs at site M12. This zone extends to middle and lower crustal depths beneath M11 and M46 with an easterly dip.

5.6 Inverse Modelling of the Responses for the TFZ to SWT

5.6.1 Purpose

The purpose of this section is to report on the modelling of the general characteristics of the upper to lower crustal structure in the vicinity of the TFZ-HLB-SWT area and to investigate the sensitivity of the MT observations to the presence of a large regional fault system, the TFZ. These goals are achieved using the 2-D inverse modelling of five MT sites crossing the region with due consideration of the data resolution.

5.6.2 2-D Inverse Modelling

The model for the TFZ-HLB-SWT area was based on the inversion of GB corrected data for the frequency range 5000 to 0.05 Hz from five MT sites (M18 to M12) and two LiMS sites (DTH009 and DTH007). The impedance decomposition results suggest a strike direction of 0^0 so modelling was performed with sites projected onto a line oriented at 90^0 E. Simultaneous inversion of the apparent resistivity, phase and tipper data of both TE and TM polarization modes was performed. Error estimates on the data were set to +/- 0.34 log units for the apparent resistivity (to accommodate to some degree for static shift effects), +/- 2.0^0 for the phase data and +/- 0.05 for the tipper. The LiMS site data were included to provide more reliable transfer function responses below 10^{-1} Hz and the confidence levels in the apparent resistivity and phase data for these sites (DTH009 and DTH007) was set accordingly with increased error levels. The frequency coverage from 10^3 to 10^{-2} Hz was achieved using 13 modelling frequencies corresponding exactly to those in the observed data. The inversion was based on a FE mesh containing146x41 elements and a 1000 Ω.m half-space starting model. The inversion terminated after four iterations with a final RMS fit of 5.41.

The resulting Occam model and a comparison of apparent resistivity, phase and tipper curve fits are shown in figure 5.11, 5.12 and 5.13. In general the TE data are fit a little better than the TM data and the phase curves are fit better than the apparent resistivity curves. The fits are closest in the 10^{-1} to 10^2 Hz range. Sites M13 and

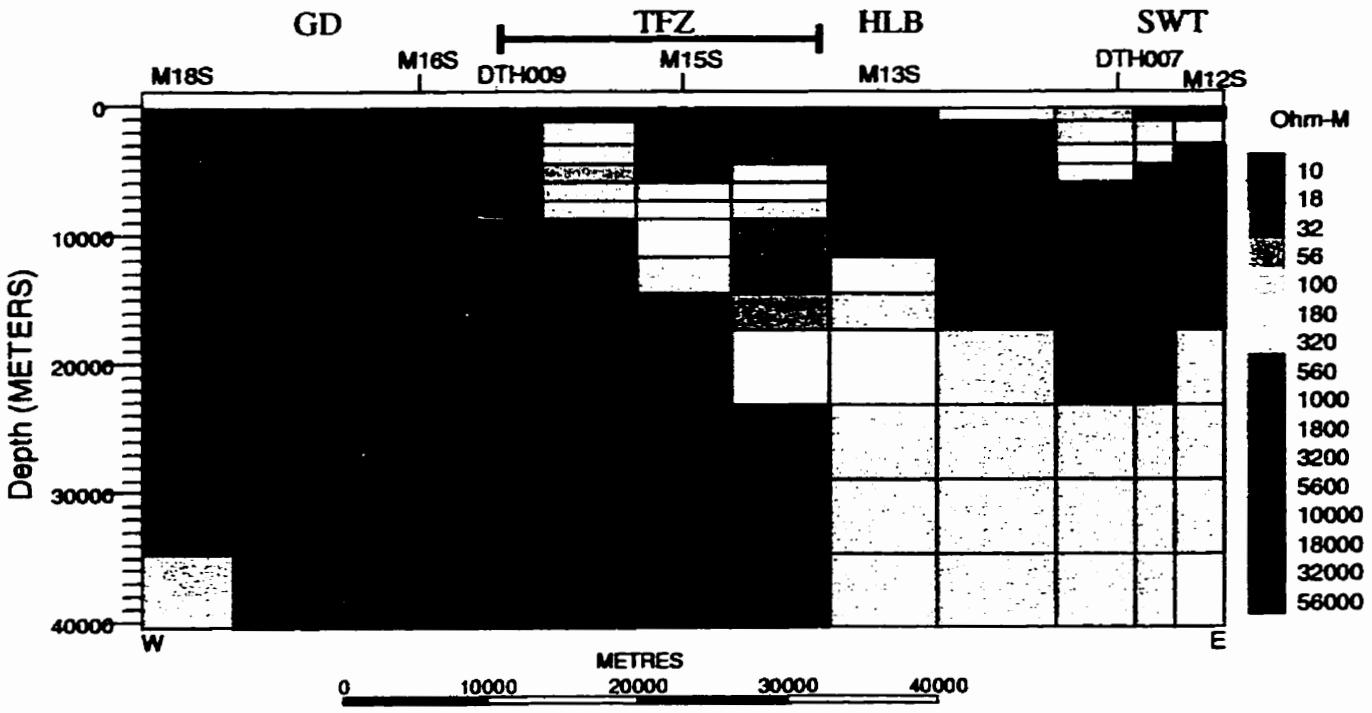

Figure 5.11 2D Occam inversion results for 7 MT/LiMS sites across the TFZ-HLB segment of the THOT transect. A linear depth resistivity section is shown after 4 iterations.

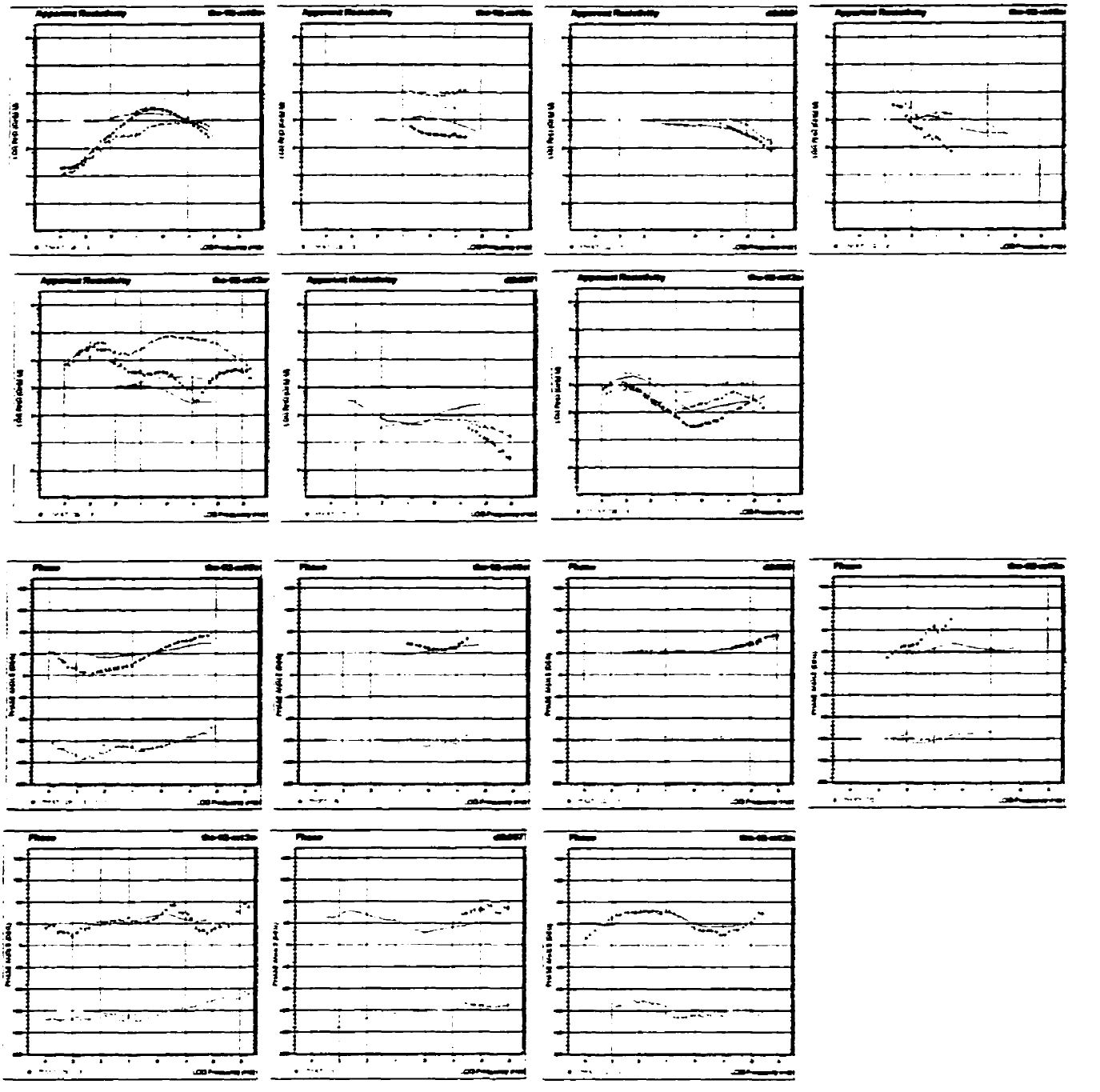

Figure 5.12 Individual TE and TM apparent resistivity and Phase curves used in the 2D Occam inversion (solid lines) across the TFZ-SWT area, superimposed with the modeled responses (solid lines) for a frequency range of 1000 to 0.01 Hz.

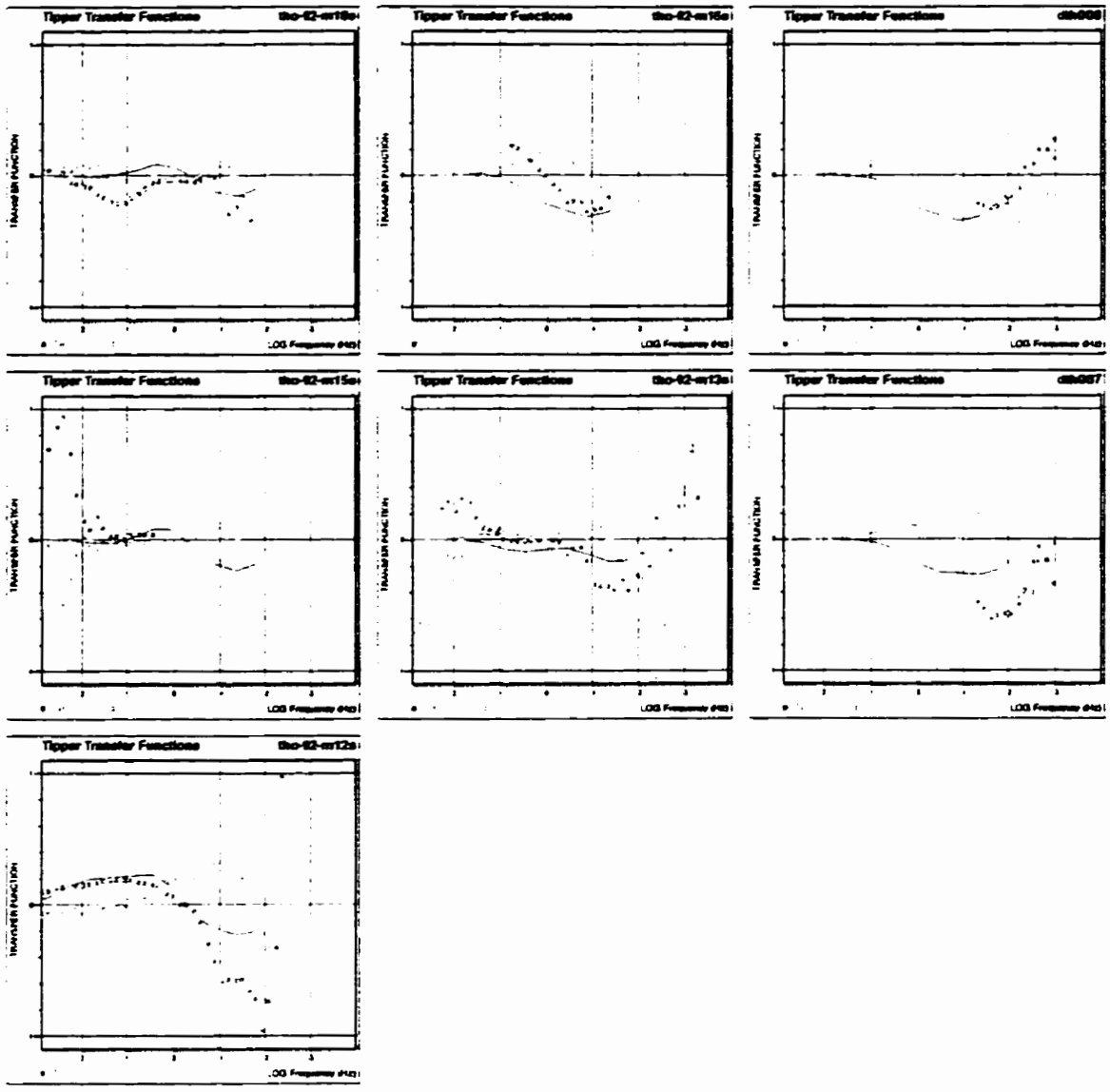

Figure 5.13 Individual TE and TM tipper data curves used in the 2D Occam inversion (solid symbols) across the TFZ-HLB area, superimposed with the modelled responses (solid lines) for a frequency range of 1000 to 0.01 Hz.

M12 have the best overall fit to the data across the frequency range modeled. Data at frequencies higher than 10 Hz is not fit well for site M18. The fact that the site M15 data included only frequencies from 1 to 10^3 Hz must be taken into consideration when assessing the geological implications of the TFZ-HLB-SWT model.. The severe editing of the data from sites M16 and M15 also diminishes the reliability and interpretability of the results from these sites. The tipper data-to-model fits is better than the apparent resistivity and phase fits for all of the MT sites at frequencies greater than 10^{-1} Hz. All components for site M12 are very well fit which provides increased confidence in the inversion result near that site.

The inversion model presented here represents a preliminary result and is meant to be used to describe the gross scale conductivity structure across the TFZ-HLB-SWT region. Future refinement of the model could include: i) reduction of phase errors for site M18 at frequencies from 1 to 10^2 Hz, for improved resolution on the upper crustal conductivity due to the fact that a higher resistivity feature is indicated in the shallow crust below this site and site M16 ii) reduction of the phase errors for frequencies above 1 Hz for the TE data for site M15 to better resolve the resistivity structure in the near surface (<10 km) of the TFZ.

5.6.3 Consideration of the Final Models

The influence of the TFZ is clearly seen in the model. There is good evidence that an east dipping conductive structure (< 200 Ω.m) extends from surface near site DTH009 to possibly 15 km beneath site M13. As in the previous 2-D inversion

results the site on the TFZ (M15) is flanked by resistive blocks extending from 5 to 20 km to the west beneath sites M18 and M16 and from surface to 12 km in the east below site M13 (the HLB). As in the previous 2-D inversion result, the crust beneath site M15 includes a low resistivity feature (20 - 200 Ω.m) at upper-middle to mid crustal depths (8-25 km), however the resistive material below site M13 extended to 25 km in the previous model (figure 5.7). Part of the reason for this difference may be seen in the fits to the data (figures 5.12 and 5.13) which indicates an improved data fit to the TE phase and tipper data for the 2-D inversion of the five TFZ-HLB SWT sites. The difference in the strike direction used in the modelling will also contribute to the difference between the previous and present 2-D inversion models. Unfortunately the low frequency data for site M15 was poor so model characteristics at greater than 20 km beneath site M15 are poorly resolved. The influence of the SWT is indicated from the 2-D inversion in the near surface at sites DTH007 and M12.

The low resistivity zone defined in the upper and mid crust at the TFZ (M15) is fairly well resolved laterally but perhaps not vertically. A sensitivity analysis was performed on the inversion model to assess the resolution of the low resistivity feature beneath site M15. The model from the 2-D Occam inversion (figure 5.11) was modified such that the low resistivity blocks in the central part of the profile were reset to 1000 Ω.m, keeping all other features as shown in figure 5.11. The response of the model was then computed using Wannamaker et al's (1984) code and compared with the observed responses and the Occam inversion model responses

shown in figure 5.12. In this case the forward modelling results showed that for sites M15, M13 and M12 the TE and TM phase curves for the modified model differed from the inversion model response at frequencies between 10^2 and 0.1 Hz. This exercise showed that the area of low resistivity in the crust under site M15 and extending towards M12 was needed to fit the data at these frequencies. It helped build confidence in the validity of the crustal structure resulting from the 2-D Occam inversion.

Finally a comment can be made about the resolution of the SWT from these data sets. In figure 5.11 the SWT appears as a low resistivity (<1000 Ω.m) zone in the upper 10 km, at the east end of the model. In figure 5.7 the SWT appears to have significantly more vertical extent, well into the mid-lower crust. The difference here is the bandwidth of data fit and the accuracy of the fit between the two models. In figure 5.7 the data below 10 Hz is preferentially fit causing increasing conductivity at depth to be emphasized in the model. In figure 5.11 the high frequency phase increase for site M12 is fit better resulting in a shallower conductive feature in the resulting model.

5.7 2-D Modelling of the GB-FFB Structure From Seismic and MT Results

5.7.1 Purpose and Justification

The geological interpretation of the GD-FFB seismic reflection profile, line 9, (see section 3.2.1) provides information by which to constrain modelling of the MT data. The seismic data can be used to verify the existence of the structures determined

from the MT data. Up to this point the results of the 2-D inversion modelling are those that best fit to the data. However, the Occam models are smoothed models that include only minimum structure and may not be reasonable geological models. A forward modelling approach allows for the inclusion of seismic and geological constraints while fitting the observed data. Whereas the optimal way to incorporate these data is through constrained inversion the forward modelling study reported below was performed during preliminary analysis prior to the tensor decomposition and inversion study. The forward modelling was based on the determinant response and will provide inferior resolution to an analysis based on both TE and TM data so it is recommended that constrained inversion be performed in the future.

5.7.2 2-D Forward Modelling

The preliminary 2-D forward modelling of the MT data was based on fitting the determinant response using the models constrained by the seismic reflection results. The 2-D modelling was undertaken using the PWD2D code (Wannamaker et al, 1984) as implemented in GEOTOOLS. A comparison of the results of the seismically-constrained forward modelling and the unconstrained inversion results permits an assessment of the resolution of the MT results. It also provides an indirect comparison of the MT and seismic results.

The first model (not shown) examined in the preliminary 2-D model was a simple representation of the seismic reflection data. It contained an easterly dipping zone of resistive (1000-5000 Ω.m), upper crustal rocks overlying increasingly more

conductive (100-500 Ω.m) mid to lower crustal rocks. The HLB-FFB region was represented with a highly resistive block (>10000 Ω.m) extending to mid crustal depths (15 km). The Phanerozoic cover in the western part of the model is represented by a thin layer (~300 m) of conductive material (<100 Ω.m). and the entire model was underlain by conductive (<50 Ω.m) mantle. The resulting forward model showed a significant contribution of the Phanerozoic material on the western section of the transect to the high frequency responses. At the lowest frequencies, all sites show a dramatic decrease in resistivity with corresponding inferred increased conductivity in the upper mantle. There was a moderate correlation of the broad scale features in the modeled results and the observed responses, indicating that this model represented a good first order fit of the observed data. However, detailed inspection revealed that a more complex model better fit both the small and some of the broad scale variations in the observed response.

Subsequent modelling employed a more complicated resistivity structure that was developed to represent better the features of the upper to mid-lower crust and the TFZ-SWT regions in particular. Figure 5.14 shows the revised 2-D model developed to simulate the observed responses based not only on the seismic data but also on the major transitions observed in the spatial MT responses. In this model the upper crust conductivity in the west part of the profile has been slightly increased while the mid to lower crust conductivity has been decreased. The area of the TFZ-HLB-SWT has become more detailed with representations of low resistivity areas for the TFZ and SWT and a highly resistive block for the HLB. A low resistivity zone has been added

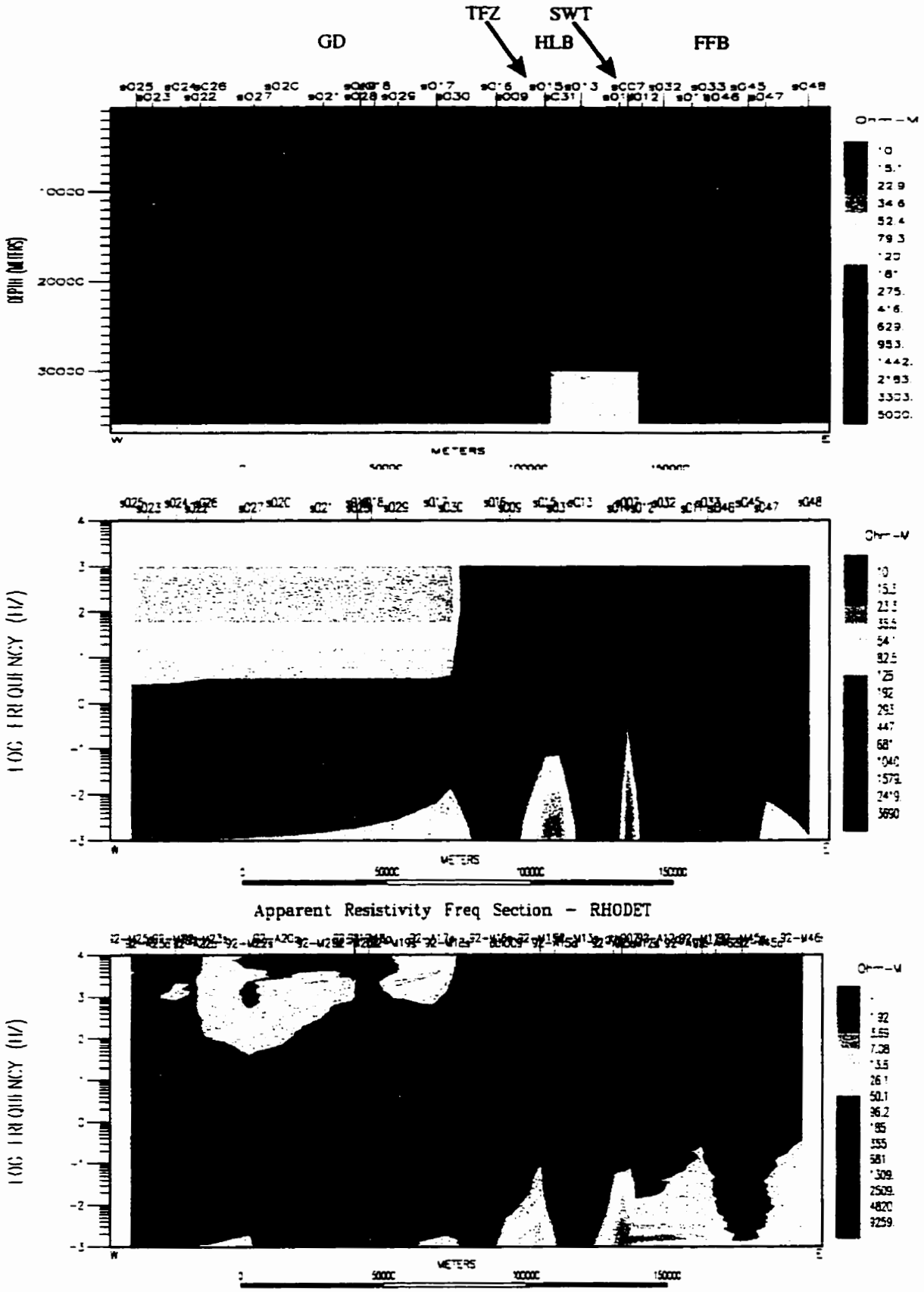

Figure 5.14 A 2-D forward model based on a detailed representation of upper to mid-lower crustal features of the seismic and MT data. The apparent resistivity pseudosection of the modeled response is shown along with the determinant apparent resistivity pseudosection for the entire GD-FFB segment from the observed data.

to the lower crust in the east of the profile but overall the model maintains the easterly dipping broad scale structure shown in the seismic section. The resulting determinant apparent resistivity pseudosection shown in figure 5.14 provides an improvement in the fit to the observed determinant data over the previous models. A comparison of the modeled and observed pseudosection data shows that:

1) the high frequency response of sites on the Phanerozoic cover is clearly modeled,

2) model apparent resistivities for frequencies between 10 and 10^{-3} Hz at sites M25 through M18 have a similar form to the observed values suggesting the crustal structure has been modeled quite well (close examination shows the model responses are less resistive than the observed responses),

3) the model pseudosection form and apparent resistivity values beneath sites M18 to M12, spanning the TFZ-HLB-SWT area, are comparable to the observed response across the whole frequency range; the signature of the TFZ, HLB and SWT is clearly observed in the model and observed data,

4) the high frequency model responses (10 to 10^{3} Hz) for sites in the eastern part of the transect (M12 to M46) match well with observed responses (close inspection shows that the low frequency model responses are more resistive than the observed responses in this part of the profile).

5.8 Comparison of the Seismically Constrained 2-D Forward Model and the 2-D Inversion Model

It is appropriate at this time to compare the seismically constrained 2-D forward model and the 2-D inversion model results. Figure 5.15 shows the 2-D inversion model superimposed on the seismic reflection data. The following differences between the forward model (Figure 5.14) and inversion model (Figure 5.15) can be noted:

1) the east end of the inversion model contains low resistivity (< 200 Ω.m) material at lower crustal depth (20-40 km),

2) the inversion model includes higher crustal resistivity between the east GD and HLB areas (sites M18 to M13),

3) the inversion model includes lower upper crustal resistivity associated with the FFB. The difference between the model and the observed responses in figure 5.14 supports this result,

4) the inversion model provides improved resolution of the TFZ, HLB, SWT and includes a resistive root to the HLB extending to 20 km depth.

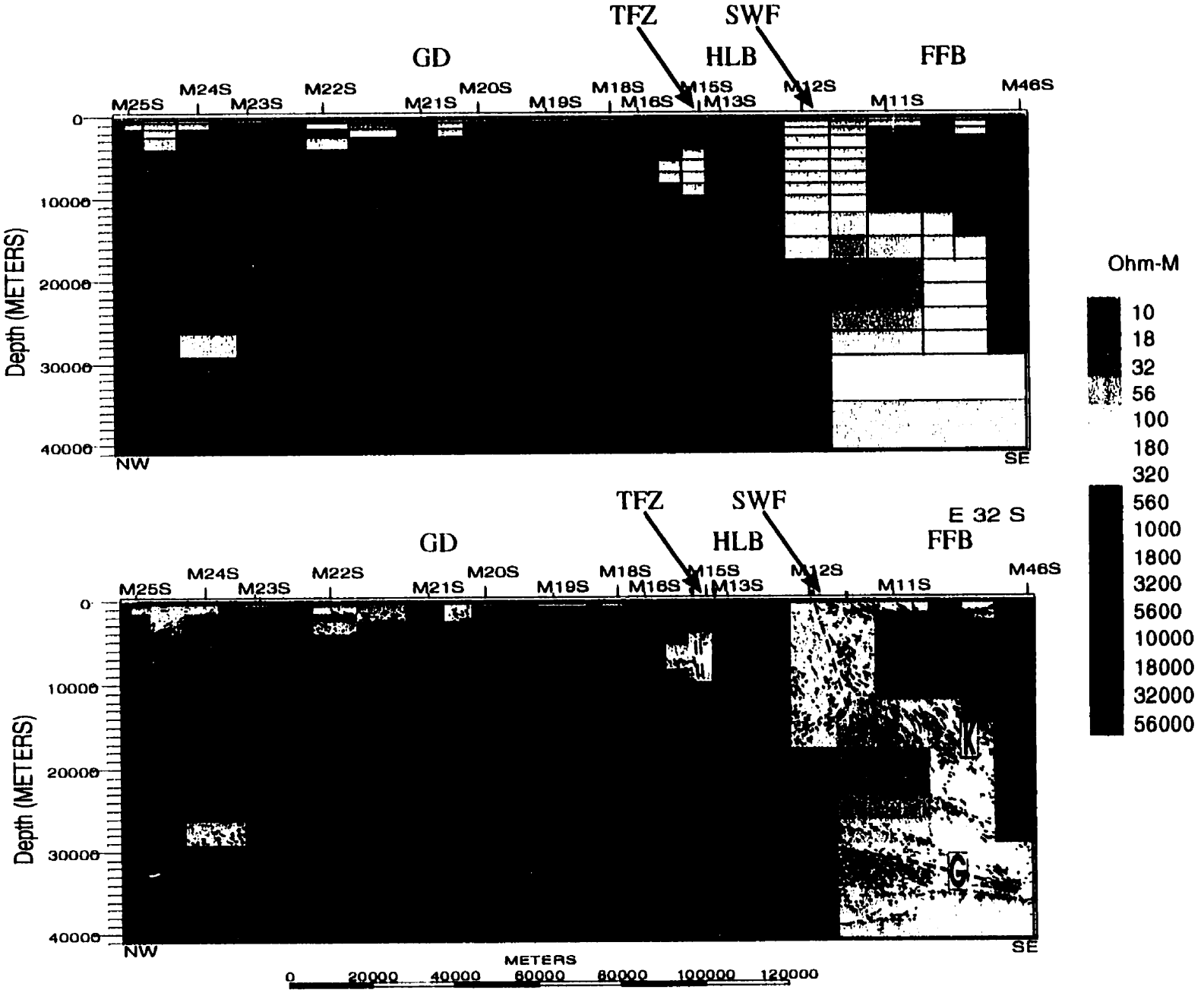

Figure 5.15 A direct comparison of the seismic reflection data with the 2D Occam inversion results for the GD-FFB segment of the THOT.

CHAPTER 6

GEOLOGICAL INTERPRETATION OF THE MT RESULTS

6.1 Indications for the Regional Conductivity Structure From the MT Data

6.1.1 Phanerozoic Results

The MT data indicates that the Phanerozoic cover is 200 to 300 m thick from site A24 to M18, thinning to the east. Modeled results (figures 5.1 and 5.2) suggest that the resistivity of this cover ranges from ~50 to 200 Ω.m and that the cover is slightly more conductive (~20-50 Ω.m) and thicker (>300 m) in the vicinity of sites M23 through A20.

The 1-D nature and unique geoelectric characteristics (i.e. low resistivity and low galvanic distortion) of the Phanerozoic cover with respect to the general geoelectric structure of the crust as a whole, have given rise to a good estimate of thickness and resistivity of the Phanerozoic units encountered in the western portion of the GD-FFB MT segment. Communications with personnel from the Manitoba Energy and Mines department (Ruth Bezys, pers. com., 1998) indicate that the thicknesses of the Phanerozoic cover derived from the MT analysis are consistent with that determined from stratigraphic well-logging programs in the area.

6.1.2 Precambrian Results

Deep seated features located on the west part of the segment beneath the Phanerozoic cover (figure 5.15) include a low resistivity zone (200 to 1000 Ω.m) extending from the mid to lower crust depths (> 20 km) beneath sites M25 and M24, and a relatively resistive zone (>500-5000 Ω.m) extending from 5 to 30 km depth beneath sites M22 through M19.

In the area of sites M18 to M12, where the surface geology shows a transition from Phanerozoic cover overlying the GD to the Precambrian rocks of the HLB and FFB the surface resistivity increases significantly. The effects of the TFZ and SWT are evident as low resistivity (<1000 Ω.m) features extending to ~15 km depth (figure 5.11 and 5.15). A high resistivity zone (1000-10000 Ω.m) extends to ~15-20 km depth beneath site M13 (located on the HLB) and is bounded to the east by the SWT.

In the eastern portion of the GD-FFB segment the crustal structure has relatively low resistivity (< 2000 Ω.m). The resistivity is especially low in the shallow (<10 km) and deep (>30 km) where it decreases to values well below 1000 Ω.m.

6.2 Resolvable Seismic/Geological Features From the MT Data

From the MT response analysis performed in chapter 4, it is noted that the overall trend of the geoelectric strike across the study area is north to NNE which is consistent with large scale trends in the surface geology and potential field data. The detailed analysis and inversion of the low frequency MT data from 14 sites across the

GD-FFB segment of the THOT profile, and the five sites straddling the TFZ-HLB-SWT, have revealed a variety of geoelectric structures spanning various crustal depths.

At this point it is appropriate to perform a more detailed comparison of the seismic data and the MT results. Figure 6.1 shows the migrated seismic reflection section along line 9, along with the geological. Also illustrated in figure 6.1 is the result of the 2-D Occam inversion of 14 MT sites across the GD-FFB transect (as shown in figure 5.7). It is plotted in the same spatial location as the seismic data. The high frequency apparent resistivity response due to the Phanerozoic cover at the west end of the GD-FFB segment is not well represented since the model included only those data up to 10^2 Hz. Figure 6.2 provides a more detailed comparison of the seismic and MT results.

As discussed in Chapter 3, Lewry et al. (1994) suggest that the seismic data shows a crustal scale culmination underlying the sub-Phanerozoic extension of the western GD and apparently coinciding with the extrapolated crest of the Nunn Lake antiform (figure 3.2). The crest of the culmination would correlate with imbricated juvenile arc rocks (Proterozoic), and the core of the culmination is believed to be composed of Archean basement. The location of the Proterozoic (arc volcanic) to Archean contact is interpreted to lie along reflector F. A comparison of the MT and seismic results (figure 6.2) suggests relatively low resistivity material (<500 Ω.m) occurs in the top few kilometres, above this culmination, and more resistive material (>500 Ω.m) in the upper crust beneath it. The resistivity is very low (100 - 500 Ω.m)

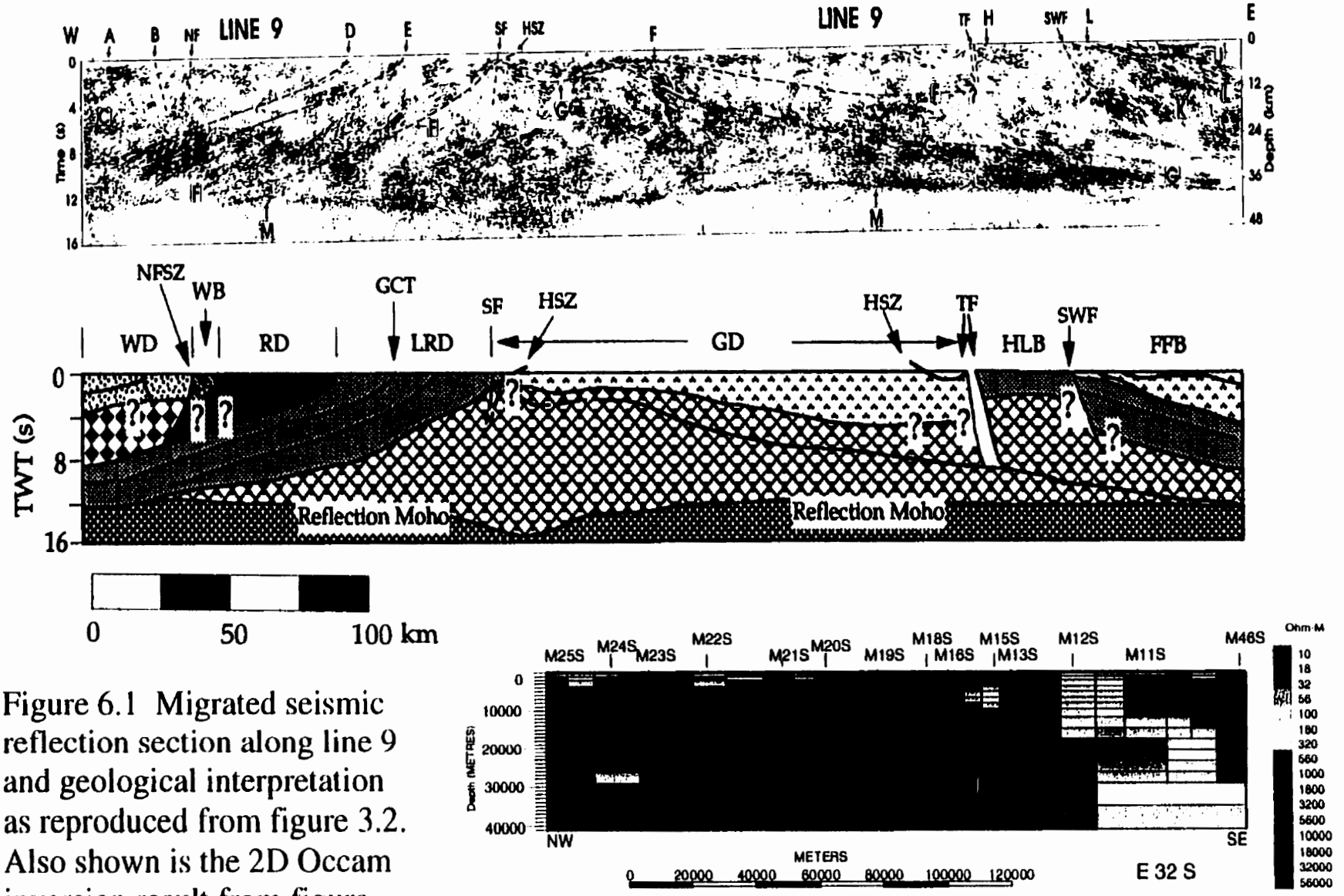

Figure 6.1 Migrated seismic reflection section along line 9 and geological interpretation as reproduced from figure 3.2. Also shown is the 2D Occam inversion result from figure 5.7.

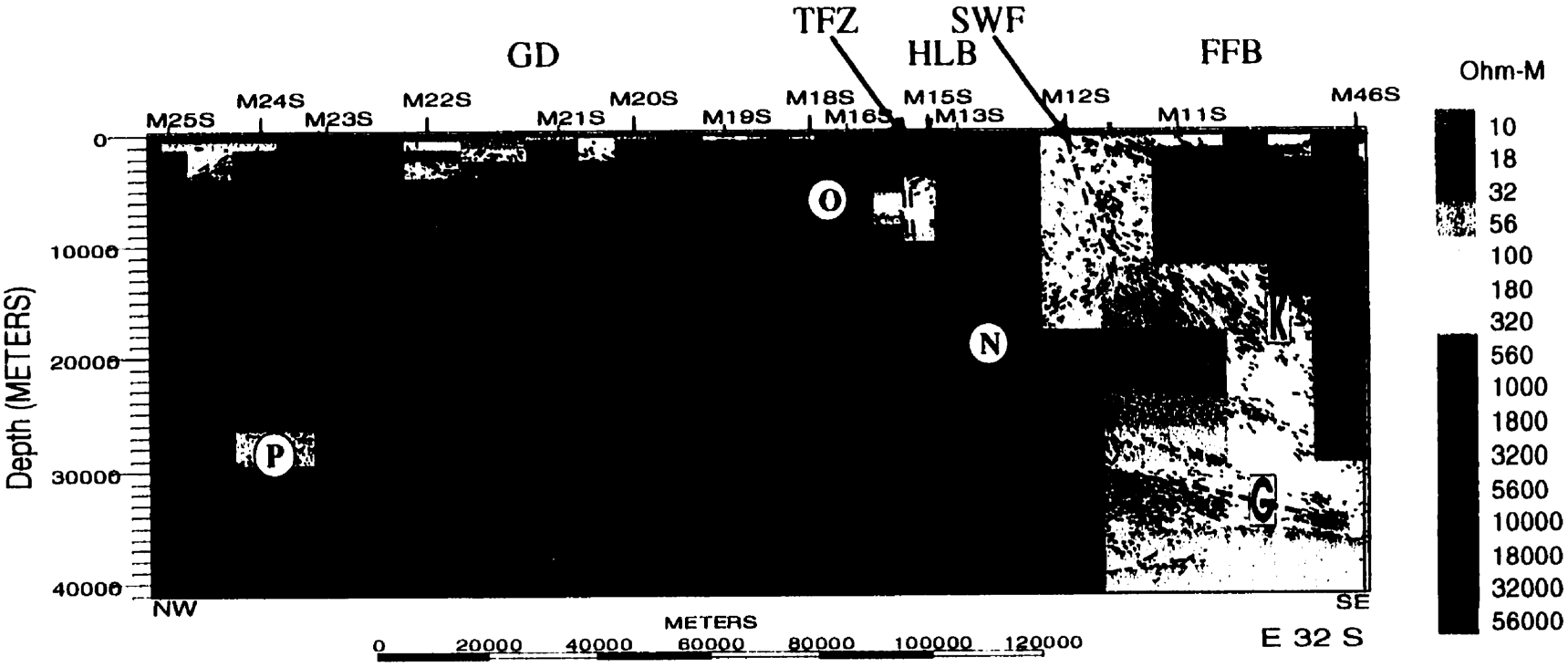

Figure 6.2 Final GD-FFB MT resistivity structure section superimposed with seismic data from line 9. Features N, O and P represent additional structures indicated by the MT results.

in the mid to lower crust, beneath M24 and M25, corresponding to crust beneath the culmination . It should be noted that the effect of the NACP has not been factored into the analysis or this interpretation and lowered resistivities at the far west end of the GD-FFB MT segment may include contributions from this feature (e.g. Jones et al., 1993).

Significant upper-crustal resistivity structure is evident in the vicinity of site M22 where the seismic data do not provide any indication of major structures. However, the seismic results do show some near-surface (0-5 km) reflectivity in this area. The reflectivity is moderately continuous but with variable dip. In addition there are west dipping deeper reflections in the Archean root (west of site M24) that can be extrapolated up-dip to the area of M22. The Archean-Proterozoic contact (F) dips east to upper-mid-crustal depths and cannot be reliably extrapolated past the TFZ with the seismic data. The geoelectric models show that both the Proterozoic and Archean material is relatively resistive to the west of the TFZ (figure 6.2). The models also show that the most resistive Archean material is mapped to the east and west of the TFZ. It appears that overall the resolvability of the Archean-Proterozoic contact (F) from the MT data is weak at best. This result is due to the fact that in general EM methods provide low resolution of resistive features. However, there is a subtle indication of an easterly dip of the upper to mid crustal resistivity structure supporting the eastward dip included in the seismic interpretation.

The TFZ-SWT region of the transect represents the most poorly resolved area in terms of direct seismic detection (Hajnal et al., 1996). Reflectors within the HLB

have been interpreted to represent southeast dipping arc derived gneisses, underlain at 10 km depth by Archean basement. Both the TFZ and the SWT are imaged only indirectly in the seismic data as prominent, steeply dipping zones of seismic 'transparency' (i.e. absence of seismic reflections) and truncation of reflections (Hajnal et al., 1996). The SWT and TFZ have been interpreted to extend to depths of 15 and 30 km respectively based on the seismic interpretation.

The MT data for the TFZ-SWT region would appear to offer more direct evidence for the depth extent and orientation of these structures. The MT data seem to clearly detect the TFZ and SWT as low to moderately resistive (100-1000 Ω.m), steeply east dipping features (figure 6.2). At the surface, the TFZ clearly separates two highly resistive zones extending to 10-15 km depth where the feature becomes obscured by a zone of moderate resistivity. The SWT is sub vertical to steeply east dipping and appears to extend to the lower crust. The HLB is resolvable as a resistive block (1000-10000 Ω.m) from the surface to at least 15 km depth. The MT results confirm that the TFZ forms the western margin of the HLB. The lower part of the HLB is less resistive than near surface (<1000 Ω.m) but the MT data suggests that deepest portion of the HLB root may extend to 20 km. These data suggest that a steeply dipping structural discontinuity may exist in the mid crust regions below the TFZ-HLB-SWT area (N, figure 6.2).

Just west of the TFZ there is a geoelectric feature that does not appear to have a corresponding seismic character (O, figure 6.2), unless it is a lack of seismic reflectivity. This feature is the highly resistive block located below sites M18 to M15

that extends to ~ 15 km depth, in the vicinity of the Proterozoic-Archean contact. The nature of this feature is unknown, however, this feature could represent an upthrusted piece of resistive Archean material buried under the Phanerozoic cover, and would offset the interpreted position of the Archean-Proterozoic contact as well as introduce a presently unknown fault feature (see figure 6.2).

East of the SWT the upper, mid-and lower crustal material become less resistive ((typically <500 Ω.m). The upper crustal rocks are of low resistivity (<300 Ω.m). The appearance of these low resistivity rocks correlates well with the surface occurrence of the thrust-imbricated juvenile rocks of the Flin Flon Belt (J, figure 6.2). The MT results suggest an easterly dip with increasing resistivity to depth where the interpretation of the seismic data indicates that the FFB rocks are underlain by more uniformly reflective domains (K), the uppermost part of which projects up-dip to arc plutonic orthogneisses and subordinate supracrustal rocks in the vicinity of the SWT (Lewry et al., 1994). These two packages of reflections are separated by a well defined zone of reflections (L) interpreted as a major structural detachment. This zone falls roughly on the transition to more resistive material in the MT data although not as nearly well defined as in the seismic image.

The Moho transition (M) is not well resolved from this model.

6.3 The Results of the MT Survey and Other Geophysical Interpretations

At this point it is interesting to reexamine the gravity and aeromagnetic data for the GD-FFB segment of the THOT to identify correlations with the MT results. The

gravity and magnetic data are described in Chapter 3 with relevant data plotted in figure 3.1.

Linear gravity and magnetic lows occur near the west end of the MT study area at the Stanley Shear Zone. This location is just west of the crustal-scale Glennie culmination where the Archean-Proterozoic contact lies within a few kilometres of the surface. To the east in the Glennie Domain, the gravity and magnetic signatures increase to positive anomalies. These anomalies coincide with the thickening of the Proterozoic rocks, indicated in the seismic data. The MT profile starts to the east of the Stanley Fault (figure 6.1) so the resistivity structure of this feature was not defined in this study. As mentioned above, the MT results suggest there is an eastward thickening of less resistive shallow crustal rocks that correlates with the seismic reflection data and the positive magnetic and gravity anomalies. All of these data are consistent with the interpretation suggesting an eastward increase in the thickness of mafic volcanic Proterozoic rocks extending as far east as the TFZ. It is interesting to note that the low resistivity material (<200 Ω.m) in the top few kilometres of the crust beneath site M22 correlates well with an anomalous positive gravity region and increasing magnetic response.

The TFZ and the SWT have prominent magnetic and gravity lows associated with them. The form of these anomalies support both the seismic and MT indications of steep easterly dips. No depth extents can be extracted reliably from the gravity or magnetic data (Thomas, 1994).

To the east end of the GD-FFB segment the gravity field decrease sharply over the FFB whereas the magnetic signature exhibits slightly negative to neutral fields (characteristic of greenstone terrains). These potential field results are coincident with a sharp decrease in resistivity exhibited in the MT data.

CHAPTER 7

CONCLUSIONS

7.1 Data Quality and Decomposition Analysis of the MT Data for the GD-FFB

Analysis of the GD-FFB MT data commenced with a review of the data quality. As discussed in section 4.4.1, unreliable data, based on relative error bars and low SNR, are primarily restricted to the 10^3 - 10^4 Hz range and the 10^{-3} - 10^{-4} Hz range. This result is especially shown by the apparent resistivity plots. In general, the magnetic components are noisier than the telluric responses in these frequency ranges. From an examination of the data from all the sites it is concluded that the most reliable data lie in the range 10^3 Hz to 10^{-3} Hz.

The data from each site were analysed using Groom-Bailey decomposition methods and were used to determine the best geoelectric strike for 2-D interpretation. The decomposed data were then grouped into separate site and frequency sets possessing common quasi-2-D response. This step was then followed by static shift correction. This analysis produced corrected TE and TM impedance data for each data set.

The analysis of the GD-FFB MT data allowed the division of the data into three distinct subsets: i) the AMT data (>10 Hz) collected over the Phanerozoic cover, ii) the low frequency MT data (<0.1 Hz) along the whole GD-FFB transect and iii) the AMT/MT data (10^3 to 10^{-2} Hz) for the region straddling the TFZ-HLB-SWT. This division of data was necessary due to the complexity of the data, including the spatial

and frequency variation of the dimensionality and geoelectric strike. The approach has yielded good spatial information about the conductivity characteristics between the surface and the lower crust.

7.2 Features Recovered From 1-D MT Data Subsets

One and two dimensional analysis of the high frequency response from the 14 sites over the Phanerozoic cover reveals similar features. The high frequency responses are primarily a result of contributions from the near-surface Phanerozoic cover, but they also indicate lateral conductivity variations in the upper crust (<10 km) of the Glennie Domain. Some general observations and implications of this data analysis include:

1) The conductive Phanerozoic units are generally 200-300 m thick with a typical resistivity of 50-200 Ω.m and thin to the east.

2) Underlying upper crustal units of the Glennie Domain exhibit high resistivity (>1000 Ω.m).

3) There is a distinct region of lower resistivity in the upper crust below sites M23 to M22.

7.3 Characteristics of and Features Recovered From the Other MT Data Subsets

The detailed analysis and inversion of the low frequency MT data from 14 sites across the GD-FFB segment of the THOT profile and those five sites straddling the

TFZ-HLB-SWT have revealed complex response characteristics and a variety of geoelectric structures spanning various crustal depths. These response characteristics include:

1) High galvanic distortion of the MT response at sites located on Precambrian rocks. This distortion meant careful tensor decomposition was necessary to recover the regional 2-D impedances required for inversion and interpretation of the data. The tensor decomposition resulted in the data being divided into two subsets for interpretation: i) The response for all sites for frequencies <0.1 Hz and ii) the TFZ-SWT sites, for frequencies 10^{3} to 10^{-2} Hz.

2) For the low frequency data set, the best estimate of the regional geoelectric strike direction is 30° to 35° N, whereas in the TFZ-SWT region the strike is between 0° to 5° N.

3) The decomposed data were static shifted such that the TE and TM modes coalesced at high frequency. The apparent resistivity values at the lowest frequencies (< 0.001 Hz), of the TE mode, were set to 50 Ω.m (which represents an approximate mean upper mantle value). The TM mode was then shifted by the same correction factor.

4) 2-D apparent resistivity and phase pseudo-sections and stitched 1-D inversion models exhibited similar geoelectric structures in both TE and TM polarization modes.

Two-dimensional inversion of the data was performed using the Occam 2-D inversion algorithm (inclusion of the static shifts was prohibited by the GEOTOOLS

implementation of the inversion code). Selective 2-D forward modelling was performed to assess the sensitivity of certain responses to a particular model feature. Geological features recovered from the MT data through modelling, inversion and comparison with the seismic and other geophysical results are:

1) The location of the Proterozoic (arc volcanic) to Archean contact is interpreted to lie along sesimic reflector F. An interpretation of the MT data (figure 6.2) indicate relatively low resistivity material (<500 Ω.m) in the top few kilometres above this contact. Low resistivity material (~200-1000 Ω.m) is indicated from mid-to lower crust at the western most sites extending east to the mid GD region. Geoelectric characteristics above this inferred contact, from the MT data, indicate that the Proterozoic and Archean material become increasingly more resistive to the east and to depth (500 - 5000 Ω.m).

2) The core of the Archean terrain (below F) also increases in resistivity to the east and the most resistive material is mapped below the region just to the west of the TFZ. Although it appears that the resolvability of the Archean-Proterozoic contact (F) from the MT data is weak at best, there is a subtle indication of easterly dip to the resistivity structure supporting the seismic interpretation.

3) Seismic feature G, interpreted to be a crustal scale detachment fault, is not resolved by the MT data. However, on the west, and more dominantly, on the east end of the profile the deep conductivity structure becomes less resistive (<200 Ω.m) below it.

4) The MT data seem to clearly detect the TFZ and SWT as low to moderately resistive (200-1000 Ω.m), steeply east dipping features. At the surface the TFZ

clearly separates two highly resistive zones extending to 10-12 km depth where the feature becomes obscured by rocks of moderate resistivity. The SWT is sub-vertical to steeply east dipping and appears to extend to the lower crust.

5) The HLB is clearly resolvable from surface to at least 15 km depth. The crust at depths of 15 to 25 km beneath the eastern HLB is less resistive than near surface (<1000 Ω.m). However, some MT model results suggest that the root of the HLB may extend beyond 20 km since a highly resistive feature is present below sites M15 and M13 beginning at this depth.

6) Just west of the TFZ there is a geoelectric feature that does not appear to have a corresponding seismic signature, except perhaps by a lack of seismic reflectors. The geoelectric feature is a highly resistive block below sites M18 to site M16 that extends to ~ 10 km. This depth is interpreted from the seismic results to be the Proterozoic-Archean contact in that area.

7) East of the SWT the MT results indicate the presence of easterly dipping, low resistivity material extending to 30 km below site M11. The resistivity of material at greater than 30 km depth on the east end of the transect is less than 20 Ω.m. The geoelectric strike appears to rotate to an ENE direction at the low frequencies for sites M12 through M46 possibly reflecting this geologic transition.

7.4 Contribution of the MT Survey to the Geological Interpretation of the GD-FFB Region and the LITHOPROBE THOT Objectives

Overall, the AMT/MT soundings along the GD-FFB segment of the THOT support the interpretation made from the seismic data. At the same time, the MT results have shown that the geoelectrical characteristics are not uniform within each package of rocks interpreted from the seismic data. This result is illustrated by the west to east decrease in resistivity observed in the upper crustal material above seismic boundary F and between seismic boundaries F and G and by the low resistivity zone in the upper crust beneath site M22. In addition the MT responses have given information on the TFZ, HLB and SWT which was only indirectly achievable with the seismic data (i.e. the depth extent and steep easterly dip). One of the main objectives of the THOT MT research was to determine the subsurface position and attitude of bounding geological margins (section 1.3). The results described above indicate that the MT data and analysis has contributed to this determination.

REFERENCES

Agarwal, A.K., Poll, H.E., and Weaver, J.T. 1993. One and two-dimensional inversion of MT data in cintinental regions; *Phys. Earth Planet. Inter.*, **81**, 155-176.

Allaart, J.H., 1976. Ketilidian mobile belt in South Greenland; in Escher, A. and Watt, W.S., eds., Geology of Greenland: Geological Survey of Greenland, Copenhagen, 120-151.

Bahr, K., 1988. Interpretation of the magnetotelluric impedance tensor: regional induction and local telluric distortion; *J. Geophys.*, **62**, 119-127.

Berdichevsky, M.N, and Dmtriev, V.I., 1976. Basic principles of interpretation of magnetotelluric sounding curves; in Geoelectric and Geothermal Studies, edited by A. Adam, 165-221, KAPG, Geophys., Monogr., Budapest.

Berdichevsky, M.N. and Dmitrev, V.I., 1976b. Distortion of magnetic and electric fields by near surface lateral inhomogeneities; Acta Geod., *Geophys. Mont. Hung.* 11, 447-483.

Berdichevsky, M.N, Vanyan, L.L. and Dmtriev, V.I., 1989. Methods used in the USSR to reduce near surface inhomogeniety effects on deep MT soundings; *Phys. Earth Planet. Inter.*, **53**., 194-206.

Best, M.E., Duncan, P., Jacobs, F.J., and Scheen, W.L. 1985. Numerical modelling methods of the electromagnetic response of three dimensional conductors in a layered earth; *Geophys.*, **50**, 665-676.

Boerner, D.E., Wright, J.A., Thurlow, J.G., and Reed, L.E., 1993. Tensor CSAMT studies at the Buchans Mine in central Newfoundland; *Geophys.*, **58**, No. 1, 12-19.

Bostick, F.X. 1977. A simple almost exact method of MT analysis; presented at the Workshop on Electrical Methods in Geothermal Exploration, USGS, Contract 14080001-8-359.

Chakridi, R., Chouteau, M. and Mareschal, M. 1992. A simple technique for analysing and partly removing galvanic distortion from the magnetotelluric impedance tensor: application to Abitibi and Kapuskasing data (Canada); *Geophys. J. Int.*, **108**, 917-929.

Chave, A.D. and Smith, J.T., 1994. On electric and magnetic galvanic distortion tensor decompositions; *J. Geophys. Res.*, **99**, 4669-4682.

Chave, A.D., Thomson, D.J., and Ander, M.E. 1987.. On the robust estimation of power spectra, coherences and transfer functions.; *J. Geop. Res.*., **92**, No. B1, 633-648.

Chouteau, M., Krivochieva, S., Castillo, R.R., Moran, T.G., and Jouanne, V.. 1994. Study of the Santa Catarina acquifer aystem (Mexico Basin) using magnetotelluric soundings; *J. App. Geophys*, **31**, 85-106.

Clowes, R.M. (editor)., 1993. LITHOPROBE Phase IV Proposal - Studies of the evolution of a continent; published by the LITHOPROBE Secretariat, The University of British Columbia, Vancouver, B.C. 290 p.

Constable, S.C., Parker, R.L. and Constable, C.G., 1987. Occam's inversion: A practical algorithm for generating smooth models from electromagnetic sounding data; *Geophys.*, **52**., 289-300.

deGroot-Hedlin, C. and Constable, S., 1990. Occam's inversion to generate smooth, two-dimensional models for magnetotelluric data; *Geophys.*, **55**, 1613-1624.

Dobrin, M.B., 1976. Introduction to Geophysical Prospecting.; McGraw-Hill Publishing, 3rd edition, 592-600.

Eggers, D.E., 1982. A eigenstate formulation of the magnetotelluric impedance tensor; *Geophys.*, **47**, 1204-1214.

Ferguson, I.J., 1988. The Tasman Project of Magnetotelluric Exploration; Ph.D. Thesis, Australian National University, Canberra, Australia.

Ferguson, I.J. and Edwards, R.N., 1993. Electromagnetic mode conversion by surface conductivity anomalies: applications for conductivity soundings; *Geophy. J. Int.*, **117**, 48-68.

Ferguson, I.J., Jones, A.G., Sheng, Y., Wu., X., and Shiozaki., I. (in press). Geoelectric response and crustal electrical-conductivity structure of the Flin Flon Belt, Trans-Hudson Orogen, Canada; *Can. J. Earth Sci.*

Geotools Corporation, 1997. Geotools MT Users Guide, 5808 Balcones Drive, Suite 202, Austin, Texas., USA.

Gamble, T.D., Goubou, W.M. and Clark, J., 1979a. Magnetotellurics with a remote reference; *Geophys.*, **44**, 53-68.

Gamble, T.D., Goubou, W.M. and Clark, J., 1979b. Error analysis for remote reference magnetotellurics; *Geophys.*, **44**, 959-968.

Gupta, J.C and Jones, A.G., 1995. Electrical conductivity structure of the Purcell anticlinorium in southeast British Columbia and northwest Montana; *Can. J. Earth Sci.*, **32**, 1564-1583.

Grant, N., 1997. Processing, interpretation and databasing of magnetotelluric data from the Trans Hudson Orogen: site by site and multi-site, multi-frequency Groom-Bailey decompositions; in LITHOPROBE, Trans-Hudson Orogen Transect, report number 62 of sixth transect workshop, 62-105.

Green, A.H.., Hajnal, Z. and Weber, W., 1985a. An evolutionary model of the western Churchill Province and western margin of the Superior Province in Canada and north central United States; *Tectonophysics*, **116**, 281-322.

Groom, R.W., and Bailey, R.C., 1989. Decomposition of magnetotelluric impedance tensors in the presence of local three-dimensional galvanic distortion; *J. Geophy. Res.*, **94**, 1913-1925.

Groom, R.W., and Bailey, R.C., 1991. Analytic investigations of the effects of near-surface three-dimensional galvanic scatters on MT tensor decompositions; *Geophys.*, **56**, 496-518.

Groom, R.W., and Bahr, K., 1992. Corrections for near surface effects: decomposition of the magnetotelluric impedance tensor and scaling corrections for regional resistivities a tutorial; *Surv. Geophys.*, **13**,341-379.

Groom, R.W., Kurtz, R.D., Jones, A.G., and Boerner, D.E., 1993. A quantitative methodology for determining the dimensionality of conductivity structure and the extraction of regional impedance responses from magnetotelluric data; *Geophy J. Int.*, **115**, 1095-1118.

Hajnal, Z., Lucas, S., White, D., Lewry, J., Bezdan, S, Stauffer, M.R. and Thomas, M.D. 1996. Seismic reflection images of high-angle faults and linked detachments in the Trans-Hudson Orogen; *Tectonics*, **15**, 427-439.

Hoffman, P.F., 1980. Wopmay Orogen: a Wilson cycle of early Proterozoic age in the northwest of the Canadian Shield; in Strangway. D.W., ed., The Continetal Crust and its Mineral Deposits: Geological Association of Canada, Special Paper **20**, 523-549.

Hoffman, P.F., 1981. Autopsy of the Athapuscow aulacogen: a failed arm affected by three collisions; in Campbell, F.H.A, ed., Proterozoic basins of Canada: Geological Survey of Canada, Paper **81-10**, 97-102.

Jiracek, G., 1984. The magnetotelluric method; lecture notes, department of Geological Sciences, San Diego State University, San Diego, CA., 54 p.

Jiracek, G.R., Rodi., W.L. and Vanyan, L.L., 1986. Implications of magnetotelluric modelling for the deep crustal environment in the Rio Grande Rift; *Phys. Earth and Planet. Inter.*

Jiracek, G.R., 1990. Near-surface and topographic distortions in electromagnetic induction; *Surv. Geophys.*, **11**, 163-203.

Jones, F.W. and Correia, A., 1992. Magnetotelluric soundings in the frequency range 0.01-130 Hz in northern Saskatchewan; in LITHOPROBE, Trans-Hudson Orogen Transect, Report Number 26 of second transect meeting, 111-116.

Jones, A.G., 1992. Electrical conductivity of the lower crust; Chapter 3, in Fountain D.., Arculus, R.J., and Kay, R.W., eds. Continental Lower Crust, Elsevier, Amsterdam, 81-143.

Jones, A.G. and Dumas, I., 1993. Electromagnetic images of a volcanic zone, *Phy. Earth. Planet. Int.*, **81**, 289-314.

Jones, A.G, Craven, J.A., McNeice, G.M., Ferguson, I.J., Boyce, T.T., Farquharson, C., and Ellis, R., 1993. North American Central Plains conductivity anomaly within the Trans-Hudson Orogen in northern Saskatchewan, Canada; *Geology*, **21**, 1027-1030.

Jones, A.G., and Grant, N.J. 1997. Geoelectric strike directions for the 1992 THOT MT data; Report of LITHOPROBE Trans Hudson Orogen Transect 7th Transect Meeting, Sakatoon.

Kanasewich, E.R., 1981. Time Sequence Analysis in Geophysics; The University of Alberta Press; Third Edition, Edmonton, Alberta, Canada, 469 p.

Kaufman, A.A. and Keller, G.V., 1981. The Magnetotelluric Sounding Method: Elsevier, Amsterdam, 445 p.

Kunetz, G., 1972. Processing and interpretation of magnetotelluric soundings; *Geophys.*, **37**, 1005-1021.

Lewry, J.F. and Collerson, K.D., 1990. The Trans-Hudson Orogen: extent, subdivision and problems; in Lewry, J.F. and Stauffer, M.R., eds., The early Proterozoic Trans-Hudson Orogen of North America; Geological Association of Canada, Special Paper, **37**, 1-14.

Lewry, J.F. Thomas, D.J., Macdonald, R., and Chiarenzilli, J., 1990. Structural relations in accreted terranes of the Trans-Hudson Orogen, Saskatchewan: Telescoping in a collisional regime?, in Lewry, J.F. and Stauffer, M.R., eds., The early Proterozoic Trans-Hudson Orogen of North America; Geological Association of Canada, Special Paper, **37**, 75-94.

Larsen, J.C., 1977. Removal of local surface conductivity effects from low frequency mantle response curves; *Acta. Geodaet., Geophys. et Montanist. Acad. Sci. Hung.* **12**, 177-181.

LaTorraca, G.A., Madden, T.R., and Korringa, J. 1986. An analysis of magnetotelluric impedance for three dimensional conductivity structures; *Geophys.*, **51**, 1819-1829.

Lewry, J.F., Hajnal, Z., Green, A., Lucas, S.B., White, D., Stauffer, M.R., Ashton, K.E., Weber, W., and Clowes, R., 1994. Structure of a Paleoproterozoic continent - continent collision zone: A LITHOPROBE seismic reflection profile across the Trans-Hudson Orogen, Canada; *Tectonophysics*, **232**, 143-160.

Lucas, S.B., Green, A., Hajnal, Z., White, D., Lewry, J., Ashton, K., Weber, W. and Clowes, R., 1993. Deep seismic profile across a Proterozoic collision zone: Surprise at depth; *Nature*, **363**, 339-342.

MacBain, J.A. and Bednar, J.B., 1986. Existence and uniqueness properties for the one-dimensional magnetotellurics inversion problem; *J. Math. Phys.*, **27**., 645-649.

Madden, T. and Nelson, P., 1964. A defence of Cagnaird's magnetotelluric method: project NR-371-401, Geophysics, Lab., MIT, 41 p.

Madden, T.R. and Mackie, R.L., 1989. Three-dimensional magnetotelluric modelling and inversion; Proc. *IEEE*, **77**, 318-333.

Marquis, G., Jones, A.G., and Hyndman, R.D., 1995. Coincident conductive and reflective middle and lower crust in southern British Columbia; *Geophys. J. Int.*, **120**, 111-131.

Parker, R.L., 1983. The magnetotelluric inverse problem; *Geophys. Surv.*, **6**, 5-25.

Parkinson, W.D., 1962. The influence of continents and oceans on geomagnetic variations., *Geophys, J. R. Astr. Soc.*, **6**, 441-449.

Patra, H.P. and Mallick, K., 1980. Geosounding Principles, Two, Time Varying Geoelectric Soundings; Elsevier, Amsterdam, 419 p.

Ranganayaki, R.P., 1984. An interpretive analysis of magnetotelluric data; *Geophys.*, **49**, 1730-1748.

Sharma, P.V., 1982. Geophysical Methods in Geology; Elsevier Publishing, Methods in Geochemistry and Geophysics, **12**, New York, New York, 290-291.

Sheriff, R.E., 1984. Encyclopedic Dictionary of Exploration Geophysics; Society of Exploration Geophysicists, Tulsa, Oklahoma, USA, 323 p.

Shulz K.J., 1987. An early Proterozoic ophiolite in the Penokean Orogen; Geological Association of Canada - Mineralogical Association of Canada, program with abstracts, 87.

Sims, P.K. and Peterman, Z.E., 1986. Early Proterozoic Central Plains Orogen: a major buried structure in north central United States; *Geology*, **14**, 488-491.

Sims, W.E. and Bostick, F.X., Jr., 1969. Methods of magnetotelluric analysis: Elec. Res. Lab., Tech. Rep. # 58, Univ. Texas, Austin.

Smith, J.T. and Booker, J.R., 1990. The rapid relaxation inverse for two-dimensional magnetotelluric data., *J. Geophys. Res.*, **96**, 3905-3922.

Spagnolini, U., 1994. Time-domain estimation of MT impedance tensor; *Geophys.*, **59**, No. 5, 712-721.

Stern, R.A., Syme, E.C., Bailes, A.H., Galley, A.G., Thomas, D.J., and Lucas, S.B., 1992. Nd-Isotopic stratigraphy of early Proterozoic Amisk Group metavolcanic rocks from the Flin-Flon Belt, Manitoba and Saskatchewan; in Radiogenic age and isotopic studies, Report # 6, Geological Survey of Canada, paper, **92-2**, 73-84.

Swift, C.W., 1967. A magnetotelluric investigation of an electrical conductivity anomaly in the southwestern United States; in Magnetotelluric Methods, Society of Exploration Geophysicists, Geophysics Reprint Series No. 5, 156-166, 1989.

Swift, C.W., 1970. Theoretical magnetotelluric and Turam response from two-dimensional inhomogeneities; reprint from *Geophys.*, **36**, 38-52: in Magnetotelluric Methods, Society of Exploration Geophysicists, Geophysics Reprint Series No. 5, 265-279, 1989.

Telford, W.M., Geldart, L.P., Sheriff, R.E., and Keys, D.A., 1976. Applied Geophysics, Cambridge University Press, London, England, 468-480.

Thomas, M.D., 1994. Potential contributions of gravity and magnetic data analysis to the Trans-Hudson Orogen Transect; in LITHOPROBE, Trans-Hudson Orogen Transect, report number 26 of second transect meeting, 73-74.

Van Schmus, W.R., 1980. Chronology of igneous rocks associated with the Penokean Orogen in Wisconsin: in Morey, G.B. and Hanson, G.N. eds., Selected studies of Archean gneiss and lower Proterozoic rocks, southern Canadian Shield : Geological Society of America, Special Paper **182**, 159-168.

Vozoff, K., 1972. The magnetotelluric method in the exploration of sedimentary basins; *Geophys.*, **37**, 98-141.

Vozoff, K., 1991. The magnetotelluric method; in Electromagnetic Methods in Applied Geophysics; M.N. Nabighian, ed., Society of Exploration Geophysicists, Tulsa, **2**, 641-711.

Wannamaker, P.E., Hohmann, G.W. and SanFilipo, W.A., 1984. Electromagnetic modelling of three-dimensional bodies in layered earth's using integral equations., *Geophys.*, **49**, 60-74.

Wannamaker, P.E., Stodt, J.A., and Rijo, L., 1986. Two-dimensional topographic responses in magnetotellurics modeled using finite elements; *Geophys.*, **51**, 2131-2144.

Wannamaker, P.E. and Hohmann, G.W., 1991. Electromagnetic induction studies; in Contributions in geomagnetism and paleomagnetism, U.S. National Report, 1987-1990., ed. Shea, M.A., American Geophysical Union, Washington D.C.

West, G.F. and Edwards, R.N., 1985. A simple parametric analysis for the electromagnetic response of an anomalous body in a host medium; *Geophys.*, **50**, 2542-2557.

Wight, D.E., and Bostick, F.X., 1980. Cascade Decimation - A technique for real time estimation of power spectra; 1980 Proceedings IEEE International Conf., on Acoustic Speech and Signal Processing, Denver, CO., 626-629.

Word, D.R., Smith, H.W. and Bostick, F.X, Jr., 1970. A investigation of the magnetotelluric tensor impedance method: Tech. Rep. 82, Electr. Geophys Lab., Univ. of Texas at Austin.

Zhang, P., Roberts, R.G. and Pedersen, L.B. 1987. Magnetotelluric strike rules; *Geophys.*, **51**, 267-278.

Zhang, P., Pedersen, L.B., Mareschal, M., and Chouteau, M., 1993. Channelling contribution to tipper vectors: a magnetic equivalent to electrical distortion; *Geophys. J. Int.*, **113**, 693-700.

Zonge, K.L. and Hughes, L.J., 1991. Controlled source audio-frequency magnetotellurics; in Electromagnetic Methods in Applied Geophysics , M.N. Nabighian, ed., Society of Exploration Geophysicists, Tulsa, **2**, 713-809.

Appendix A1: MT Site Coordinates for GD-FFB Portion of the THOT

This appendix contains the latitude, longitude and UTS coordinates of each of the AMT, MT and LiMS sites reported in this thesis for the THOT Lithoprobe transect.

Appendix A1. MT Site Coordinates for GD-FFB Portion of the THOT

Station	Lat. (deg:min:sec:)	Long. (deg:min:sec)	Easting (m)	Northing (m)
THO-92-M25S	54:47:04 N	105:14:36 W	484450 Z13	6070550 Z13
THO-92-A23A	54:46:28 N	105:09:03 W	489800 Z13	6069300 Z13
THO-92-M24S	54:44:59 N	104:59:40 W	500100 Z13	6068000 Z13
THO-92-A22A	54:43:34 N	104:52:49 W	507700 Z13	6064300 Z13
THO-92-M23S	54:42:16 N	104:49:21 W	311200 Z13	6061900 Z13
THO-92-M22S	54:38:12 N	104:34:18 W	527900 Z13	6054300 Z13
THO-92-A20A	54:37:27 N	104:25:35 W	537300 Z13	6053000 Z13
THO-92-M21S	54:36:27 N	104:11:47 W	551800 Z13	6051100 Z13
THO-92-A19A	54:35:40 N	103:59:53 W	NA	NA
THO-92-M20S	54:35:01 N	103:59:33 W	565100 Z13	6048700 Z13
THO-92-A18A	54:30:21 N	103:54:22 W	570700 Z13	6040200 Z13
THO-92-M19S	54:29:52 N	103:46:37 W	579400 Z13	6939500 Z13
THO-92-A17A	NA	NA	NA	NA
THO-92-M18S	54:32:32 N	103:29:37 W	597600 Z13	6044800 Z13
THO-92-M16S	54:41:03 N	103:16:07 W	611600 Z13	6060700 Z13
DTH009	54:41:43 N	103:11:03 W	NA	NA
THO-92-M15S	54:43:30 N	102:59:50 W	629000 Z13	6065600 Z13
THO-92-A15A	54:45:33 N	102:55:30 W	633500 Z13	6697000 Z13
THO-92-M13S	54:50:03 N	102:49:05 W	640200 Z13	6078300 Z13

Appendix A1. (cont'd)

THO-92-A13A	54:50:40 N	102:36:45 W	653300 Z13	6079900 Z13
DTH007	54:49:30 N	102:33:50 W	NA	NA
THO-92-M12S	54:50:35 N	102:29:00 W	661800 Z13	6080050 Z13
THO-92-A12A	54:51:35 N	102:21:35 W	669600 Z13	6082200 Z13
THO-92-A11A	54:52:10 N	102:12:25 W	679200 Z13	6083700 Z13
THO-92-M11S	54:51:45 N	102:07:20 W	684800 Z13	6083100 Z13
THO-92-A46A	54:50:47 N	102:02:57 W	689460 Z13	6081678 Z13
THO-92-M45S	54:50:46 N	101:54:41 W	313115 Z14	6081561 Z14
THO-92-A45A	54:52:33 N	101:49:07 W	319175 Z14	6084601 Z14
THO-92-M46S	54:51:53 N	101:34:49 W	334396 Z14	6082581 Z14

*** A denotes an AMT site, M denotes an MT site, D denotes a LiMS site**

Appendix A2: GD-FFB MT sites, frequency ranges and discarded data

This appendix contains a list of the AMT, MT and LiMS sites used in the analysis of the GD-FFB MT data set. The frequency range of data used as well as an identification of frequencies deemed to be inapprpriate for use and the sources of the 'bad' data are given.

Appendix A2. GD-FFB MT sites, frequency ranges and discarded data

Station	Frequency Range	Bad Frequencies	Source	Comments
THO-92-A24A	10000-10	3750,2304,1536	telluric/mag	
THO-92-M25S	10000-0.0005	3750,3072	telluric/mag	
THO-92-A23A	10000-10	all good		
THO-92-M24S	10000-0.0005	3072,2304,1536, <0.003	magnetic	
THO-92-A22A	10000-10	3750,3072,2304 1152,768	magnetic	
THO-92-M23S	10000-0.0005	3072,2304,1536, <0.003	magnetic	
THO-92-M22S	10000-0.0005	3750,1152, <0.001	magnetic	
THO-92-A20A	10000-10	2304,1536,9,12, 18,24,36,48,	telluric/mag	
THO-92-M21S	10000-0.0005	3750,3072,2304, 1536,1152,768, <0.001	telluric/mag	
THO-92-A19A	10000-10	1536,2304		
THO-92-M20S	10000-0.0005	1536, <0.001	telluric	
THO-92-M18A	10000-10	a3072,2304	magnetic	

Appendix A2. (cont'd)

Station	Frequency Range	Bad Frequencies	Source	Observations
THO-92-M19S	10000-0.0005	3750,3072,2304 1536,1152, 768 <0.001	telluric/mag	
THO-92-A17A	10000-10	3750,3072	magnetic	
THO-92-M18S	10000-0.0005	<0.01		
THO-92-M16S	10000-0.0005	>10, <0.001	magnetic	
DTH009	0.05-0.0001	all good		
THO-92-M15S	10000-0.0005	> 768, < 3	telluric/mag	
THO-92-A15A	10000-10	all good		
THO-92-M13S	10000-0.0005	all good		
DTH007	0.05-0.0001	all good		
THO-92-M12S	10000-0.0005	3750,3072, <0.005	magnetic	
THO-92-A12A	10000-10	3072,2304,1536 1152	telluric/mag	
THO-92-A11A	10000-10	3750,3072,2304 1536	telluric/mag	
THO-92-M11S	10000-0.0005	>10, <0.1	telluric/mag	
THO-92-A46A	10000-10	3750	magnetic	
THO-92-M45S	10000-0.0005	all bad		site omitted

Appendix A2. (cont'd)

Station	Frequency Range	Bad Frequencies	Source	Observations
THO-92-A45A	10000-10	5000,3750,3072 2304,1536	magnetic	
THO-92-M46S	10000-0.0005	5000,3750,3072 2304,1536,1152, <0.01	telluric/mag	

Appendix B: Unconstrained Groom-Bailey Decomposition Results and Wall Paper Plots

This appendix shows the results of the Groom-Bailey decomposition analysis performed on the GD-FFB MT data. For each site there a three sets of results shown:

1) the 3-D unconstrained Groom-Bailey parameterization permiting both the distortion parameters and the 2-D regional strike to vary with frequency for sites M25 to M46. Each plot shows the standard parameter display of the i) resdual error fit, ii) azimuthal paramters: strike, twist, shear channeling, iii) regional impedance estimate and iv) regional phases is used;

2) the GB determined fits of the GB model to the impedance data;

3) the 'Wall paper' plots of the Groom-Bailey parameterization for the twist and shear with corresponding residual error, varying the strike angle between 0 to 90^0 in 3 degree increments for sites M25 to M46.

THO-92-M25S

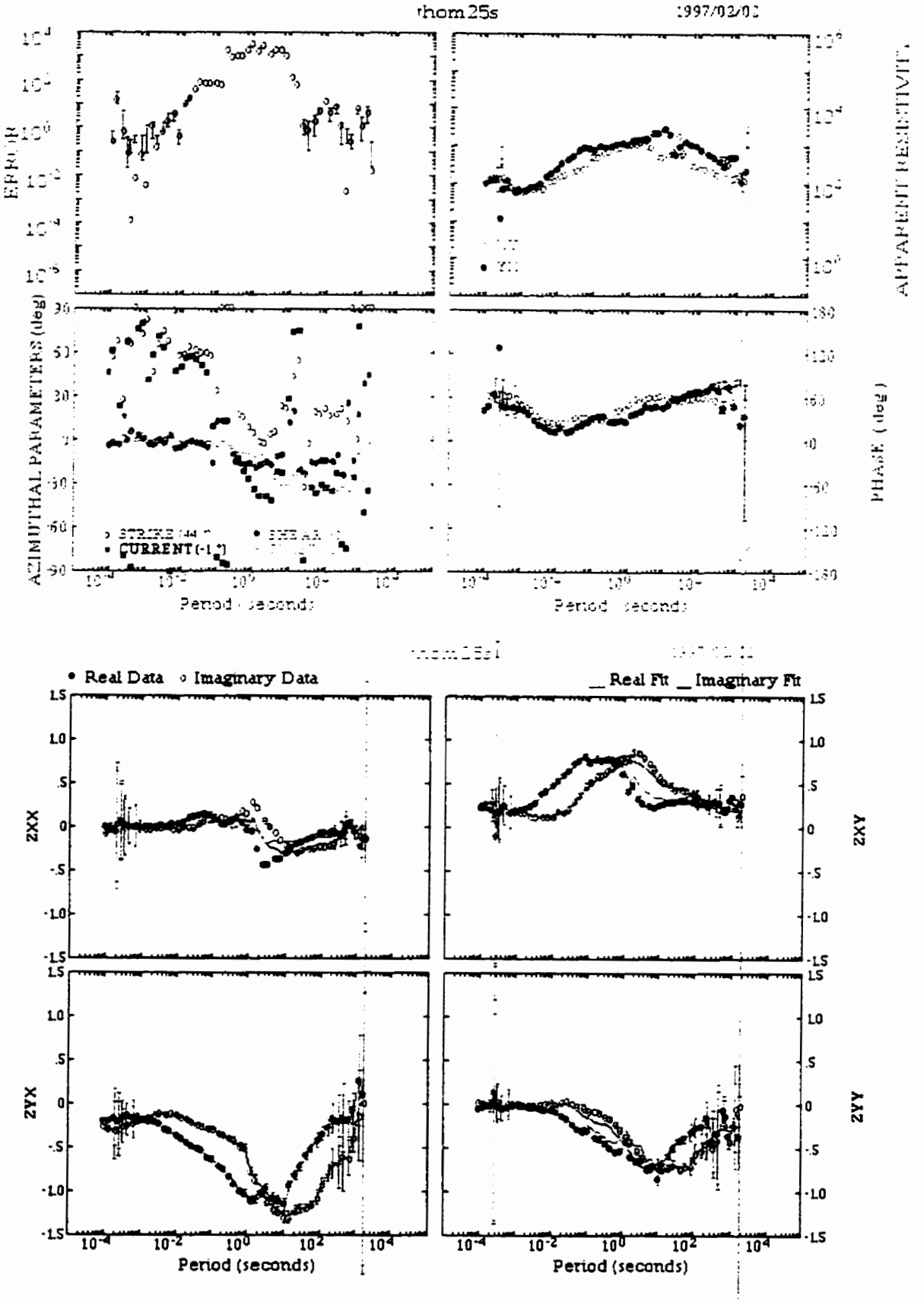
thom25s
1997/02/02
AZIMUTHAL PARAMETERS (deg)
APPARENT RESISTIVITY
PHASE (deg)
CURRENT (-L°)
Period (seconds)
• Real Data ◦ Imaginary Data
_ Real Fit _ Imaginary Fit
ZXX
ZXY
ZYX
ZYY
Period (seconds)

THO-92-M25S

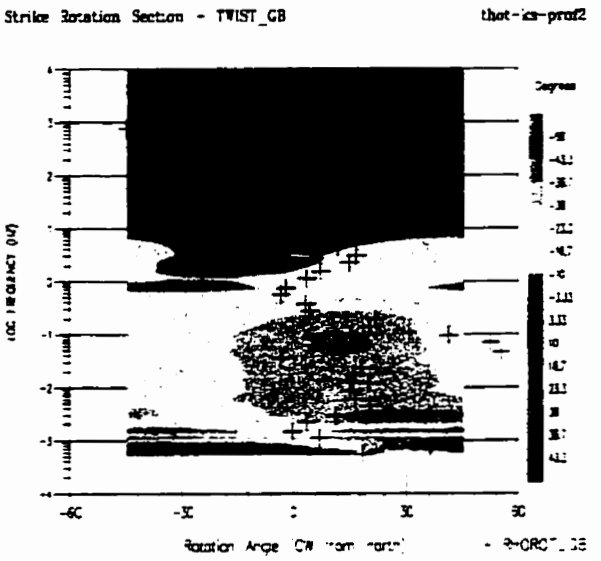
Strike Rotation Section - TWIST_GB
that-ks-prof2
Degrees
Rotation Angle (CW from north)

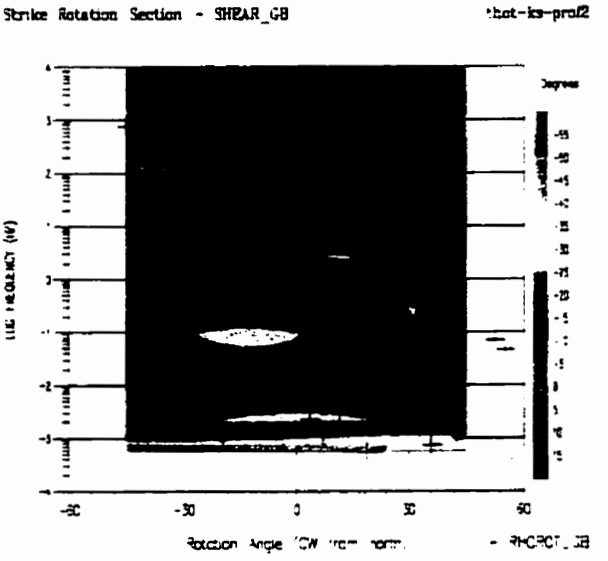
Strike Rotation Section - SHEAR_GB
that-ks-prof2
Degrees
Rotation Angle (CW from north)

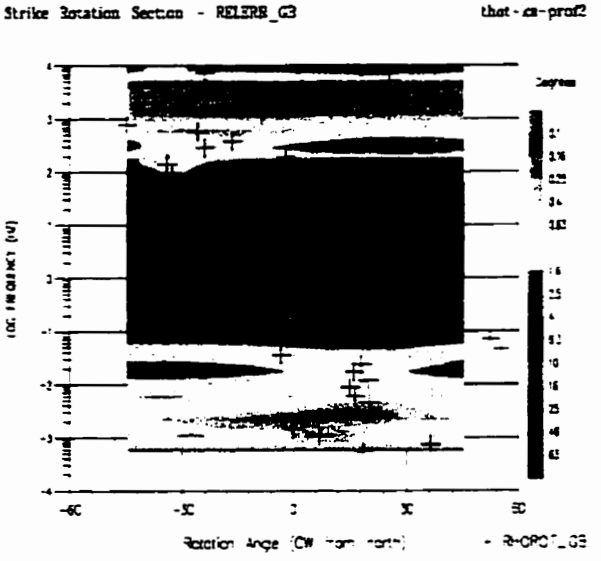
Strike Rotation Section - RELERR_G3
that-ks-prof2
Degrees
Rotation Angle (CW from north)

THO-92-A23A

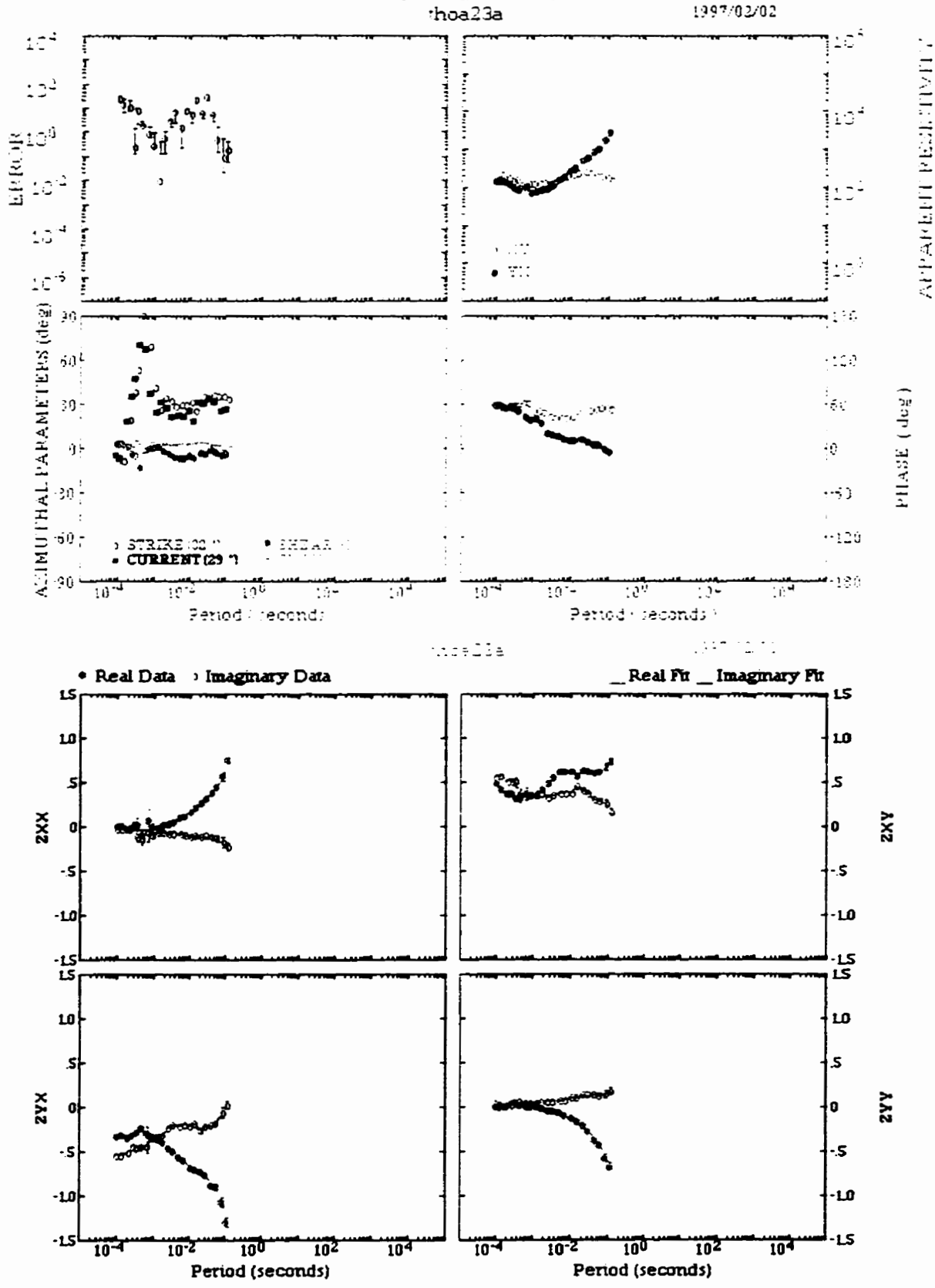
thoa23a
1997/02/02
AZIMUTHAL PARAMETERS (deg)
CURRENT (29 °)
Period (seconds)
PHASE (deg)
Real Data
Imaginary Data
Real Fit
Imaginary Fit
ZXX
ZXY
ZYX
ZYY
Period (seconds)

THO-92-A23A

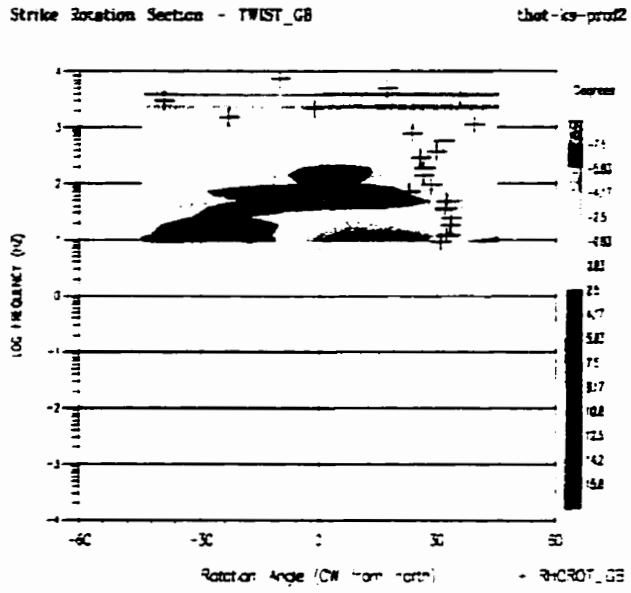
Strike Rotation Section - TWIST_GB
that-ks-prof2
Degrees
LOG FREQUENCY (HZ)
-60
-30
0
30
60
Rotation Angle (CW from north)
- RHCROT_GB

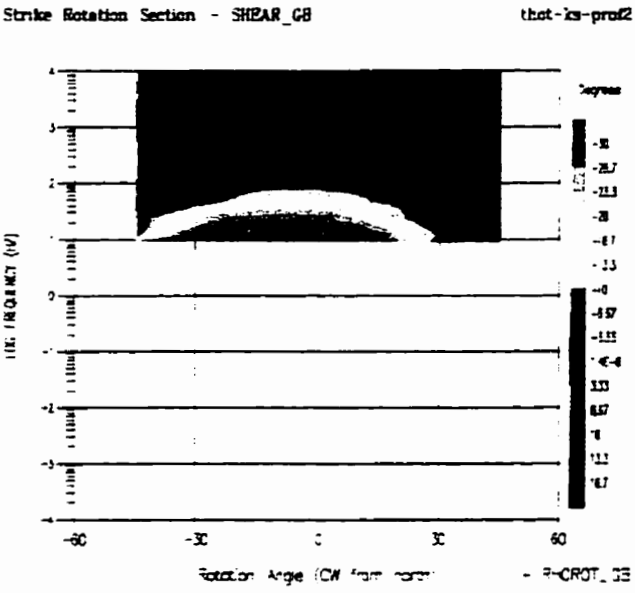
Strike Rotation Section - SHEAR_GB
that-ks-prof2
Degrees
LOG FREQUENCY (HZ)
-60
-30
0
30
60
- RHCROT_GB

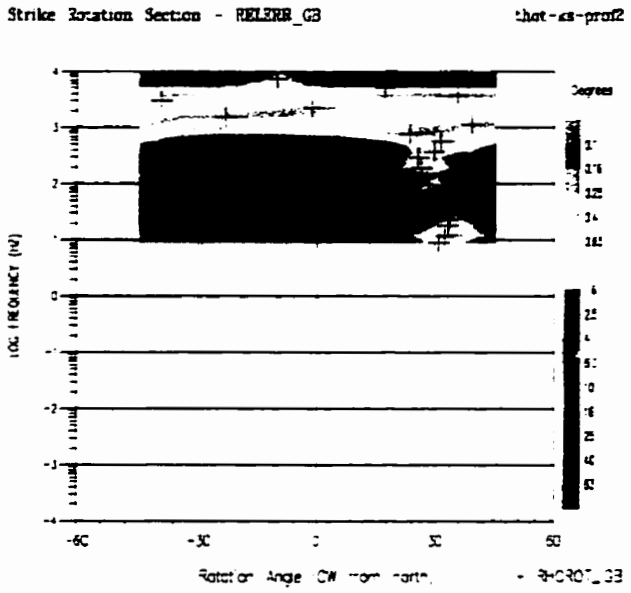
Strike Rotation Section - RELERR_GB
that-ks-prof2
Degrees
LOG FREQUENCY (HZ)
-60
-30
0
30
60
- RHCROT_GB

THO-92-M24S

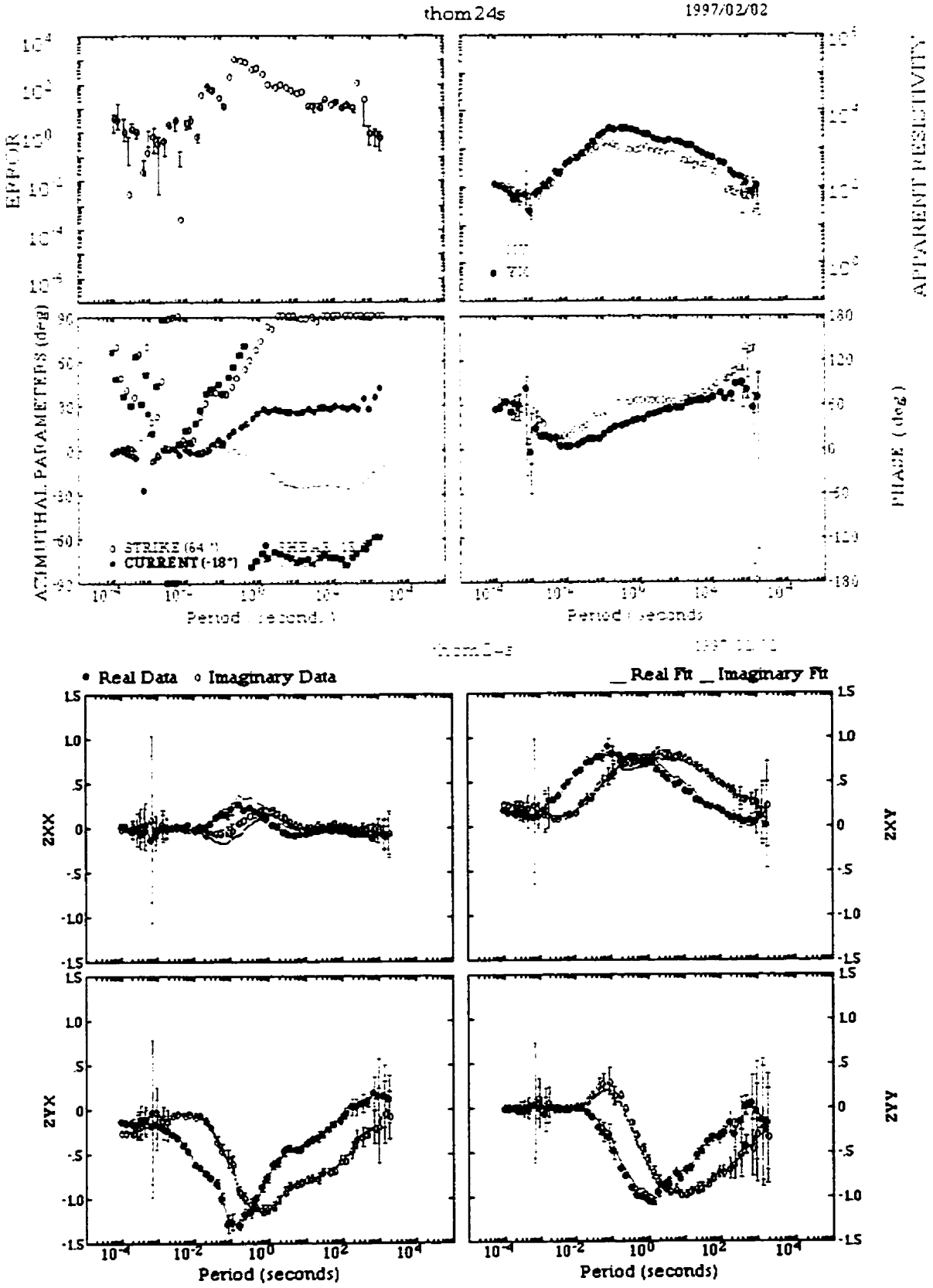
thom24s
1997/02/02
ERROR
APPARENT RESISTIVITY
AZIMUTHAL PARAMETERS (deg)
PHASE (deg)
STRIKE (64°)
CURRENT (-18°)
Period (seconds)
• Real Data ○ Imaginary Data
_ Real Fit _ Imaginary Fit
ZXX
ZXY
ZYX
ZYY
Period (seconds)
Period (seconds)

THO-92-M24S

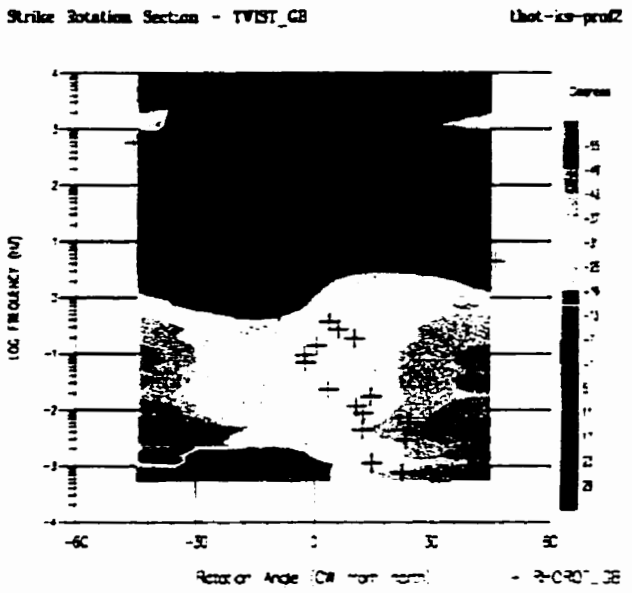
Strike Rotation Section - TWIST_GB
thot-ks-prof2
LOG FREQUENCY (HZ)
Rotation Angle (CW from north)

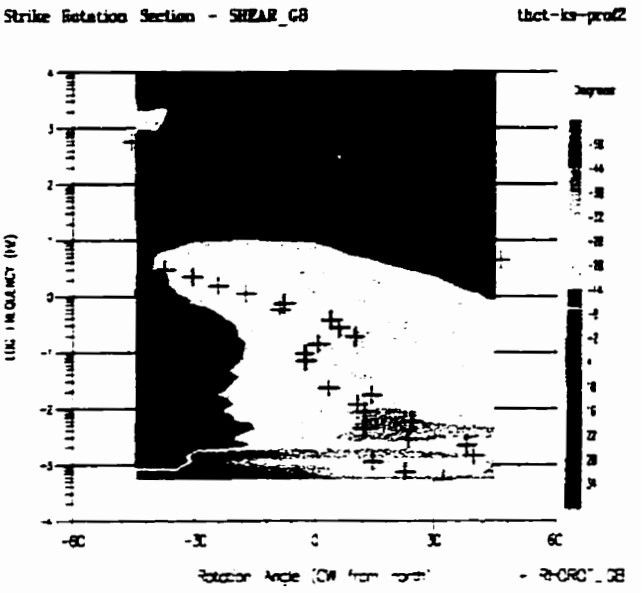
Strike Rotation Section - SHEAR_GB
thot-ks-prof2
LOG FREQUENCY (HZ)
Rotation Angle (CW from north)

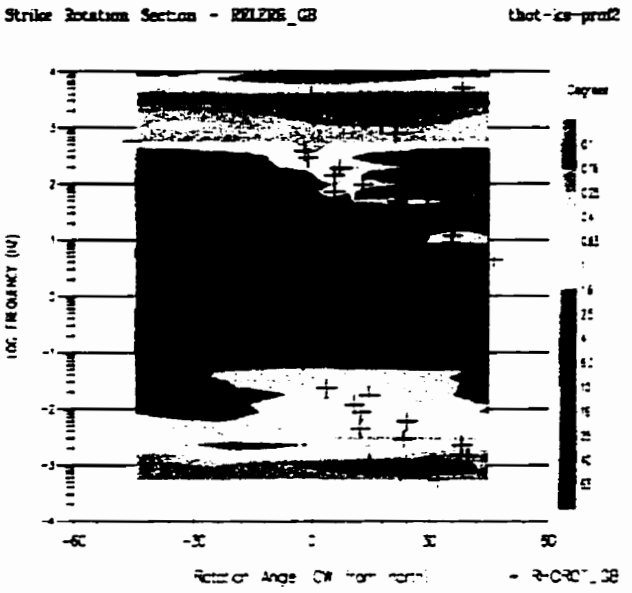
Strike Rotation Section - BELZRS_GB
thot-ks-prof2
LOG FREQUENCY (HZ)
Rotation Angle (CW from north)

THO-92-A22A

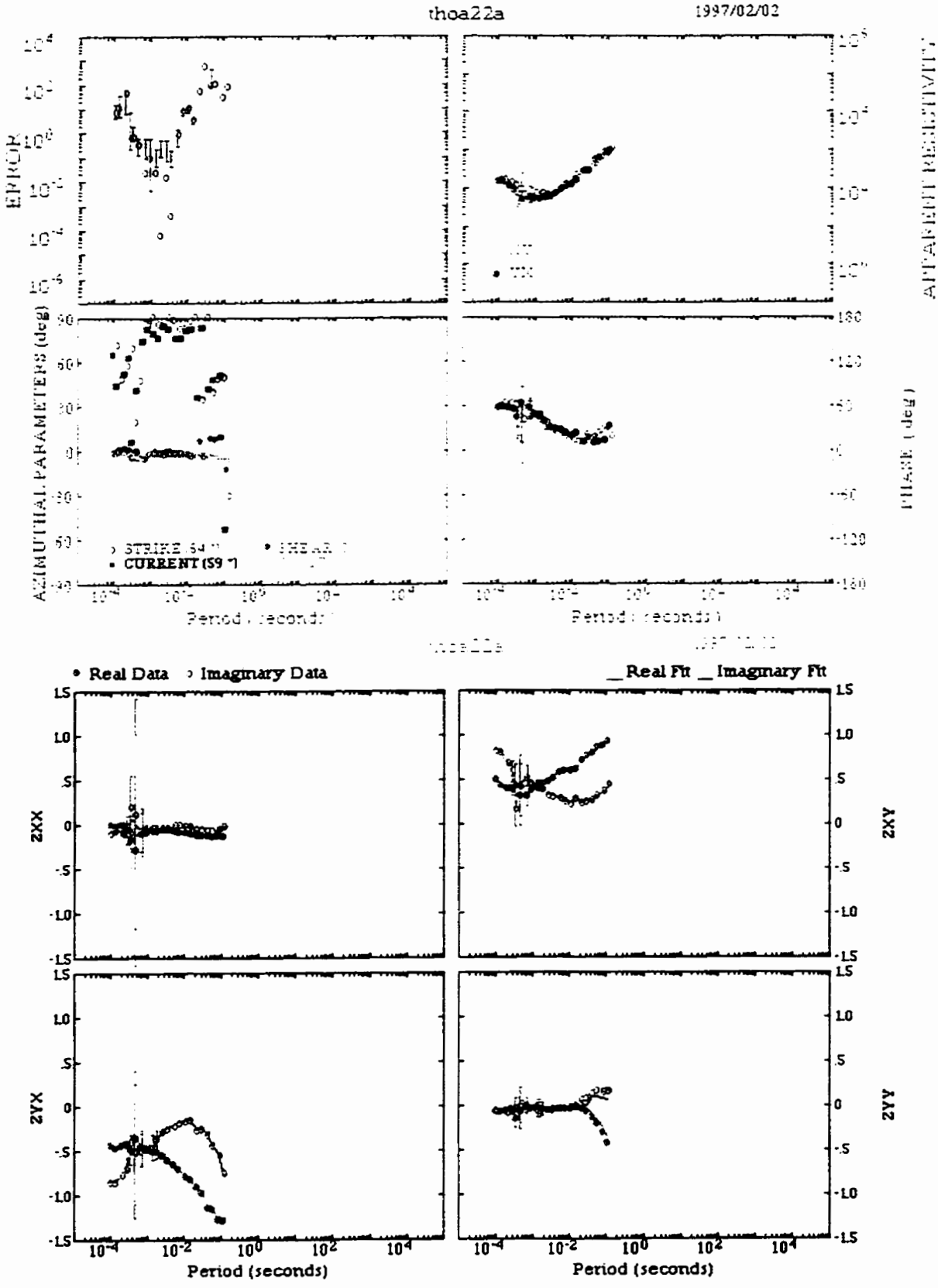
thoa22a
1997/02/02
ERROR
AZIMUTHAL PARAMETERS (deg)
APPARENT RESISTIVITY
PHASE (deg)
CURRENT (S9 °)
Period (seconds)
Real Data
Imaginary Data
Real Fit
Imaginary Fit
ZXX
ZXY
ZYX
ZYY
Period (seconds)

THO-92-A22A

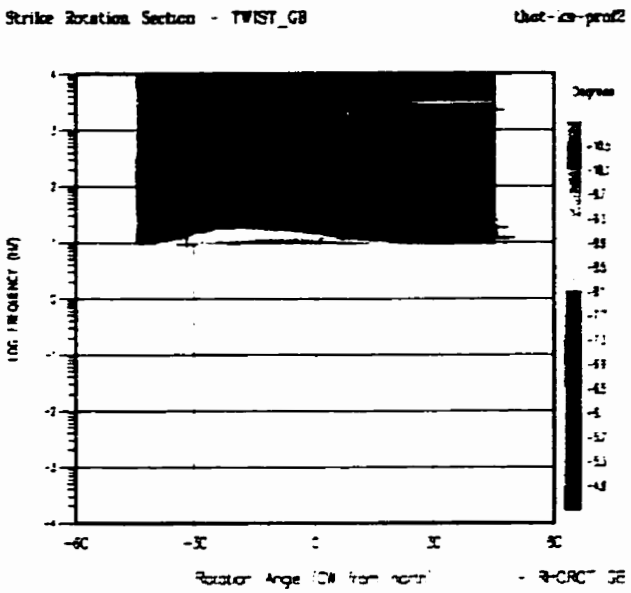
Strike Rotation Section - TWIST_GB
LOG FREQUENCY (HZ)
Rotation Angle (CW from north)

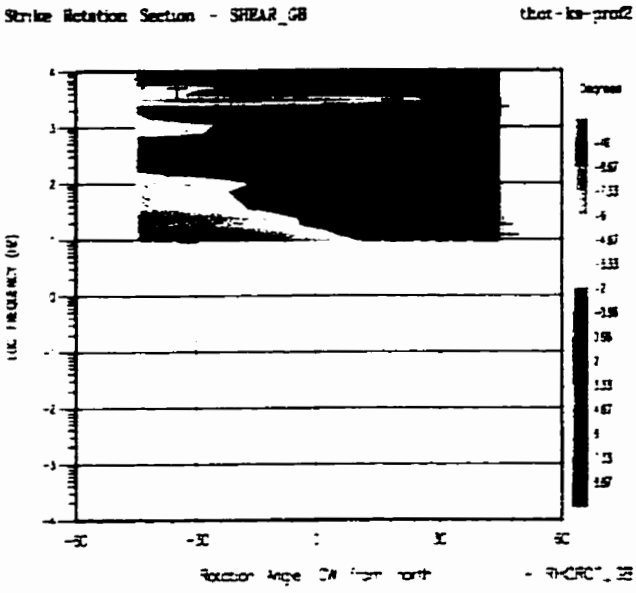
Strike Rotation Section - SHEAR_GB
LOG FREQUENCY (HZ)
Rotation Angle (CW from north)

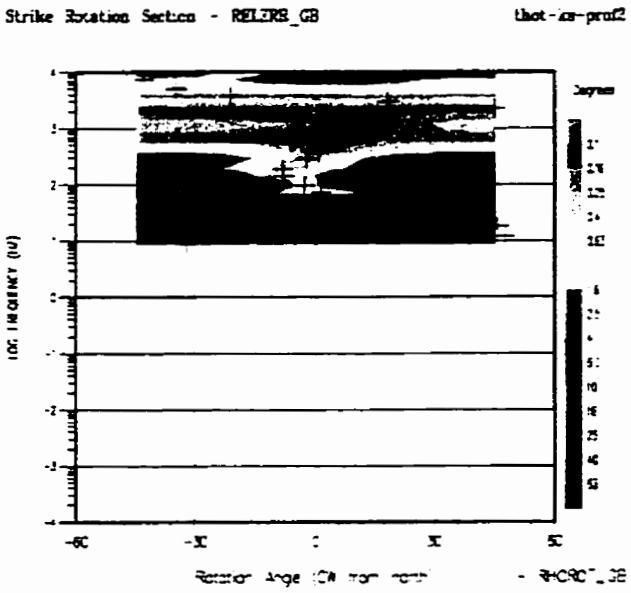
Strike Rotation Section - RELERS_GB
LOG FREQUENCY (HZ)
Rotation Angle (CW from north)

THO-92-M22S

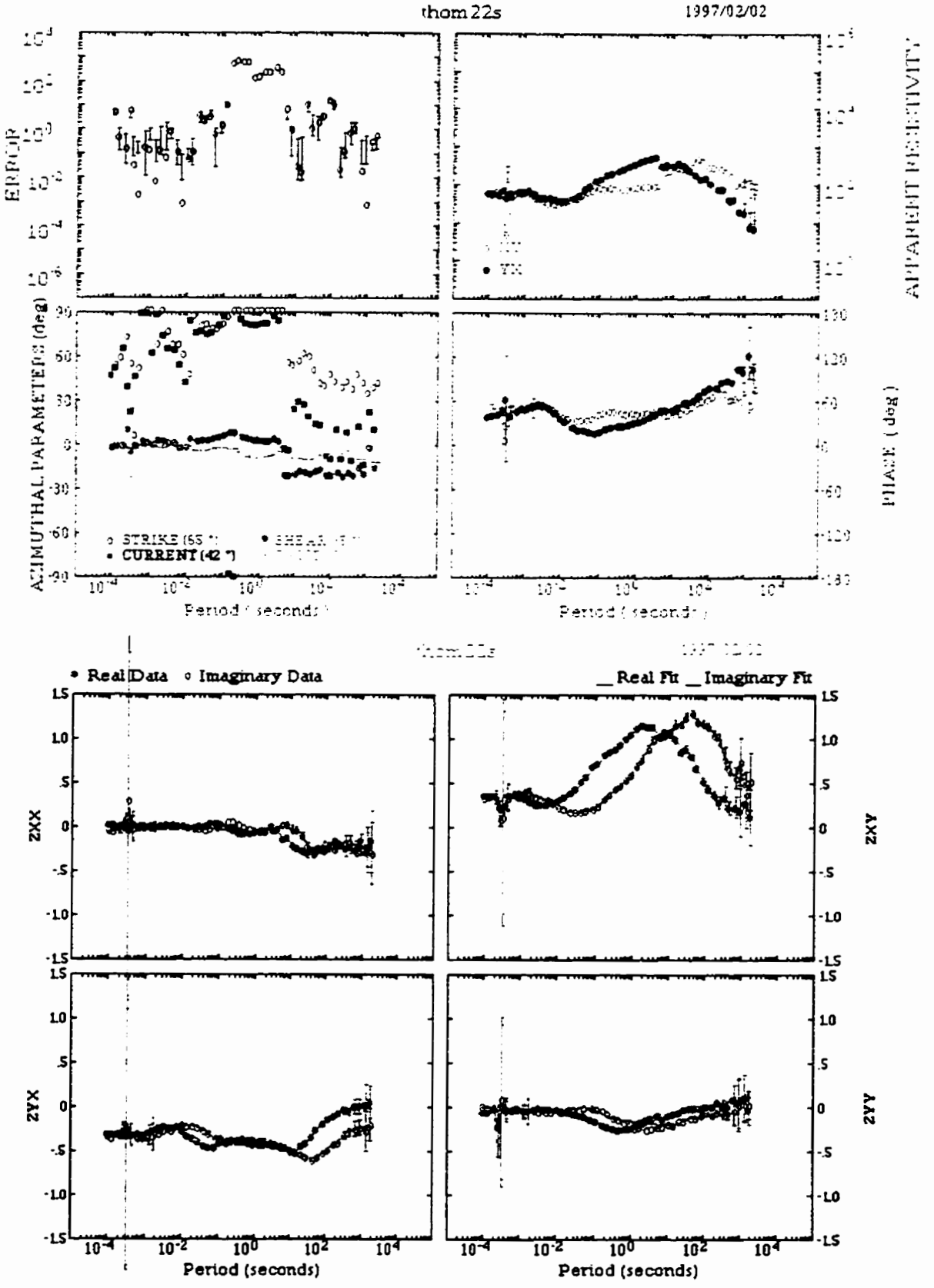
thom22s
1997/02/02
AZIMUTHAL PARAMETERS (deg)
STRIKE (65 °)
CURRENT (42 °)
Period (seconds)
APPARENT RESISTIVITY
PHASE (deg)
Real Data
Imaginary Data
Real Fit
Imaginary Fit
ZXX
ZXY
ZYX
ZYY
Period (seconds)

THO-92-M22S

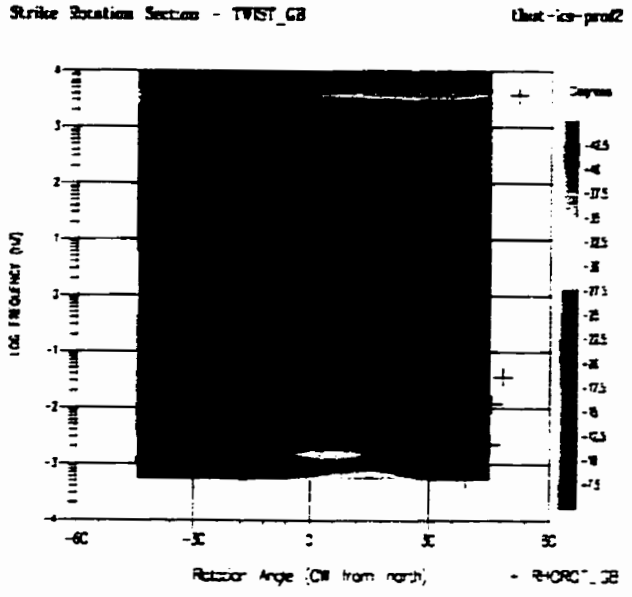
Strike Rotation Section - TWIST_GB
thot-ics-prof2
LOG FREQUENCY (HZ)
Rotation Angle (CW from north)

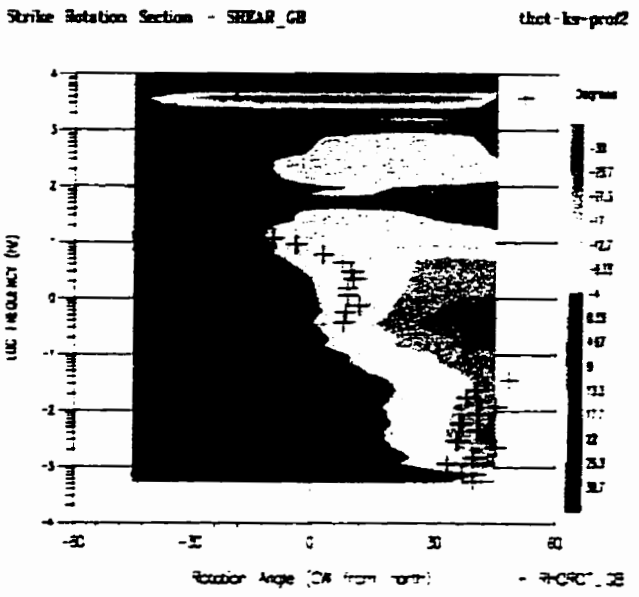
Strike Rotation Section - SHEAR_GB
thot-ics-prof2
LOG FREQUENCY (HZ)
Rotation Angle (CW from north)

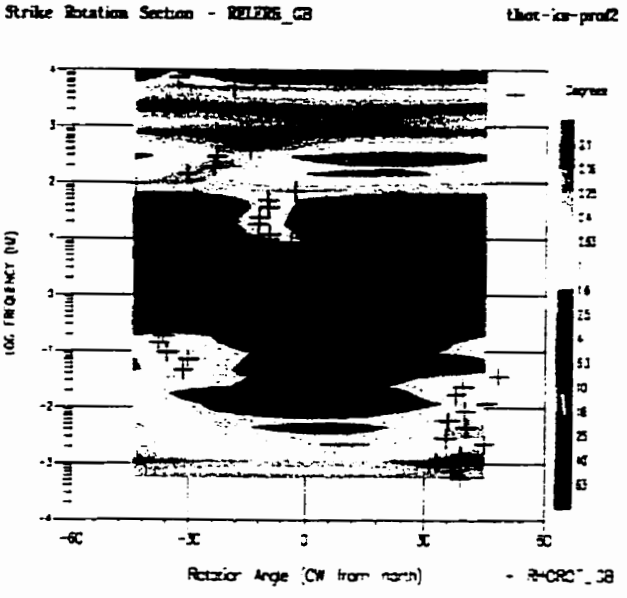
Strike Rotation Section - RELERR_GB
thot-ics-prof2
LOG FREQUENCY (HZ)
Rotation Angle (CW from north)

THO-92-A20A

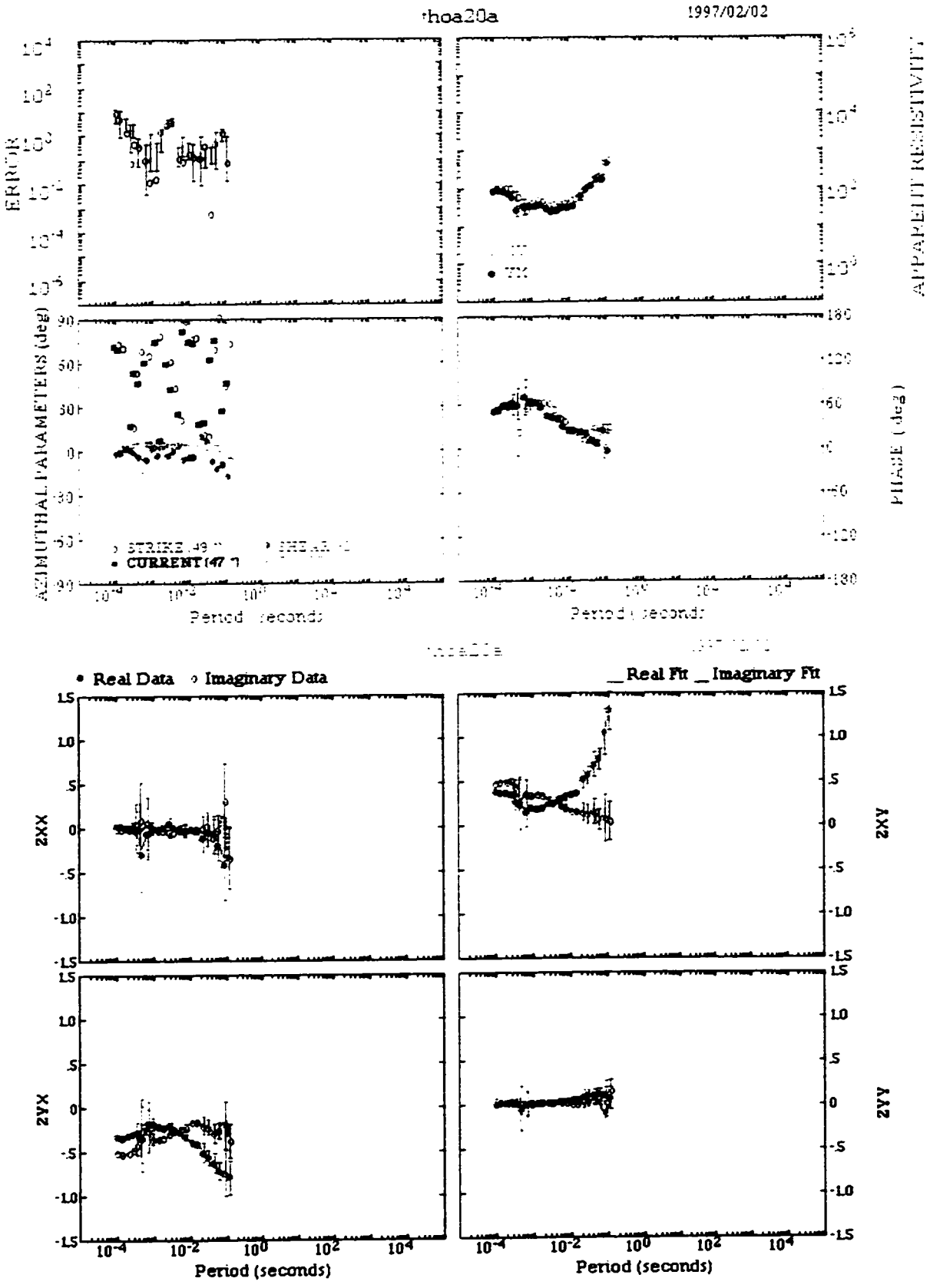
thoa20a
1997/02/02
ERROR
AZIMUTHAL PARAMETERS (deg)
APPARENT RESISTIVITY
PHASE (deg)
Period (seconds)
CURRENT
Real Data
Imaginary Data
Real Fit
Imaginary Fit
ZXX
ZXY
ZYX
ZYY
Period (seconds)

THO-92-A20A

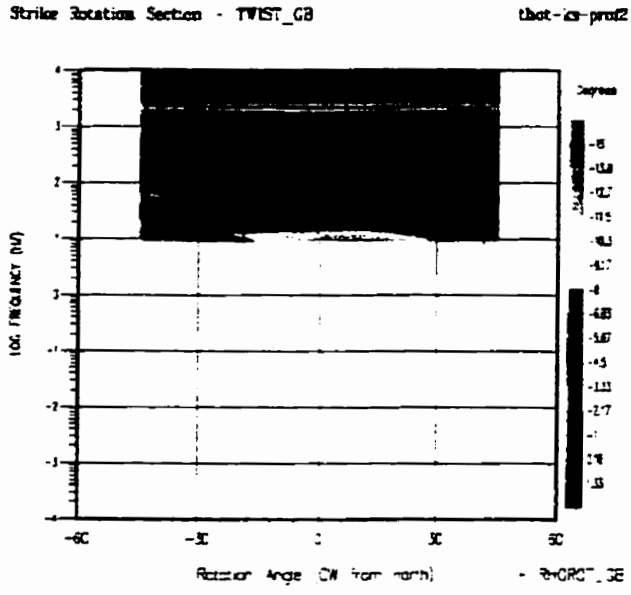
Strike Rotation Section - TWIST_GB
thet-ks-prof2
LOG FREQUENCY (hZ)
Rotation Angle (CW from north)

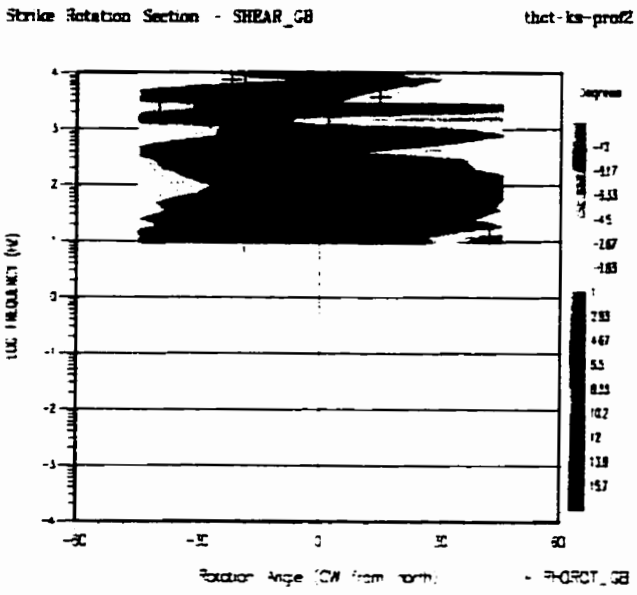
Strike Rotation Section - SHEAR_GB
thet-ks-prof2
LOG FREQUENCY (hZ)
Rotation Angle (CW from north)

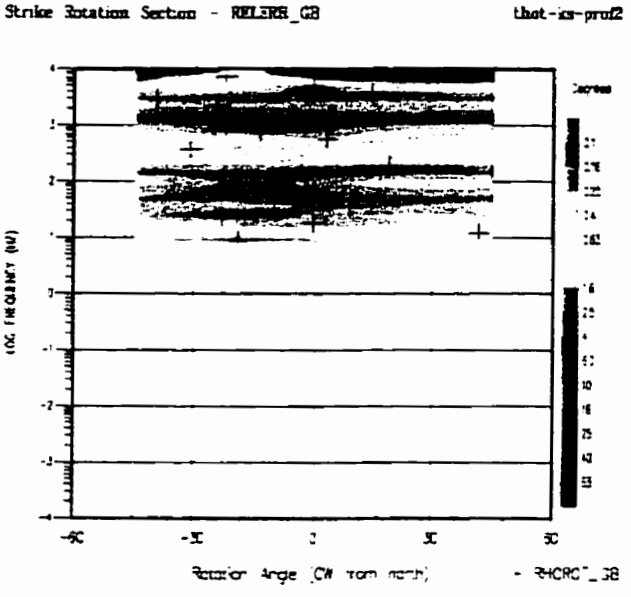
Strike Rotation Section - ROLLERB_GB
thet-ks-prof2
LOG FREQUENCY (hZ)
Rotation Angle (CW from north)

THO-92-M21S

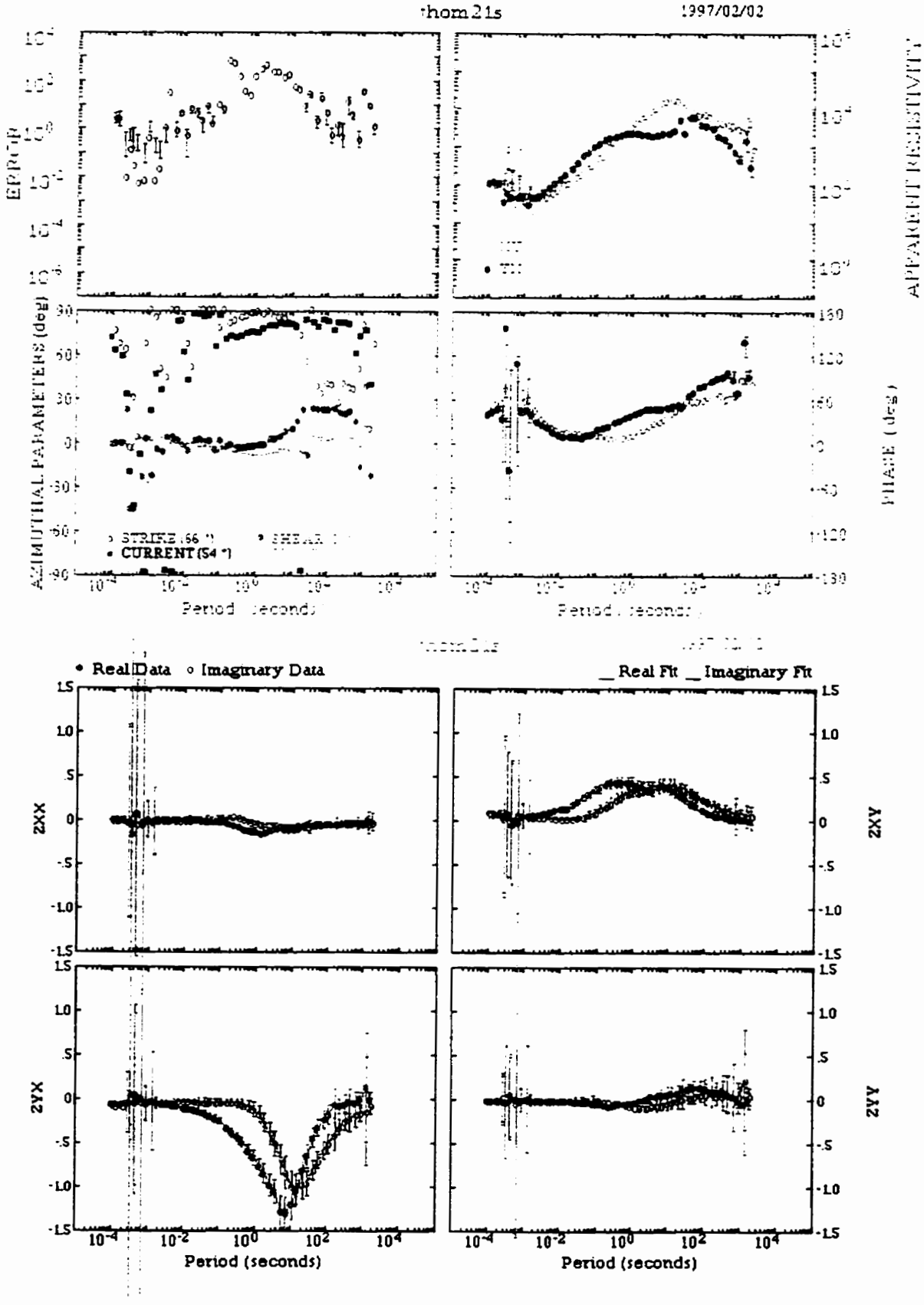
thom21s
1997/02/02
AZIMUTHAL PARAMETERS (deg)
APPARENT RESISTIVITY
PHASE (deg)
CURRENT (54 °)
Period (seconds)
Real Data
Imaginary Data
Real Fit
Imaginary Fit
ZXX
ZXY
ZYX
ZYY
Period (seconds)

THO-92-M21S

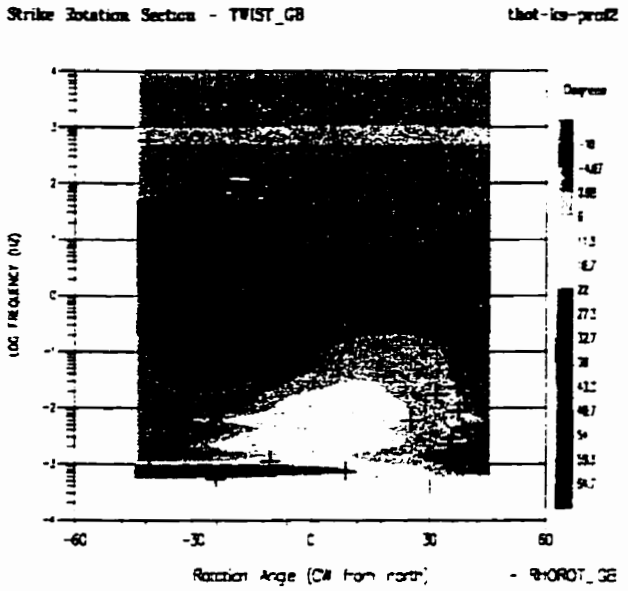
Strike Rotation Section - TWIST_GB
thot-ks-prof2
LOG FREQUENCY (HZ)
Degrees
-60
-30
0
30
60
Rotation Angle (CW from north)
- RHOROT_GB

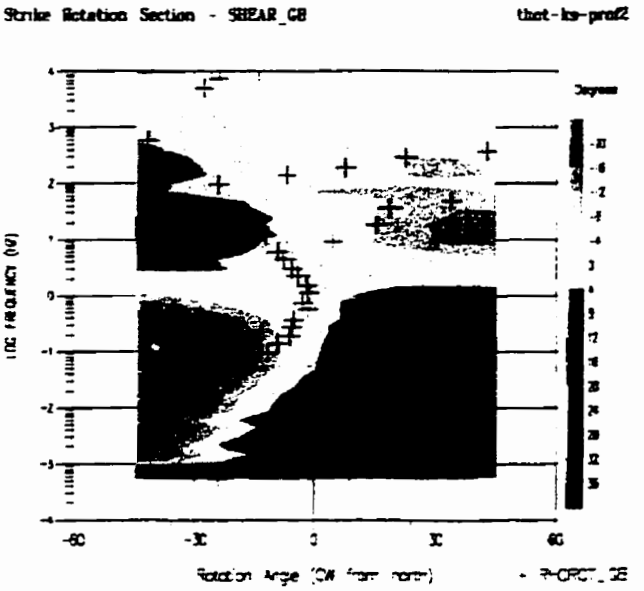
Strike Rotation Section - SHEAR_GB
thot-ks-prof2
LOG FREQUENCY (HZ)
Degrees
-60
-30
0
30
60
Rotation Angle (CW from north)

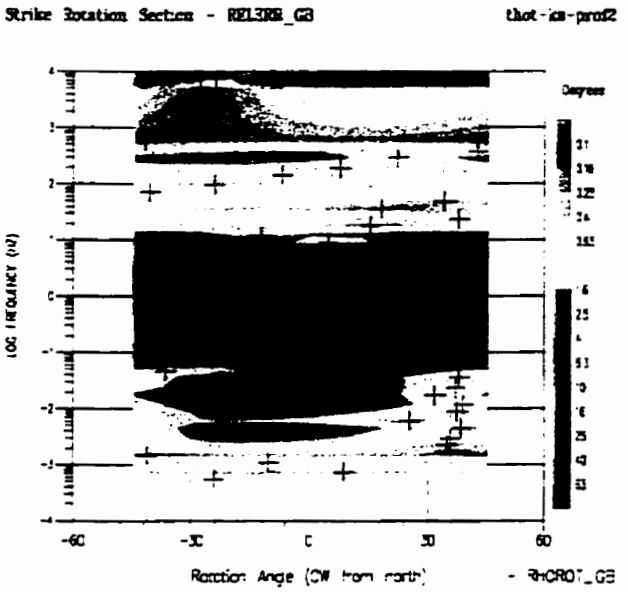
Strike Rotation Section - RELBEN_GB
thot-ks-prof2
LOG FREQUENCY (HZ)
Degrees
-60
-30
0
30
60
Rotation Angle (CW from north)
- RHOROT_GB

THO-92-A19A

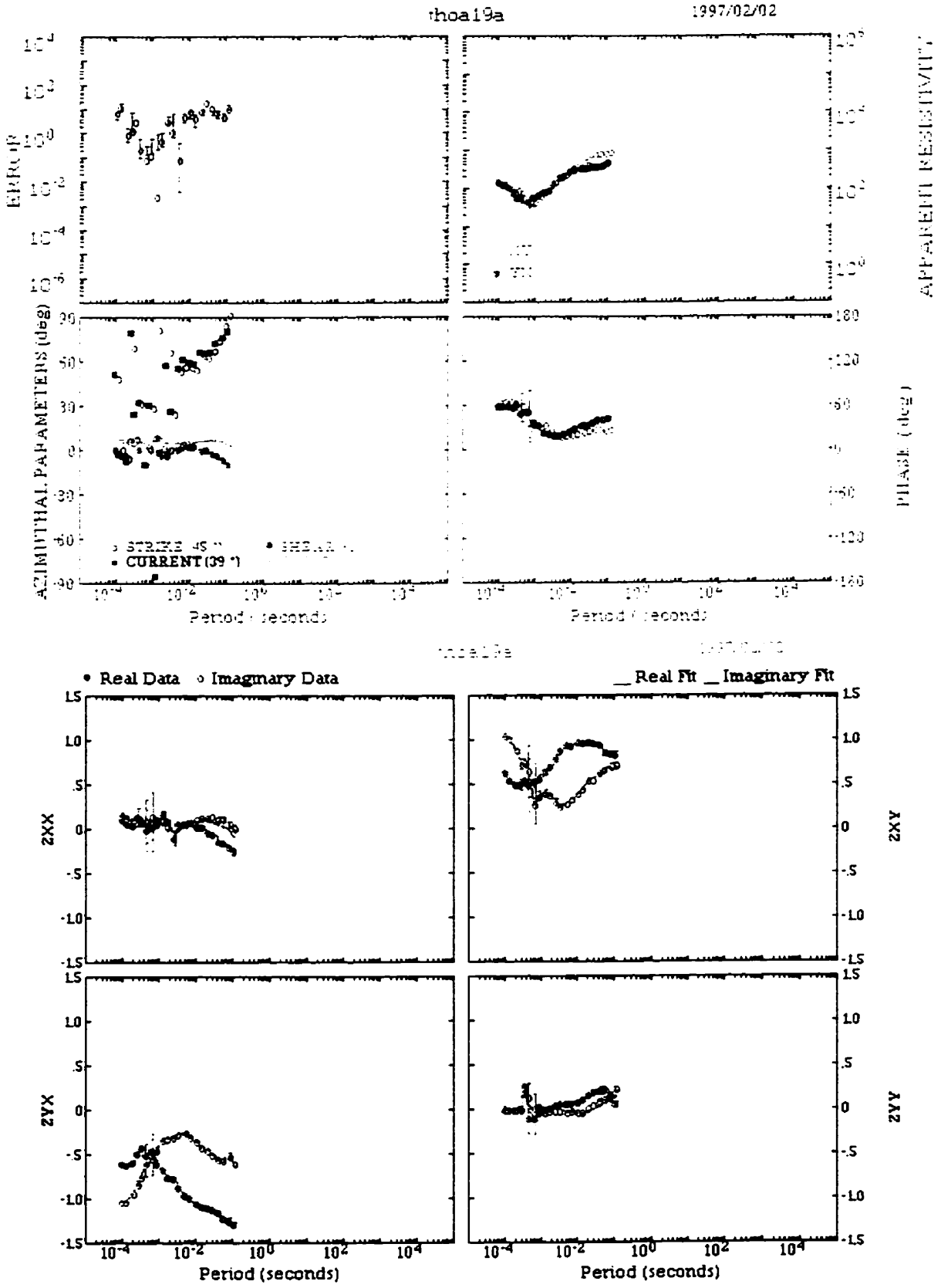
thoa19a
1997/02/02
AZIMUTHAL PARAMETERS (deg)
APPARENT RESISTIVITY
PHASE (deg)
CURRENT (39 °)
Period (seconds)
• Real Data ○ Imaginary Data
_ Real Fit _ Imaginary Fit
ZXX
ZXY
ZYX
ZYY
Period (seconds)

THO-92-A19A

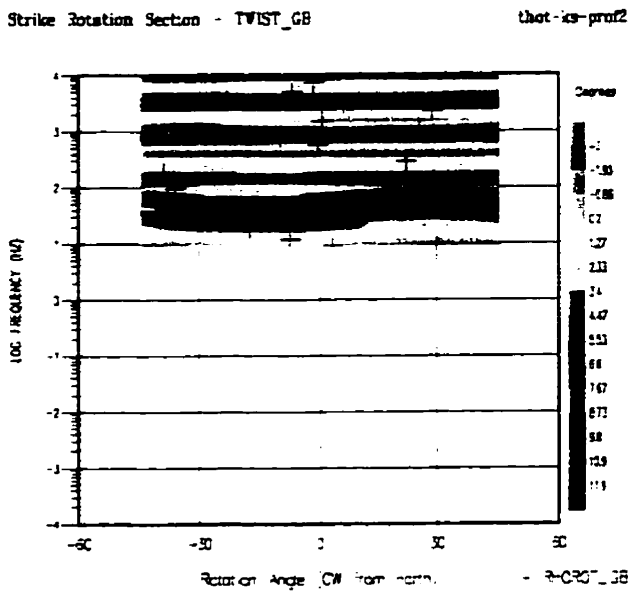
Strike Rotation Section - TWIST_GB
thot-ks-prof2
Degrees
LOG FREQUENCY (Hz)
-60
-30
0
30
60
Rotation Angle (CW from north)

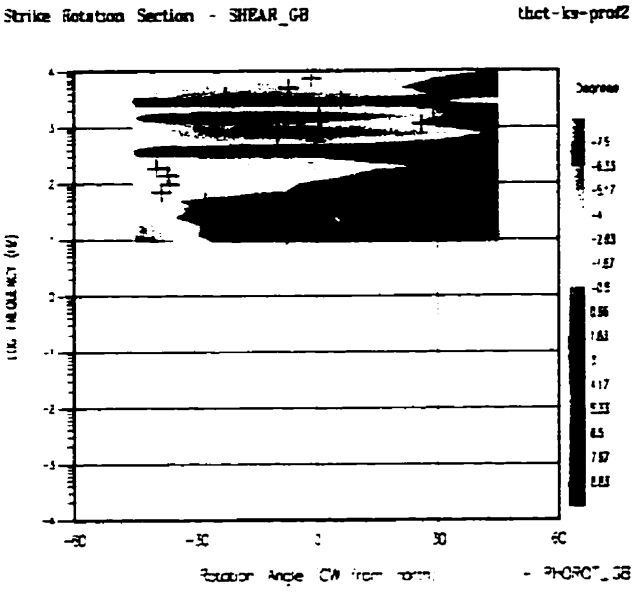
Strike Rotation Section - SHEAR_GB
thot-ks-prof2
Degrees
LOG FREQUENCY (Hz)
-60
-30
0
30
60
Rotation Angle (CW from north)

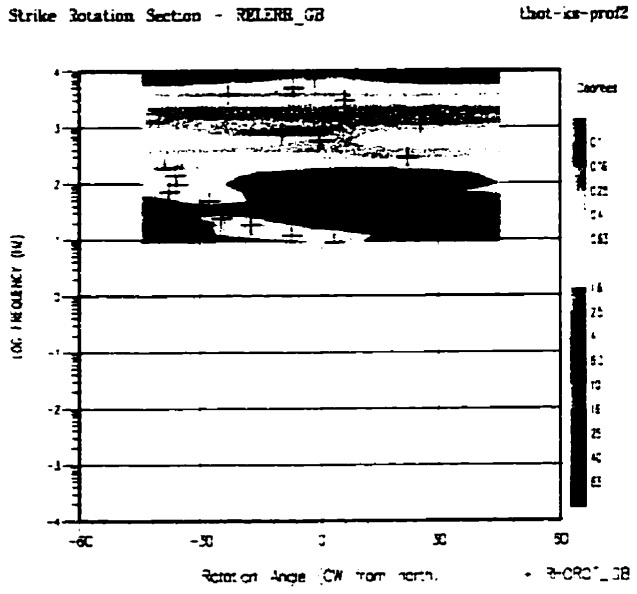
Strike Rotation Section - RELERR_GB
thot-ks-prof2
Degrees
LOG FREQUENCY (Hz)
-60
-30
0
30
60
Rotation Angle (CW from north)

THO-92-M20S

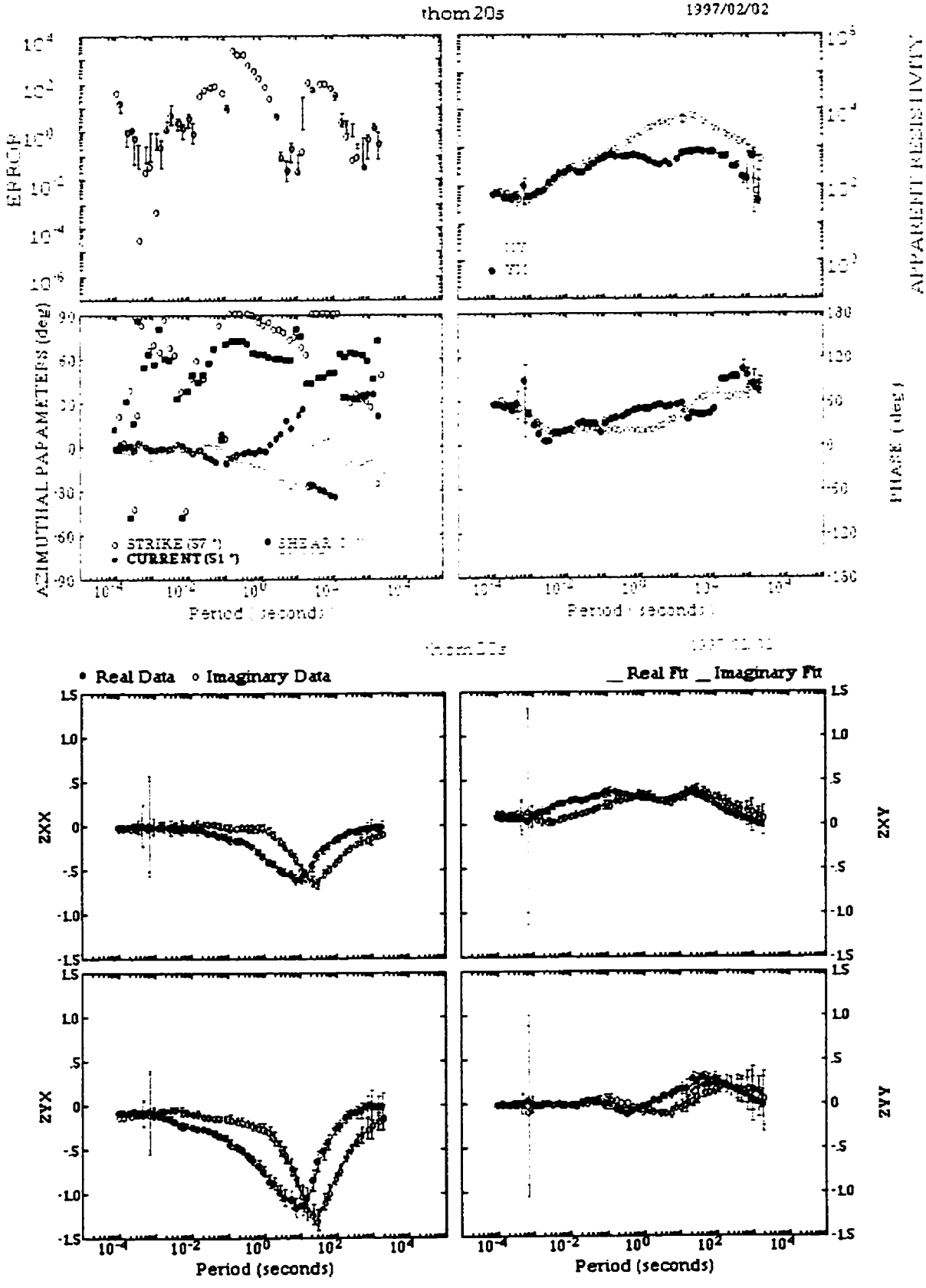
thom20s
1997/02/02
ERROR
APPARENT RESISTIVITY
AZIMUTHAL PAPAMETERS (deg)
PHASE (deg)
STRIKE (57 °)
CURRENT (51 °)
Period (seconds)
Real Data
Imaginary Data
Real Fit
Imaginary Fit
ZXX
ZXY
ZYX
ZYY
Period (seconds)

THO-92-M20S

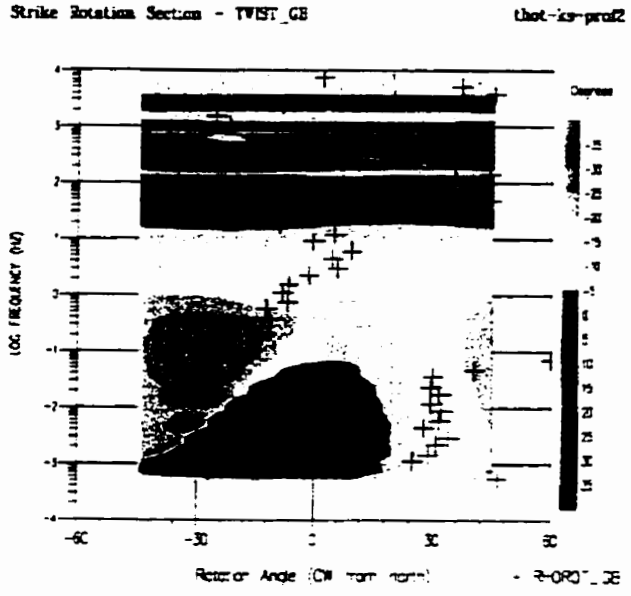
Strike Rotation Section - TWIST_GB
thot-ks-prof2
Degrees
LOG FREQUENCY (Hz)
-60
-30
0
30
60
Rotation Angle (CW from north)

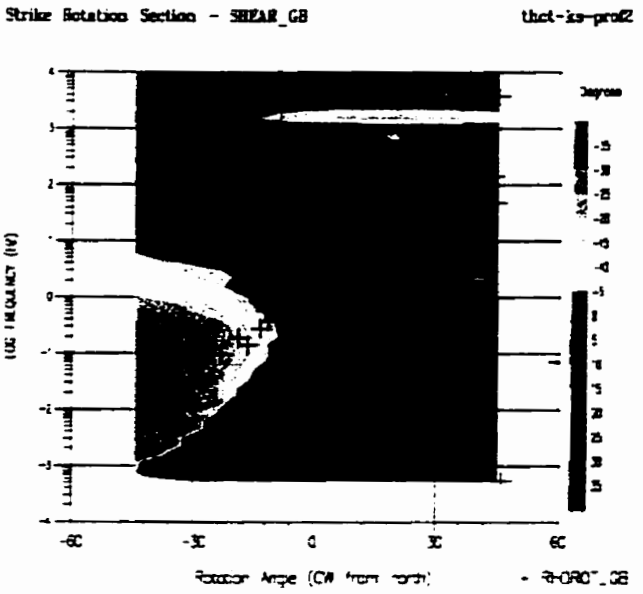
Strike Rotation Section - SHEAR_GB
thot-ks-prof2
Degrees
LOG FREQUENCY (Hz)
-60
-30
0
30
60
Rotation Angle (CW from north)

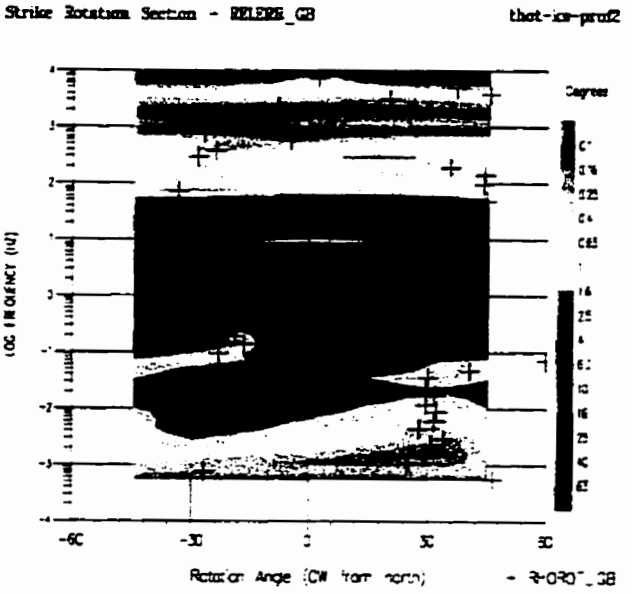
Strike Rotation Section - RELERR_GB
thot-ks-prof2
Degrees
LOG FREQUENCY (Hz)
-60
-30
0
30
60
Rotation Angle (CW from north)

THO-92-A18A

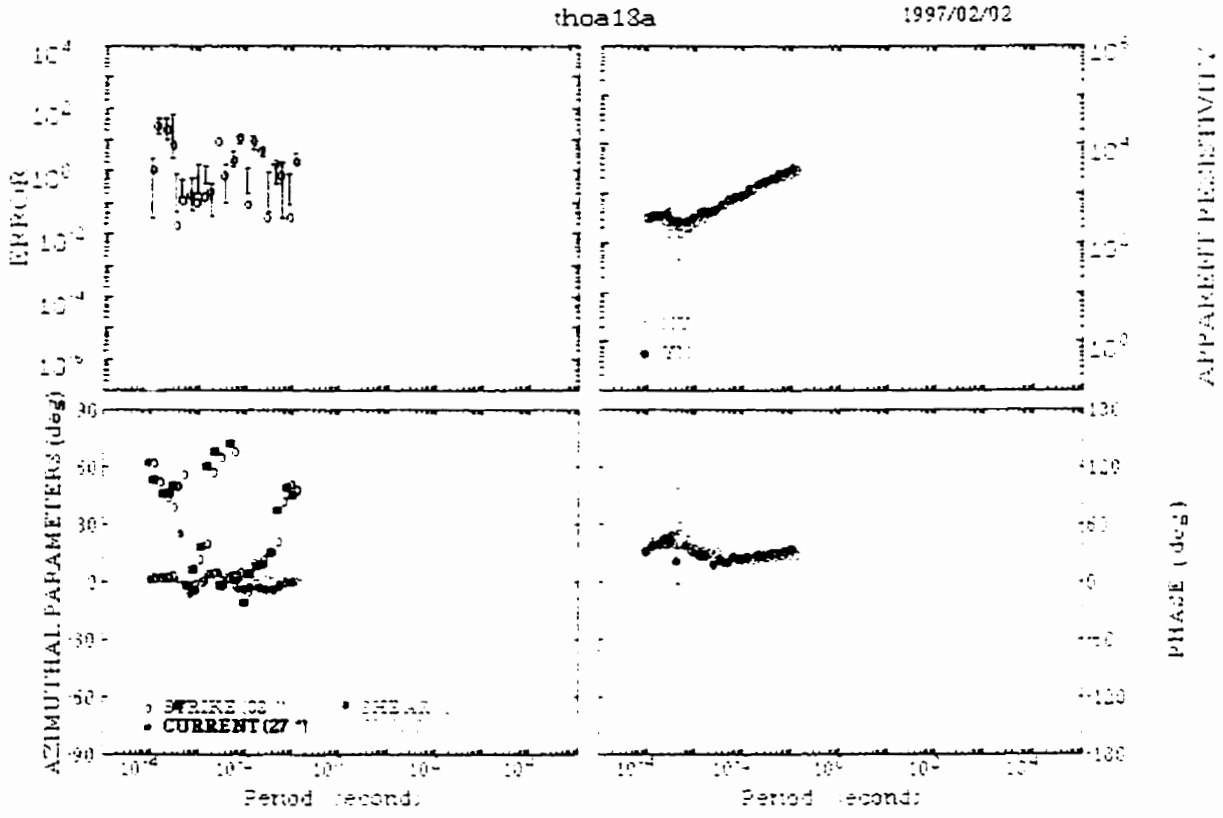
thoa18a
1997/02/02
ERROR
AZIMUTHAL PARAMETERS (deg)
APPARENT RESISTIVITY
PHASE (deg)
CURRENT (27 °)
Period (seconds)
Period (seconds)

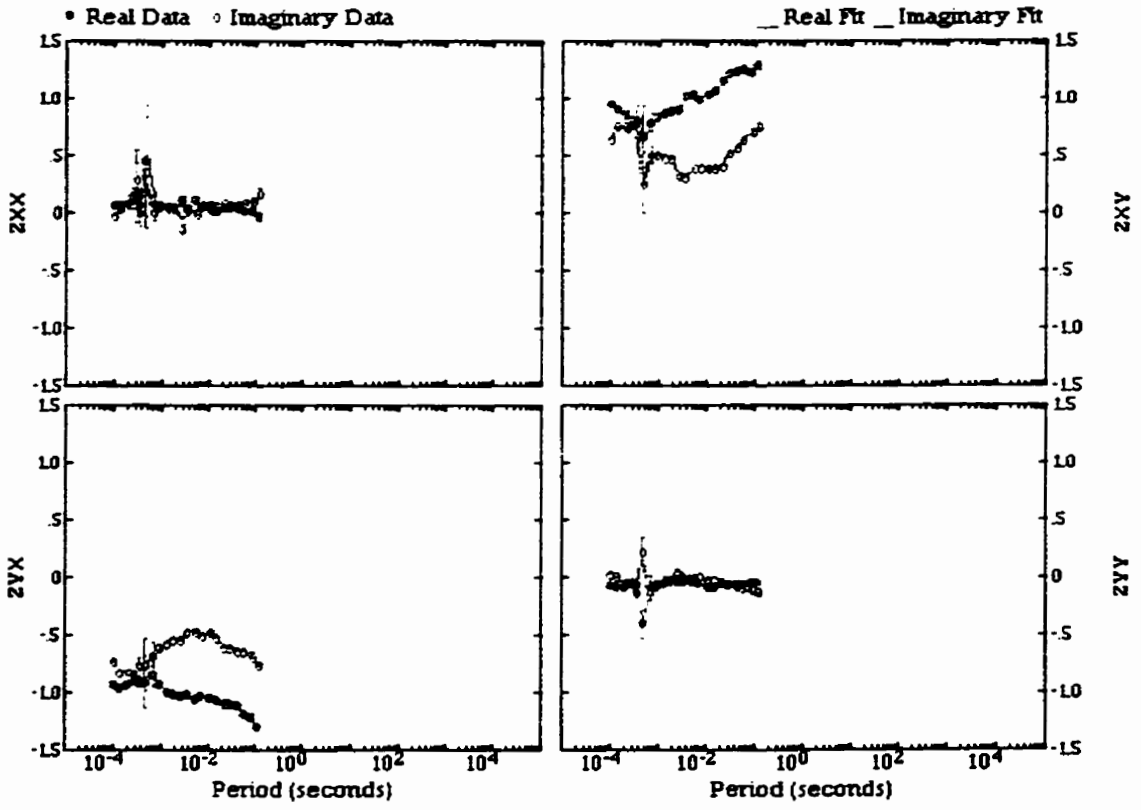
• Real Data ◦ Imaginary Data
_ Real Fit _ Imaginary Fit
ZXX
ZXY
ZYX
ZYY
Period (seconds)
Period (seconds)

THO-92-A18A

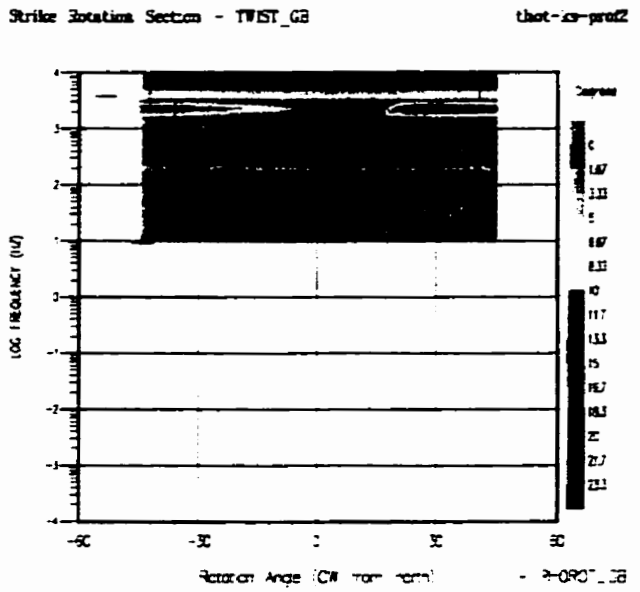
Strike Rotation Section - TWIST_GB
thot-ks-prof2
LOG FREQUENCY (Hz)
Rotation Angle (CW from norm)

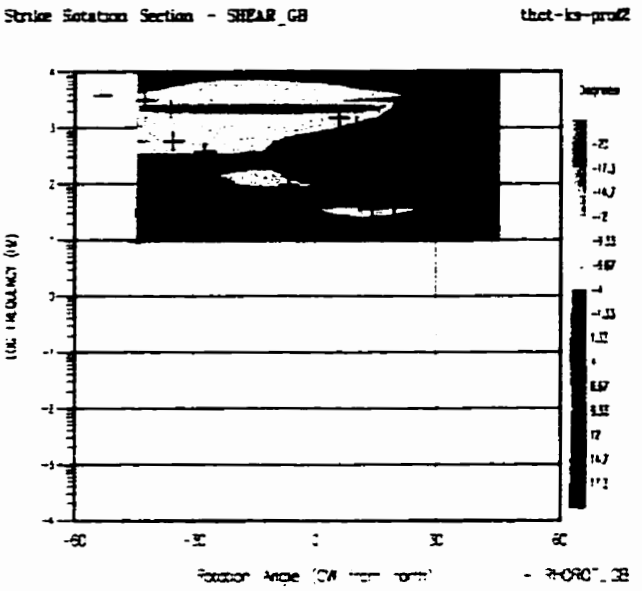
Strike Rotation Section - SHEAR_GB
thot-ks-prof2
LOG FREQUENCY (Hz)

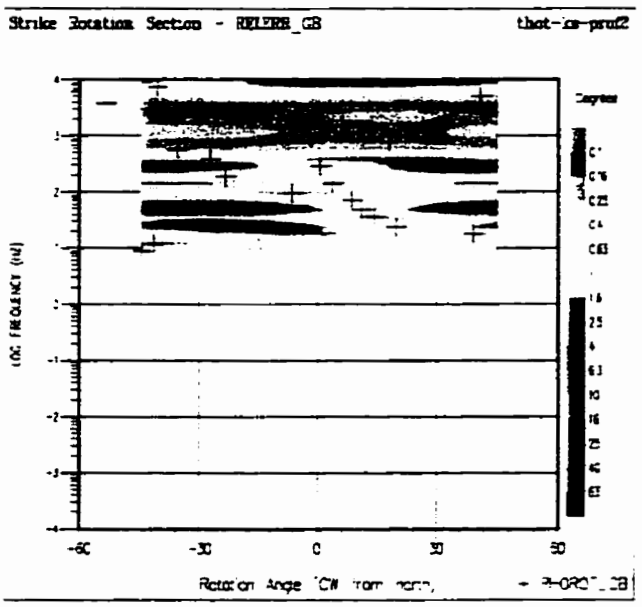
Strike Rotation Section - RELERR_GB
thot-ks-prof2
LOG FREQUENCY (Hz)
-60
-30
0
30
60

THO-92-M19S

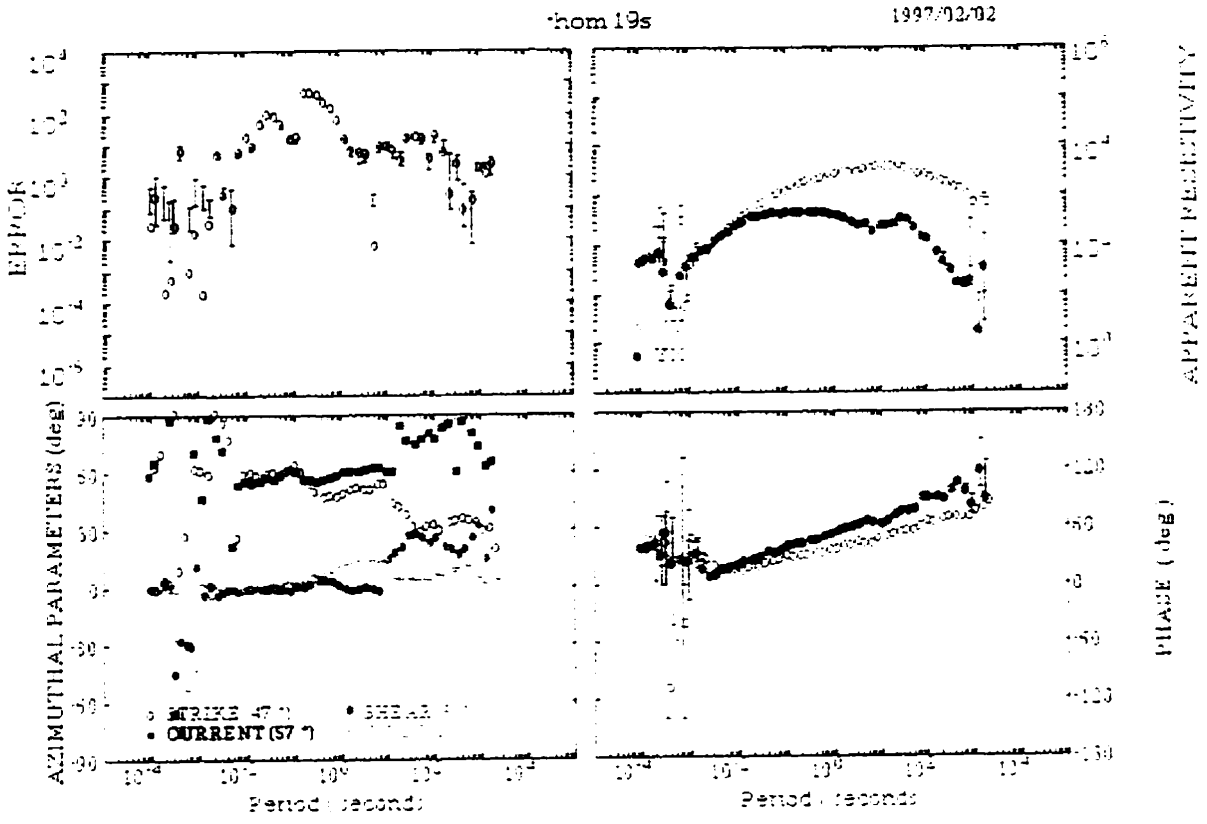
thom19s
1997/02/02
APPARENT RESISTIVITY
PHASE (deg)
AZIMUTHAL PARAMETERS (deg)
STRIKE
SHEAR
CURRENT (57 °)
Period (seconds)

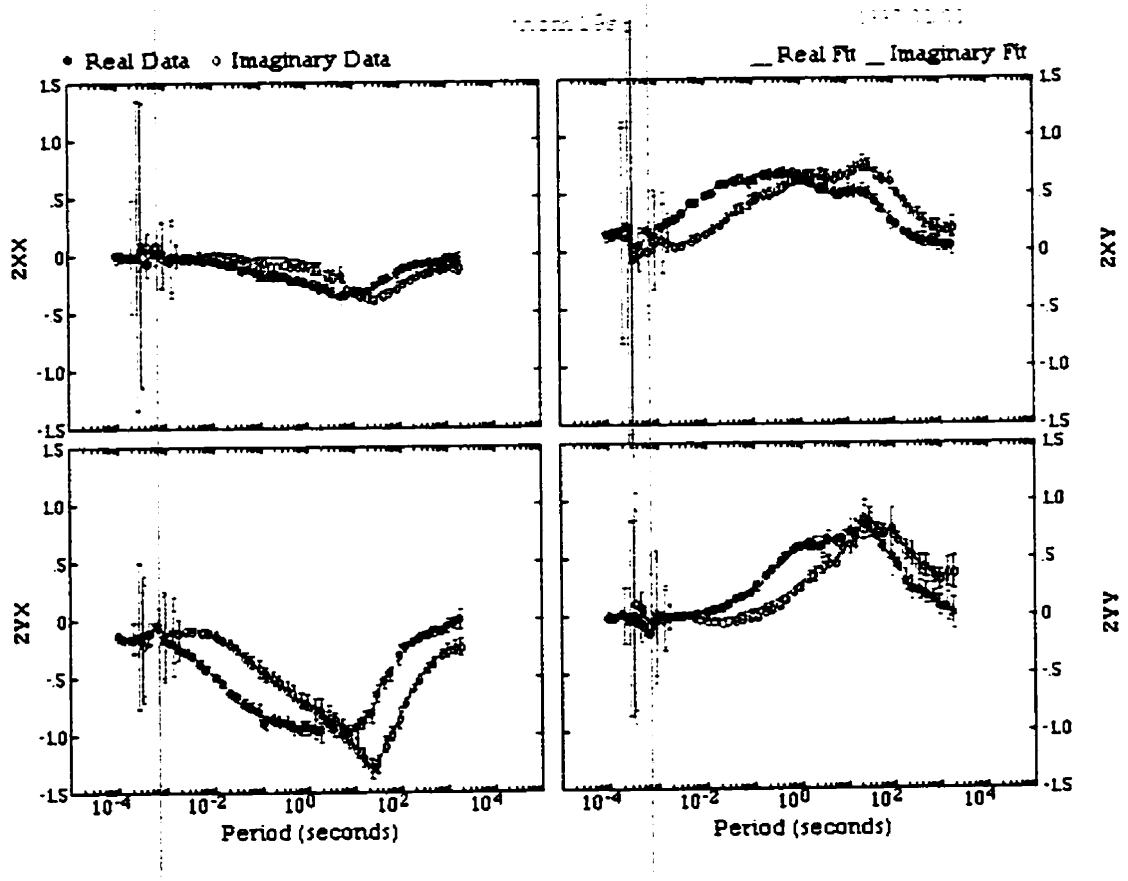
• Real Data ○ Imaginary Data
_ Real Fit _ Imaginary Fit
ZXX
ZXY
ZYX
ZYY
Period (seconds)

THO-92-M19S

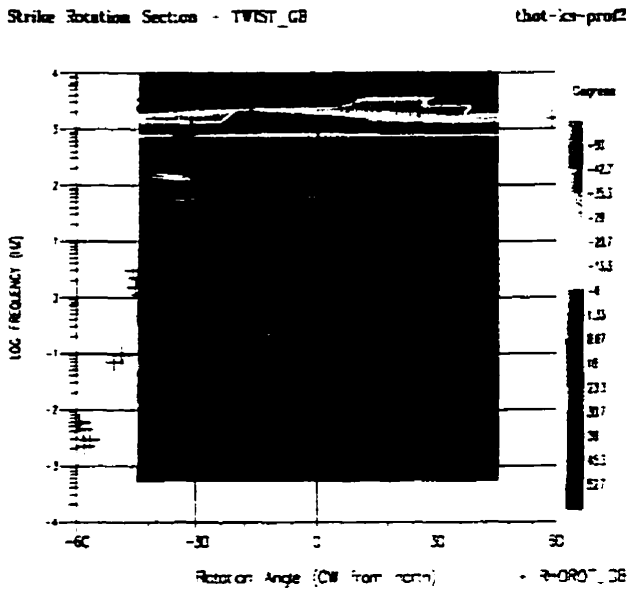
Strike Rotation Section - TWIST_GB
thot-ks-prof2
LOG FREQUENCY (Hz)
Degrees
-60
-30
0
30
60
Rotation Angle (CW from north)

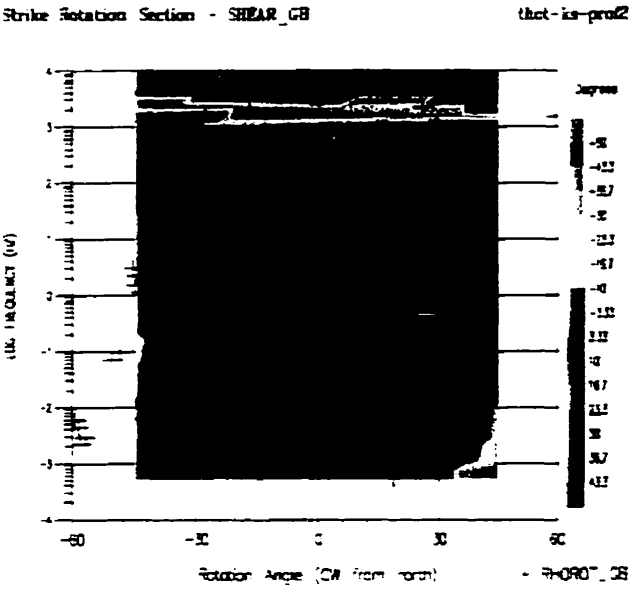
Strike Rotation Section - SHEAR_GB
thot-ks-prof2
LOG FREQUENCY (Hz)
Degrees
-60
-30
0
30
60
Rotation Angle (CW from north)

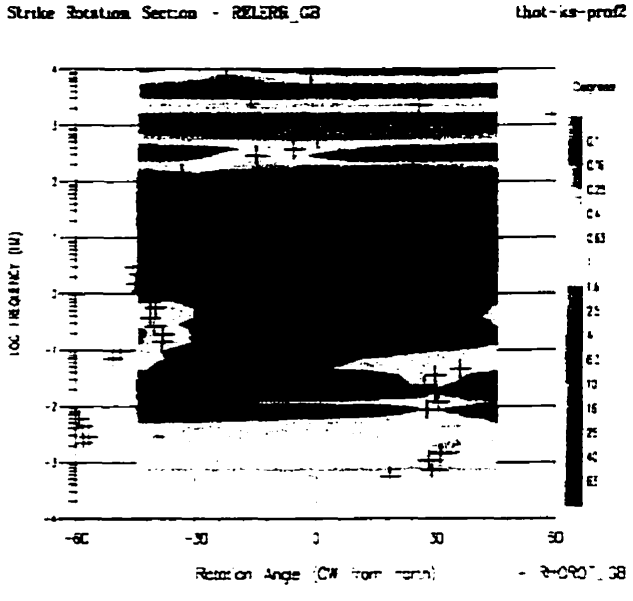
Strike Rotation Section - RELERR_GB
thot-ks-prof2
LOG FREQUENCY (Hz)
Degrees
-60
-30
0
30
60
Rotation Angle (CW from north)

THO-92-A17A

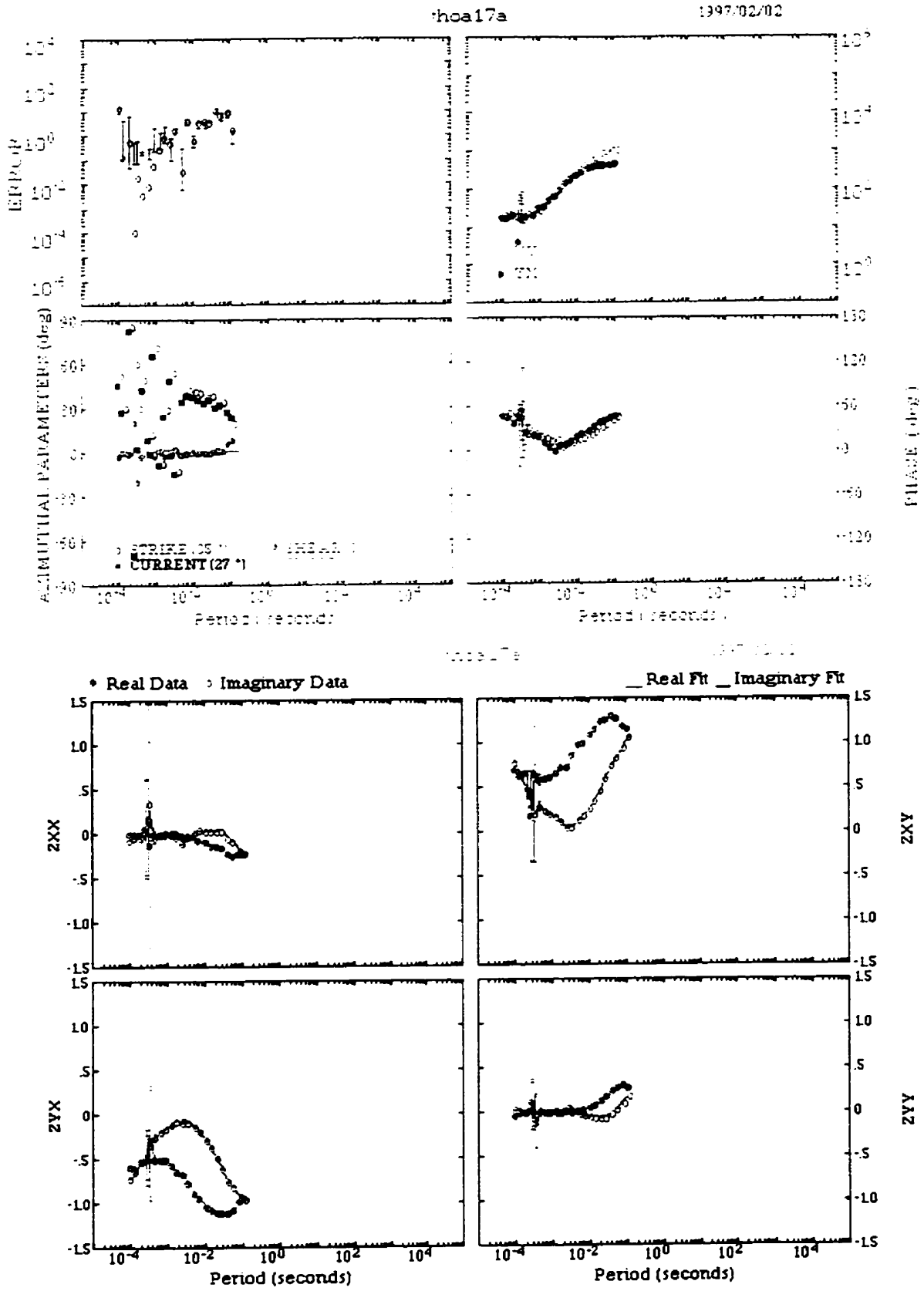
thoa17a
1997/02/02
CURRENT (27 °)
Period (seconds)
Real Data
Imaginary Data
Real Fit
Imaginary Fit
ZXX
ZXY
ZYX
ZYY
Period (seconds)
Period (seconds)

THO-92-A17A

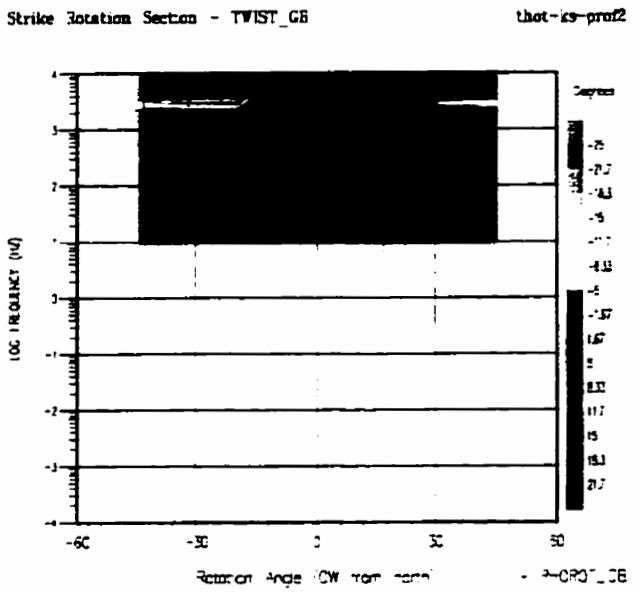
Strike Rotation Section - TWIST_GB
thot-ics-prof2
LOG FREQUENCY (Hz)
-60
-30
0
30
60
Rotation Angle (CW from horn)
- PHOROT_GB

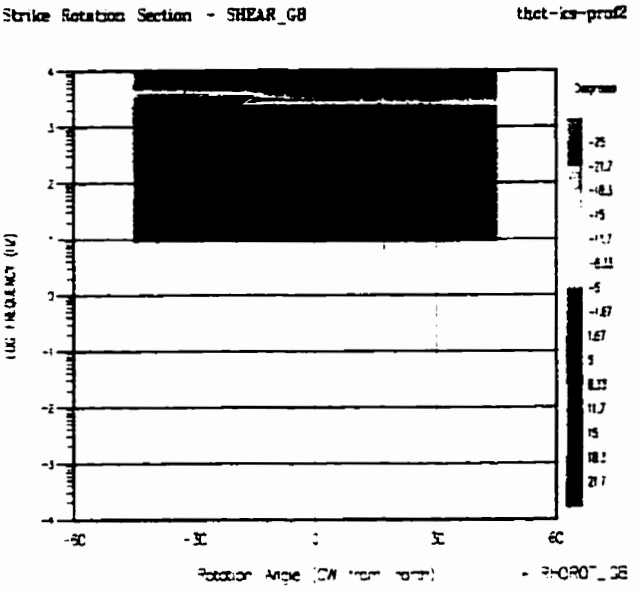
Strike Rotation Section - SHEAR_GB
thot-ics-prof2
LOG FREQUENCY (Hz)
-60
-30
0
30
60
Rotation Angle (CW from horn)
- PHOROT_GB

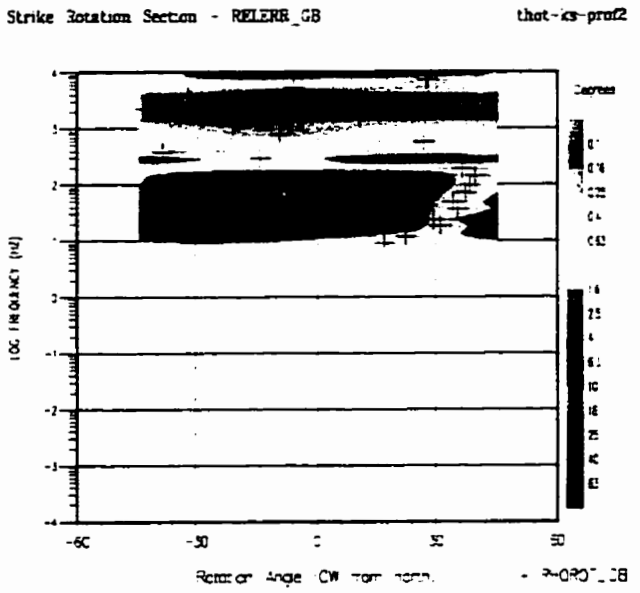
Strike Rotation Section - RELERR_GB
thot-ics-prof2
LOG FREQUENCY (Hz)
-60
-30
0
30
60
Rotation Angle (CW from horn)
- PHOROT_GB

THO-92-M18S

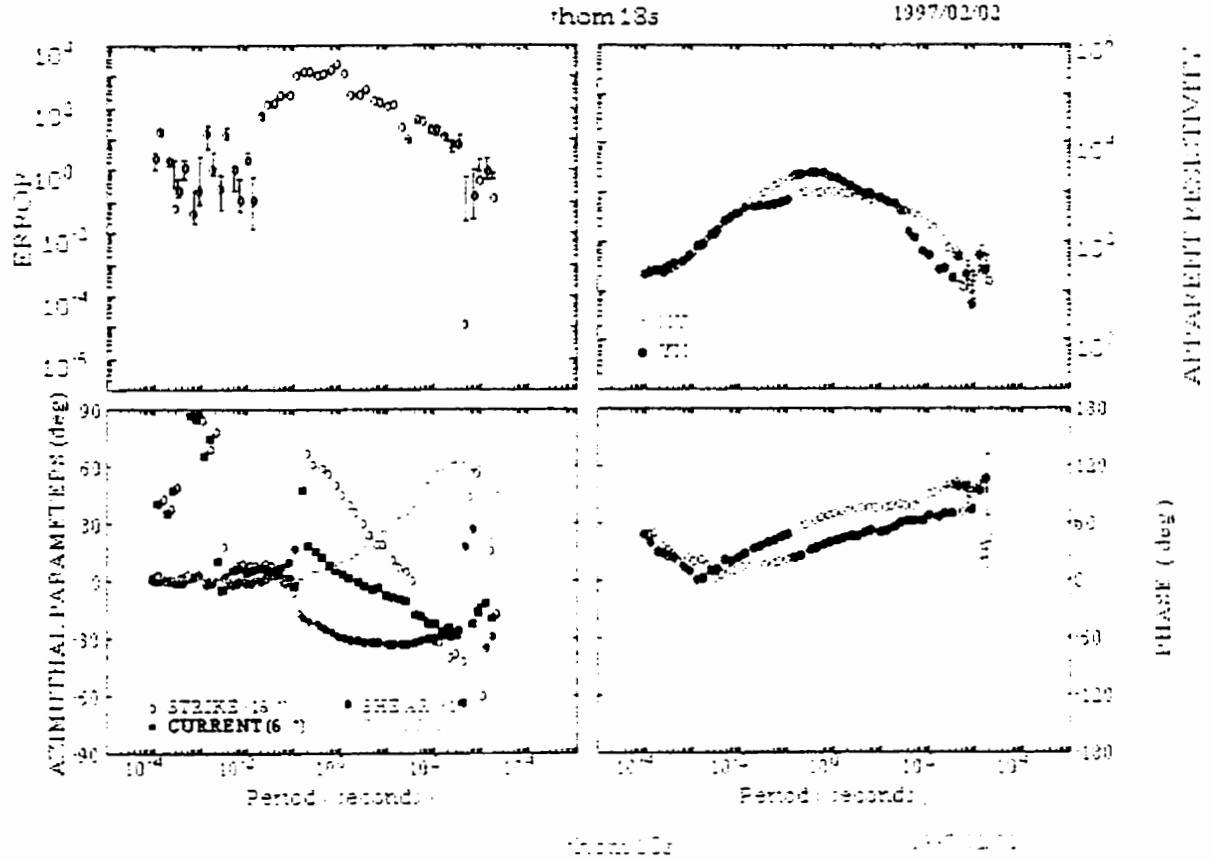
thom18s
1997/02/02
ERROR
AZIMUTHAL PARAMETERS (deg)
STRIKE (6 °)
CURRENT (6 °)
Period (seconds)
APPARENT RESISTIVITY
PHASE (deg)

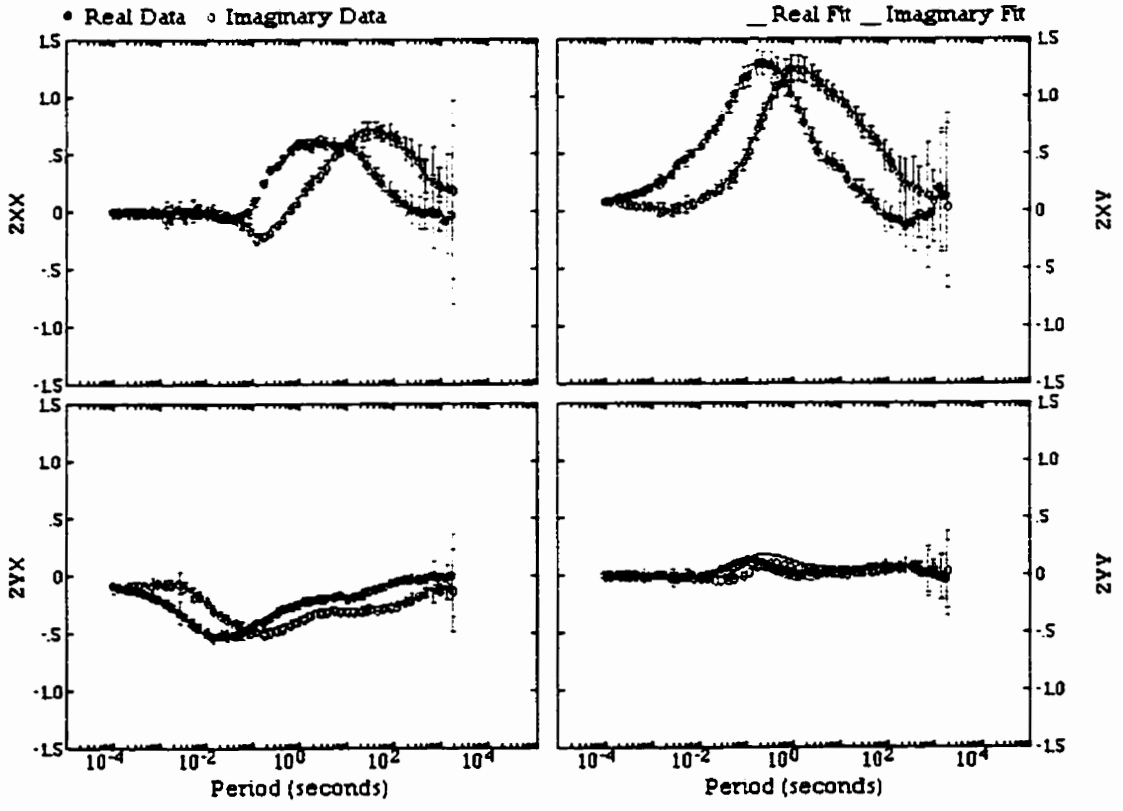
Real Data
Imaginary Data
Real Fit
Imaginary Fit
ZXX
ZXY
ZYX
ZYY
Period (seconds)
Period (seconds)

THO-92-M18S

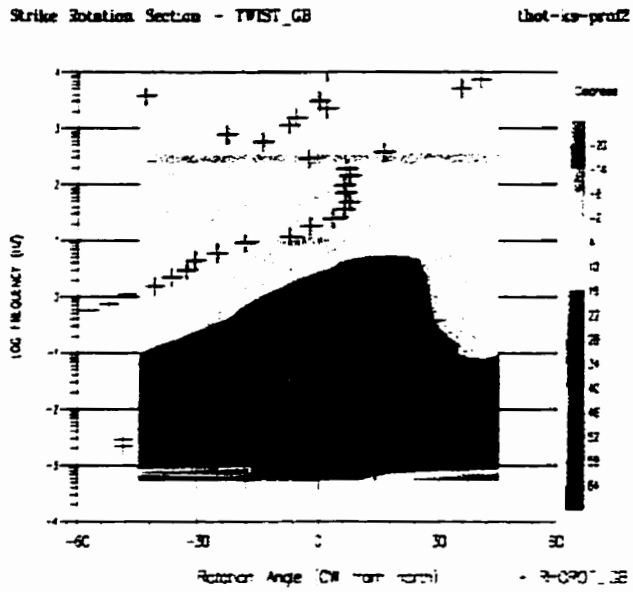
Strike Rotation Section - TWIST_GB
thot-ics-prof2
Degrees
LOG FREQUENCY (Hz)
-60
-30
0
30
60
Rotation Angle (CW from north)

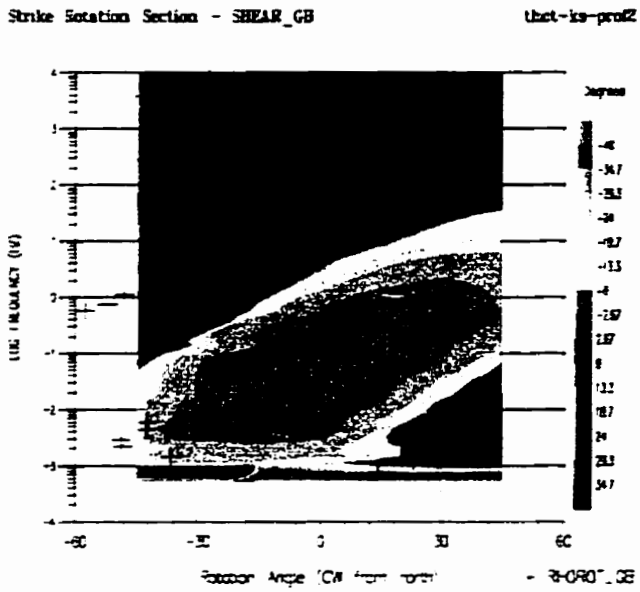
Strike Rotation Section - SHEAR_GB
thot-ics-prof2
Degrees
LOG FREQUENCY (Hz)
-60
-30
0
30
60
Rotation Angle (CW from north)

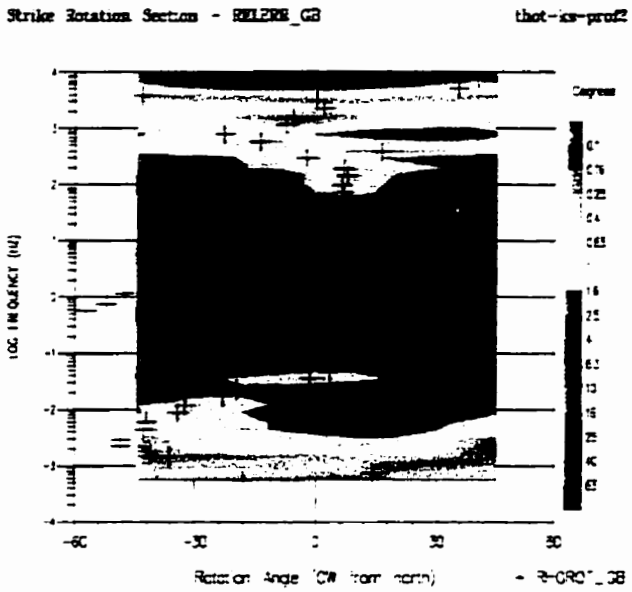
Strike Rotation Section - RELZRR_GB
thot-ics-prof2
Degrees
LOG FREQUENCY (Hz)
-60
-30
0
30
60
Rotation Angle (CW from north)

THO-92-M16S

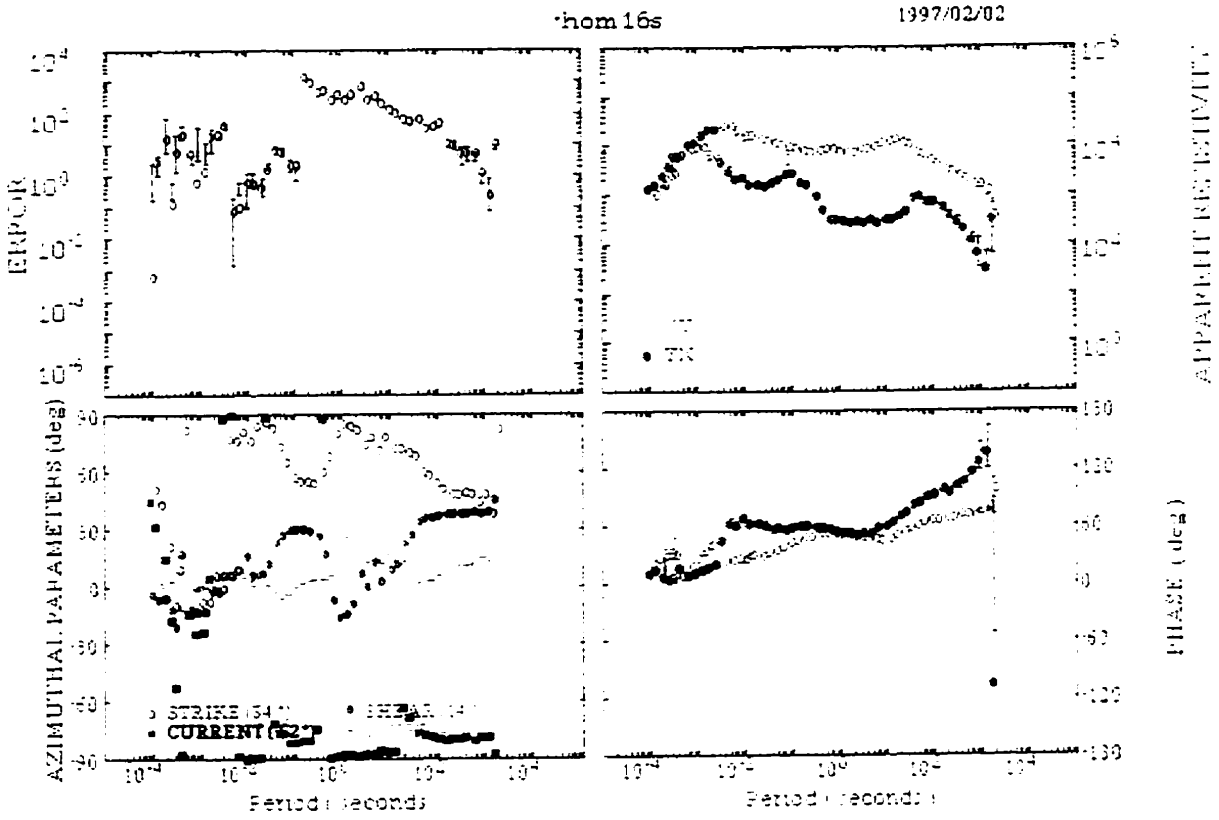
thom16s
1997/02/02
ERROR
AZIMUTHAL PARAMETERS (deg)
APPARENT RESISTIVITY
PHASE (deg)
Period (seconds)
CURRENT

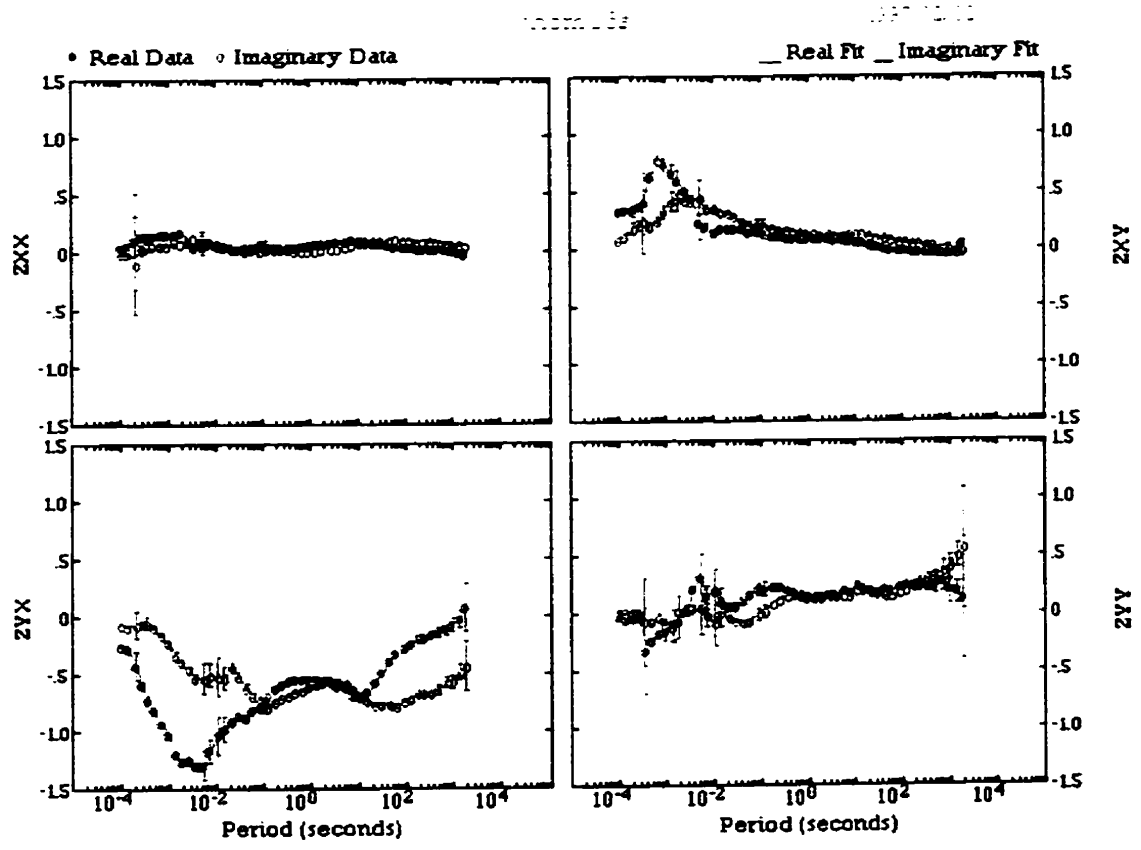
Real Data
Imaginary Data
Real Fit
Imaginary Fit
ZXX
ZXY
ZYX
ZYY
Period (seconds)

THO-92-M16S

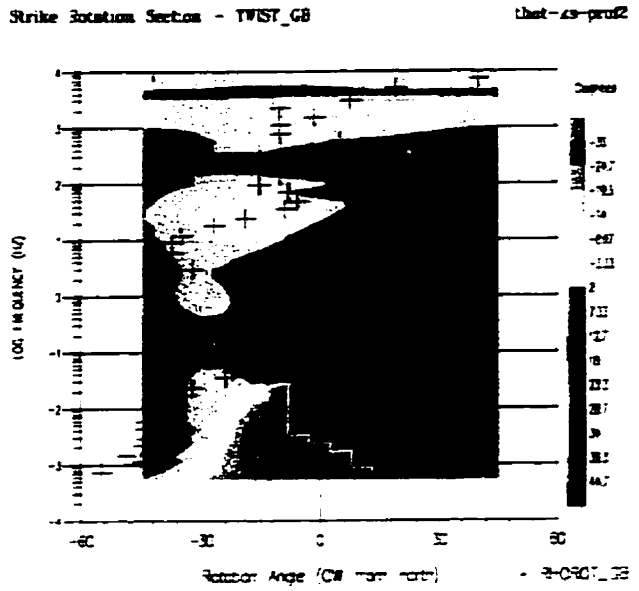
Strike Rotation Section - TWIST_GB
-60
-30
0
30
60
Rotation Angle (CW from north)

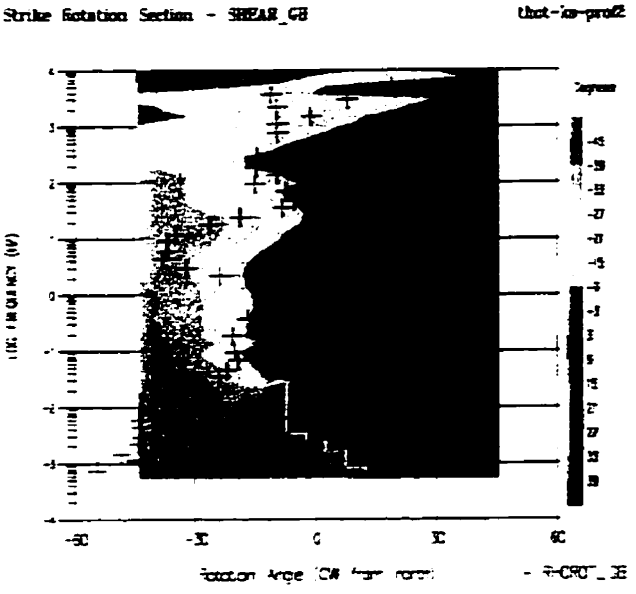
Strike Rotation Section - SHEAR_GB
-60
-30
0
30
60
Rotation Angle (CW from north)

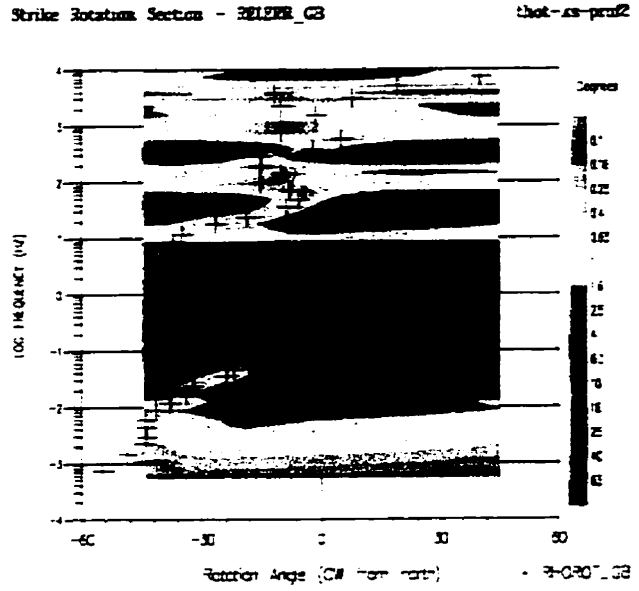
Strike Rotation Section
-60
-30
0
30
60
Rotation Angle (CW from north)

DTH009

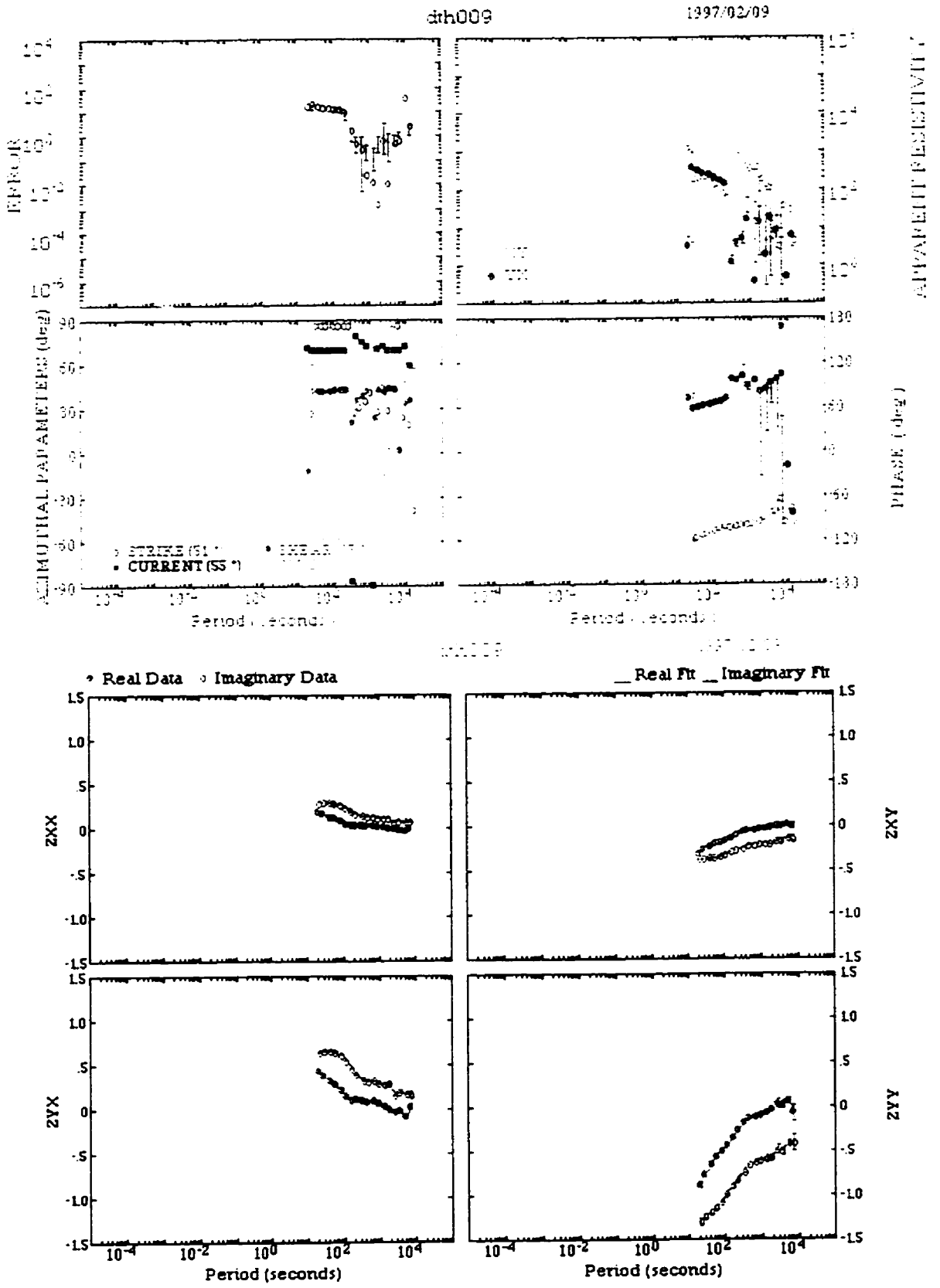
dth009
1997/02/09
AZIMUTHAL PARAMETERS (deg)
STRIKE (51°)
CURRENT (55°)
Period (seconds)
Real Data
Imaginary Data
Real Fit
Imaginary Fit
ZXX
ZXY
ZYX
ZYY
Period (seconds)

DTH009

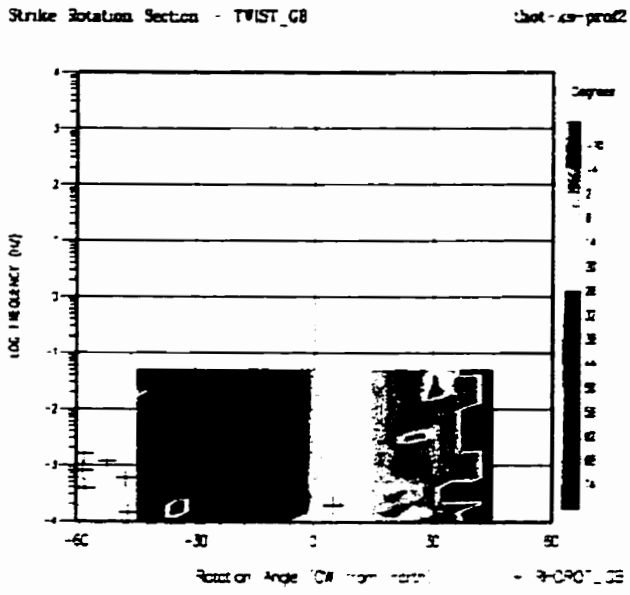
Strike Rotation Section - TWIST_G8
-60
-30
0
30
60

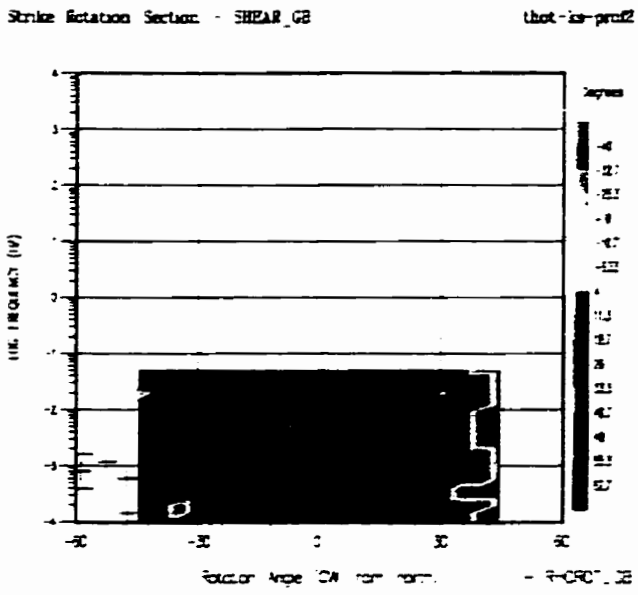
Strike Rotation Section - SHEAR_G8
-60
-30
0
30
60

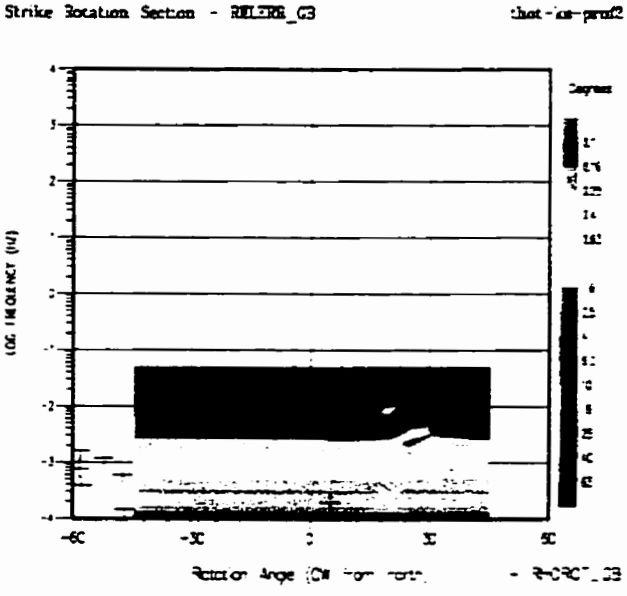
Strike Rotation Section - BELTRR_G3
-60
-30
0
30
60

THO-92-M15S

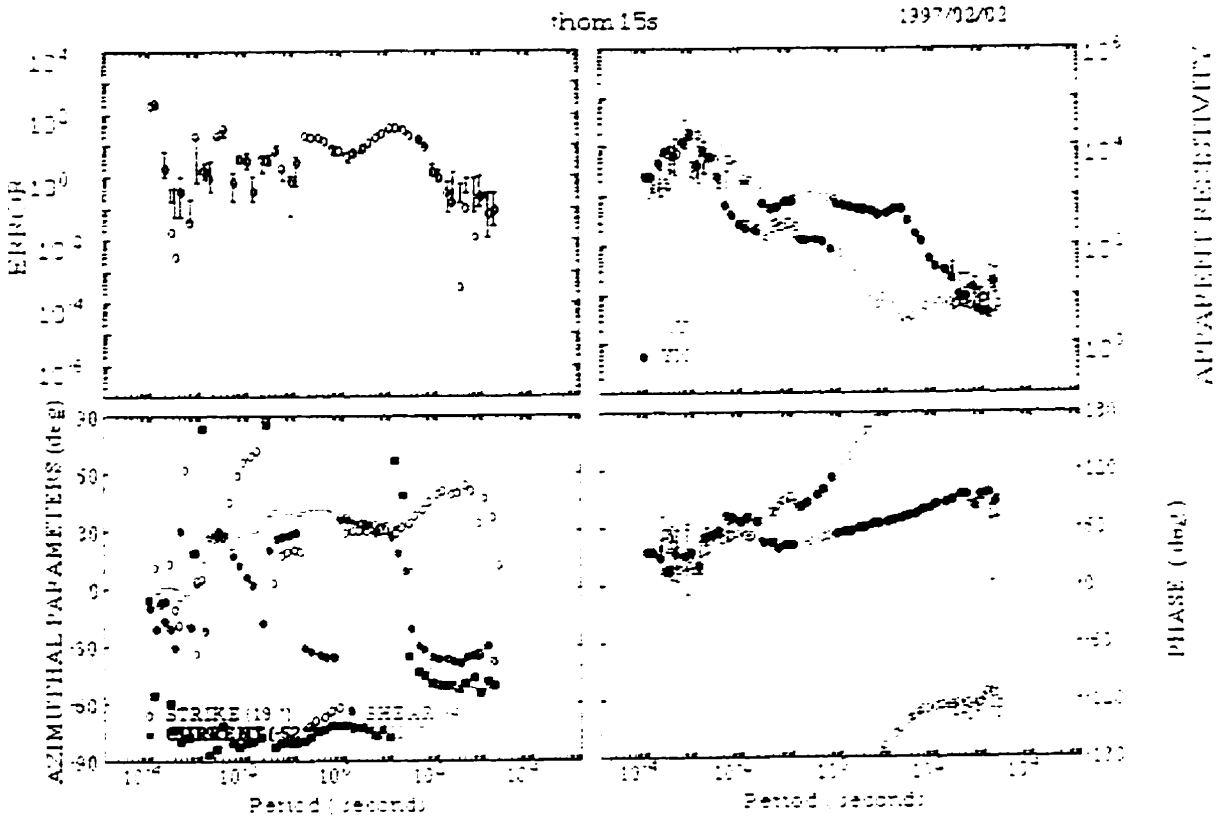
thom15s
1997/02/02
AZIMUTHAL PARAMETERS (deg)
Period (seconds)
PHASE (deg)

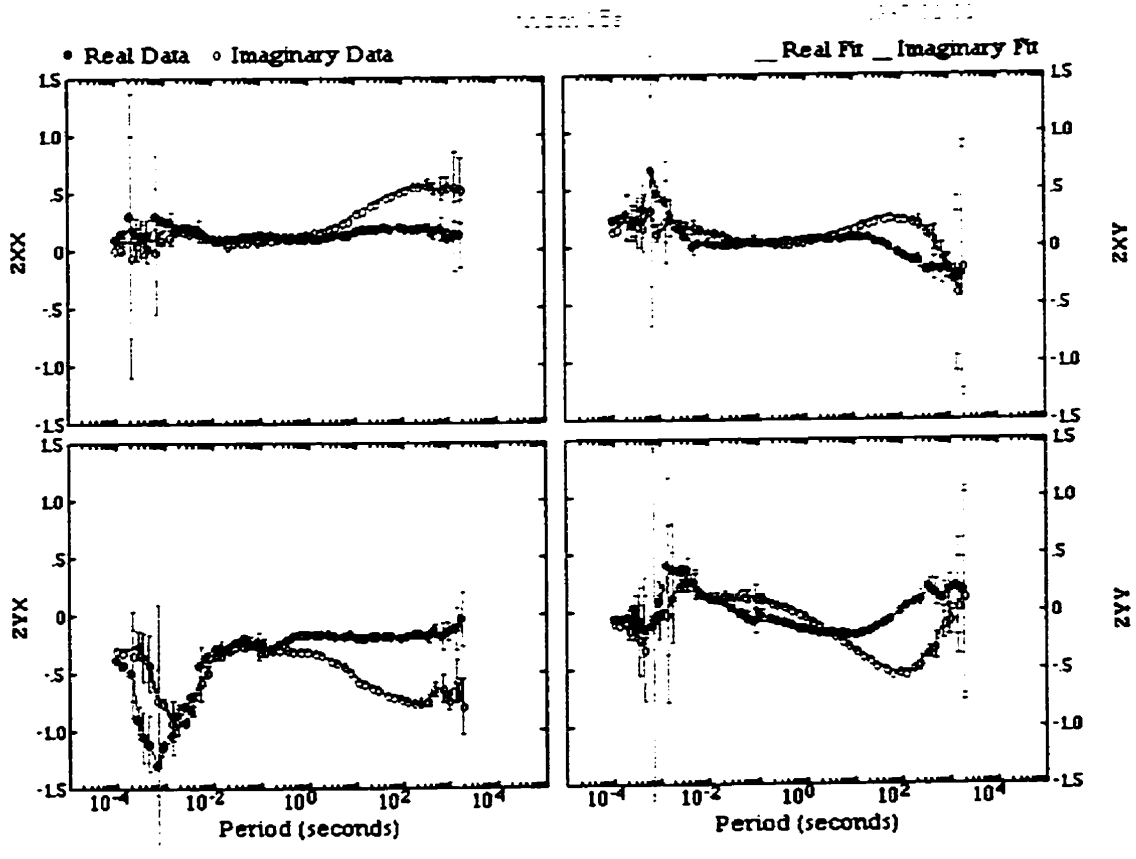
• Real Data ◦ Imaginary Data
_ Real Fit _ Imaginary Fit
ZXX
ZXY
ZYX
ZYY
Period (seconds)
Period (seconds)

THO-92-M15S

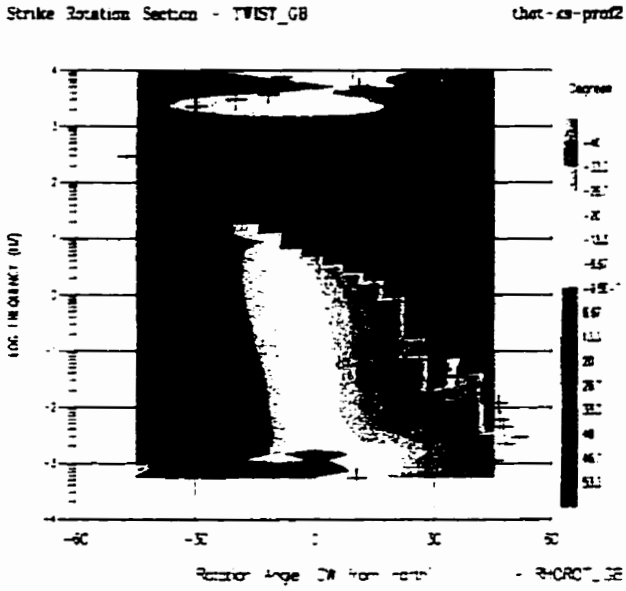
Strike Rotation Section - TWIST_GB
that-ks-prof2
Degrees
LOG FREQUENCY (HZ)
Rotor Angle CW from north

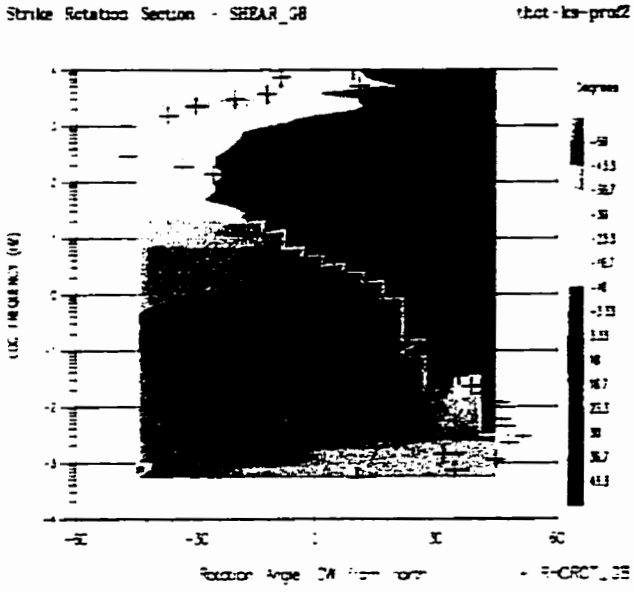
Strike Rotation Section - SHEAR_GB
that-ks-prof2
Degrees
LOG FREQUENCY (HZ)
Rotor Angle CW from north

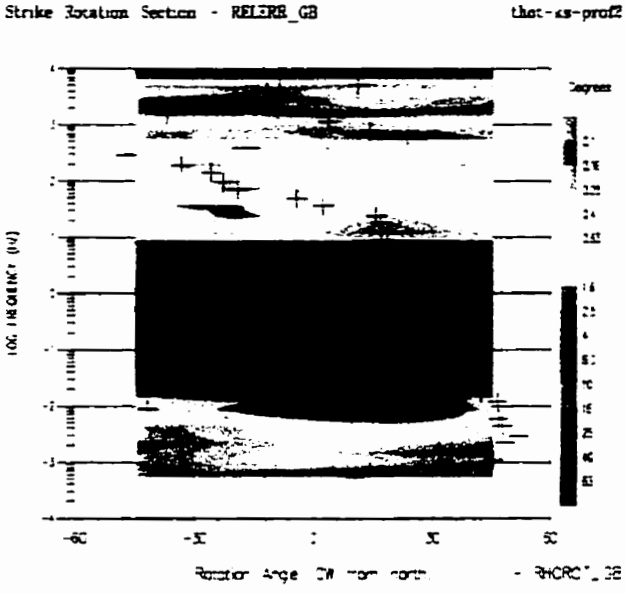
Strike Rotation Section - RELERR_GB
that-ks-prof2
Degrees
LOG FREQUENCY (HZ)
Rotor Angle CW from north

THO-92-A15A

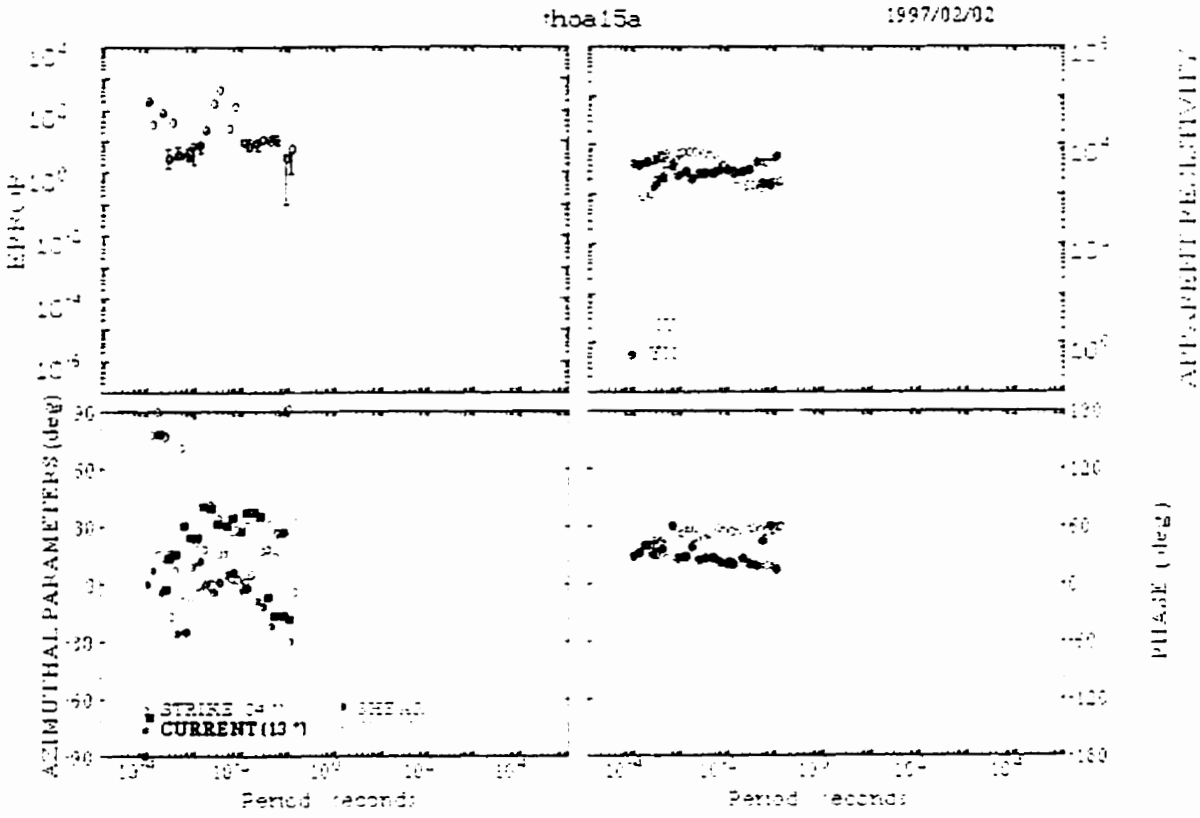
thoa15a
1997/02/02
AZIMUTHAL PARAMETERS (deg)
CURRENT (13 °)
Period (seconds)
Period (seconds)

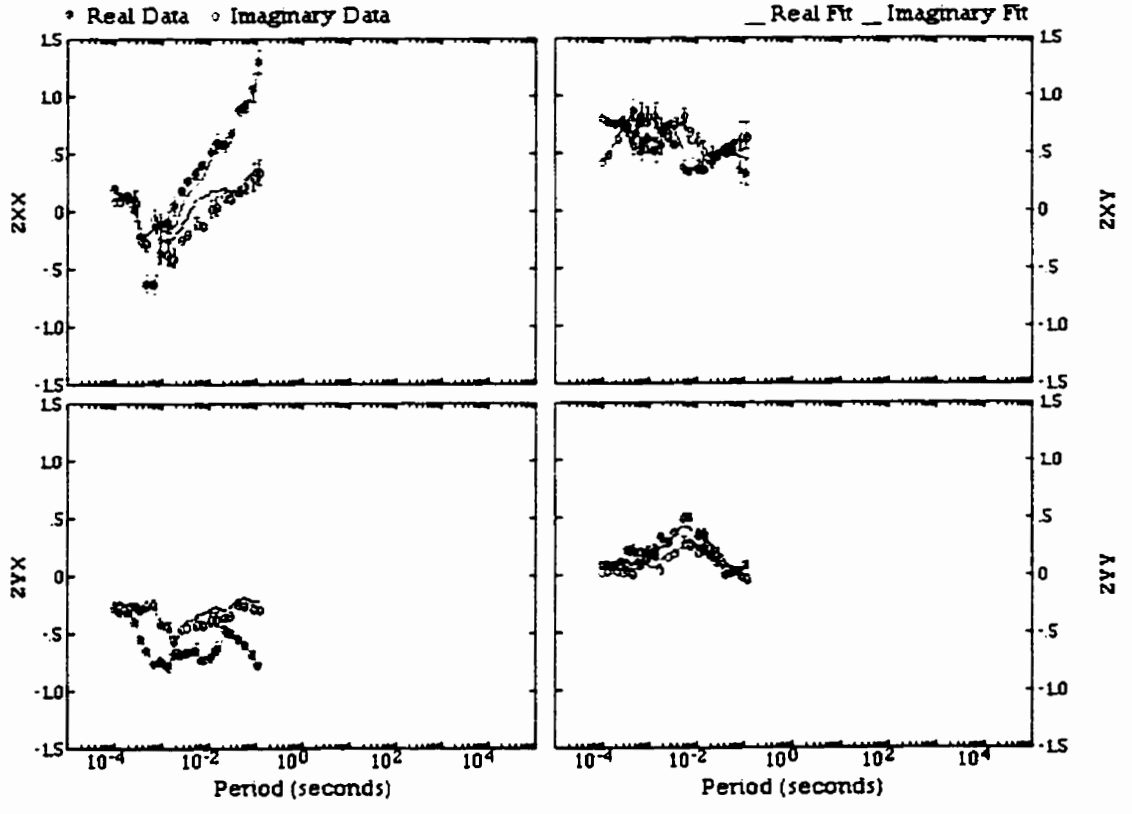
Real Data
Imaginary Data
Real Fit
Imaginary Fit
ZXX
ZXY
ZYX
ZYY
Period (seconds)
Period (seconds)

THO-92-A15A

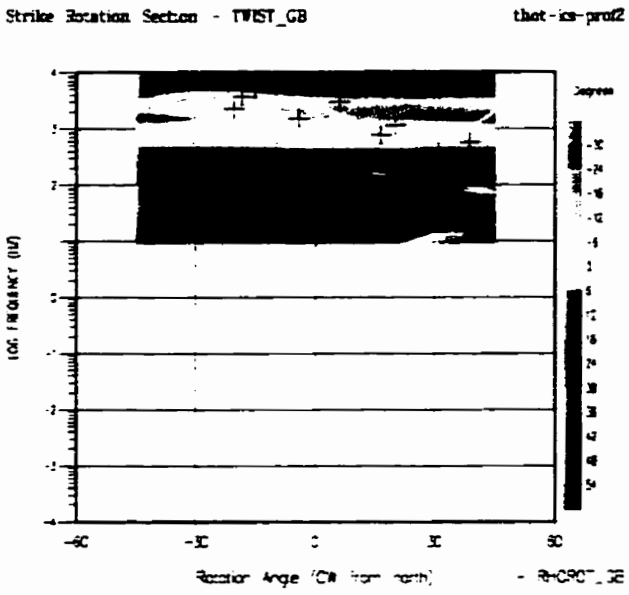
Strike Rotation Section - TWIST_GB
thot-ks-prof2
Degrees
LOG FREQUENCY (Hz)
Rotation Angle (CW from north)

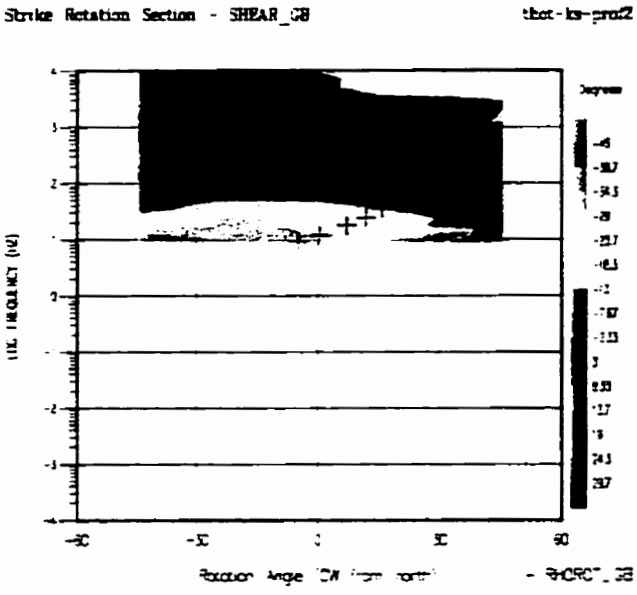
Strike Rotation Section - SHEAR_GB
thot-ks-prof2
Degrees
LOG FREQUENCY (Hz)
Rotation Angle (CW from north)

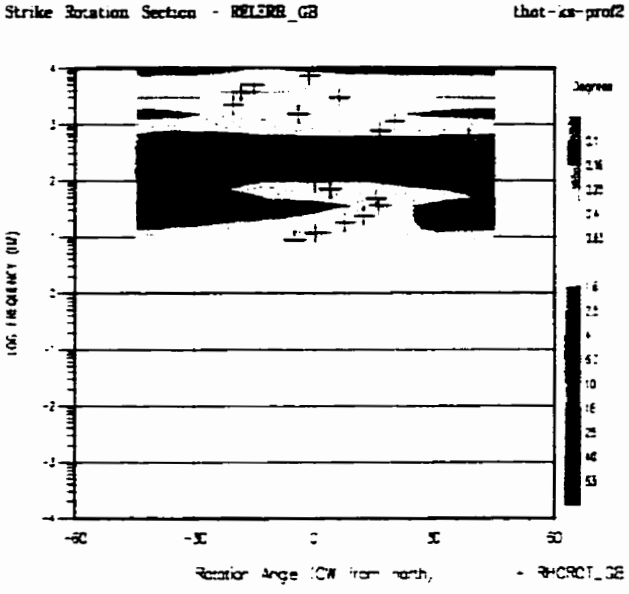
Strike Rotation Section - RELERR_GB
thot-ks-prof2
Degrees
LOG FREQUENCY (Hz)
Rotation Angle (CW from north)

THO-92-M13S

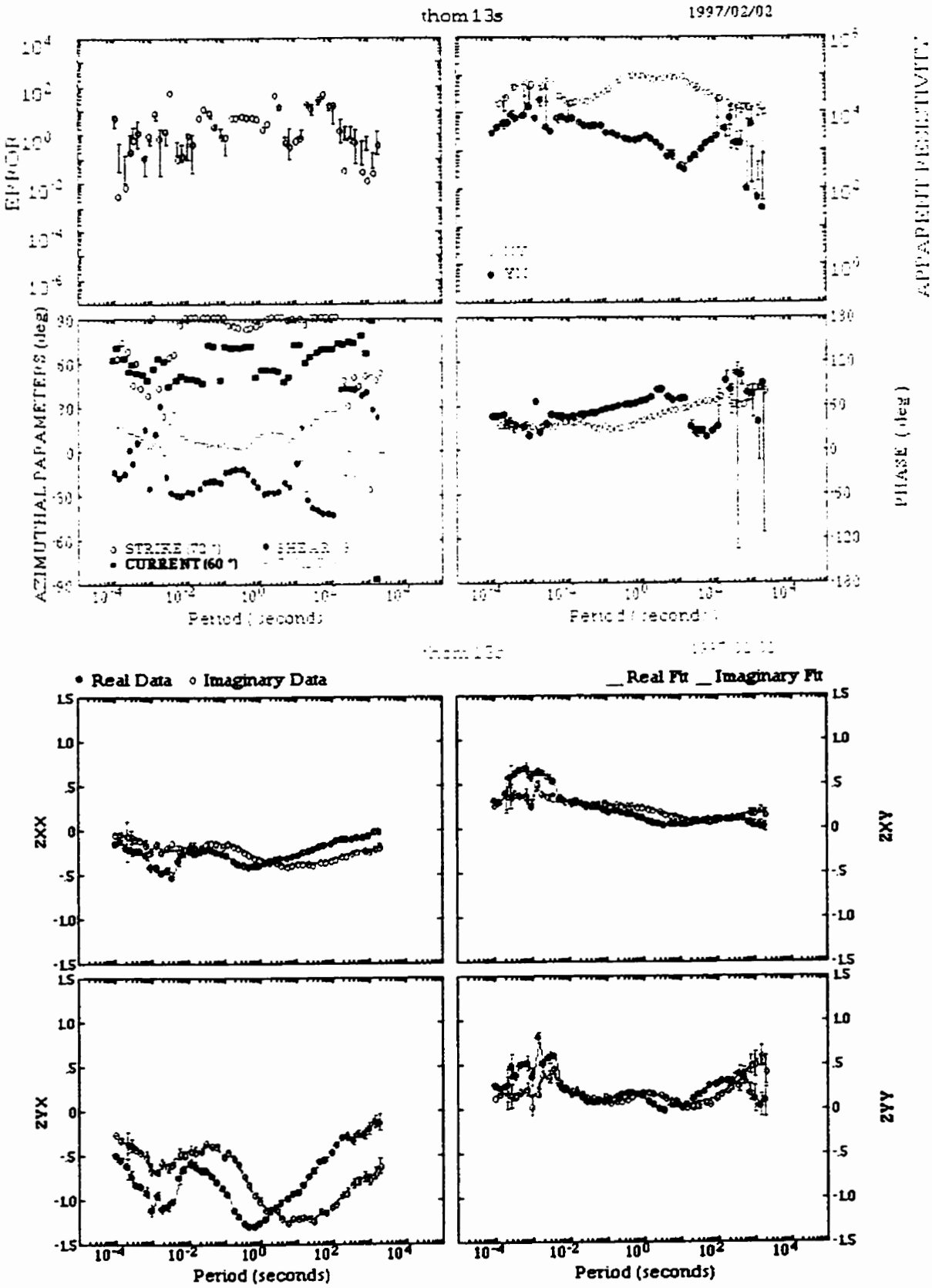
thom13s
1997/02/02
AZIMUTHAL PARAMETERS (deg)
CURRENT (60 °)
Period (seconds)
APPARENT RESISTIVITY
PHASE (deg)
Real Data
Imaginary Data
Real Fit
Imaginary Fit
ZXX
ZXY
ZYX
ZYY
Period (seconds)

THO-92-M13S

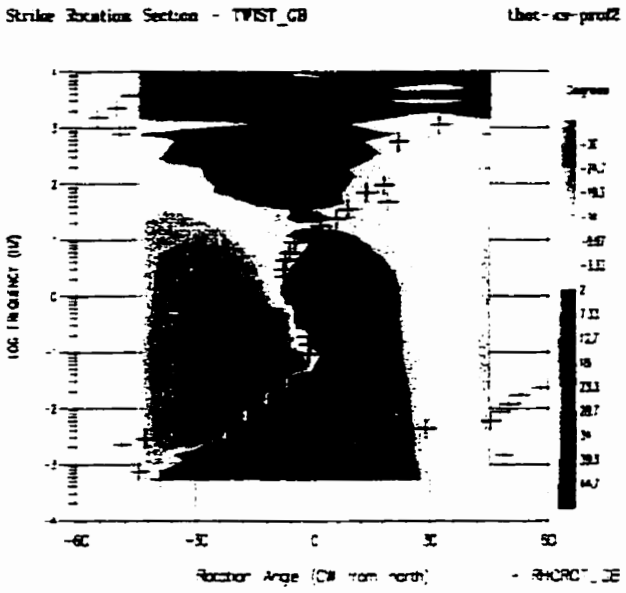
Strike Rotation Section - TWIST_GB
thet-ks-prof2
Degrees
Rotation Angle (CW from north)

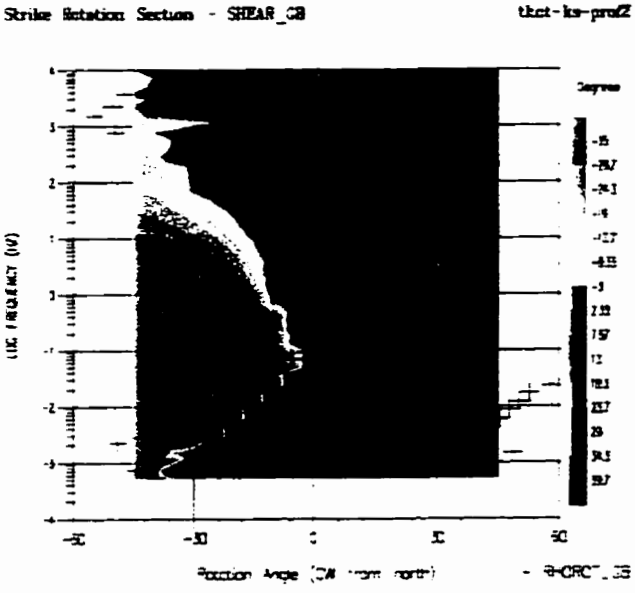
Strike Rotation Section - SHEAR_GB
thet-ks-prof2
Degrees
Rotation Angle (CW from north)

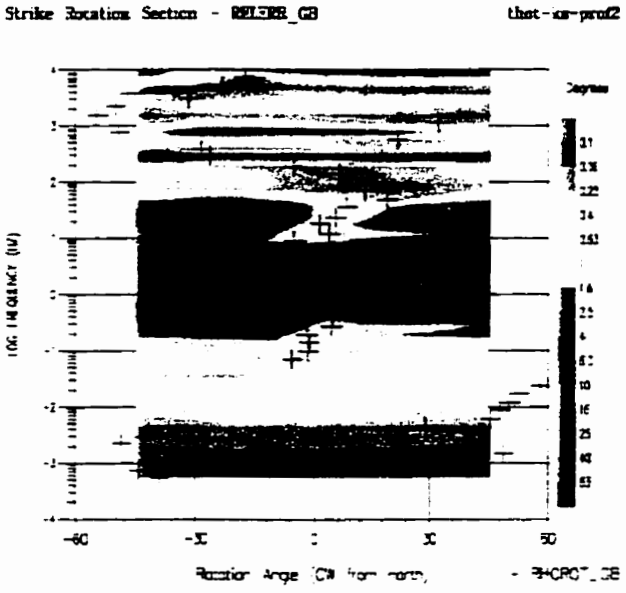
Strike Rotation Section - RELIEF_GB
thet-ks-prof2
Degrees
Rotation Angle (CW from north)

THO-92-A13A

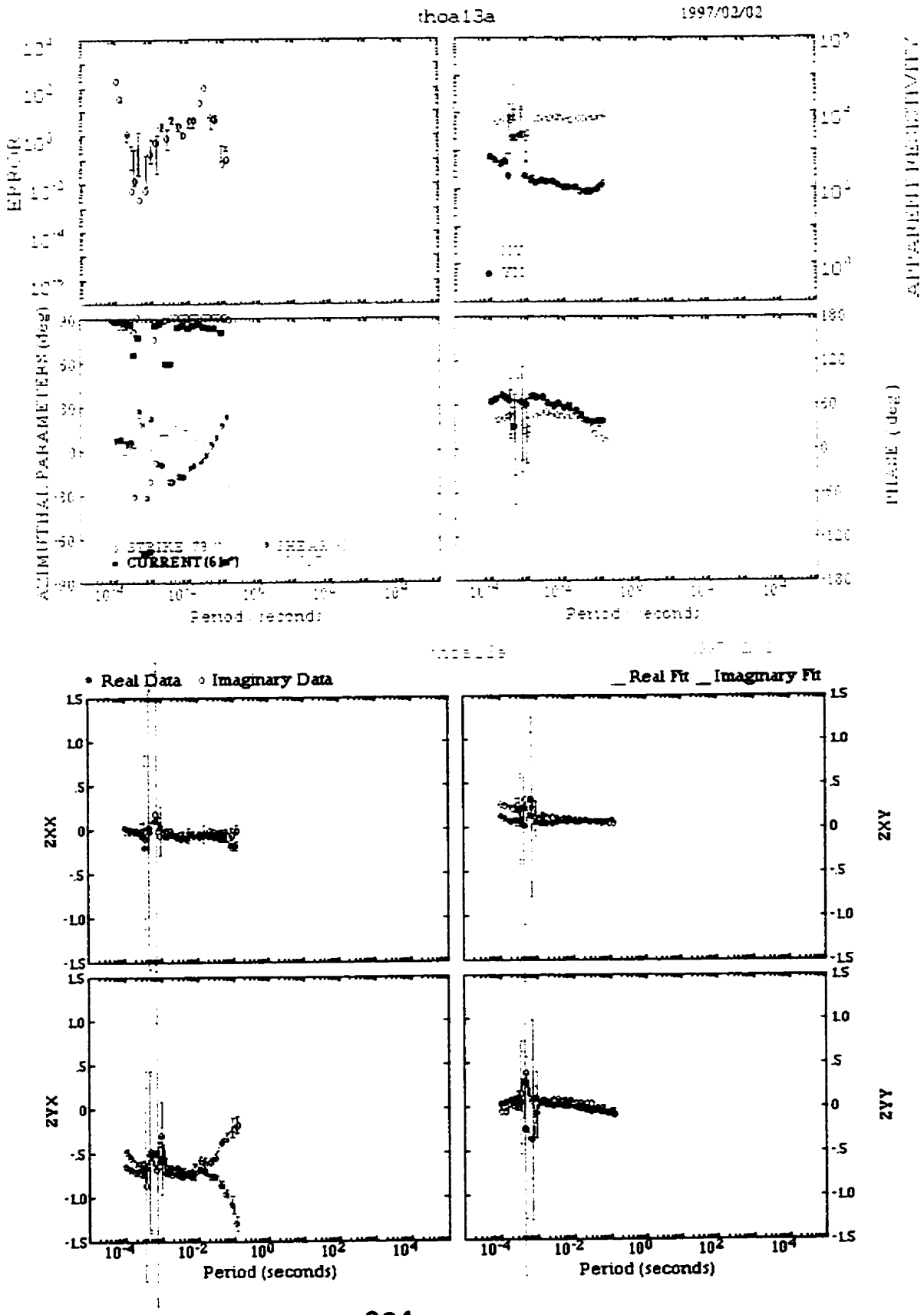
thoa13a
1997/02/02
AZIMUTHAL PARAMETERS (deg)
CURRENT (6
Period (seconds)
Real Data
Imaginary Data
Real Fit
Imaginary Fit
ZXX
ZXY
ZYX
ZYY
Period (seconds)

THO-92-A13A

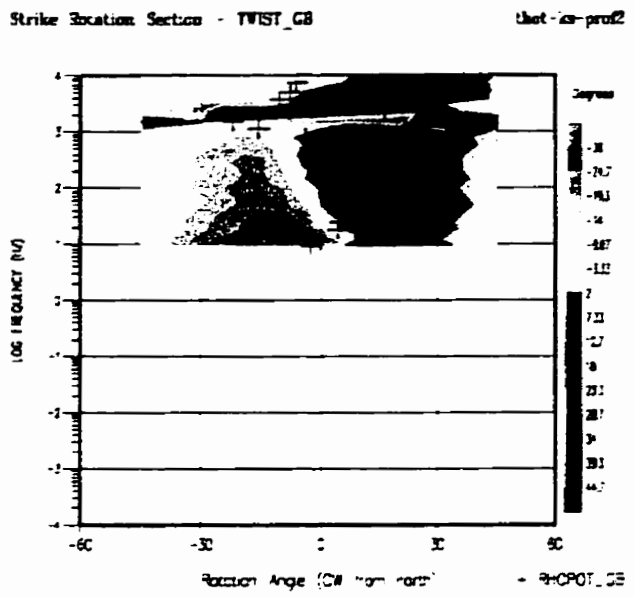
Strike Rotation Section - TWIST_C8
LOG FREQUENCY (Hz)
Rotation Angle (CW from north)

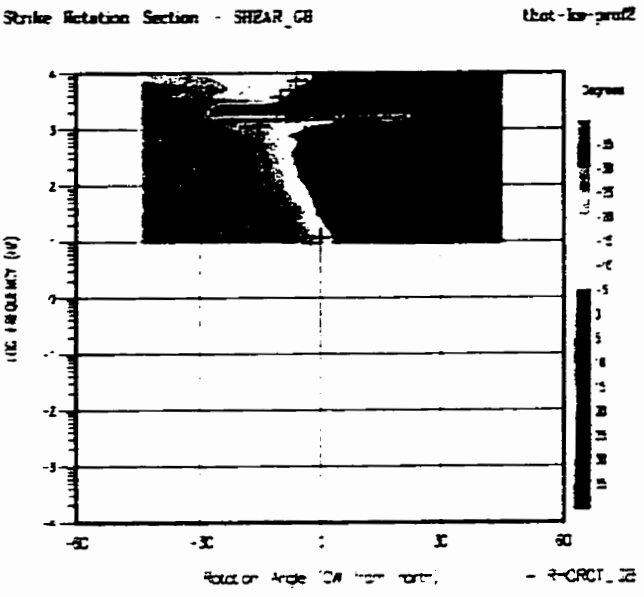
Strike Rotation Section - SHEAR_C8
LOG FREQUENCY (Hz)
Rotation Angle (CW from north)

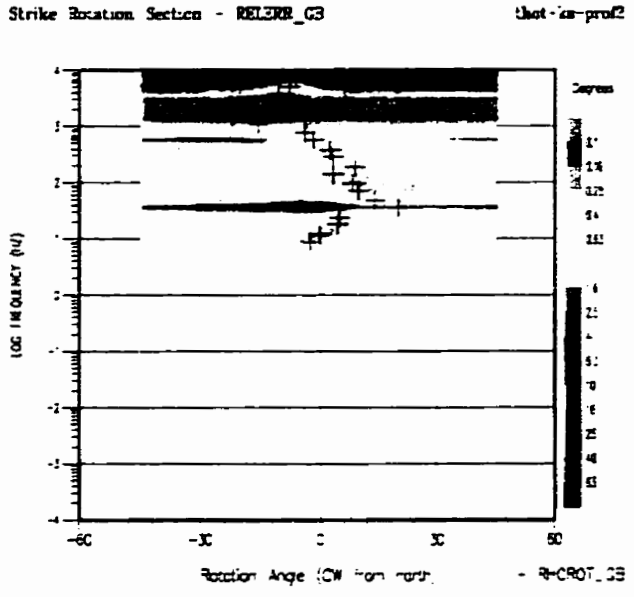
Strike Rotation Section - RELERR_C8
LOG FREQUENCY (Hz)
Rotation Angle (CW from north)

DTH007

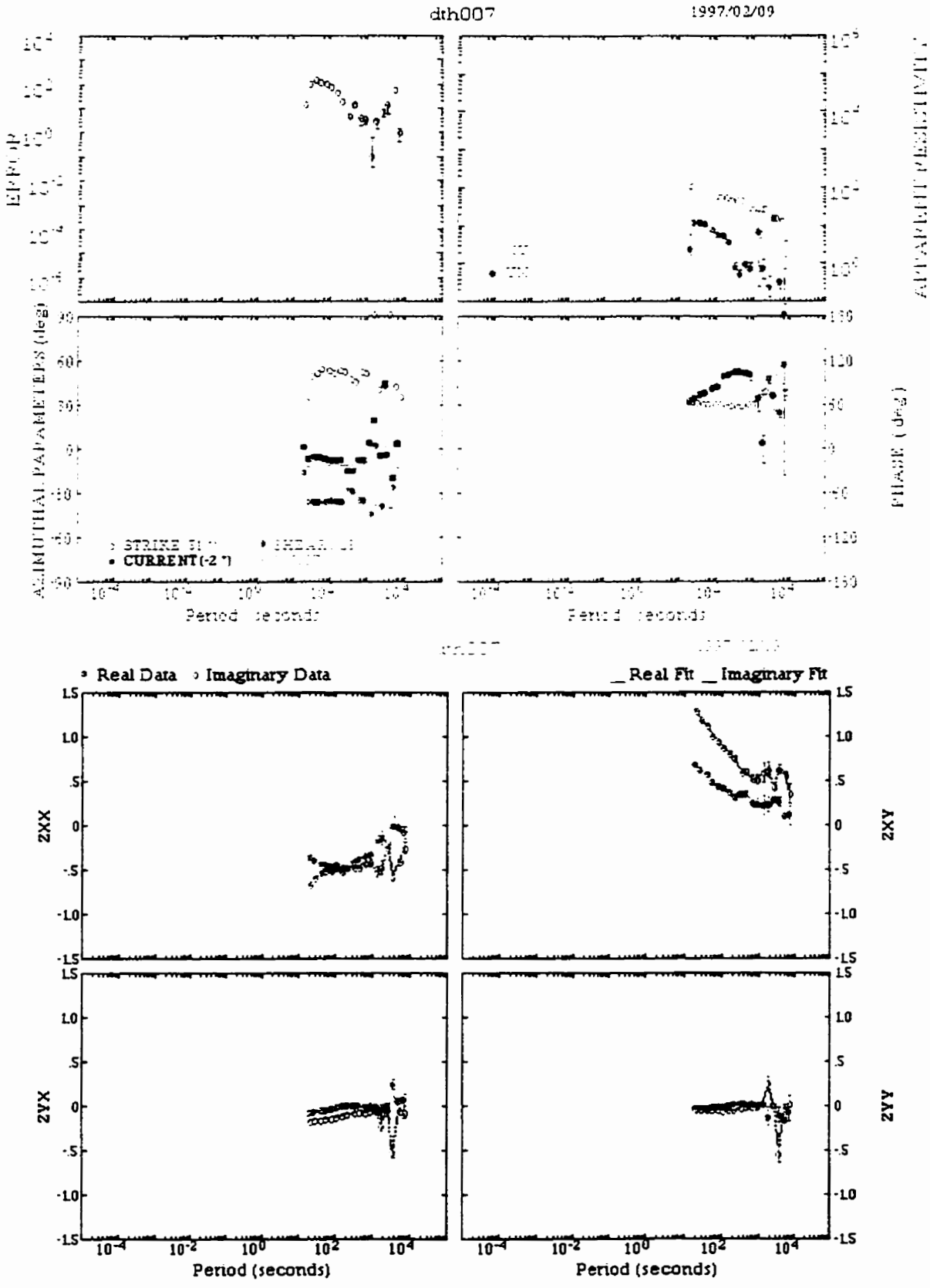
dth007
1997/02/09
AZIMUTHAL PARAMETERS (deg)
CURRENT(-2°)
Period (seconds)
Real Data
Imaginary Data
Real Fit
Imaginary Fit
ZXX
ZXY
ZYX
ZYY
Period (seconds)
Period (seconds)

DTH007

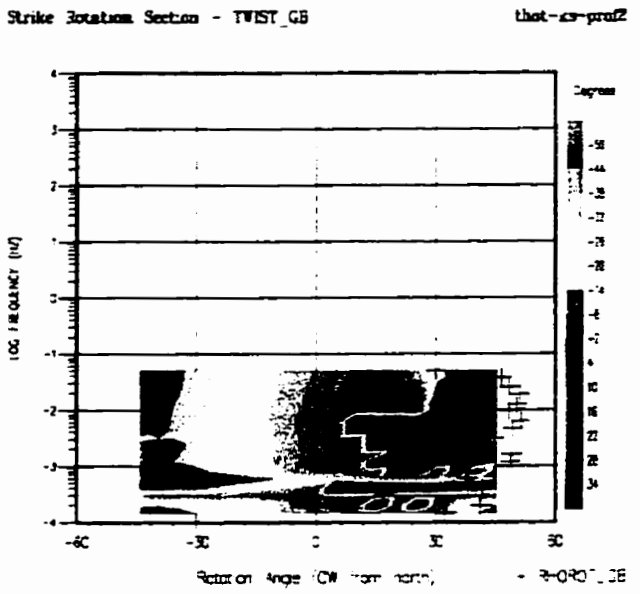
Strike Rotation Section - TWIST_GB
that-ks-prof2
Degrees
LOG FREQUENCY (Hz)
-60
-30
0
30
60
Rotation Angle (CW from north)

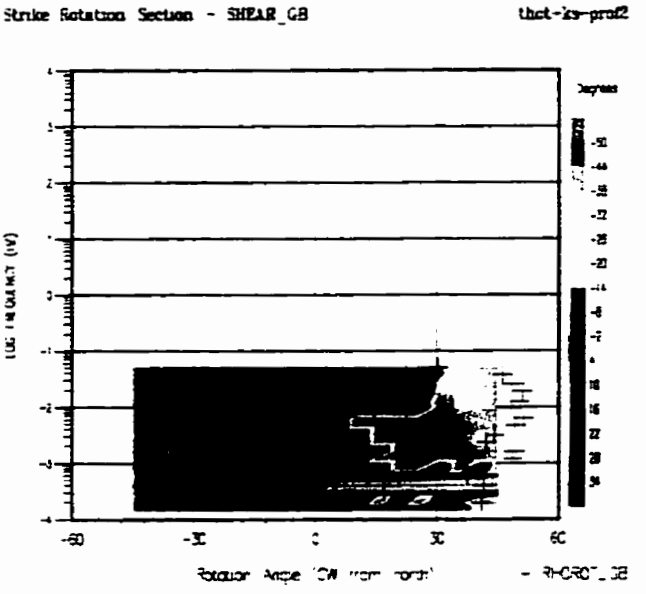
Strike Rotation Section - SHEAR_GB
that-ks-prof2
Degrees
LOG FREQUENCY (Hz)
-60
-30
0
30
60
Rotation Angle (CW from north)

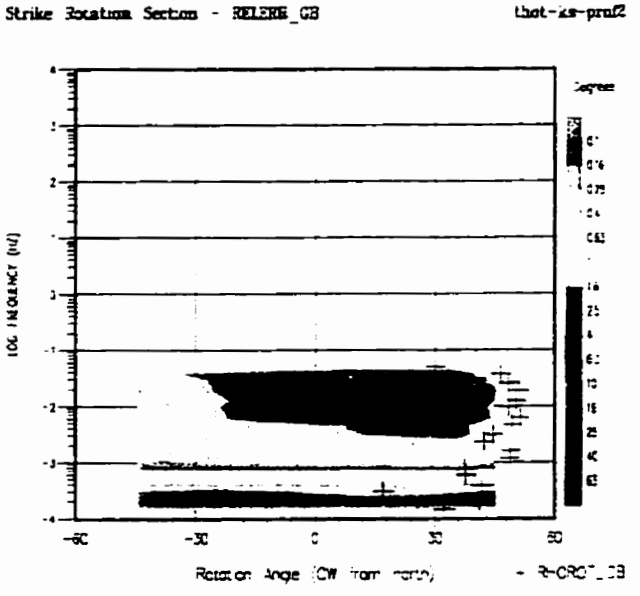
Strike Rotation Section - RELERR_GB
that-ks-prof2
Degrees
LOG FREQUENCY (Hz)
-60
-30
0
30
60
Rotation Angle (CW from north)

THO-92-M12S

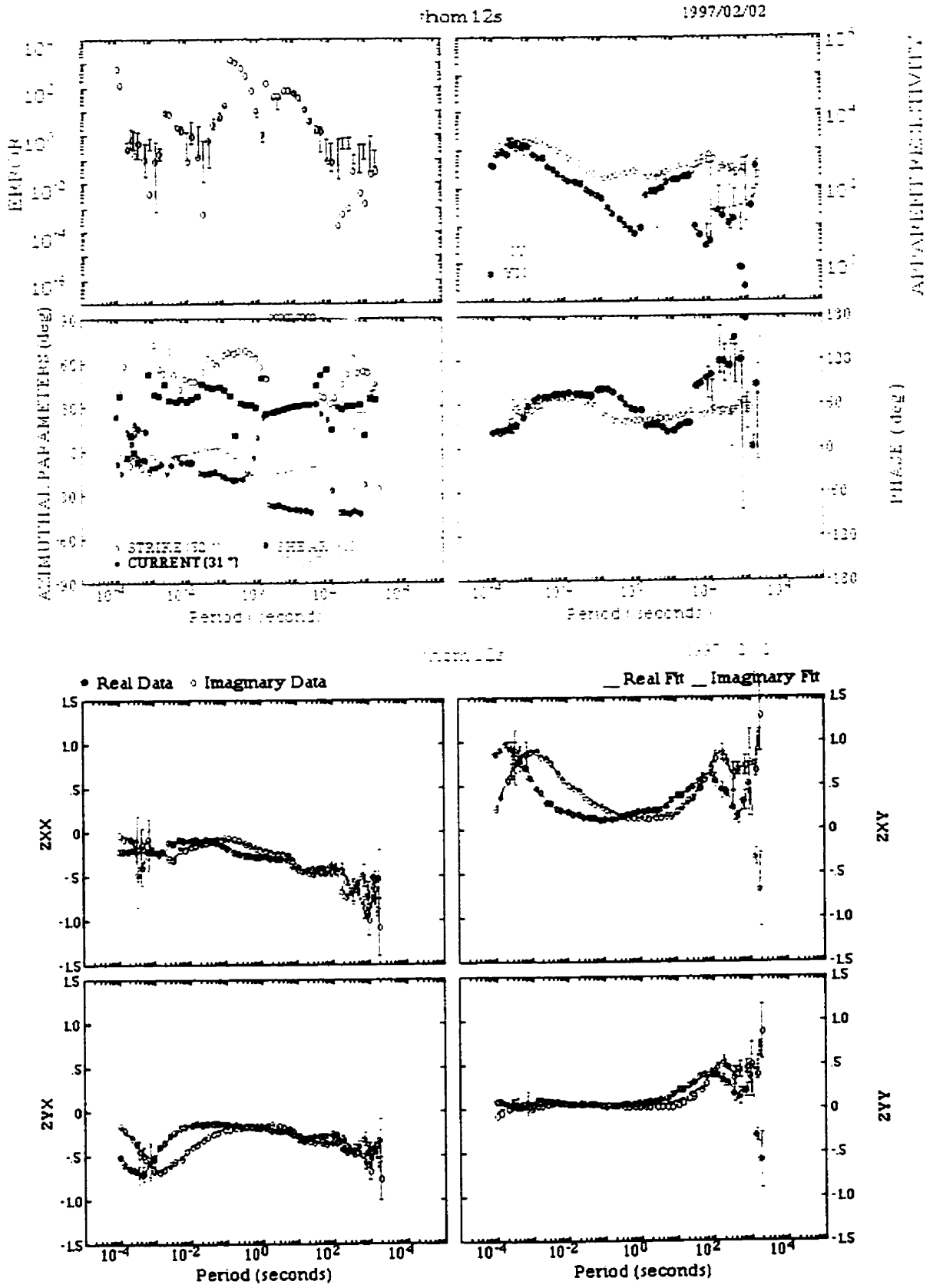
thom12s
1997/02/02
AZIMUTHAL PARAMETERS (deg)
CURRENT (31 °)
Period (seconds)
PHASE (deg)
Real Data
Imaginary Data
Real Fit
Imaginary Fit
ZXX
ZXY
ZYX
ZYY
Period (seconds)

THO-92-M12S

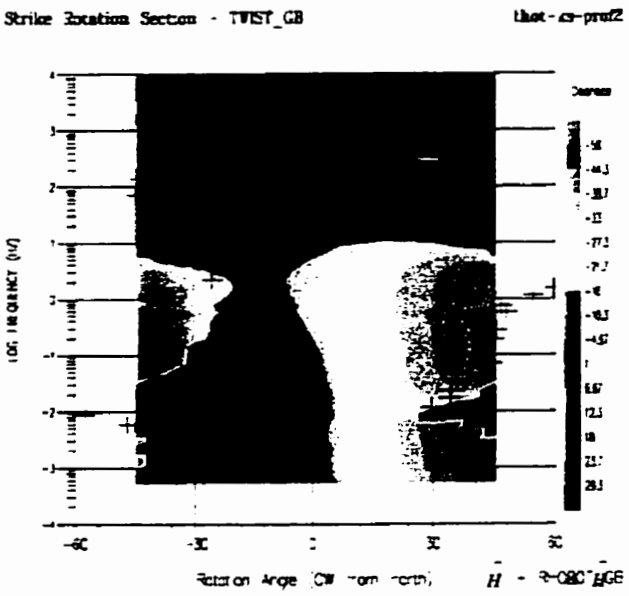
Strike Rotation Section - TWIST_GB
Rotation Angle (CW from north)

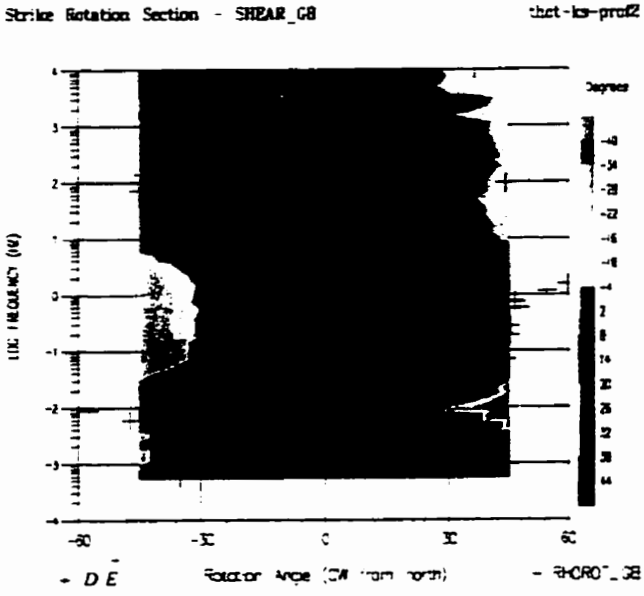
Strike Rotation Section - SHEAR_GB
Rotation Angle (CW from north)

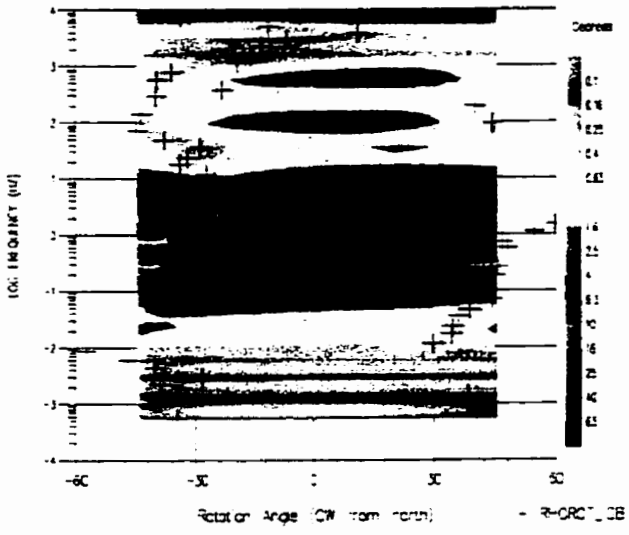
Strike Rotation Section - RELERR_G3
Rotation Angle (CW from north)

THO-92-A12A

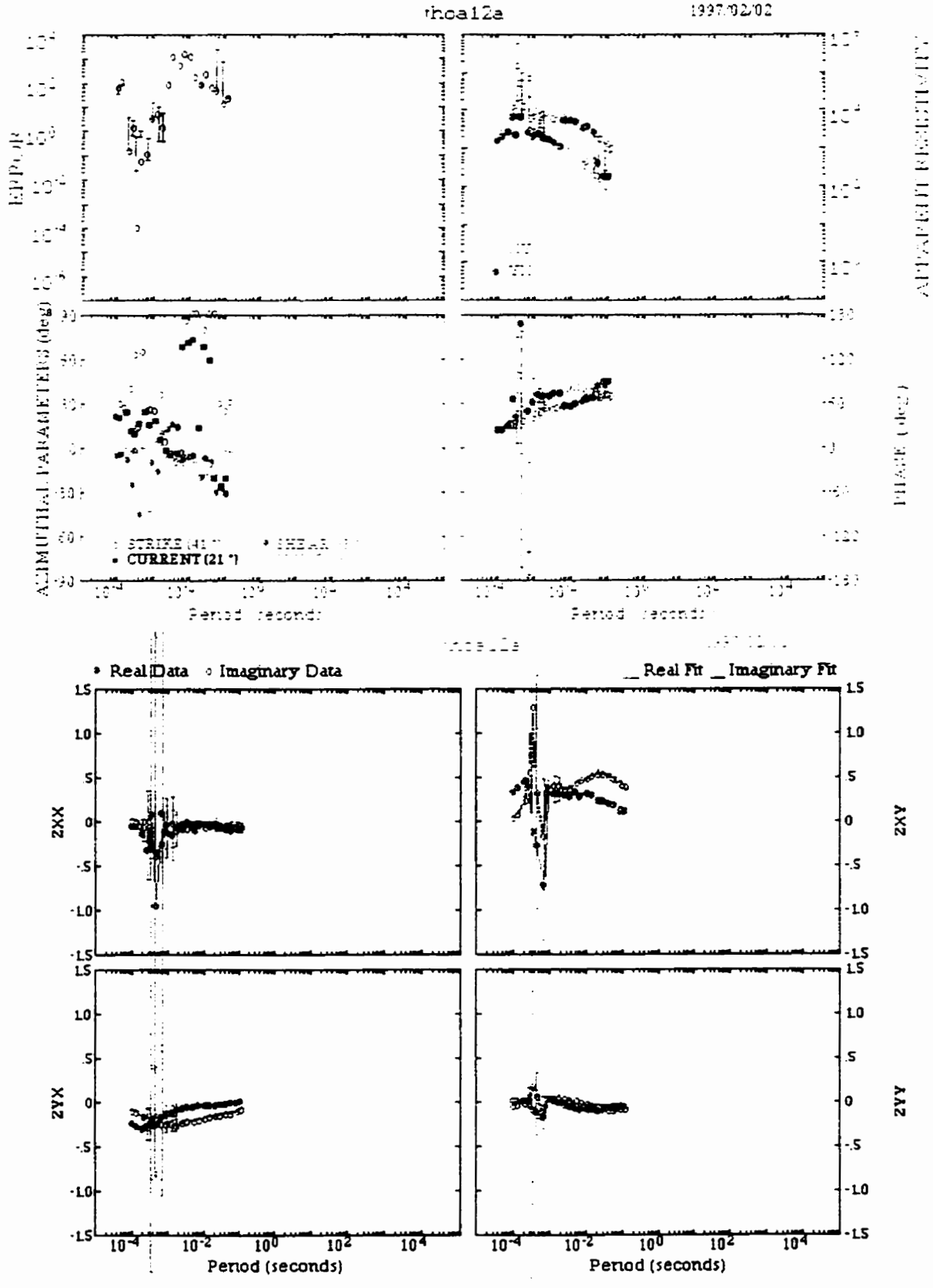
rhoa12a
1997/02/02
CURRENT (21 °)
Period (seconds)
Real Data
Imaginary Data
Real Fit
Imaginary Fit
ZXX
ZXY
ZYX
ZYY
Period (seconds)

THO-92-A12A

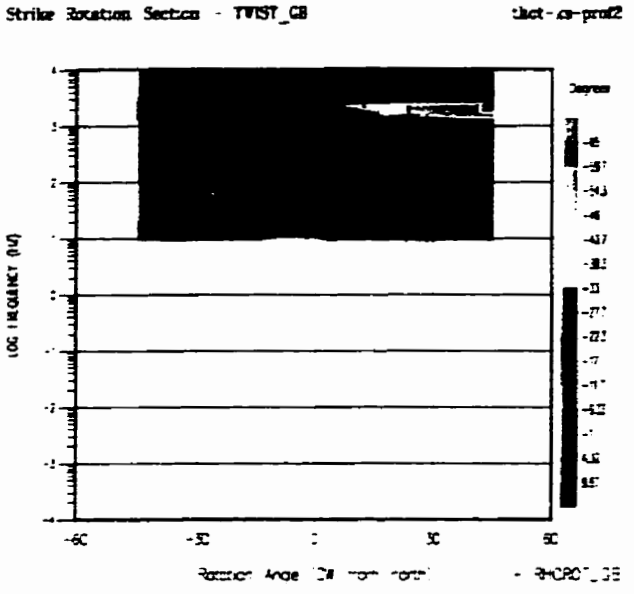
Strike Rotation Section - TWIST_GB
Degrees
Rotation Angle (CW from north)

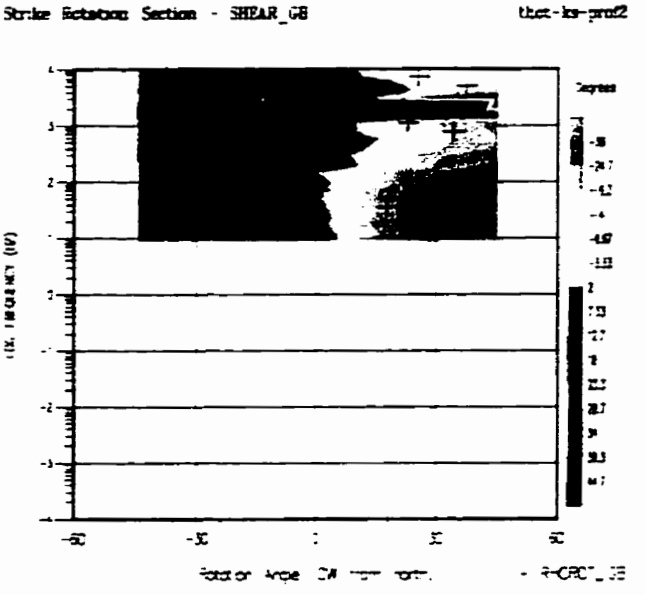
Strike Rotation Section - SHEAR_GB
Degrees
Rotation Angle (CW from north)

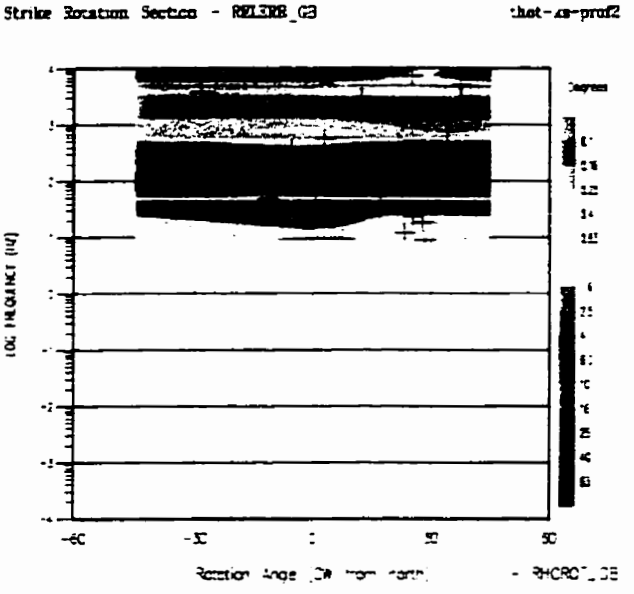
Strike Rotation Section - RELERR_GB
Degrees
Rotation Angle (CW from north)

THO-92-A11A

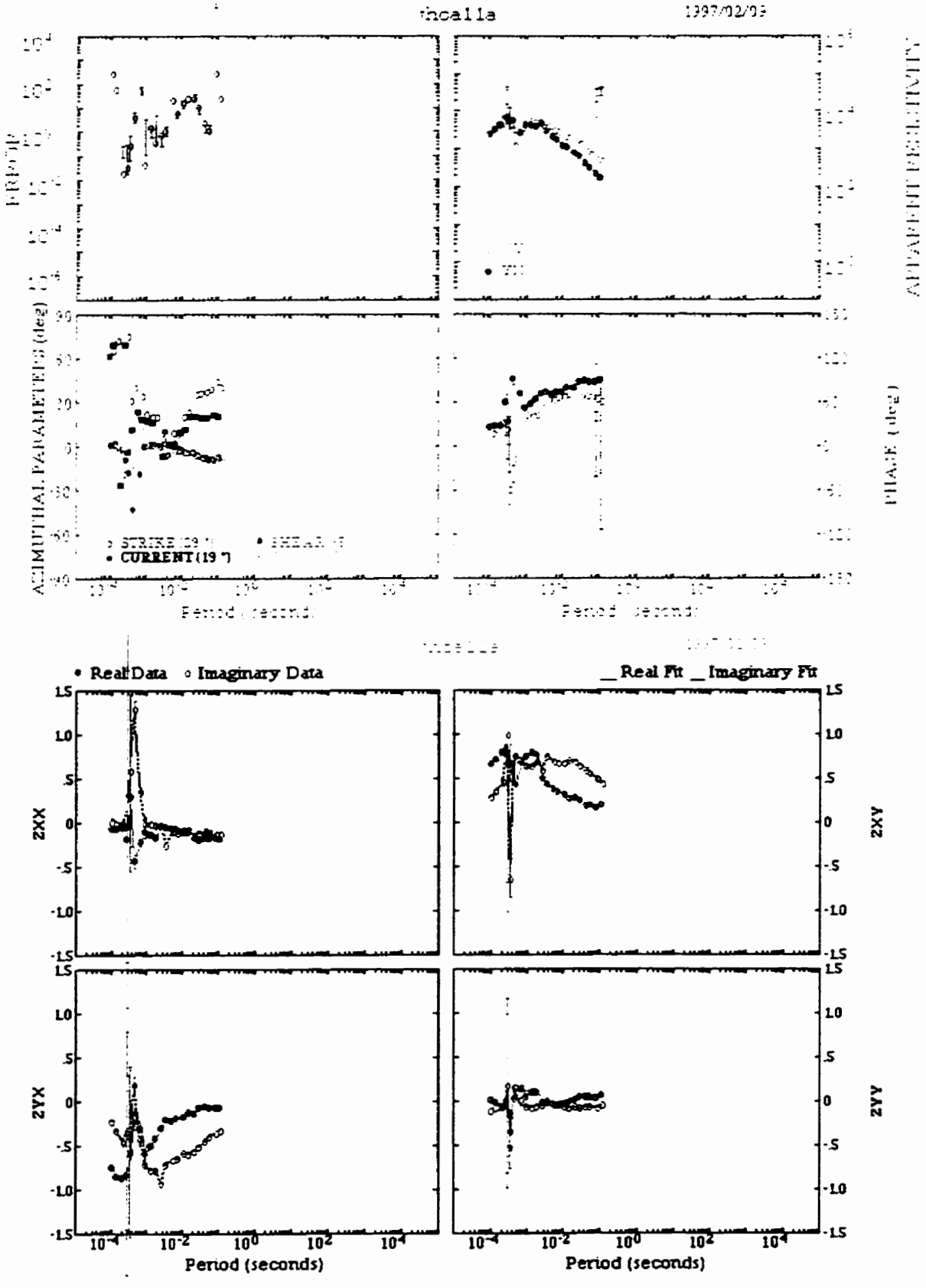
thoa11a
1997/02/09
AZIMUTHAL PARAMETERS (deg)
STRIKE (19°)
CURRENT (19°)
Period (seconds)
APPARENT RESISTIVITY
PHASE (deg)
Real Data
Imaginary Data
Real Fit
Imaginary Fit
ZXX
ZXY
ZYX
ZYY
Period (seconds)

THO-92-A11A

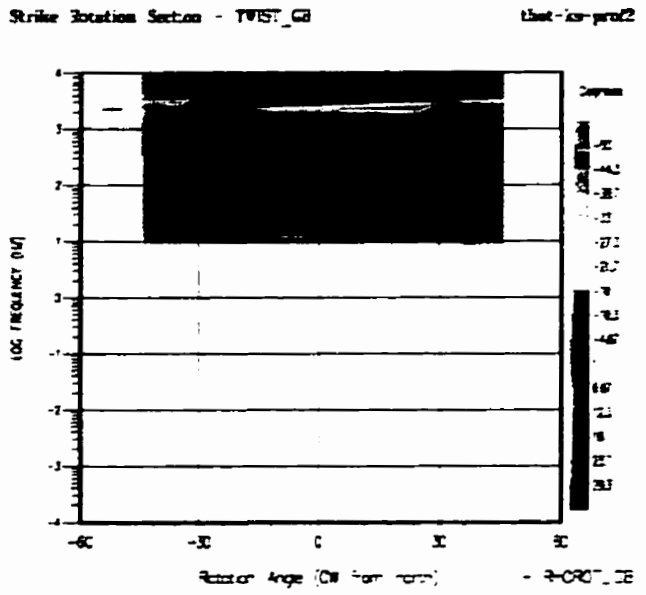

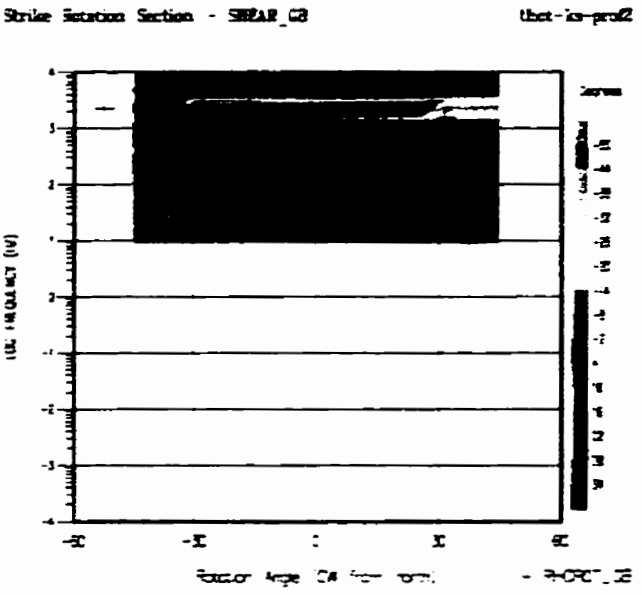

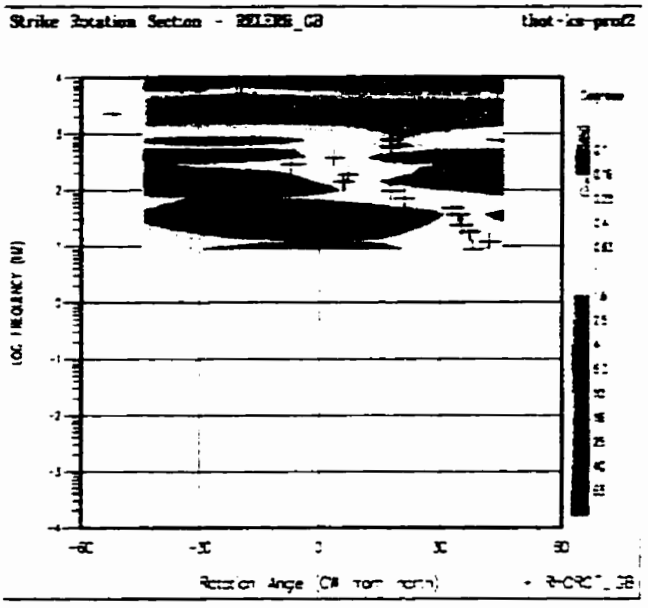

THO-92-M11S

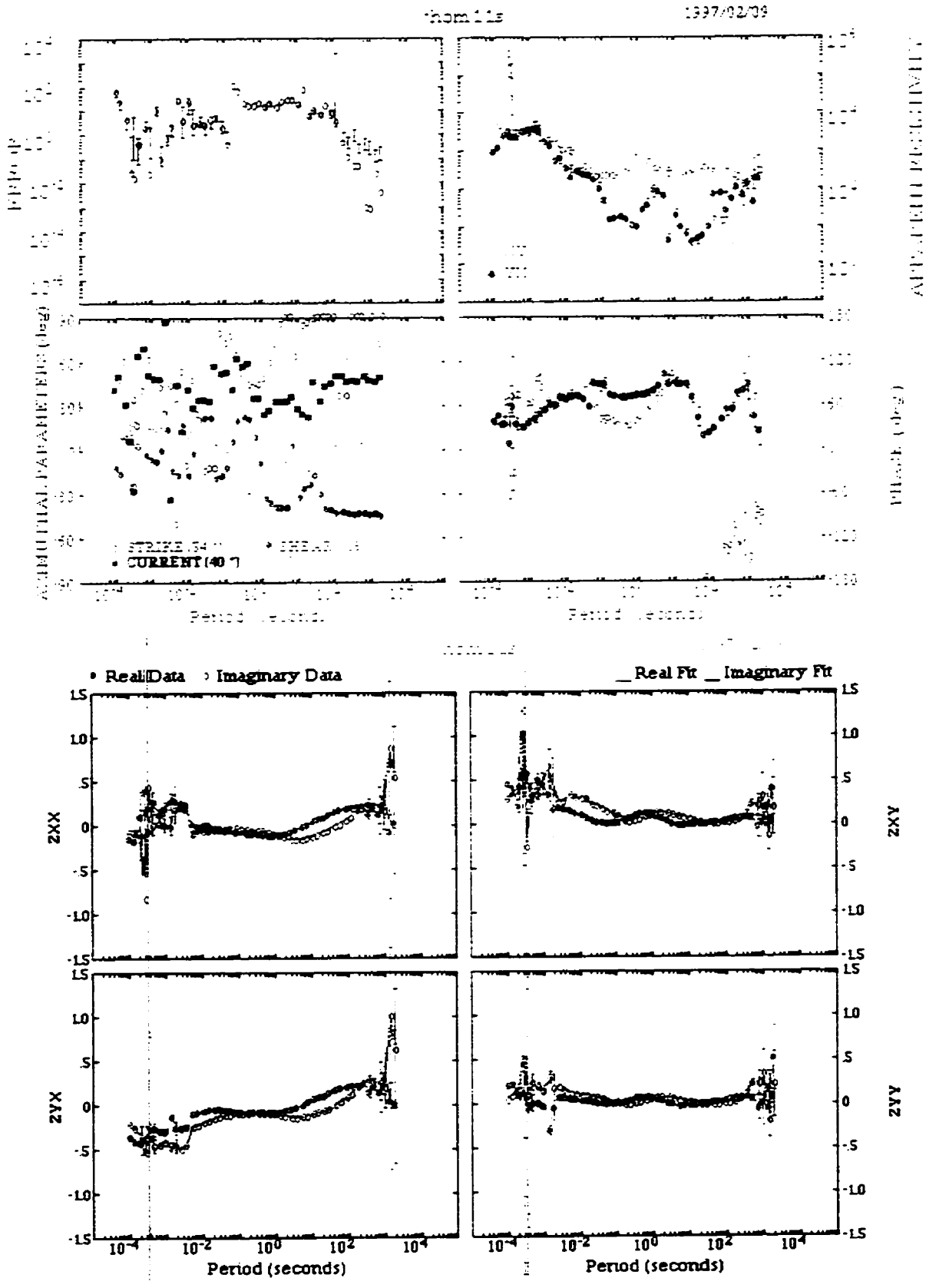
thom11s
1997/02/09
CURRENT (40 °)
Real Data
Imaginary Data
Real Fit
Imaginary Fit
ZXX
ZXZ
ZYX
ZYZ
Period (seconds)
Period (seconds)

THO-92-M11S

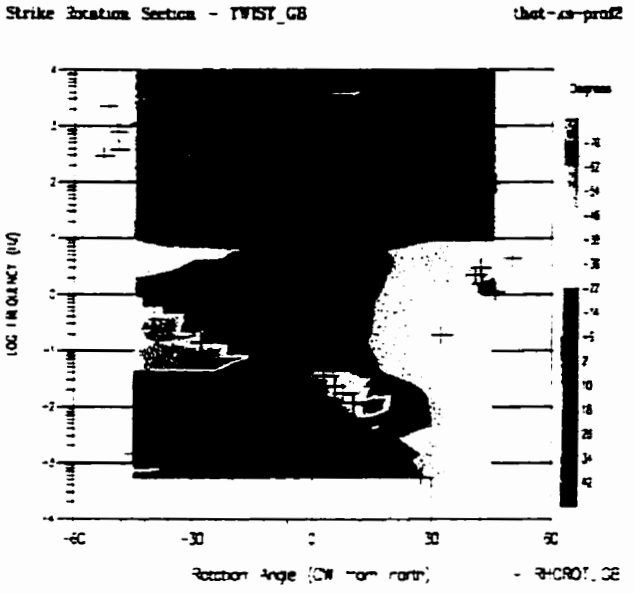
Strike Location Section - TWIST_GB
thot-xs-prof2
Degrees
-60
-30
0
30
60
Rotation Angle (CW from north)

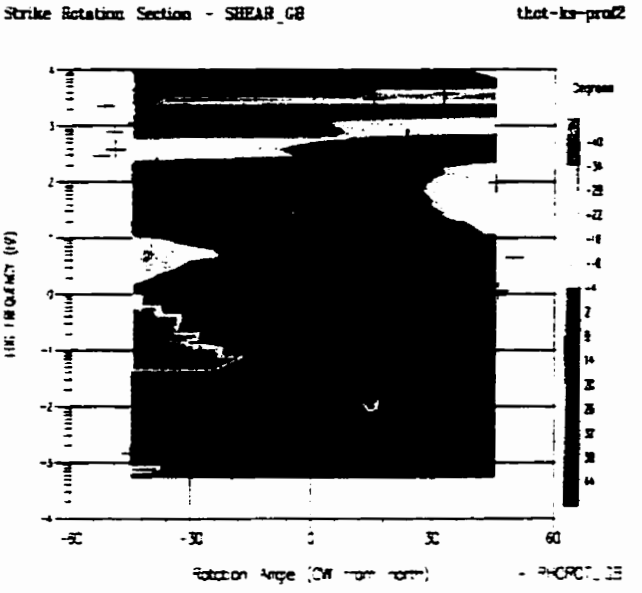
Strike Rotation Section - SHEAR_GB
thot-ks-prof2
Degrees
-60
-30
0
30
60
Rotation Angle (CW from north)

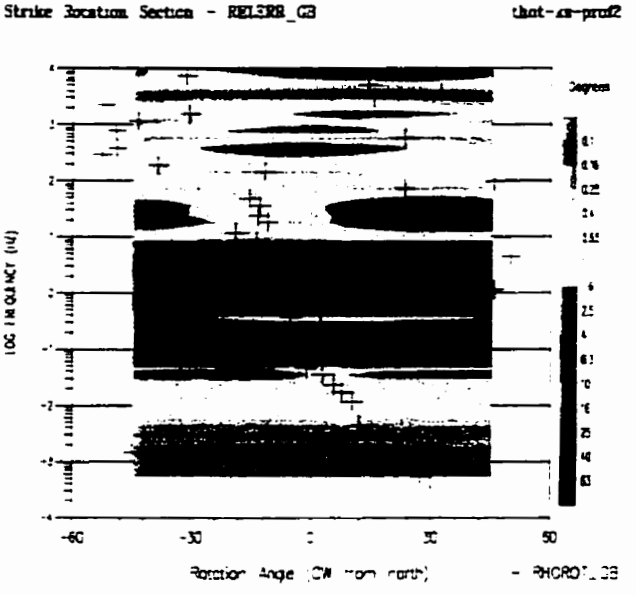
Strike Location Section - RELSRR_GB
thot-xs-prof2
Degrees
-60
-30
0
30
60
Rotation Angle (CW from north)

THO-92-A46A

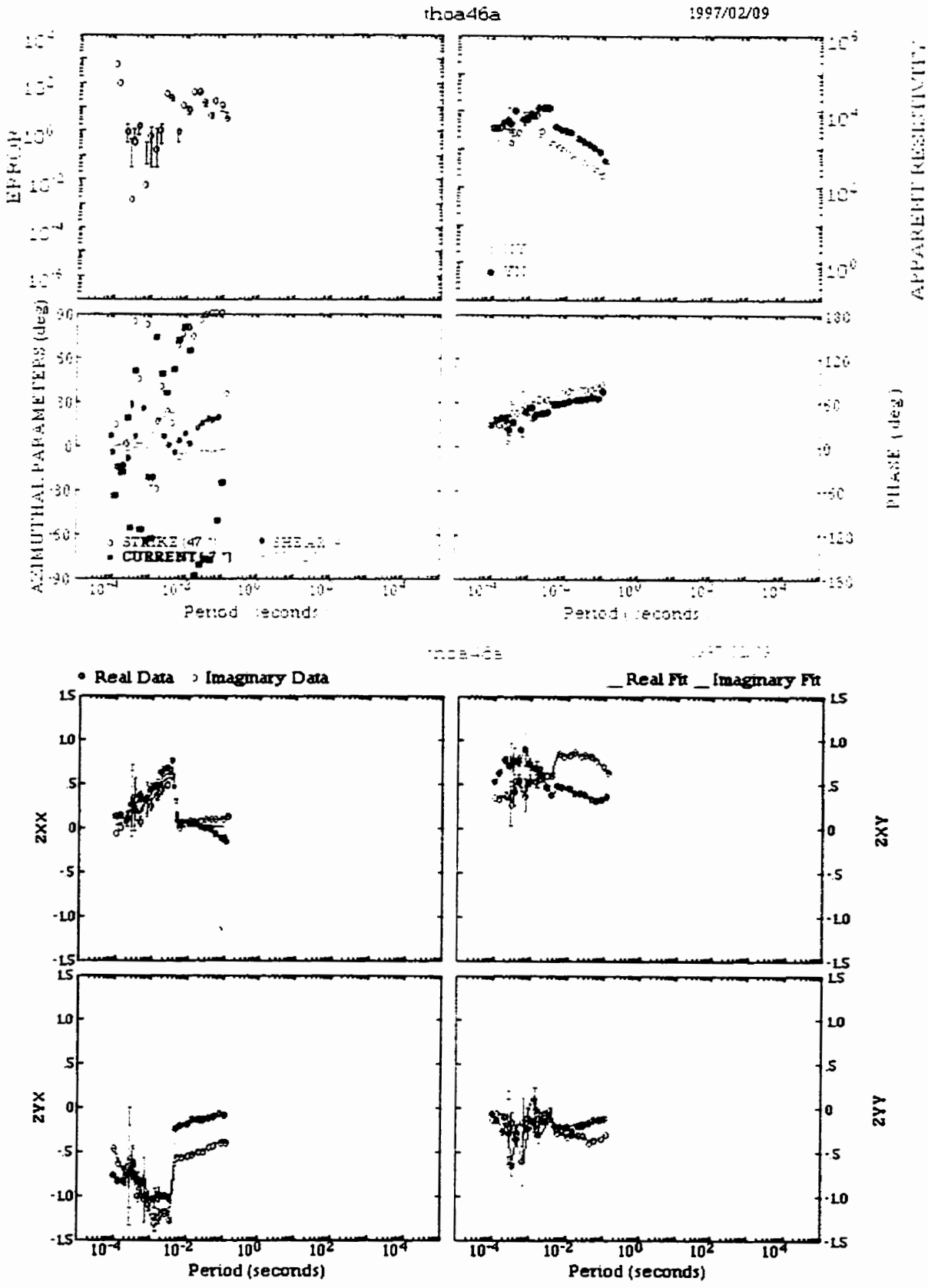
thoa46a
1997/02/09
APPARENT RESISTIVITY
PHASE (deg)
AZIMUTHAL PARAMETERS (deg)
Period (seconds)
Real Data
Imaginary Data
Real Fit
Imaginary Fit
ZXX
ZXY
ZYX
ZYY

THO-92-A46A

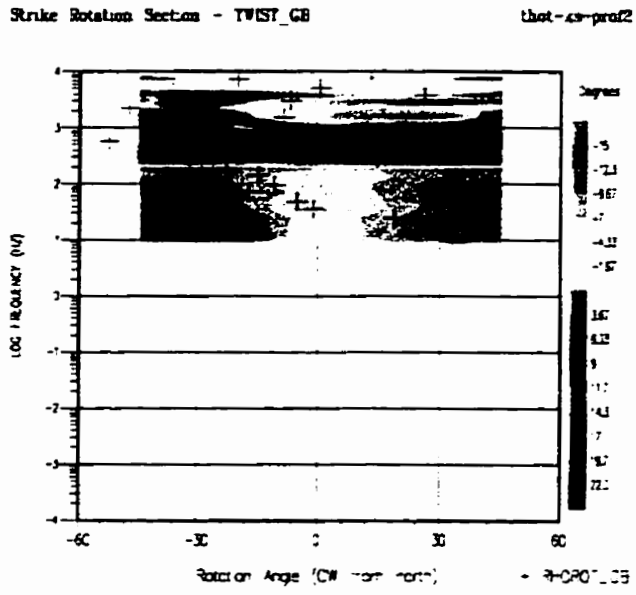
Strike Rotation Section - TWIST_GB
thot-xs-prof2
LOG FREQUENCY (Hz)
Degrees
-60
-30
0
30
60
Rotation Angle (CW from north)

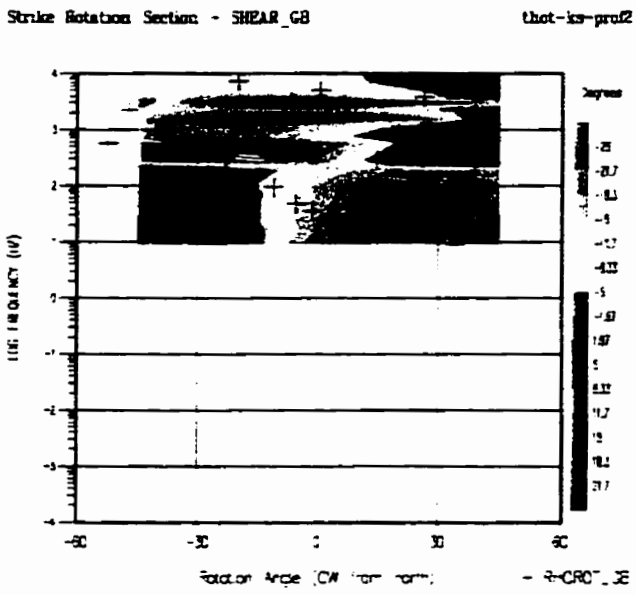
Strike Rotation Section - SHEAR_GB
thot-xs-prof2
LOG FREQUENCY (Hz)
Degrees
-60
-30
0
30
60
Rotation Angle (CW from north)

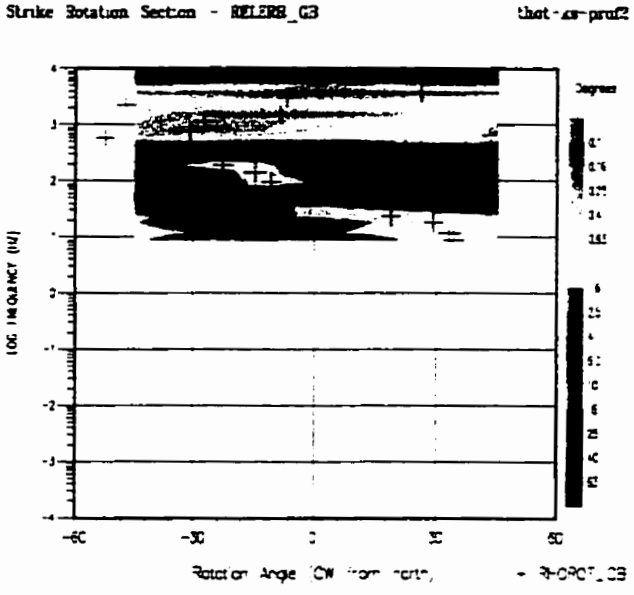
Strike Rotation Section - RELERR_GB
thot-xs-prof2
LOG FREQUENCY (Hz)
Degrees
-60
-30
0
30
60
Rotation Angle (CW from north)

THO-92-M45S

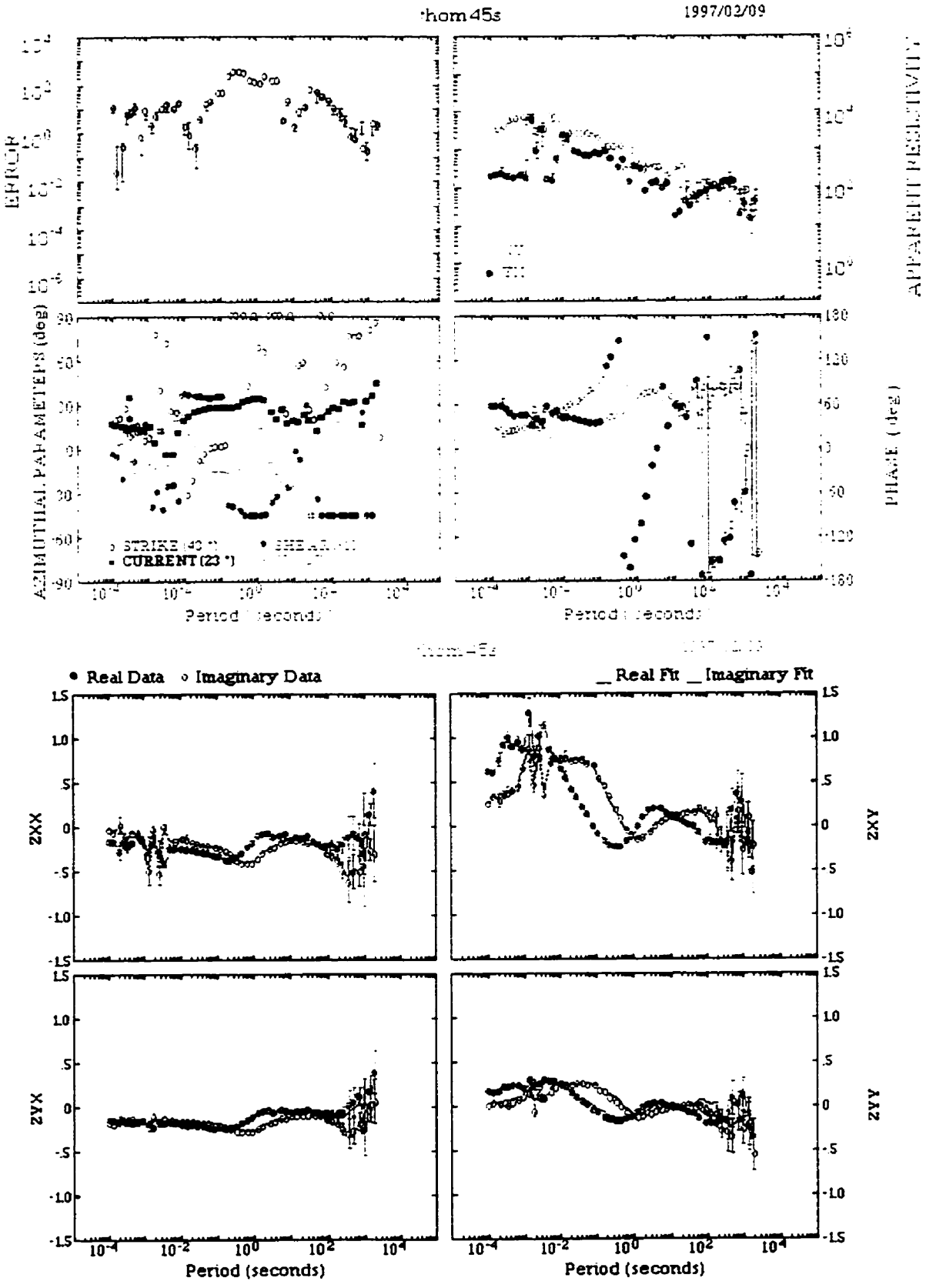
thom45s
1997/02/09
ERROR
APPARENT RESISTIVITY
AZIMUTHAL PARAMETERS (deg)
PHASE (deg)
CURRENT (23 °)
Period (seconds)
Real Data
Imaginary Data
Real Fit
Imaginary Fit
ZXX
ZXY
ZYX
ZYY
Period (seconds)

THO-92-M45S

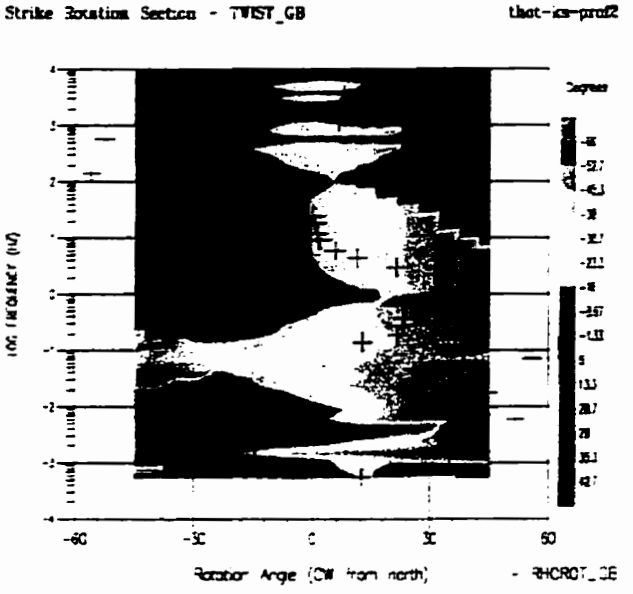
Strike Rotation Section - TWIST_GB
Rotation Angle (CW from north)

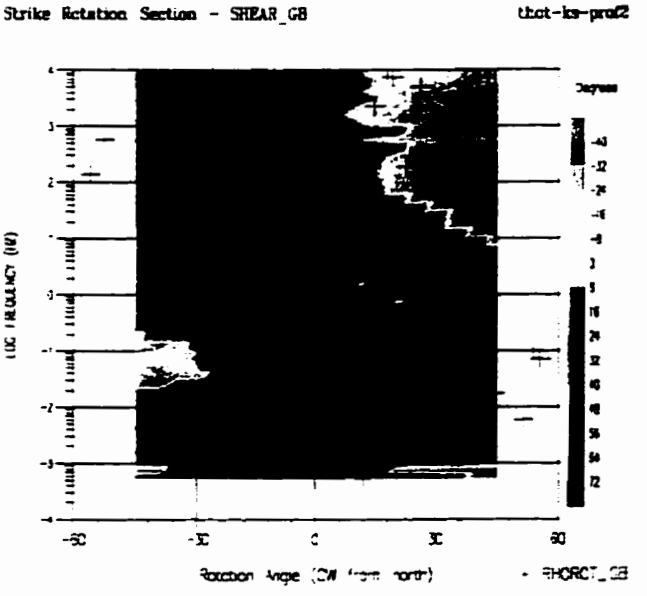
Strike Rotation Section - SHEAR_GB
Rotation Angle (CW from north)

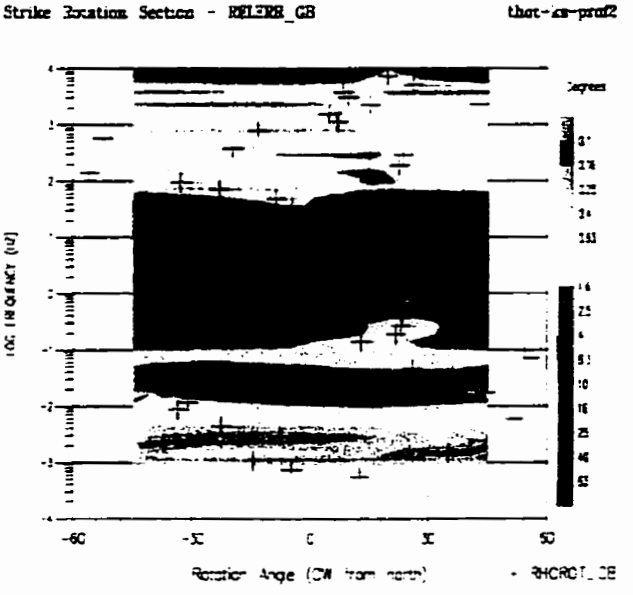
Strike Rotation Section - RELERR_GB
Rotation Angle (CW from north)

THO-92-A45A

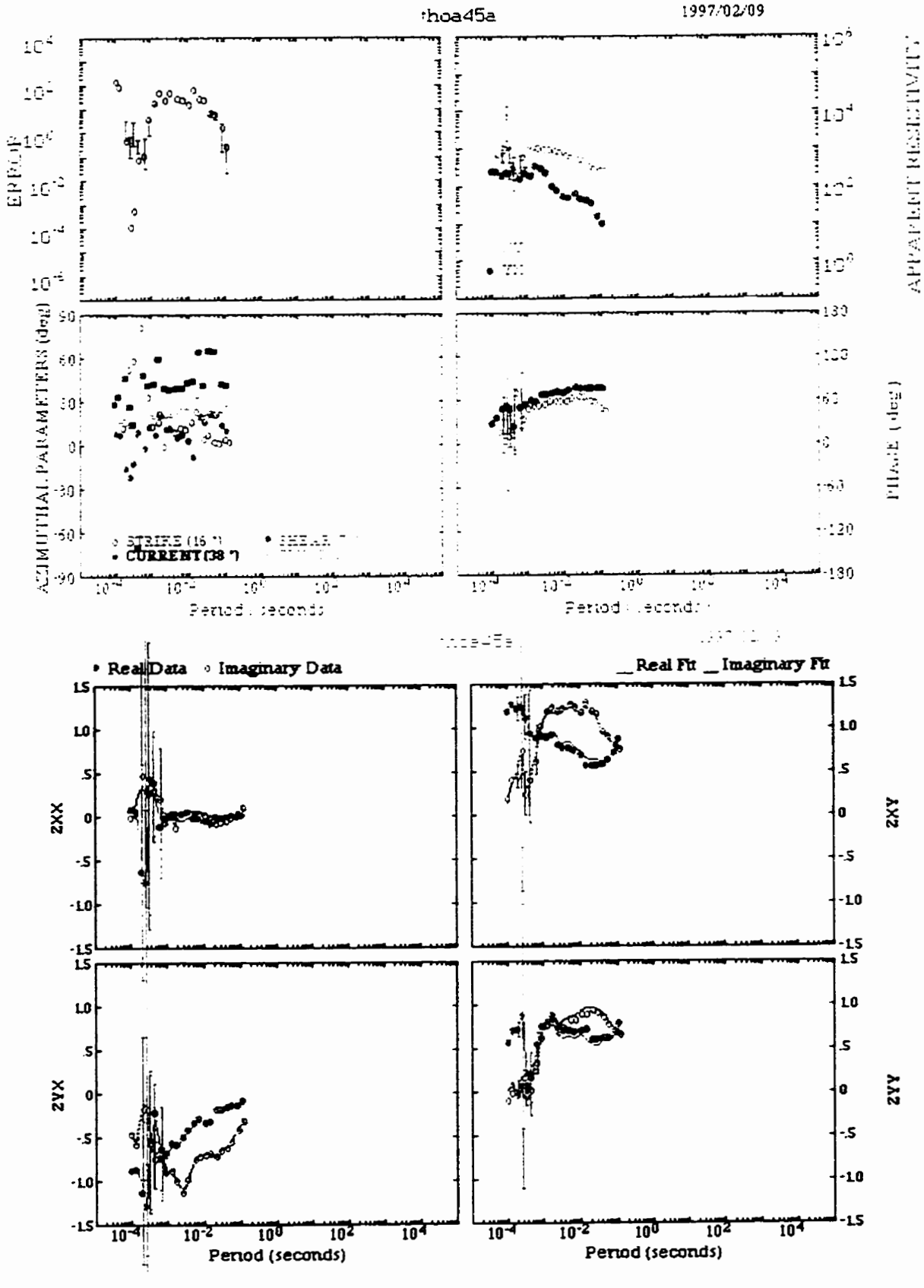
thoa45a
1997/02/09
AZIMUTHAL PARAMETERS (deg)
APPARENT RESISTIVITY
PHASE (deg)
Period (seconds)
STRIKE (16 °)
CURRENT (38 °)
Real Data
Imaginary Data
Real Fit
Imaginary Fit
ZXX
ZXY
ZYX
ZYY
Period (seconds)

THO-92-A45A

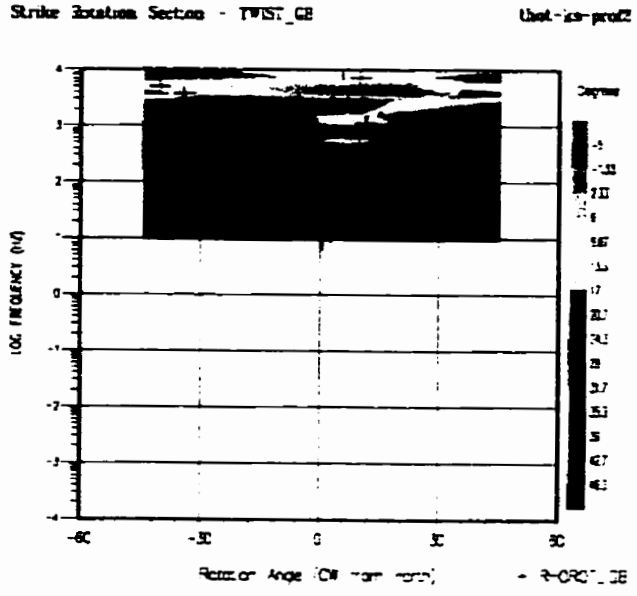
Strike Location Section - TWIST_CB
thot-ks-prof2
LOG FREQUENCY (HZ)
Rotation Angle (CW from north)

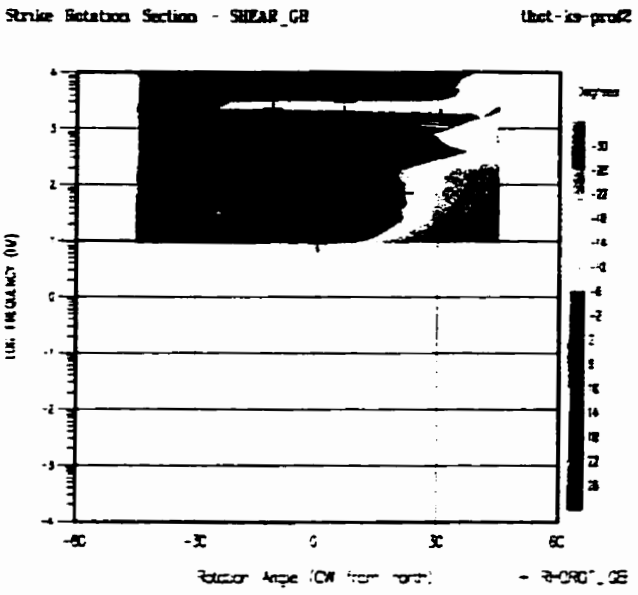
Strike Rotation Section - SHEAR_CB
thot-ks-prof2
LOG FREQUENCY (HZ)
Rotation Angle (CW from north)

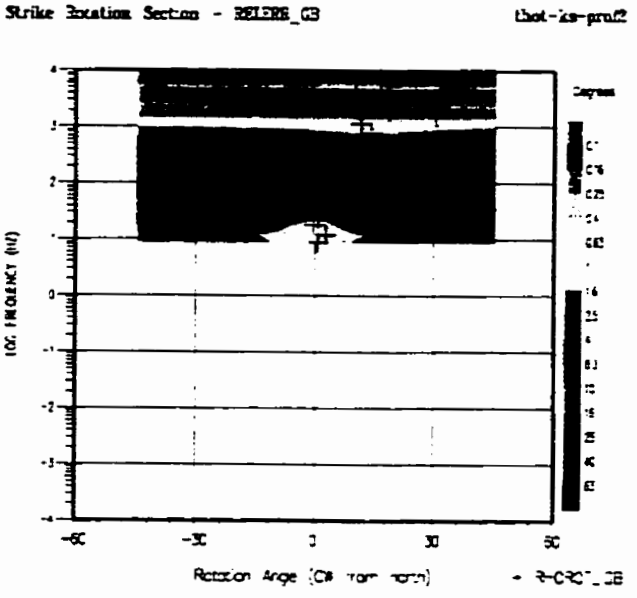
Strike Location Section - BENDS_CB
thot-ks-prof2
LOG FREQUENCY (HZ)
Rotation Angle (CW from north)

THO-92-M46S

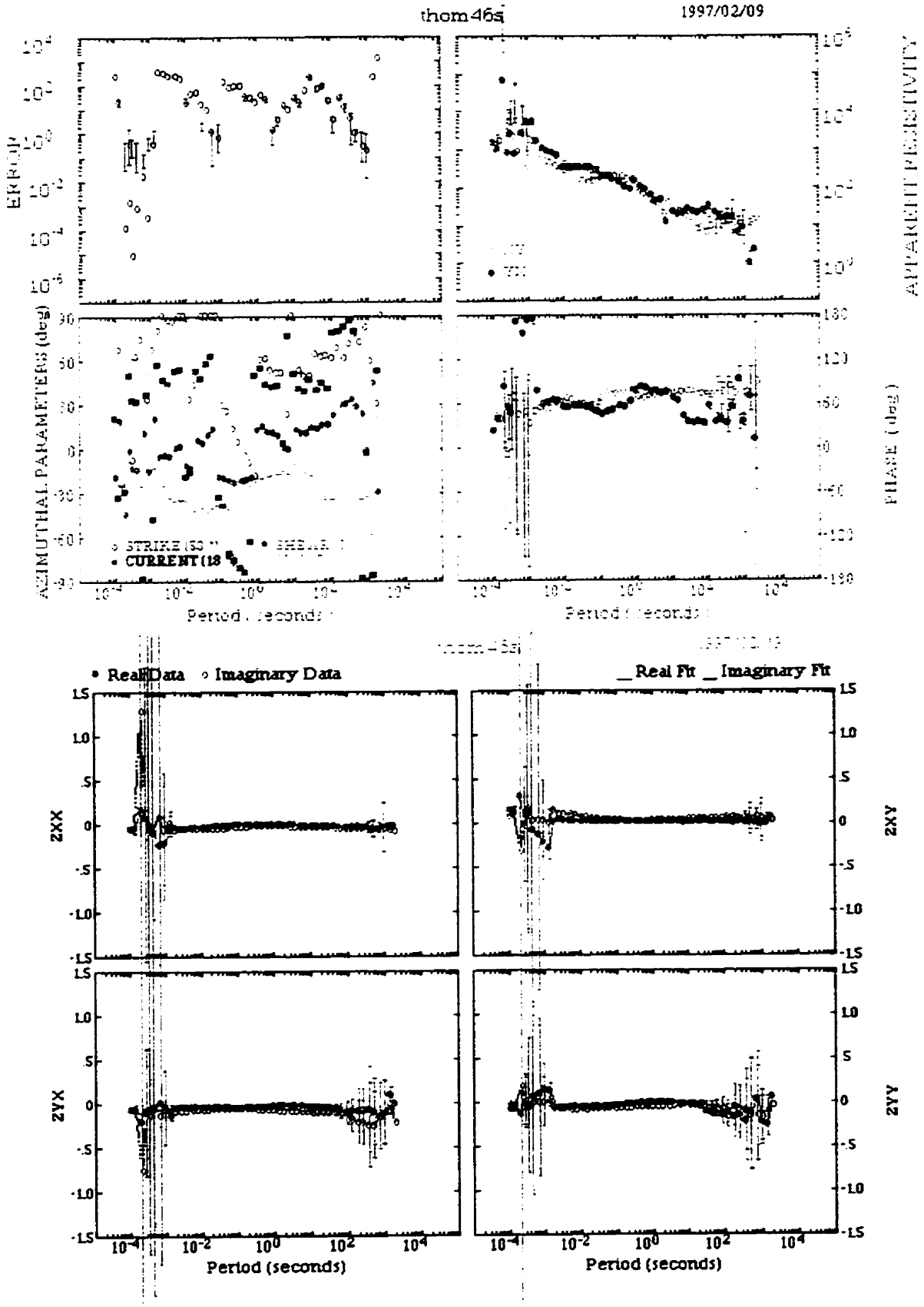
thom46s
1997/02/09
ERROR
AZIMUTHAL PARAMETERS (deg)
APPARENT RESISTIVITY
PHASE (deg)
STRIKE (
CURRENT (
Period (seconds)
Real Data
Imaginary Data
Real Fit
Imaginary Fit
ZXX
ZXY
ZYX
ZYY
Period (seconds)

THO-92-M46S

Strike Rotation Section - TWIST_GB thot-ks-prof2

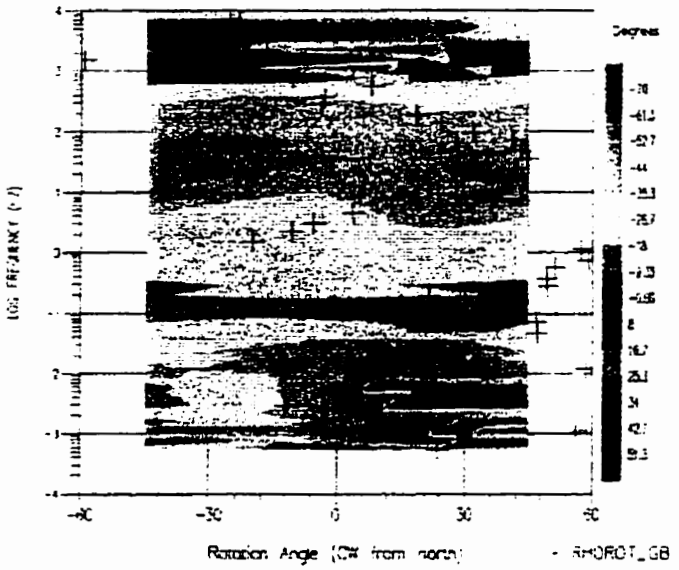

Strike Rotation Section - SHEAR_GB thot-ks-prof2

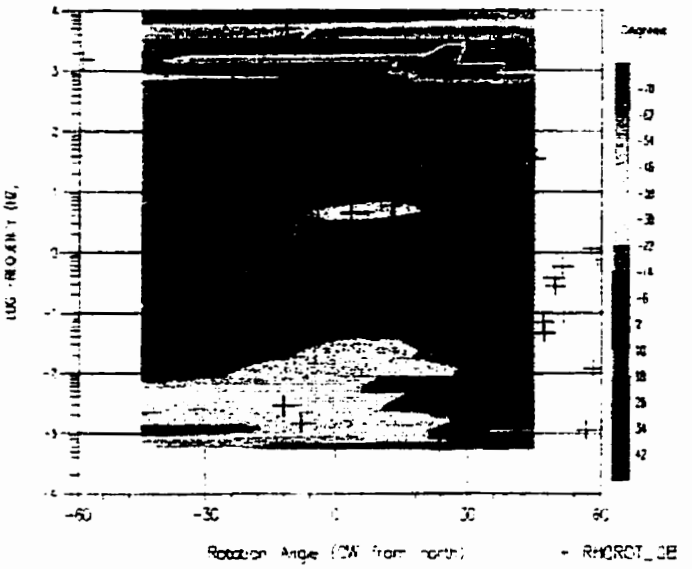

Strike Rotation Section - RELSRE_GB thot-ks-prof2

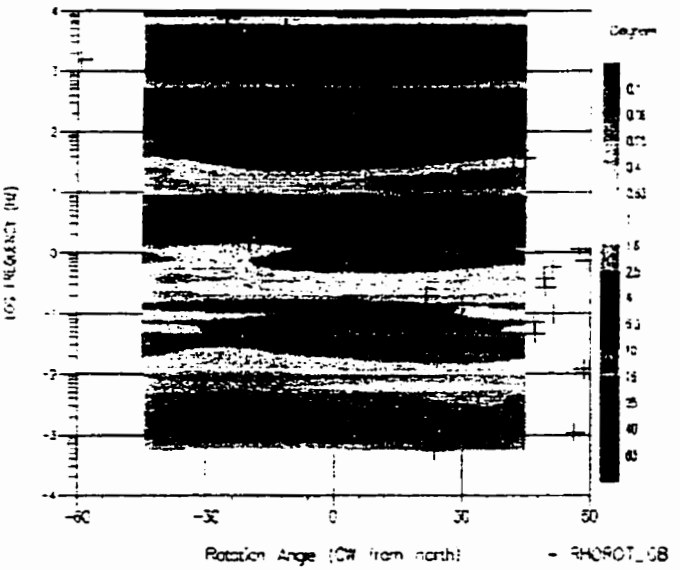

Appendix C: Fully Constrained GB 3-D Model Parameterization

1) All Sites <0.1Hz

This appendix shows two sets of results for the fully constrained GB decomposition results using strike, twist and shear values as outlined for sites M25 to M46 in Table 4.2 for each site in this data subset. Standard plotting parameters are as described in Appendix B.

THO-92-M25S

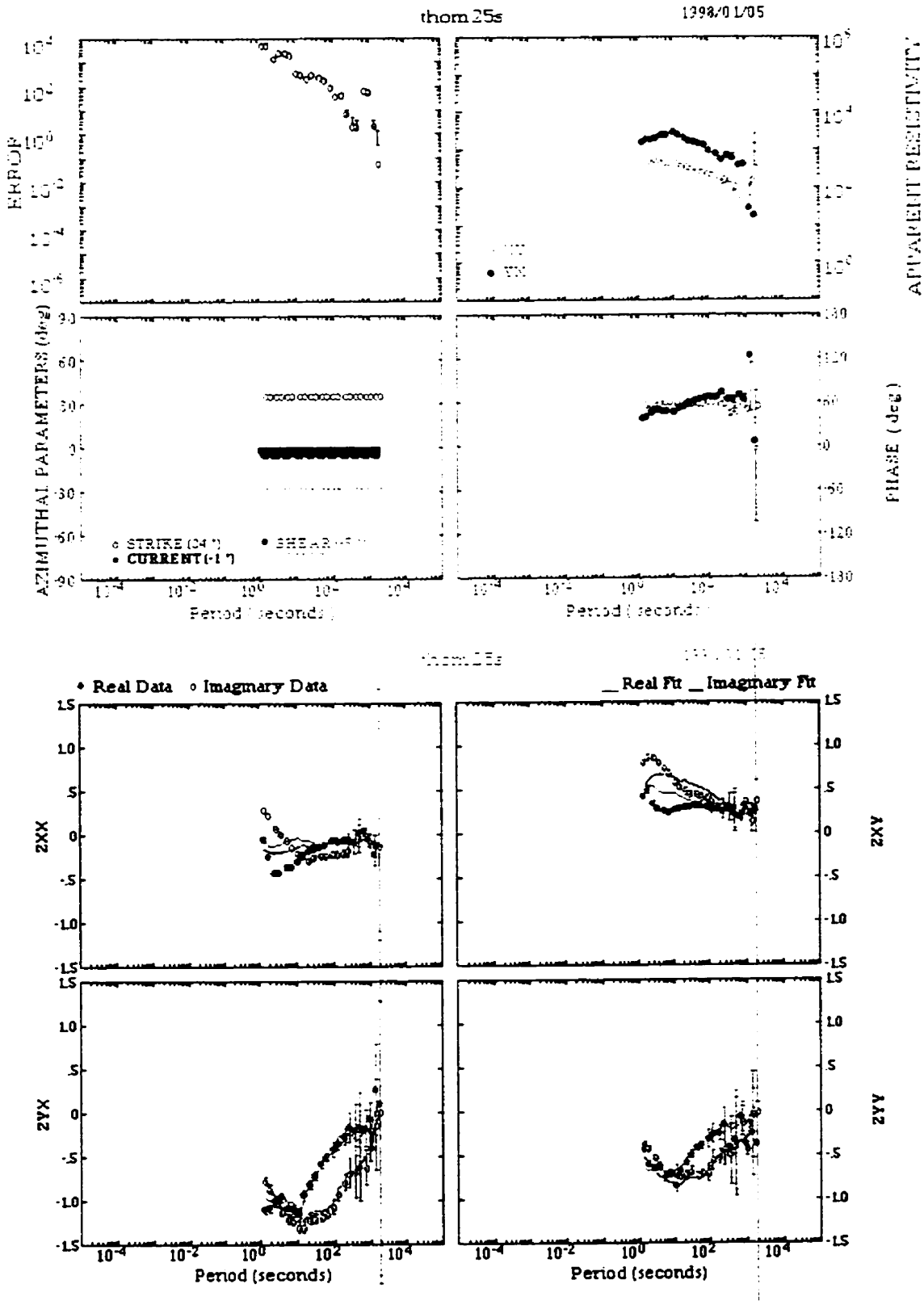
thom25s
1398/01/05
ERROR
APPARENT RESISTIVITY
AZIMUTHAL PARAMETERS (deg)
PHASE (deg)
STRIKE (34°)
CURRENT (-1°)
Period (seconds)
Real Data
Imagmary Data
Real Fit
Imagmary Fit
ZXX
ZXY
ZYX
ZYY
Period (seconds)

THO-92-M24S

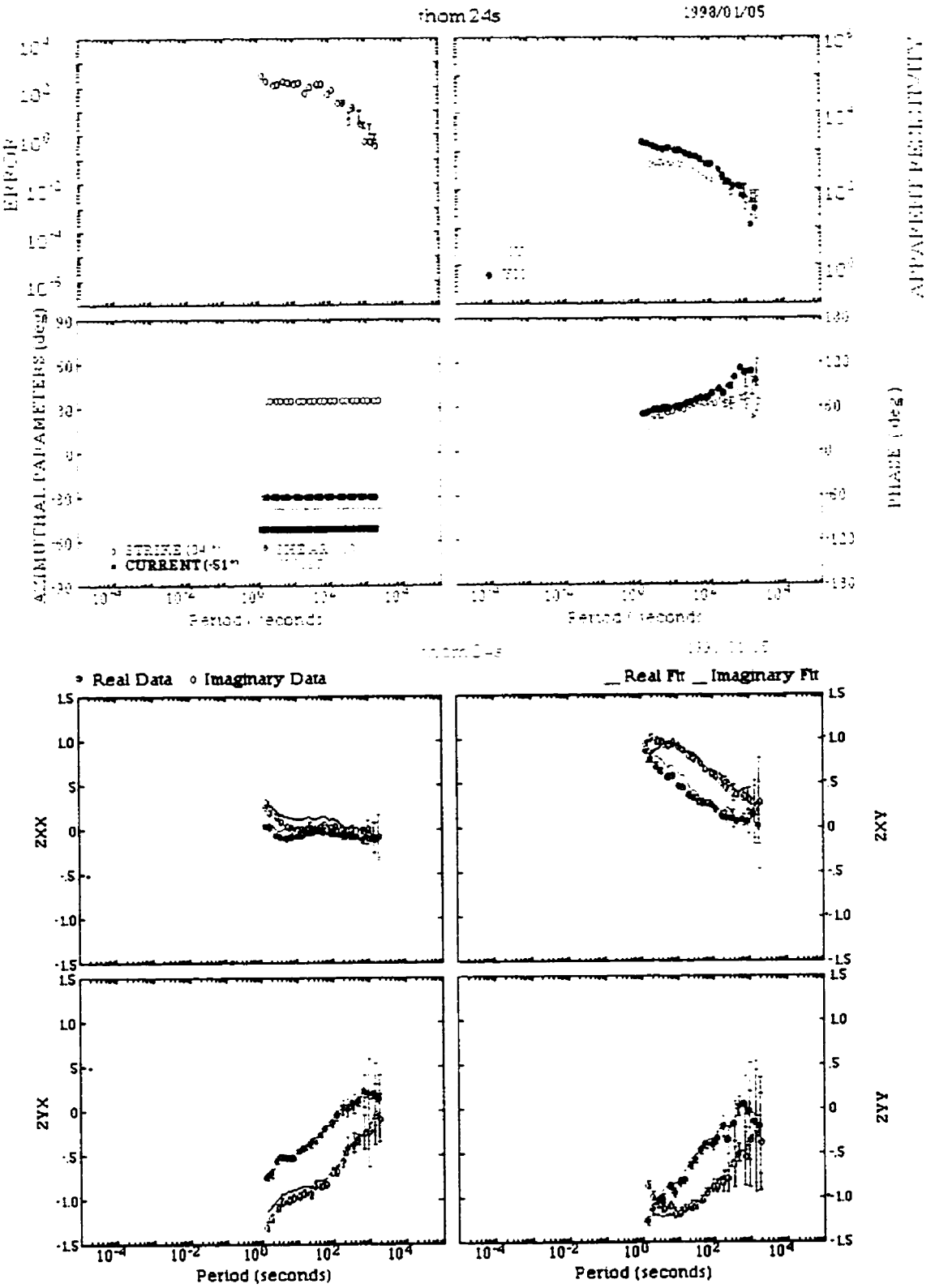
thom24s
1998/01/05
CURRENT(-51°
Period (seconds)
Real Data
Imaginary Data
Real Fit
Imaginary Fit
ZXX
ZXY
ZYX
ZYY
Period (seconds)

THO-92-M23S

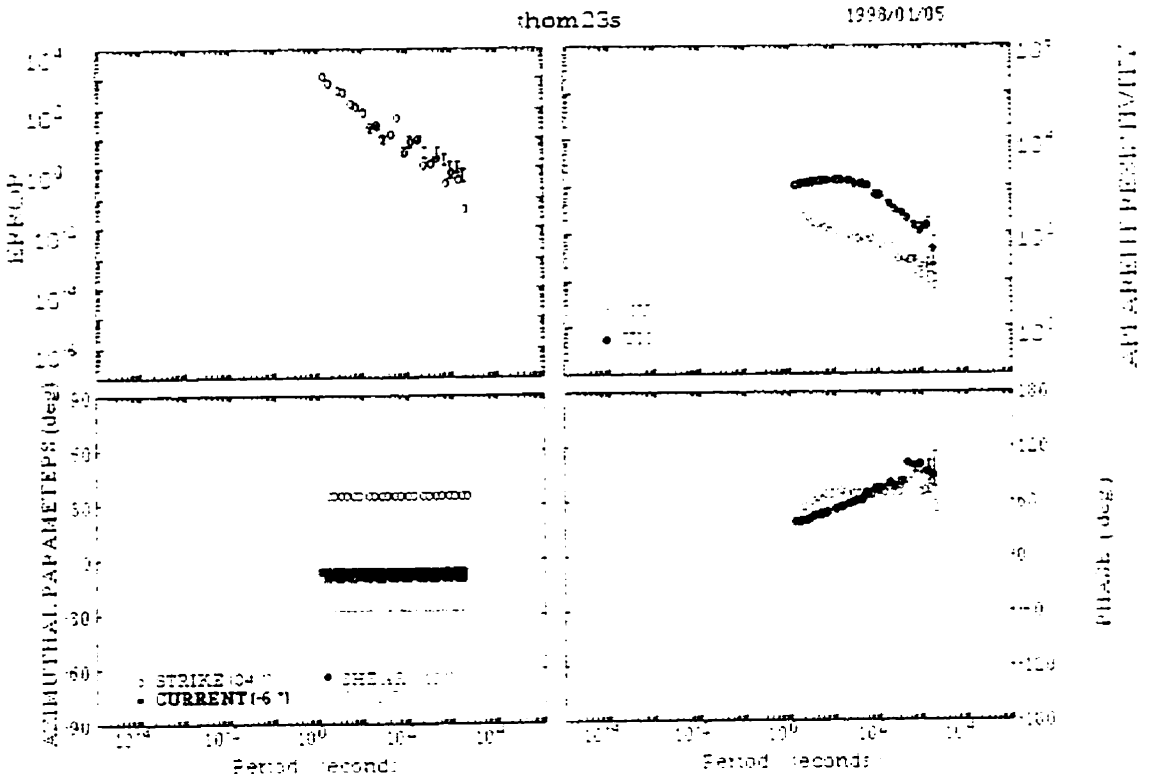
thom23s
1998/01/05
AZIMUTHAL PARAMETERS (deg)
STRIKE
CURRENT (-6 °)
Period (seconds)

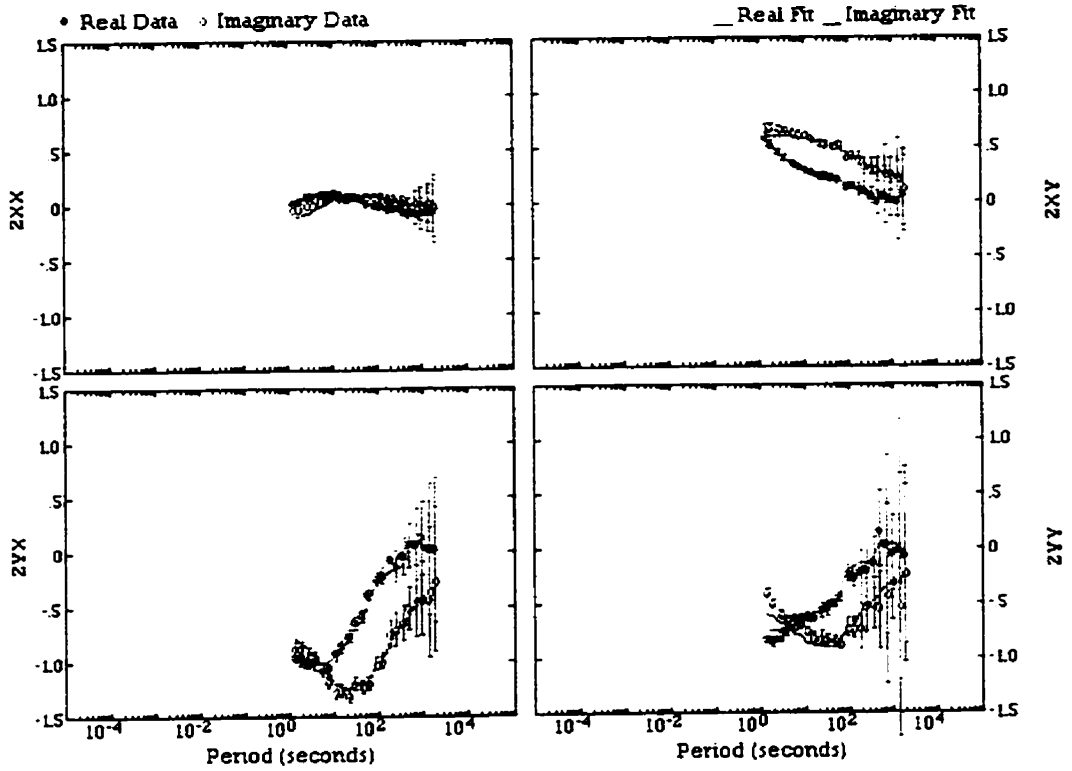
• Real Data ◦ Imaginary Data
_ Real Fit _ Imaginary Fit
ZXX
ZXZ
ZYX
ZYZ
Period (seconds)
Period (seconds)

THO-92-M22S

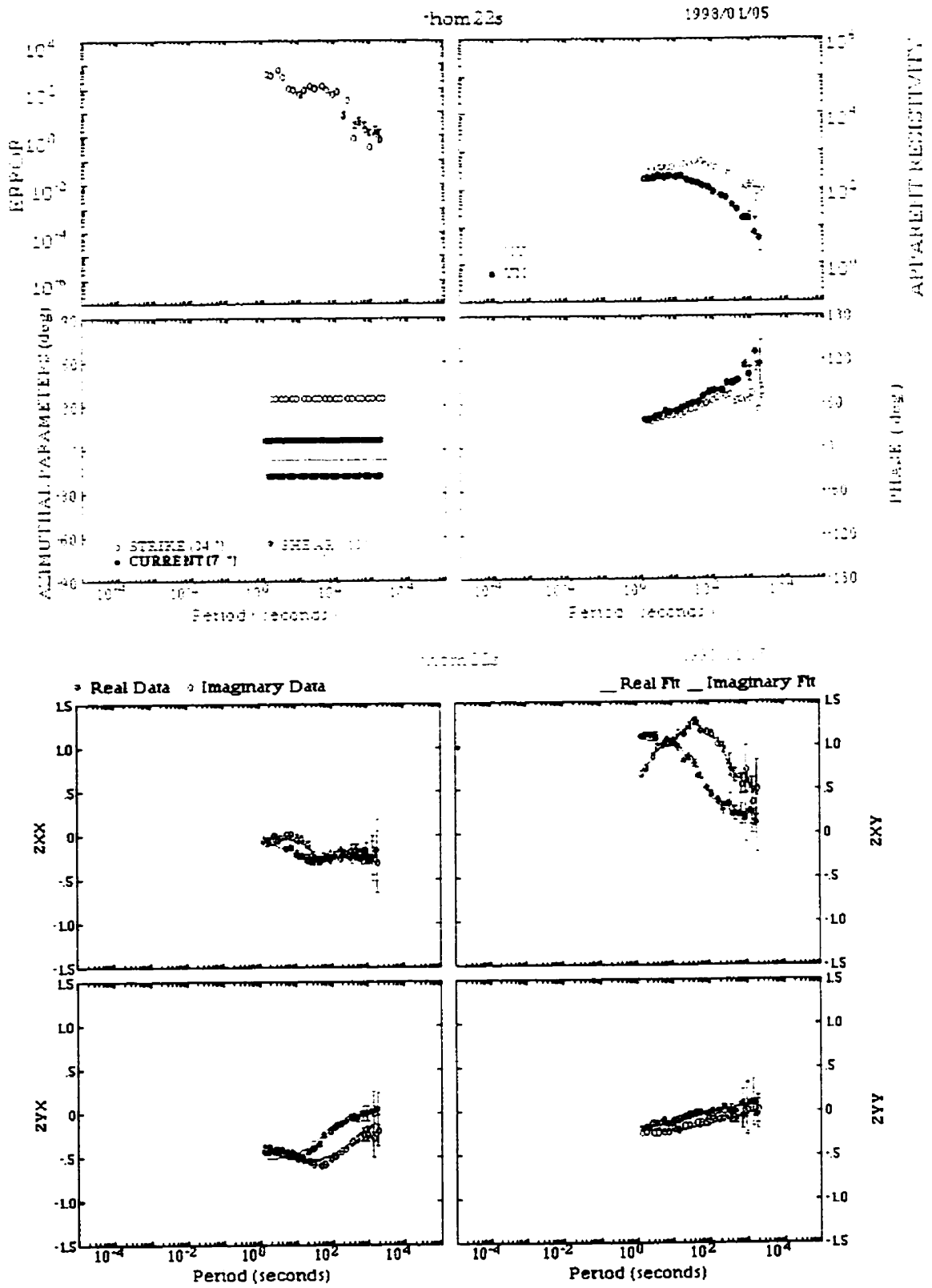
thom22s
1993/01/05
AZIMUTHAL PARAMETERS (deg)
CURRENT (7 °)
Period (seconds)
Real Data
Imaginary Data
Real Fit
Imaginary Fit
ZXX
ZXY
ZYX
ZYY
Period (seconds)
Period (seconds)

THO-92-M21S

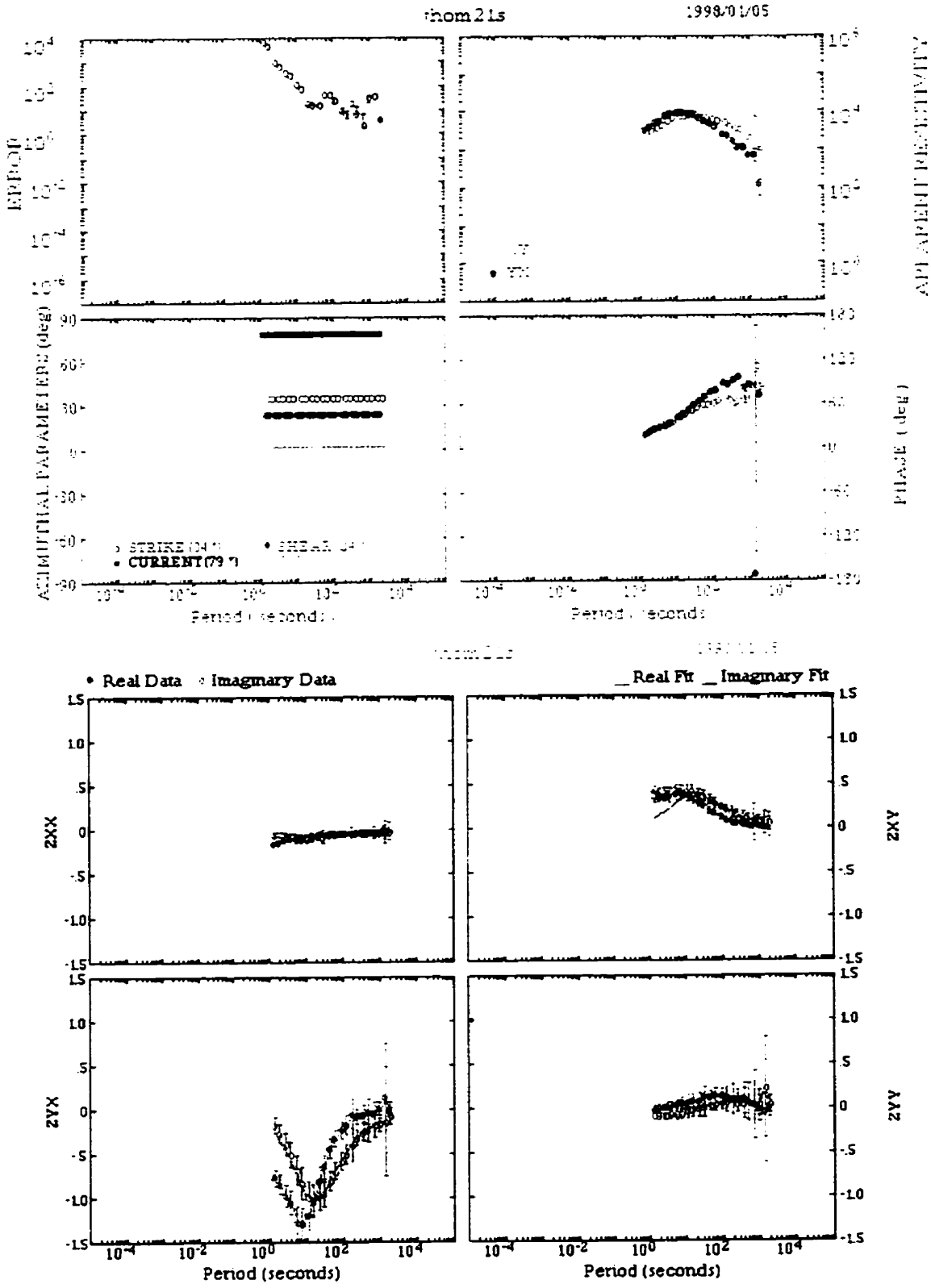
thom21s
1998/01/05
Period (seconds)
CURRENT
Real Data
Imaginary Data
Real Fit
Imaginary Fit
ZXX
ZXY
ZYX
ZYY
Period (seconds)

THO-92-M20S

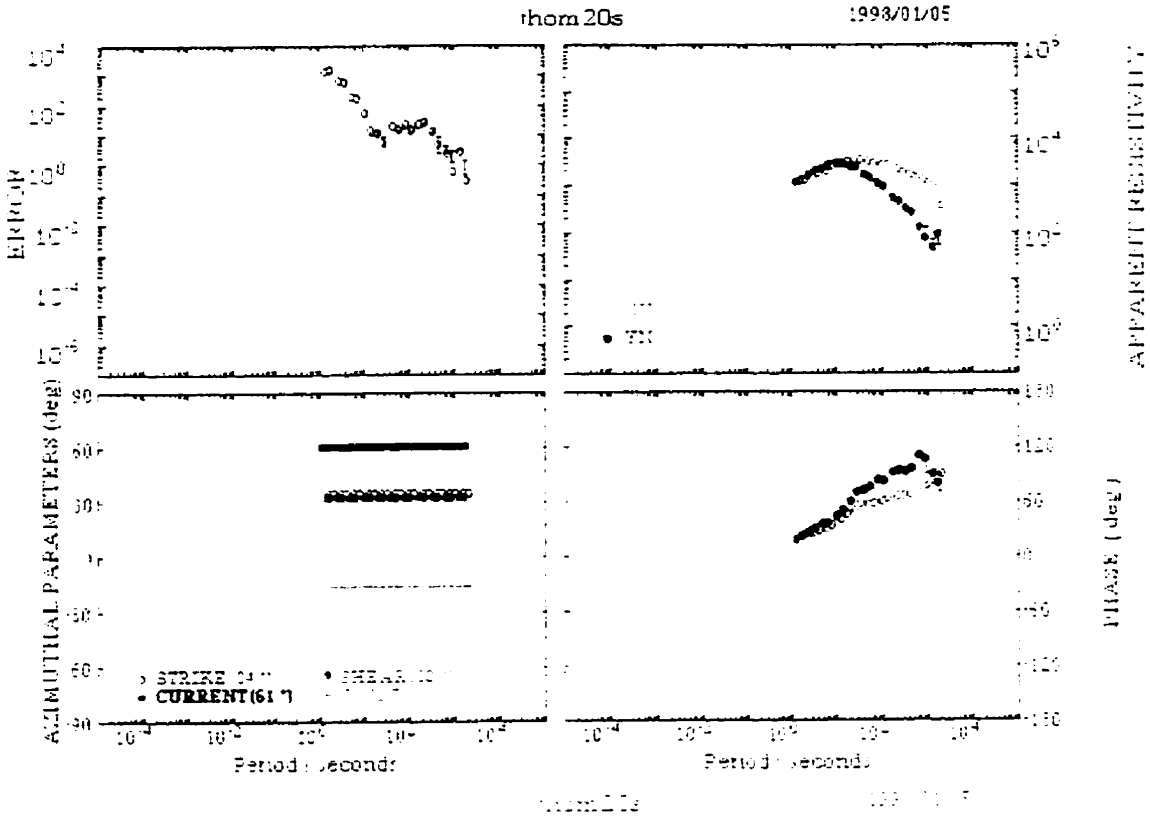
thom 20s
1998/01/05
AZIMUTHAL PARAMETERS (deg)
CURRENT(61°)
Period (seconds)
Period (seconds)

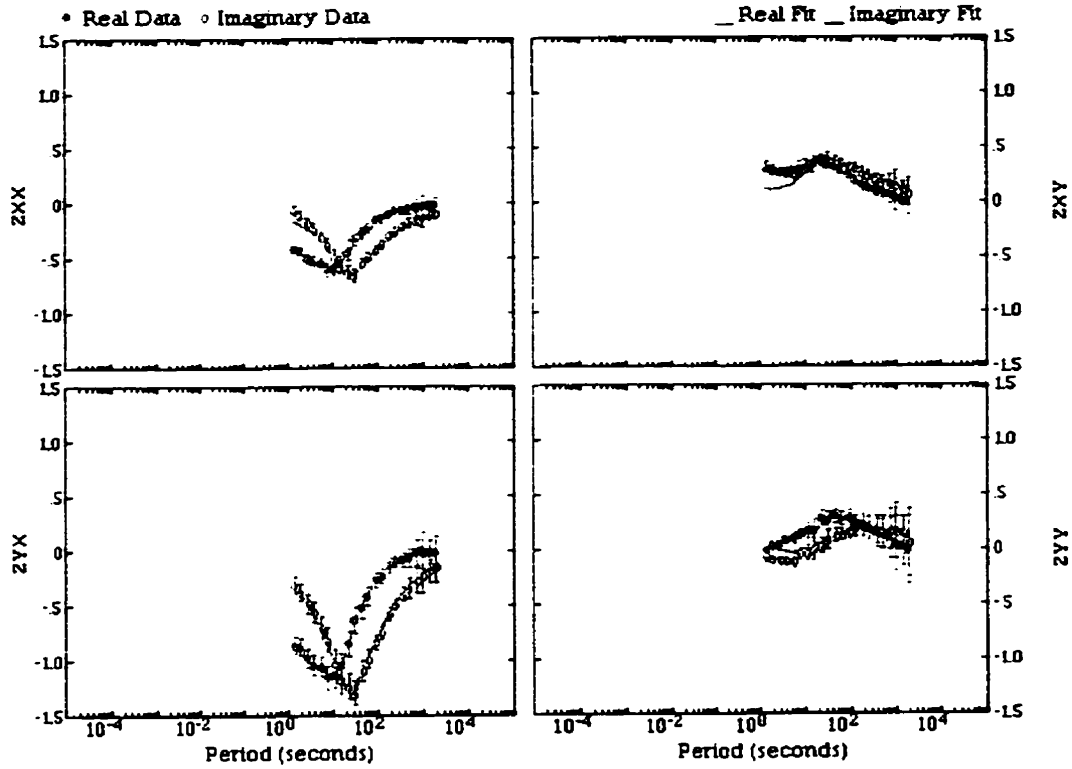
• Real Data ◦ Imaginary Data
_ Real Fit _ Imaginary Fit
ZXX
ZXY
ZYX
ZYY
Period (seconds)
Period (seconds)

THO-92-M19S

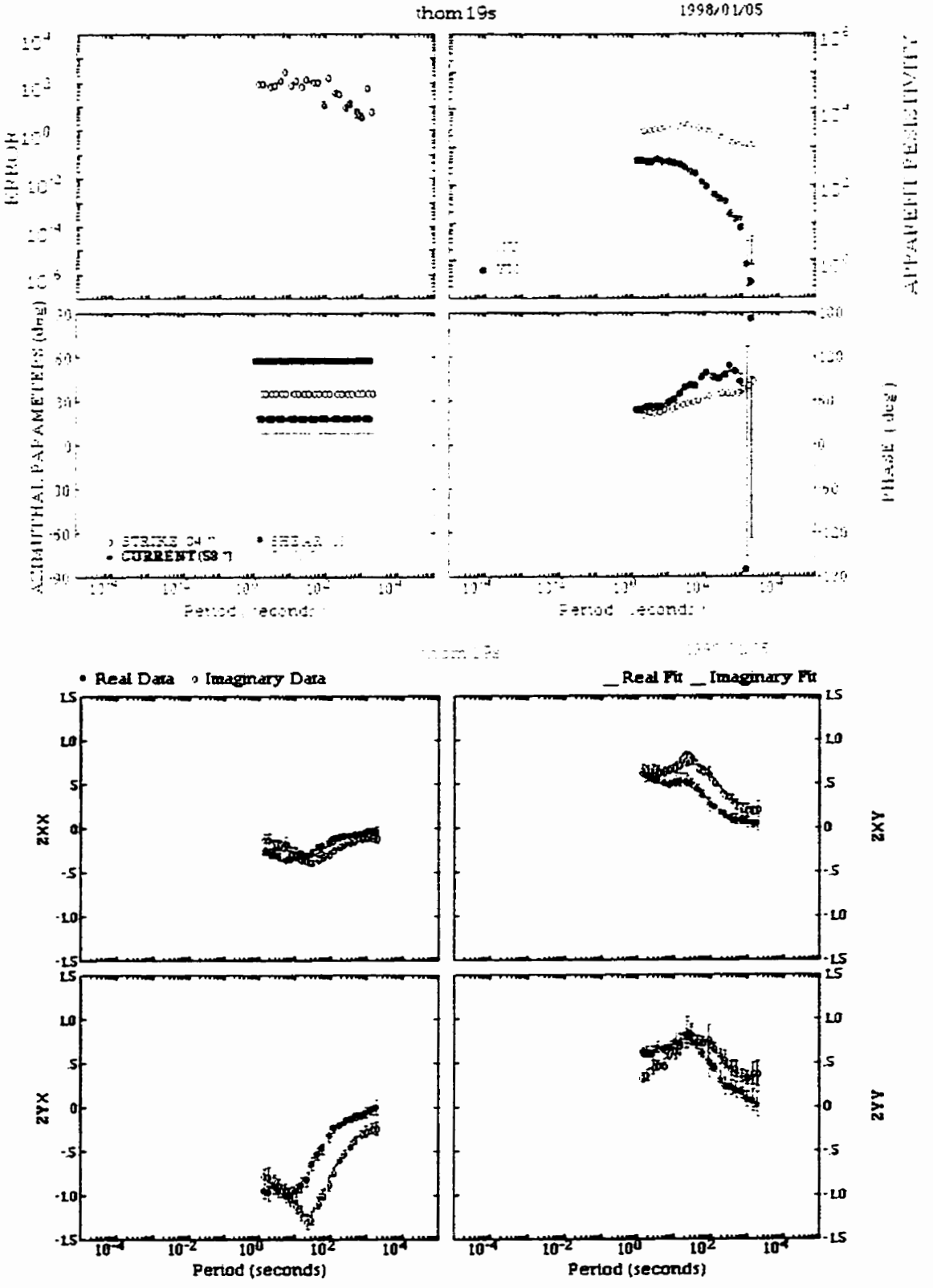
thom19s
1998/01/05
Period (seconds)
CURRENT(S8)
Real Data
Imaginary Data
Real Fit
Imaginary Fit
ZXX
ZXY
ZYX
ZYY
Period (seconds)

THO-92-M18S

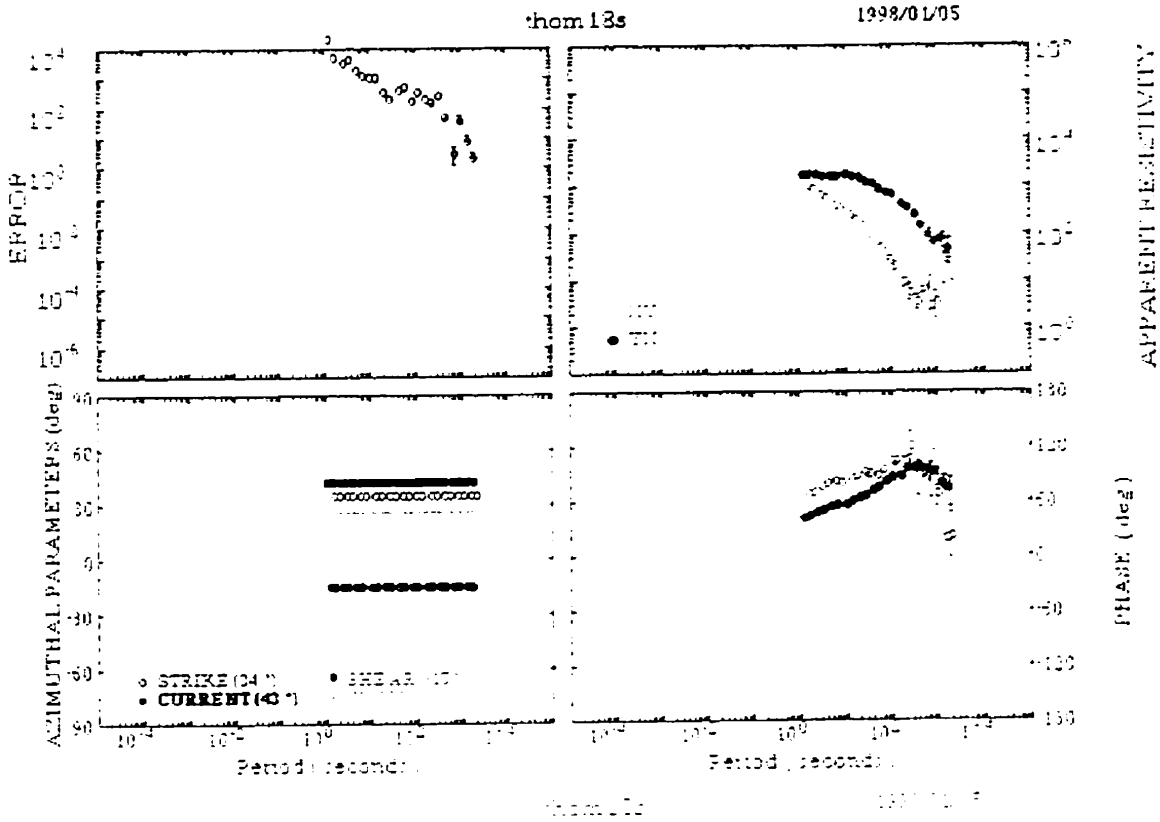
thom18s
1998/01/05
ERROR
APPARENT RESISTIVITY
AZIMUTHAL PARAMETERS (deg)
PHASE (deg)
STRIKE (34 °)
CURRENT (40 °)
Period (seconds)

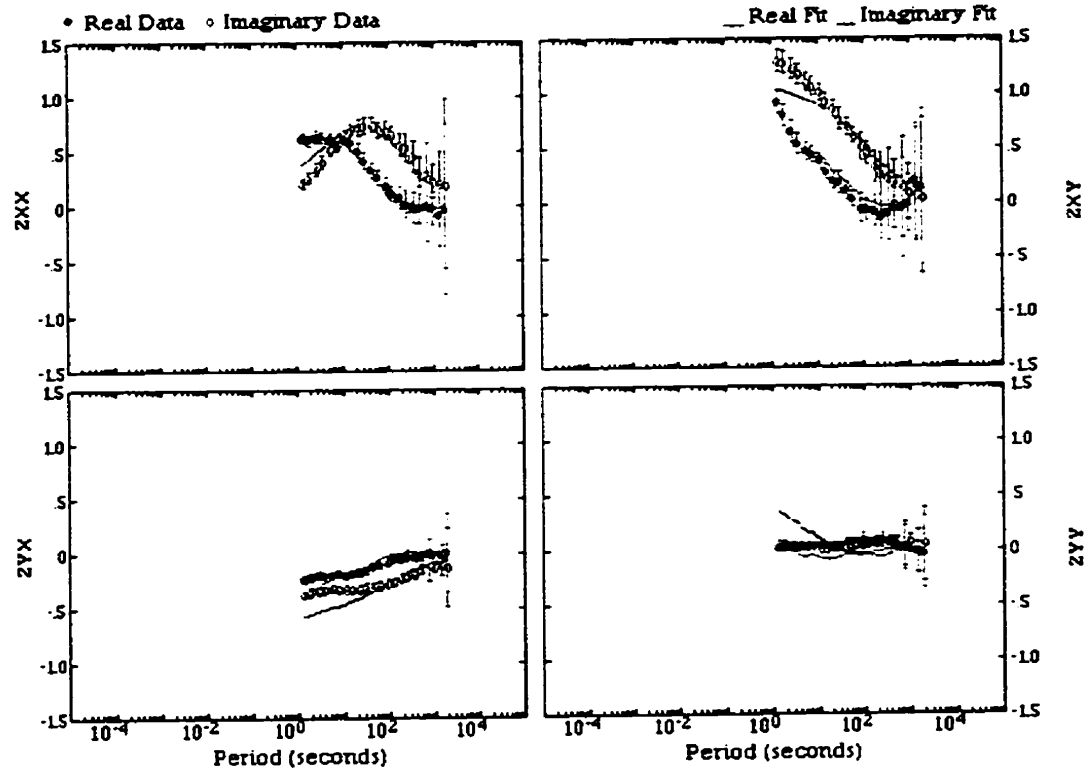
Real Data
Imaginary Data
Real Fit
Imaginary Fit
ZXX
ZXY
ZYX
ZYY
Period (seconds)
Period (seconds)

THO-92-M16S

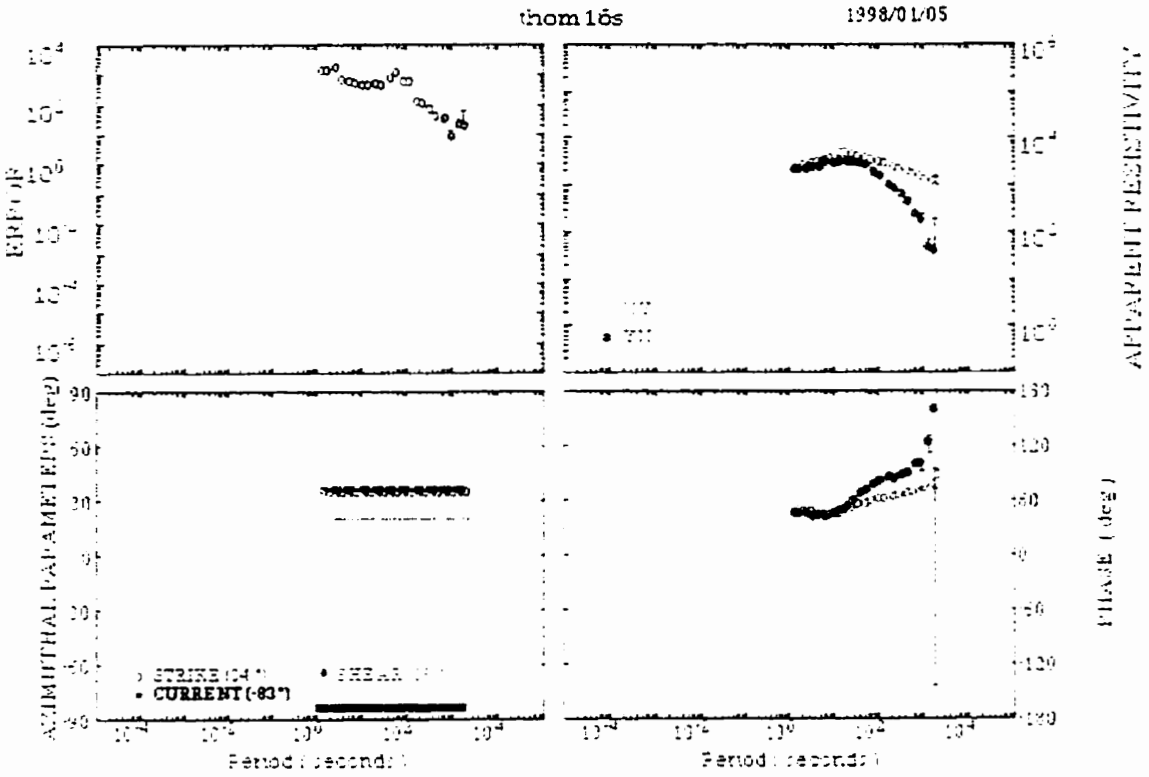
thom16s
1998/01/05
CURRENT (-83°)
Period (seconds)

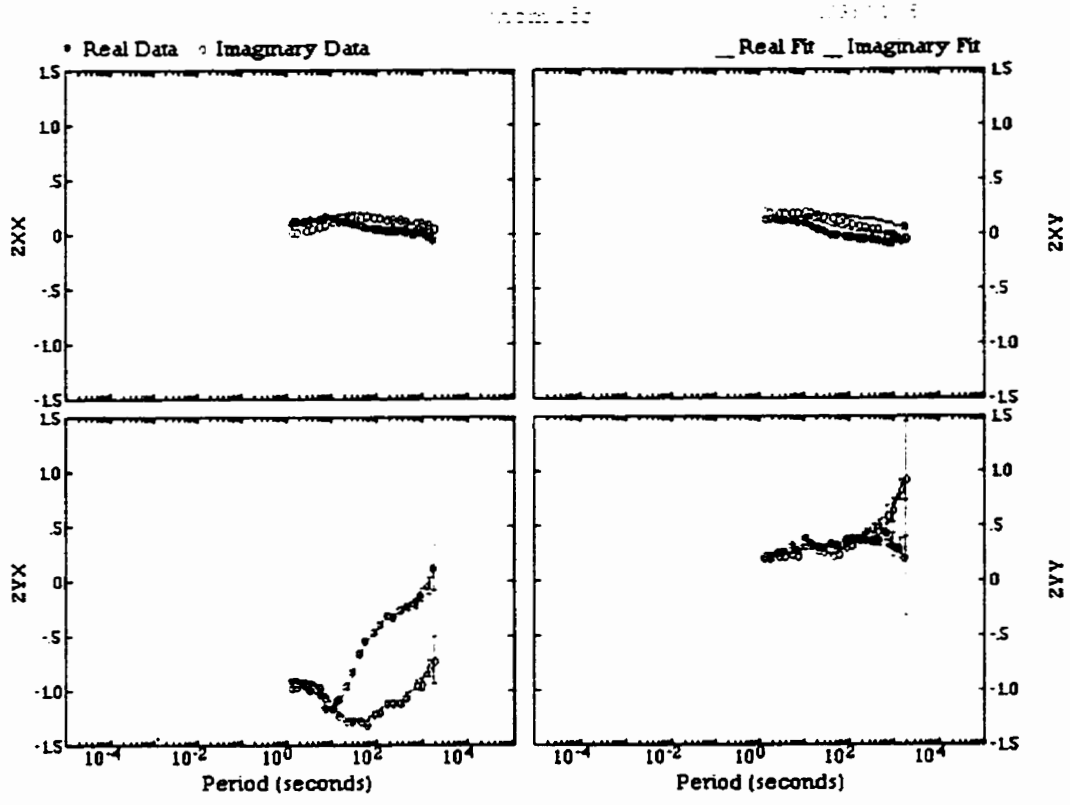
Real Data
Imaginary Data
Real Fit
Imaginary Fit
ZXX
ZXY
ZYX
ZYY
Period (seconds)
Period (seconds)

THO-92-M15S

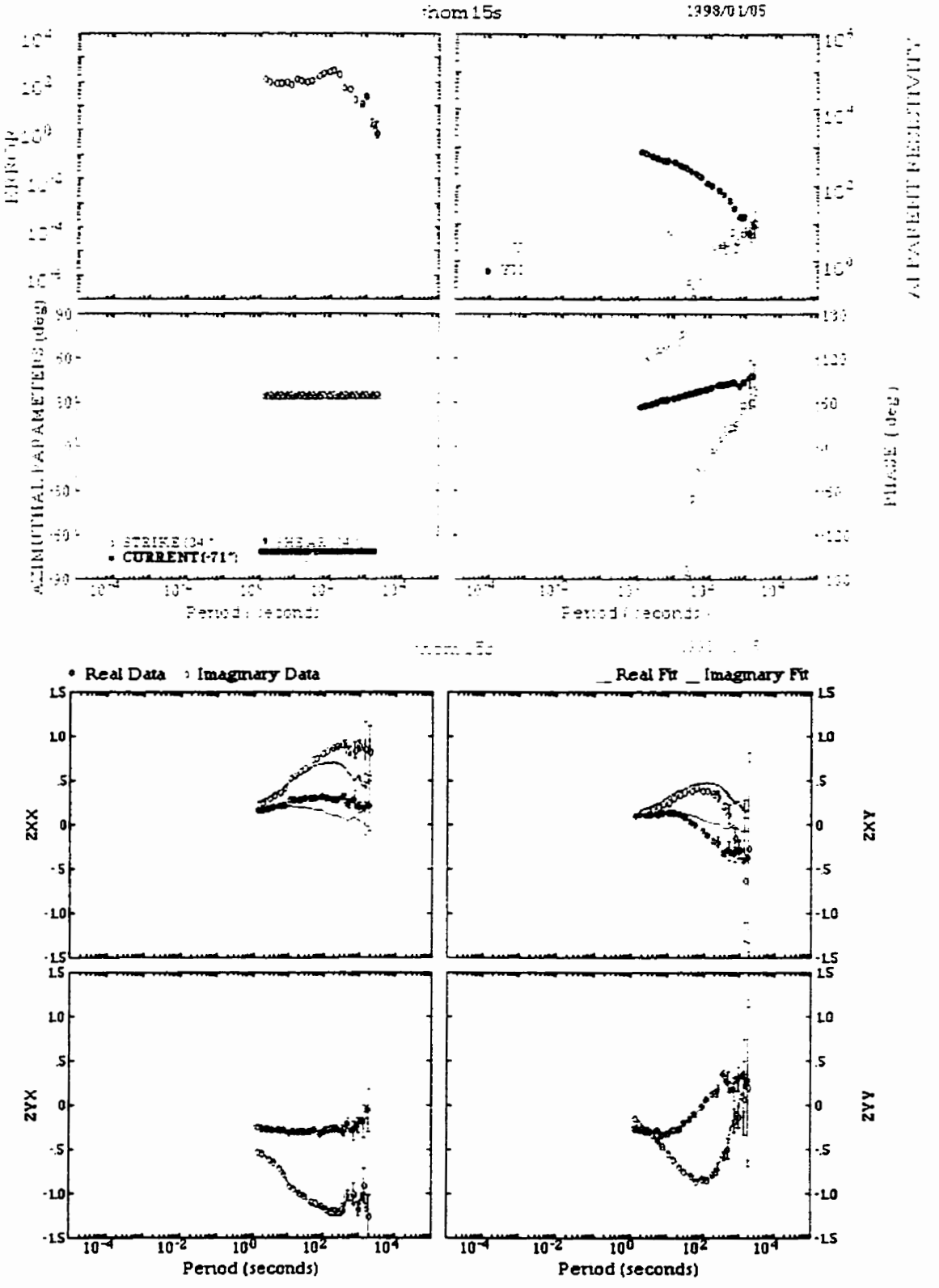
thom15s
1998/01/05
AZIMUTHAL PARAMETERS (deg)
STRIKE (34°)
CURRENT (-71°)
Period (seconds)
APPARENT RESISTIVITY
PHASE (deg)
Real Data
Imaginary Data
Real Fit
Imaginary Fit
ZXX
ZXY
ZYX
ZYY
Period (seconds)

THO-92-M13S

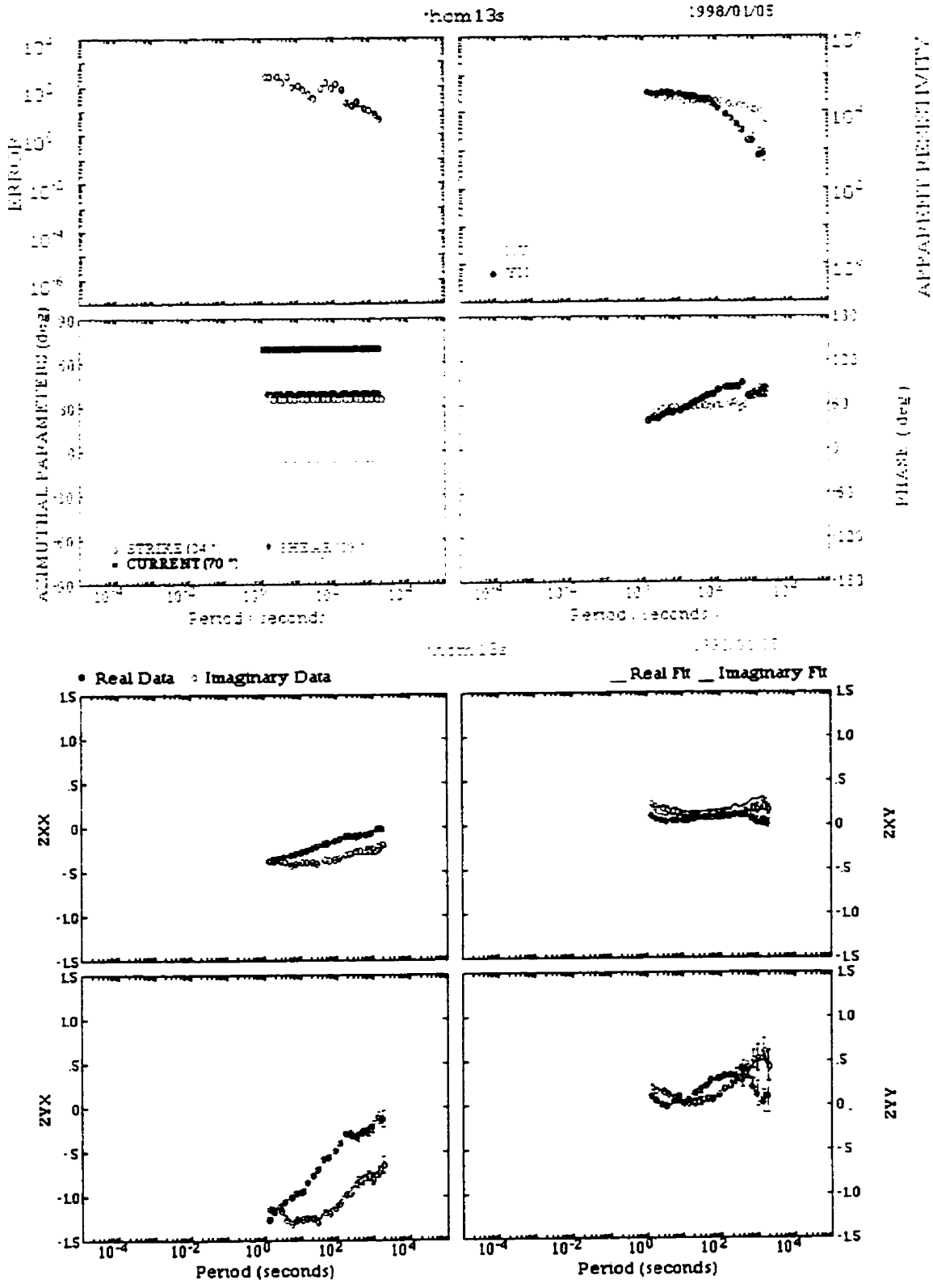
thom13s
1998/01/05
ERROR
APPARENT RESISTIVITY
AZIMUTHAL PARAMETERS (deg)
PHASE (deg)
CURRENT (70 °)
Period (seconds)
Real Data
Imaginary Data
Real Fit
Imaginary Fit
ZXX
ZXY
ZYX
ZYY
Period (seconds)

THO-92-M12S

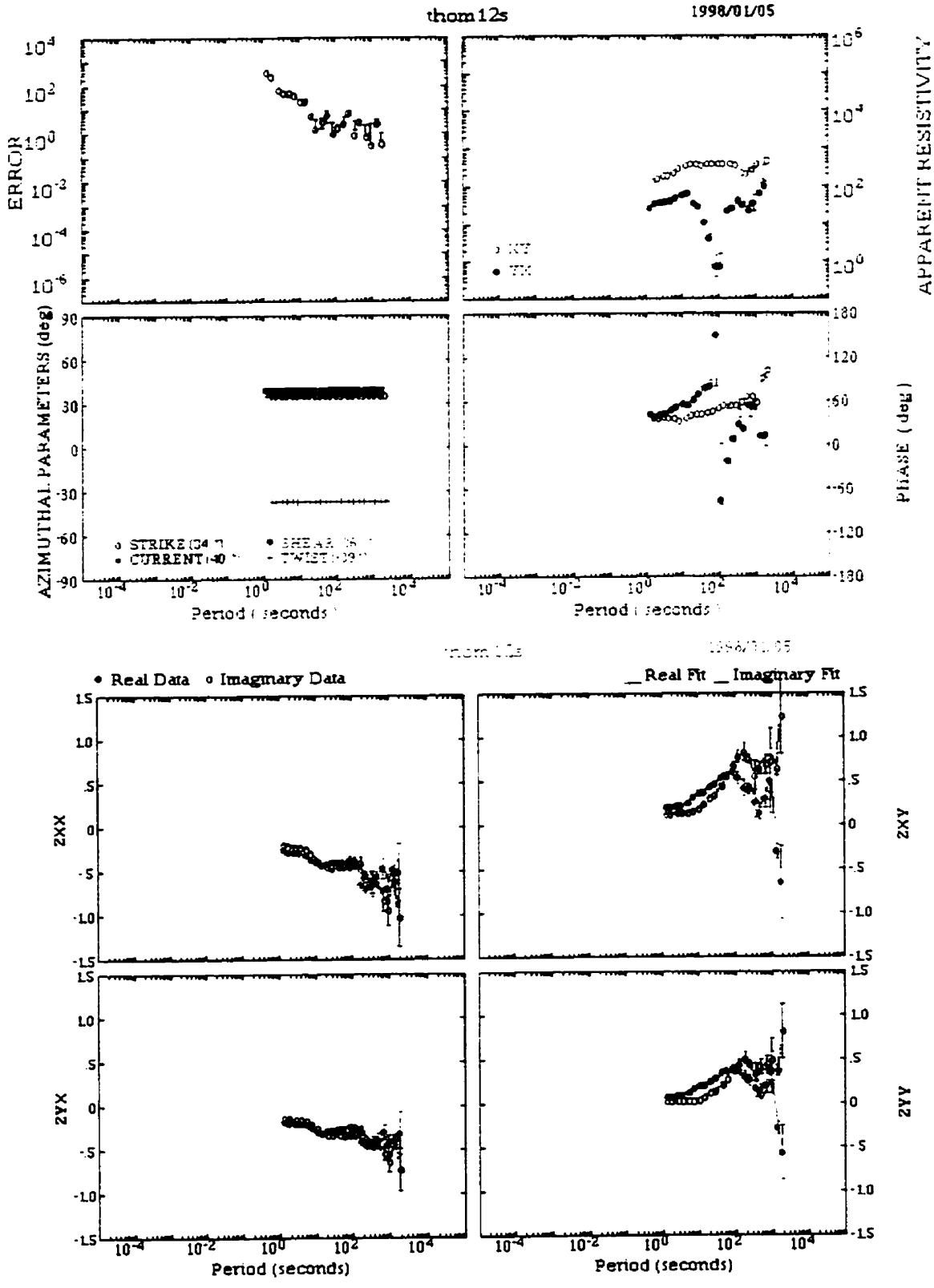
thom12s
1998/01/05
ERROR
APPARENT RESISTIVITY
AZIMUTHAL PARAMETERS (deg)
PHASE (deg)
Period (seconds)
STRIKE
CURRENT
Real Data
Imaginary Data
Real Fit
Imaginary Fit
ZXX
ZXY
ZYX
ZYY
Period (seconds)

THO-92-M11S

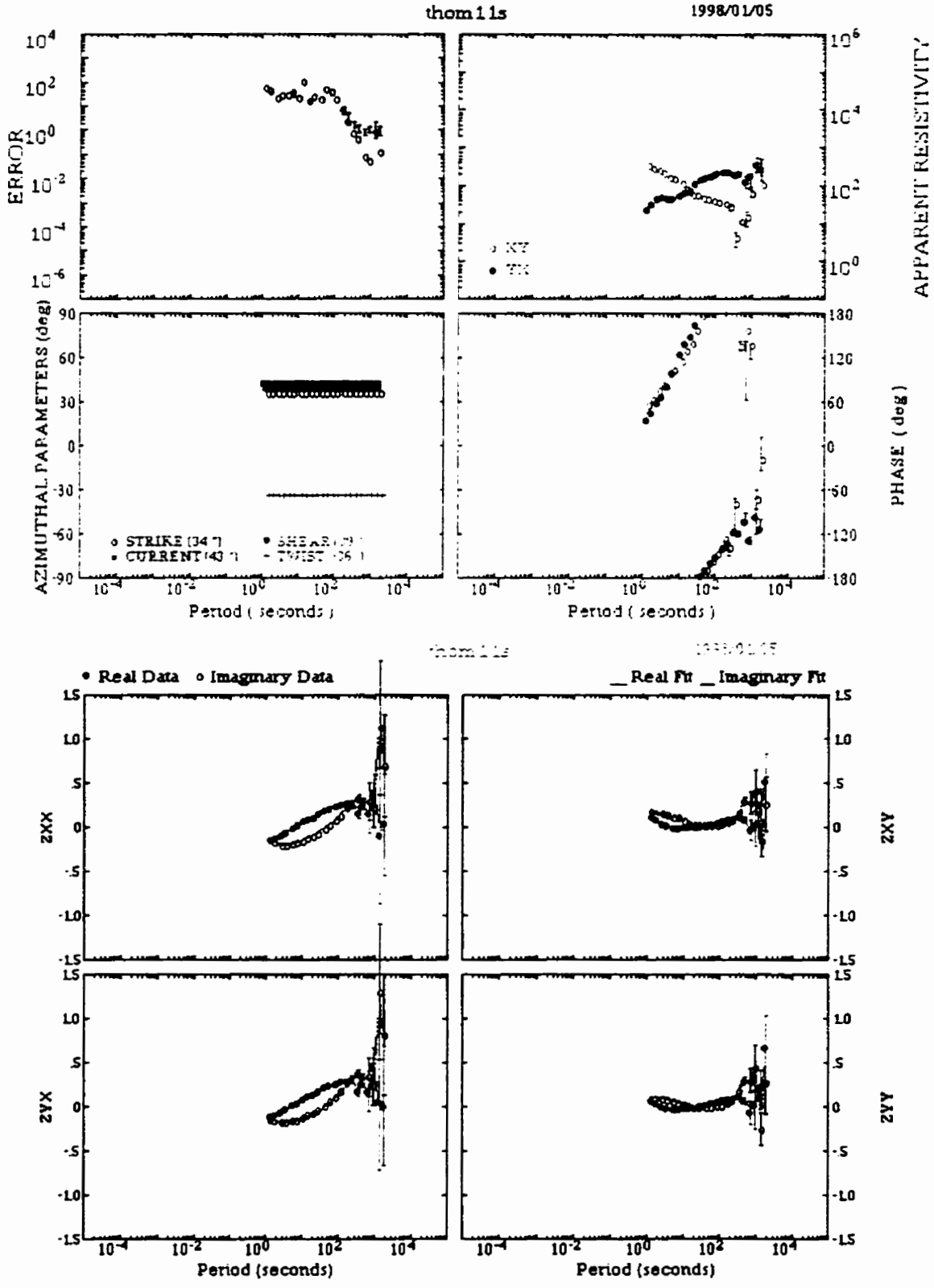
thom11s
1998/01/05
ERROR
APPARENT RESISTIVITY
AZIMUTHAL PARAMETERS (deg)
PHASE (deg)
Period (seconds)
Real Data
Imaginary Data
Real Fit
Imaginary Fit
ZXX
ZXY
ZYX
ZYY

THO-92-M46S

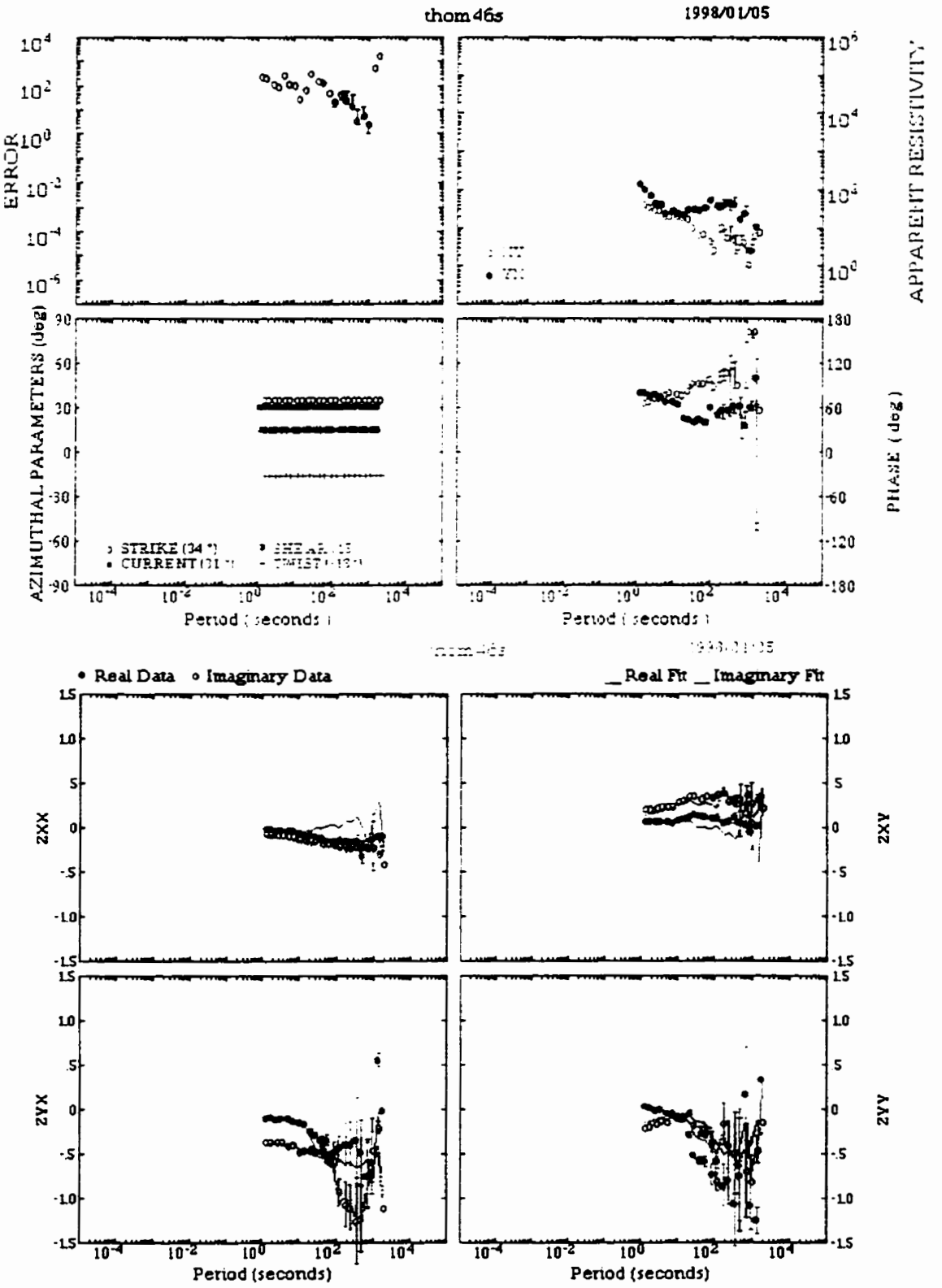
thom46s
1998/01/05
ERROR
APPARENT RESISTIVITY
AZIMUTHAL PARAMETERS (deg)
PHASE (deg)
STRIKE (34 °)
CURRENT (31 °)
Period (seconds)
Real Data
Imaginary Data
Real Fit
Imaginary Fit
ZXX
ZXY
ZYX
ZYY
Period (seconds)

2) Tabbernor Fault Zone to Sturgeon Weir Thrust (0.01 - 1000 Hz)

This appendix shows two sets of results for the fully constrained GB decomposition results using strike, twist and shear values as outlined for sites M18 to M12 in Table 4.3 for each site in this data subset. Standard plotting parameters are as described in Appendix B.

THO-92-M18S

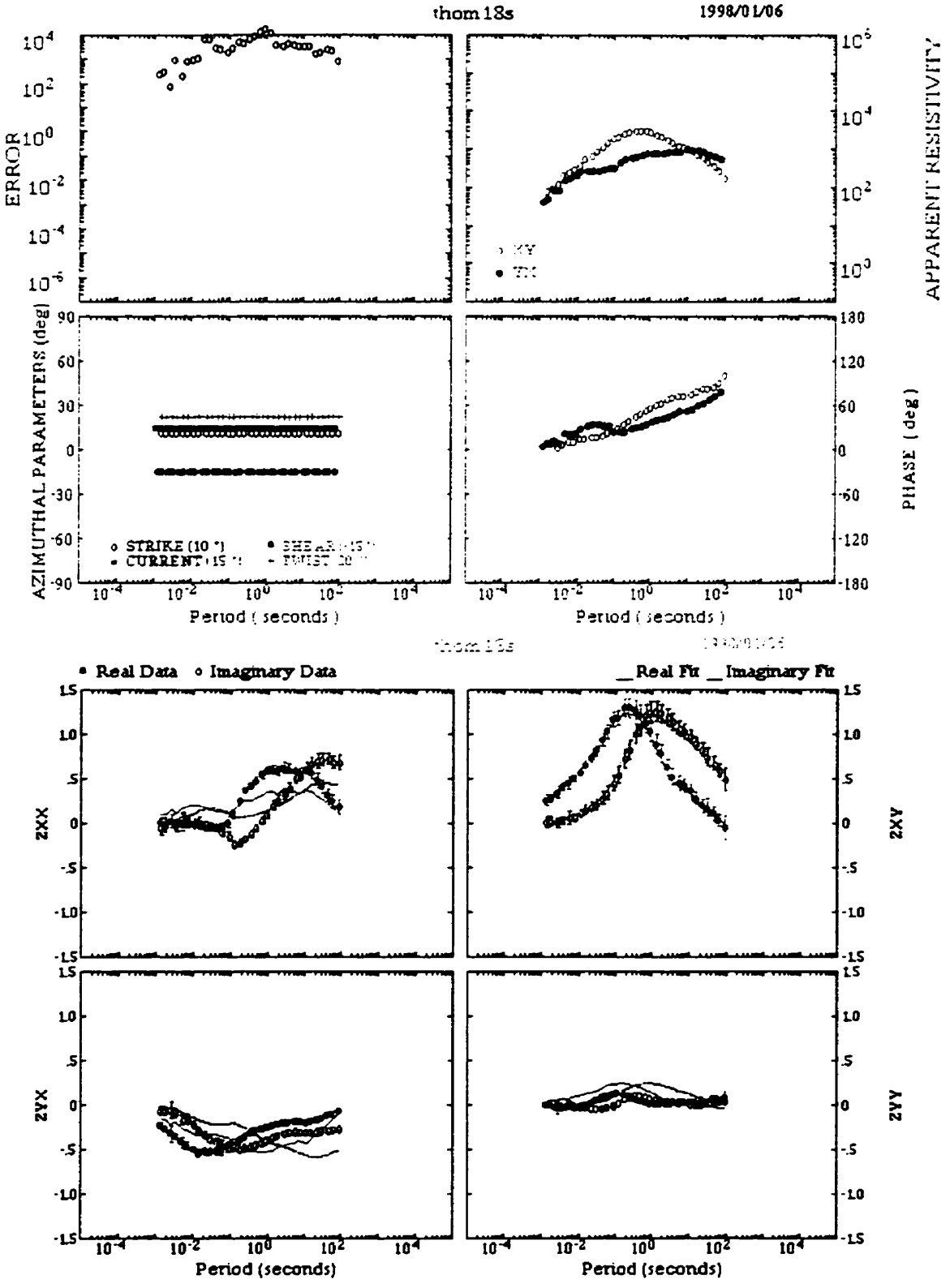
thom18s
1998/01/06
ERROR
APPARENT RESISTIVITY
AZIMUTHAL PARAMETERS (deg)
PHASE (deg)
STRIKE (10 °)
CURRENT
Period (seconds)
Real Data
Imaginary Data
Real Fit
Imaginary Fit
ZXX
ZXY
ZYX
ZYY
Period (seconds)

THO-92-M16S

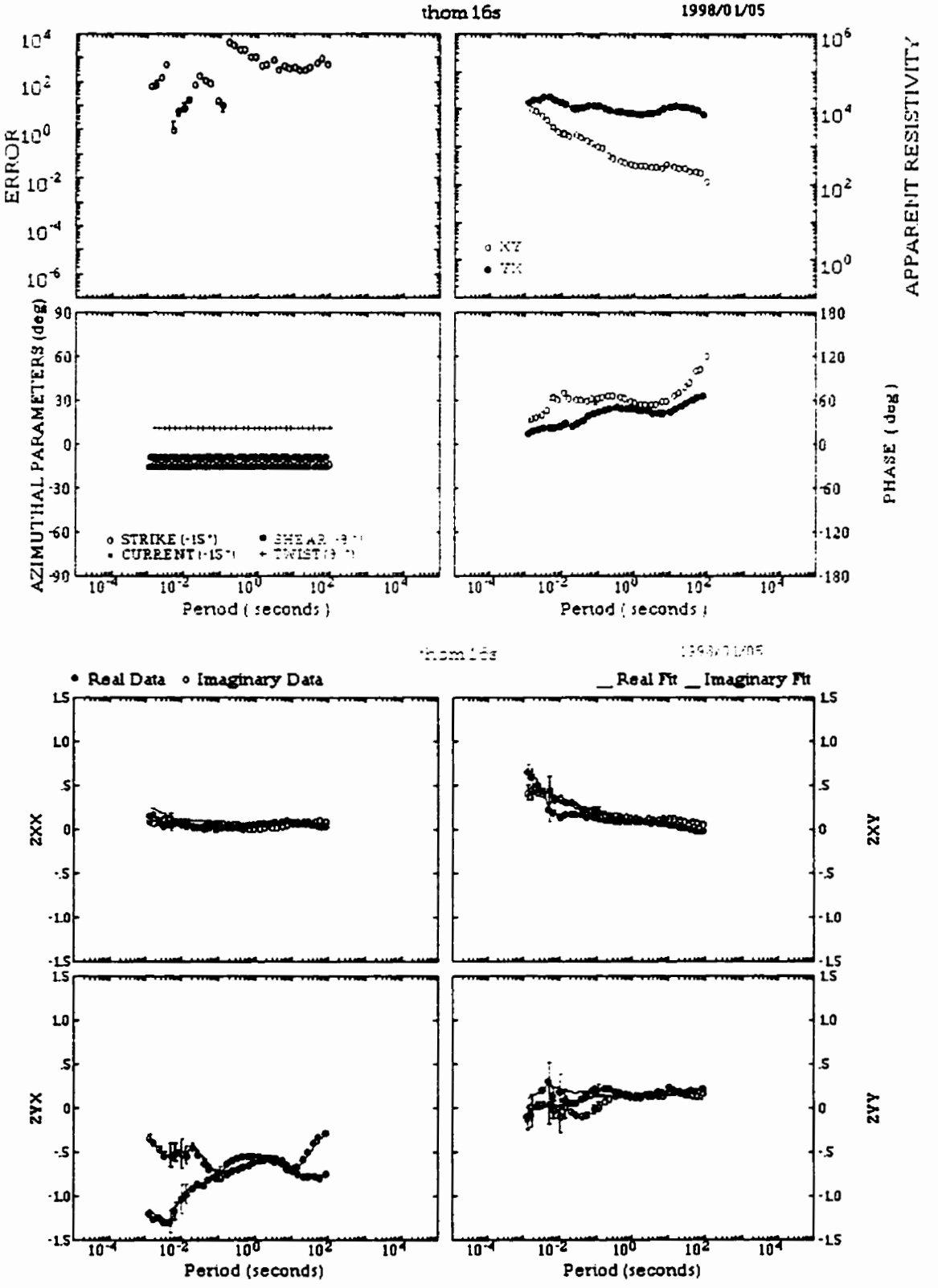
thom16s
1998/01/05
ERROR
APPARENT RESISTIVITY
AZIMUTHAL PARAMETERS (deg)
PHASE (deg)
STRIKE (-15°)
Period (seconds)
Real Data
Imaginary Data
Real Fit
Imaginary Fit
ZXX
ZXY
ZYX
ZYY

THO-92-M15S

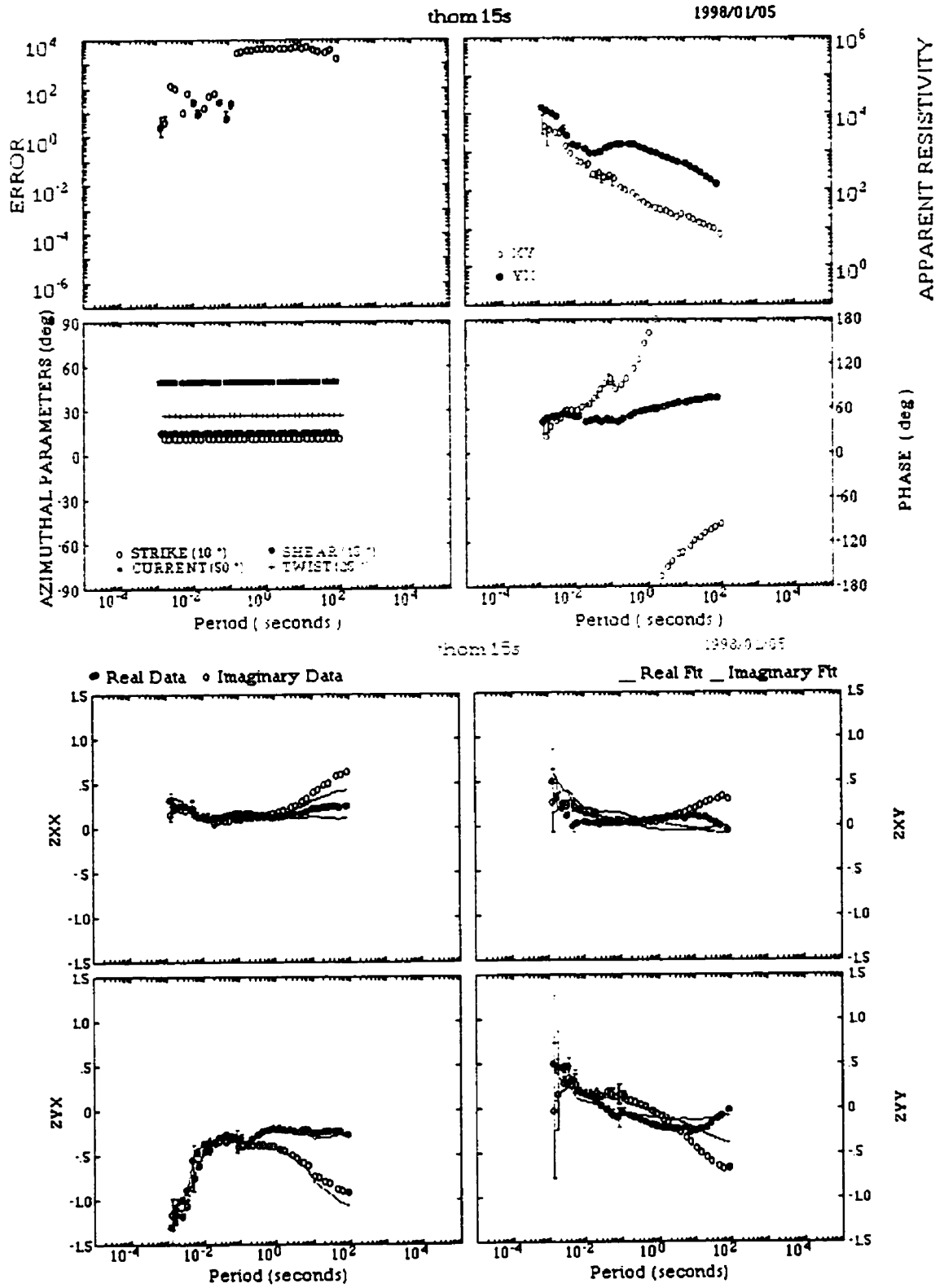
thom 15s
1998/01/05
ERROR
APPARENT RESISTIVITY
AZIMUTHAL PARAMETERS (deg)
PHASE (deg)
Period (seconds)
Real Data
Imaginary Data
Real Fit
Imaginary Fit
ZXX
ZXY
ZYX
ZYY
Period (seconds)

THO-92-M13S

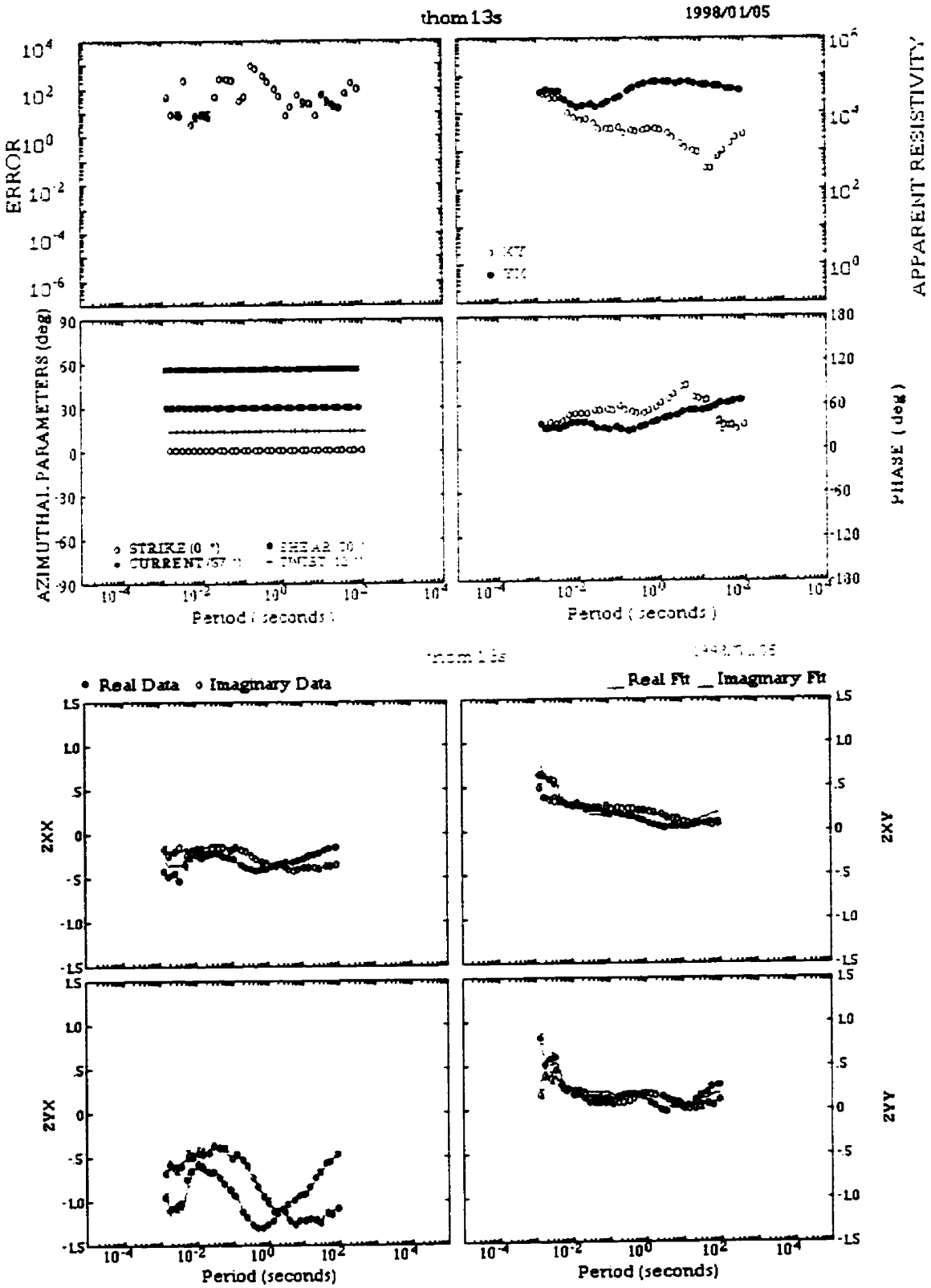
thom13s
1998/01/05
ERROR
APPARENT RESISTIVITY
AZIMUTHAL PARAMETERS (deg)
PHASE (deg)
STRIKE (0 °)
CURRENT
Period (seconds)
Real Data
Imaginary Data
Real Fit
Imaginary Fit
ZXX
ZXY
ZYX
ZYY
Period (seconds)

THO-92-M12S

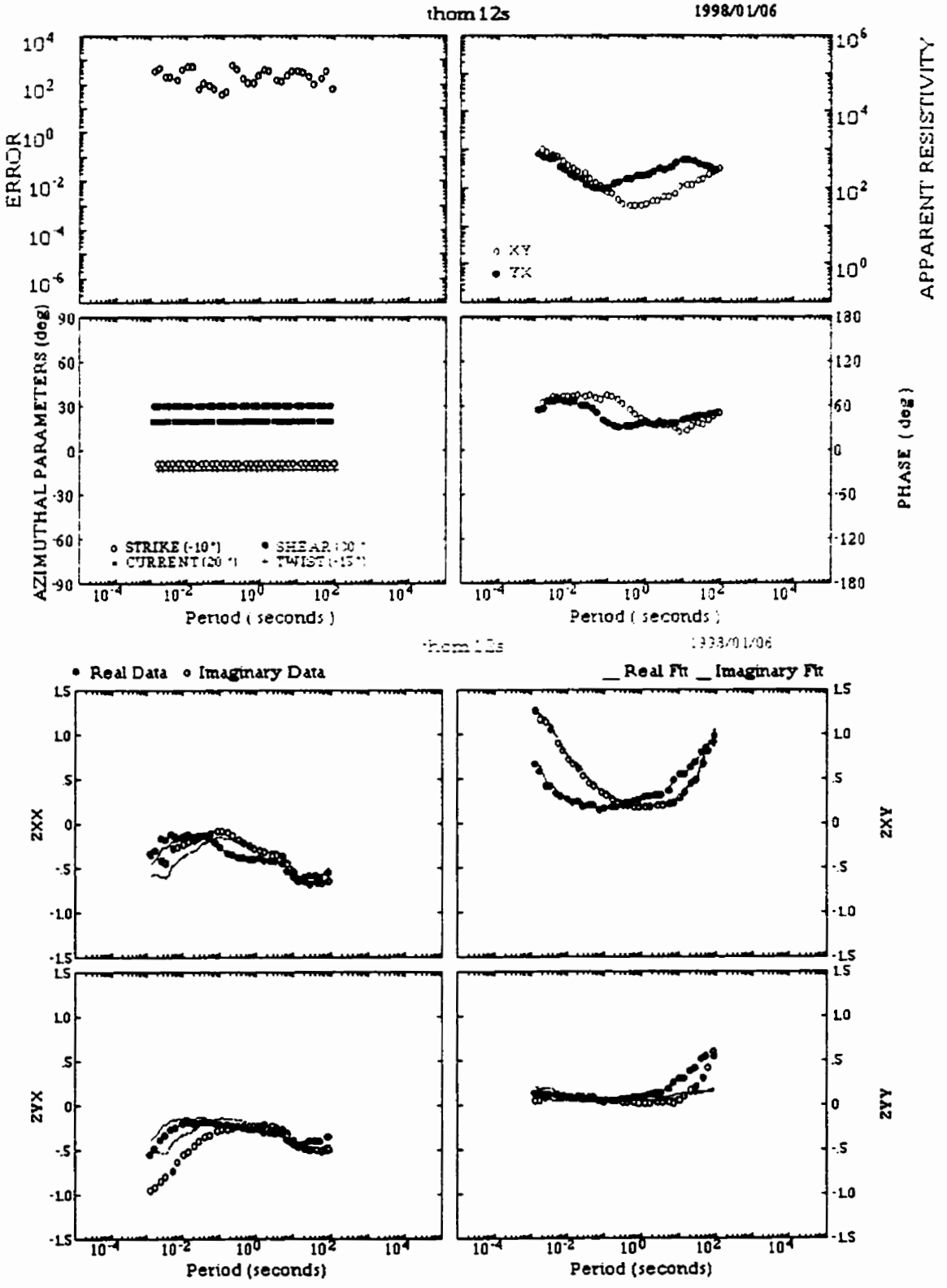
thom12s
1998/01/06
ERROR
APPARENT RESISTIVITY
AZIMUTHAL PARAMETERS (deg)
PHASE (deg)
XY
YX
STRIKE (-10°)
CURRENT (20°)
Period (seconds)
Real Data
Imaginary Data
Real Fit
Imaginary Fit
ZXX
ZXY
ZYX
ZYY

IMAGE EVALUATION
TEST TARGET (QA-3)

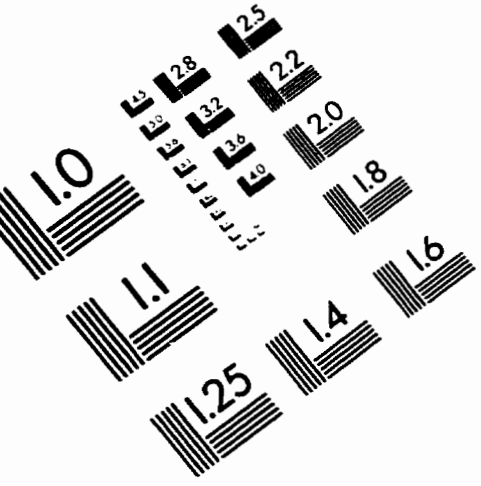

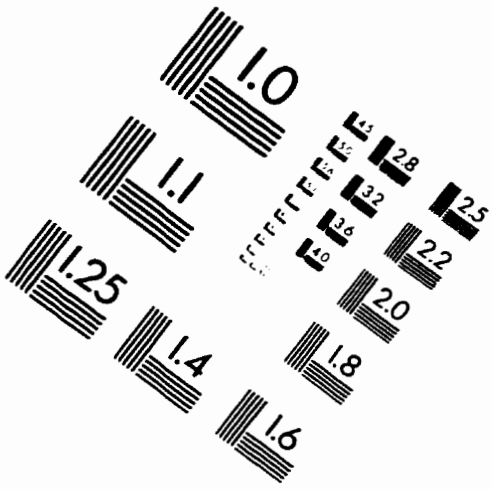

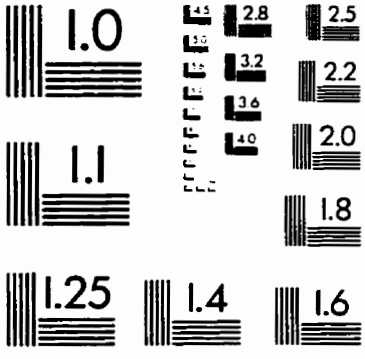

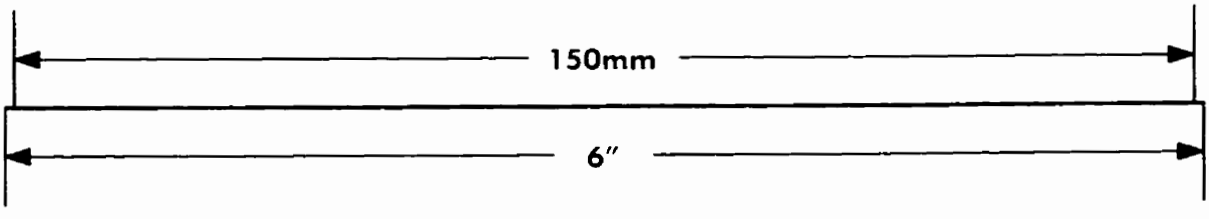

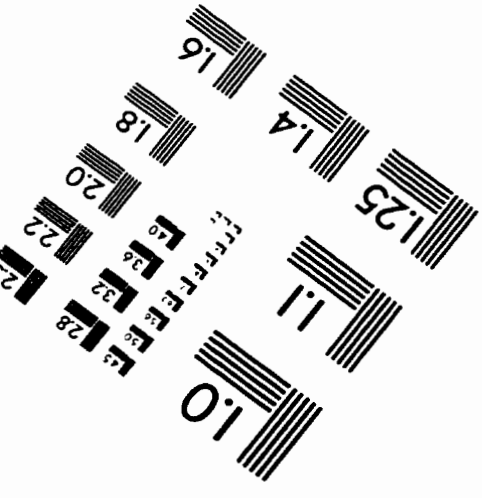

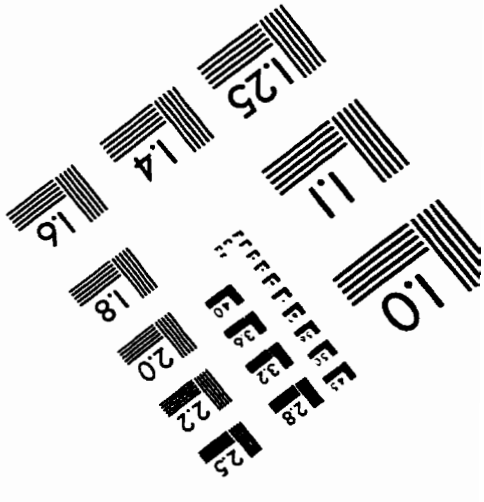

APPLIED IMAGE, Inc
1653 East Main Street
Rochester, NY 14609 USA
Phone: 716/482-0300
Fax: 716/288-5989